Squaramide-based interpenetrated networks for load-bearing applications

Chen, Y.

Squaramide-based Interpenetrated Networks for Load-bearing Applications

Proefschrift

ter verkrijging van
de graad van doctor aan de Universiteit Leiden,
op gezag van rector magnificus prof. dr. ir. H. Bijl,
volgens besluit van het college voor promoties
te verdedigen op vrijdag 8 november 2024
klokke 10:00 uur

door

Ying Chen
geboren te Zhejiang, China
in 1992

Promotores
Prof. dr. A. Kros
dr. R.E. Kieltyka

Promotiecommissie
Prof. dr. M. Ubbink
Prof. dr. R.T. Dame
Prof. dr. I.K. Voets (Eindhoven University of Technology)
Prof. dr. I. Meulenbelt (Leiden University Medical Center)
dr. L.M.M. Jawerth

The cover artwork of this thesis is inspired by Vasily Kandinsky's 1923 painting “Circles in a Circle”.

ISBN: 978-94-6506-487-1

Table of contents

Chapter 1

Introduction

1.1. The concept and design of 3D cell culture models *in vitro*

In the 1980s, Mina Bissell demonstrated the significance of the culture environment on cellular behaviour paving the way for *in vitro* 3D cell culture.[1,2] In this study she investigated casein production in mouse mammary epithelial cells when cultured in an extracellular matrix (ECM) derived from Engelbreth-Holm-Swarm (EHS) tumor cells that resembles the *in vivo* basement membrane. Distinct morphological differences between cells cultured on tissue culture plastic and in the EHS matrix were observed, with the latter exhibiting the formation of structures that comprise the secretory alveoli. Since this seminal finding, 3D cell models continue to show their utility in closing the gap with the *in vivo* condition in relation to 2D culture.[3,4] 3D cellular models better replicate characteristics of the natural tissue environment that can have an effect on cell morphology, proliferation, and differentiation.[3,4] Today, 3D cell culture is being explored broadly in several areas that can impact healthcare including tissue regeneration, therapeutic applications, pharmaceutical research, and diseases modeling.[5,6]

Hydrogels are gel-like materials that are composed of insoluble macromolecular chains that absorb and retain significant quantities (> 90%) of water or biological fluid, offering a versatile platform for various biomedical applications.[7] The hydrogel materials used for 3D cell culture can be natural or synthetic.[8] Natural hydrogels are obtained from animals and plant sources, such as Matrigel, collagen, hyaluronic acid, cellulose, or alginate. A commonly used matrix is Matrigel (EHS matrix) that forms hydrogels between 22-37 °C. It mainly consists of laminin (~60%), collagen IV (~30%), entactin (~8%) and the heparin sulfate proteoglycan perlecan (~2-3%).[9,10] Moreover, it possesses intrinsic soluble factors (e.g., chemokines, growth factors, and integrin ligands) that target transmembrane proteins involved in important cell signaling pathways.[7,11] Recent applications of this material in cell culture involve 3D (stem) cell expansion and organoid assembly.[12] However, it is a costly material that shows inconsistency between lots. Additionally, the incapability to further tune the low stiffness of Matrigel makes it unsuitable for some applications along with decoupling of various cues.[13] Synthetic hydrogels demonstrate the potential to overcome these challenges as they offer the potential to control and customize the cell microenvironment. They can be prepared from a range of synthetic polymers and combined with natural polymers providing handles to modulate their chemical and physical properties. This section is expanded on in 1.14.

1.2. The Extracellular matrix (ECM) of cell niche

The extracellular matrix of all tissues consists of an acellular fibrous protein network. This natural material not only physically support cells, but also guides their behaviour. A range of insoluble proteins (e.g., collagens, fibronectin, heparan sulfate), growth factors (e.g., transforming growth factor-β (TGF-β), vascular endothelial growth factor (VEGF)), and other secreted proteins (e.g., proteolytic enzymes, protease inhibitors) can be found within this material.[2,14] The precise composition and presentation (e.g., density, stiffness, topography, fiber size and orientation, chemical/physical properties) of the ECM is specific to a given tissue, and adapts constantly to its environment.[15,16]

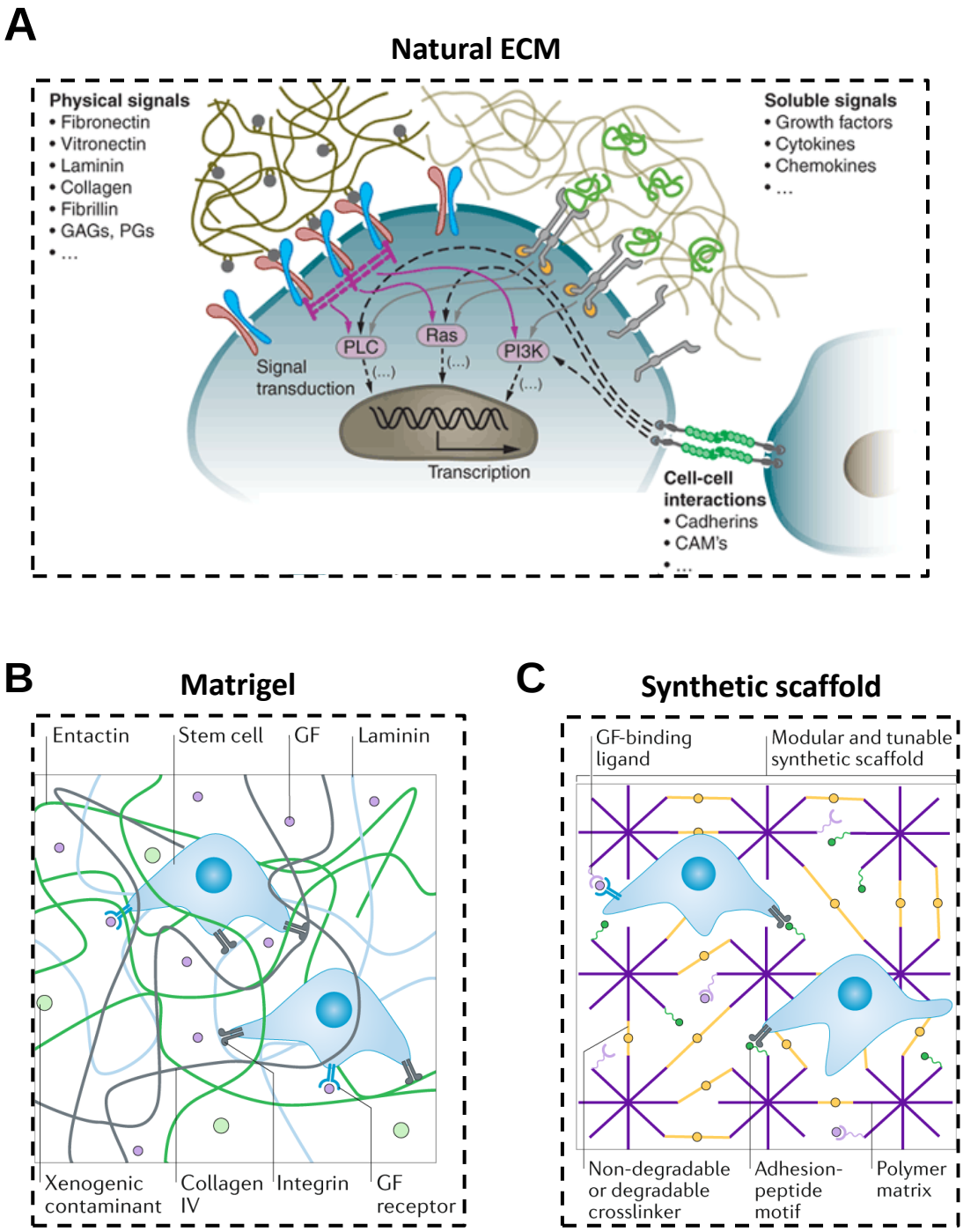

Figure 1.1. Dynamic interactions between cells and different ECMs (natural ECM[17], Matrigel and synthetic scaffold[9]) which is regulated by the complex and mutual molecular interactions occurring between cells and their surrounding environment. Images adapted from references.

1.3. The relevance of mechanics on cell behaviour in disease

Cells continuously adapt the stiffness of their environment *in vivo* to accommodate external forces, otherwise known as mechanical homeostasis.[18] However, this balance can be disrupted in disease states where changes in matrix deposition, removal, and restructuring occur lead to aberrant cell behaviors. For instance, tumor formation can be promoted by mechanical cues from cancerous tissues that trigger biochemical signaling cascades stimulating cell cycle progression and motility.[19] In blood vessels, low and/or high shear stresses can activate or inhibit angiogenic signaling pathways during embryonic development. For adult blood vessels that generally encounter large shear forces,

low shear forces in curved and branched regions trigger abnormal signaling and the start of diseases such as artherosclerosis.[20] Thus, alteration of mechanical homeostasis can lead to disease progression and understanding how cells interact with their environment mechanically, or the study of mechanobiology is critical to understand disease and its treatment.

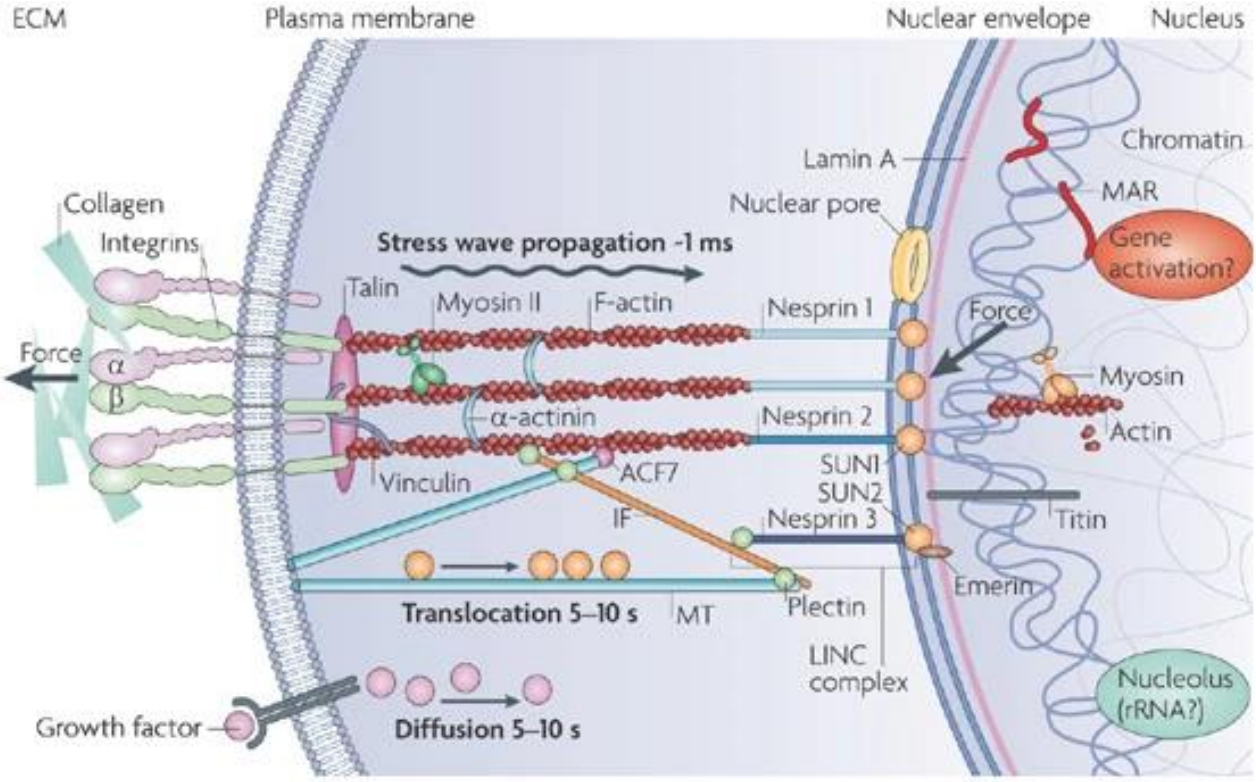

Figure 1.2. The transfer of external mechanical signals into the cell nucleus.[21] When an external force is applied on integrins on the ECM, it is initially concentrated at focal adhesions and transmitted to filamentous (F)-actin. This F-actin is bundled by α-actinin and tensioned by myosin II, creating prestress in the cell. The force could be transferred through multiple pathways within the cell due to the close connection with microtubules (MTs) and intermediate filaments (IFs). MTs and IFs are connected with Nesprin 1-3 that could further transmit force signal to SUN1 and SUN2 on the nuclear. The entire process can occur about 1ms. The force directed into the nuclear scaffold can impact gene activation within milliseconds of surface deformation. In contrast, it needs several seconds for growth factors to transfer the signal into the nuclear and cause changes. Image adapted from reference.

1.4. Mechanotransduction governs cell-matrix crosstalk

Mechanotransduction is the conversion of mechanical forces cells sense from their microenvironment extracellularly into intracellular biochemical signals.[21] Transmembrane mechanosensitive receptors or integrins provide a link from the ECM to the cytoskeleton to facilitate this process.[21,22] When integrins are subjected to force, a series of structural modifications are triggered translating the mechanical stimulus into a chemical signal that impacts gene expression within the nucleus. [21] Such as the tracts of disulfide bonds are involved in the conformational changes of the protein through bond opening and closing.[23] They can interact with a diverse ECM proteins (e.g., collagen, fibronectin) enabling cellular sensing and response to external mechanical stimuli, and thus are behind numerous cellular activities including cell motility, proliferation, and differentiation.[21,22]

Besides sensing the physical properties of their surroundings, cells also exert mechanical forces on their environment.[24] Cells generate force through cell-matrix adhesions and actin-myosin interactions. When the matrix is soft, the adhesion to the matrix is low with little focal adhesions and reduced actin fiber alignment. Whereas when the matrix is stiffened, cell adhesion to it increases

recruiting vinculin to the focal adhesions and actin fiber bundling generate higher traction forces.[25] Cells have the ability to enhance the rigidity of their matrix up to 15 µm radially from themselves by the mechanical strain they impose on their matrix to adjust the surrounding environments.[26] Bundling and alignment of the cell's actin filaments then occurs permitting the cell to exert more force forming a positive feedback loop. This further remodels the ECM and its mechanics with lasting changes, even after the cells have been removed.[27-31] This two-way communication between cells and ECM mechanics is referred to as mechanoreciprocity.[28]

The elastic modulus or stiffness of the matrix was believed to be the most important mechanical property in mechanobiology over several decades. However, recent studies show that more complex mechanical characteristics such as strain stiffening, viscoelasticity and poroelasticity can majorly influence numerous cell behaviours that are critical in development and disease.[32] In the next sections, I will examine these various mechanical properties in detail.

1.4.1. Stiffness

The stiffness of a hydrogel is its resistance to deformation under an applied force and is described by the elastic modulus (G') or Young's modulus (E).[33,34] Differences in tissue stiffness of various tissues in the human body range from very soft (e.g., brain, several Pa - 1 kPa) to very stiff (e.g., bone, 10 kPa - 15 MPa).[35] Since the recognition that substrate stiffness influences cell behaviour over two decades ago, the amount of research on this topic continues to grow as this mechanical parameter has been implicated in numerous developmental (e.g., embryogenesis) and disease (e.g., tumor metastases) processes.[36-39] On a scan of hydrogel stiffnesses (1-100 kPa) developed by Chen and co-workers, fibroblasts were demonstrated to elongate on a stiffer hydrogel and align in the direction of the exerted force on a more stiff hydrogel.[40] The impact of stiffness on cell behaviour can be further seen from the work of Weaver and co-workers that demonstrated breast cancer cells (Basal-like and Her2 tumor subtypes) derived from stiff matrix (~5 kPa)were more invasive and resistant to chemotherapy (paclitaxel) to cells (Luminal A and B subtypes) grown on a soft matrix (400 Pa), the stiffness of the matrix affected gene activation implicated in cancer cell signaling and motility (TGFβ, YAP), providing a potential mechanism for how matrix stiffness can promote cancer progression.[41-45] These studies point that the ECM affects cancer cell behavior and highlight an opening for new therapies that target it to prevent or slow tumor growth.

1.4.2. Nonlinear elasticity

Hydrogels that show a non-linear response to applied mechanical stress or strain are called strain stiffening or non-linear elastic. This phenomenon is typically associated with biopolymer networks such as fibrin or collagen. Beyond a particular threshold the materials' stiffness increase, arising from the non-linear relationship between force and extension in individual filaments that resist stretching.[46-50] Their elastic behavior arises due to the ability to resist bending and stretching of their semi-flexible filaments that can be described by two theoretical frameworks. Bending of the filaments results in a non-affine type of deformation that is enthalpic,[47] whereas their stretching is affine and can be described as an entropic spring with a uniform distribution of strain and alignment in response to the strain direction.[46-51] Strain-stiffening can drive the transmission of mechanical stimuli to organize cells over considerable distances, typically on the order of hundreds of microns[47,52] The critical stress or deviation from linearity for several biopolymers is typically less than 20 Pa[47,52,53] Once this critical stress is exceeded, cells are limited to perceiving and modifying the material within its linear elastic region.[47] Kouwer and co-workers demonstrated this strain-stiffening property can exist in hydrogels consisting

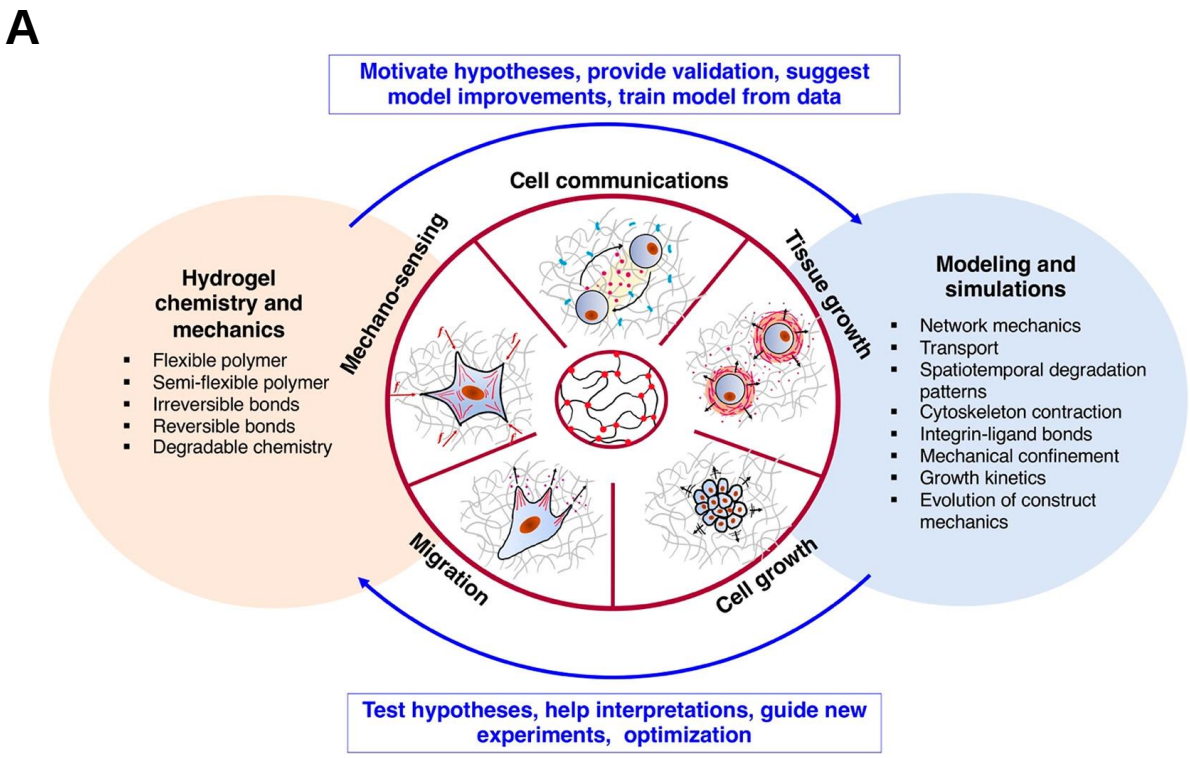

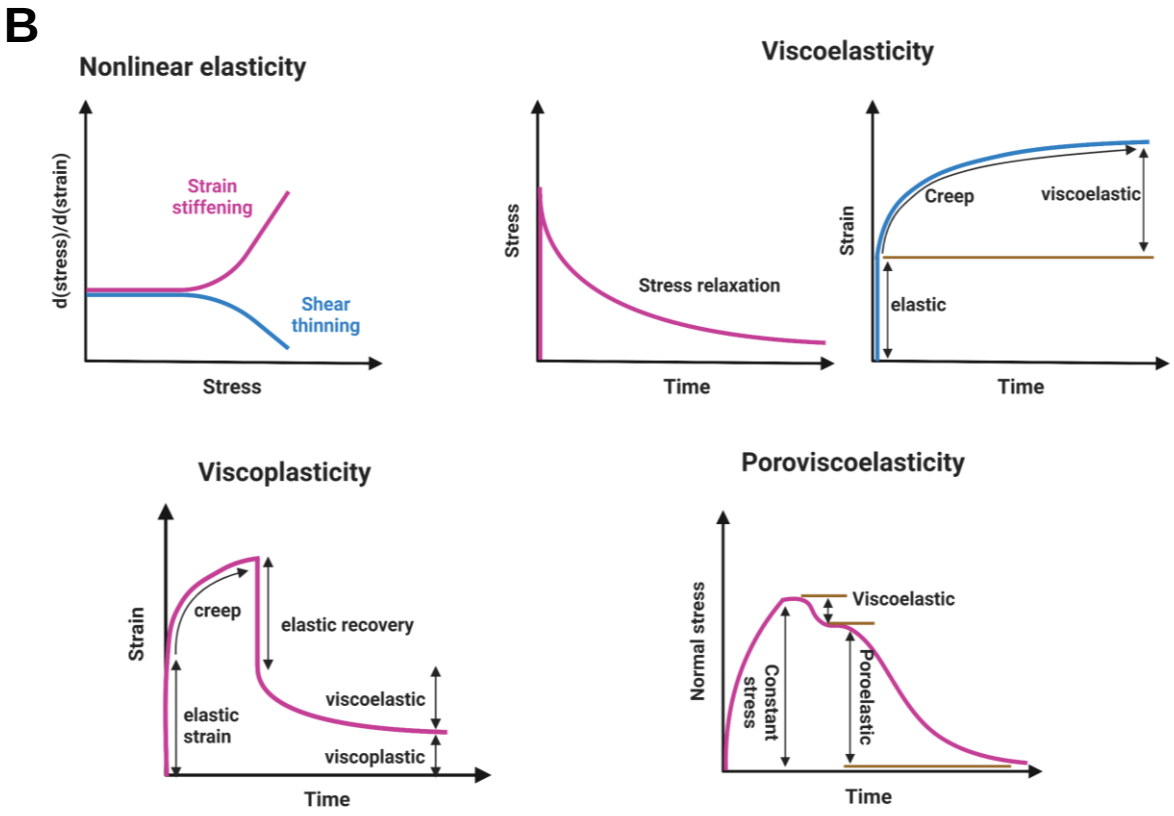

Figure 1.3. (A) Summary of the key interactions between cells and hydrogels upon cell encapsulation.[59] (B) Mechanical properties of (bio)materials can be assessed using a range of rheological tests, picture made in Biorender.

of grafted polyisocyanopeptide (PIC)-polymers.[54-56] These polymers can access parallel intramolecular hydrogen bonds along the backbone similar to proteins and form a semi-flexible fiber network. The polymers can undergo considerable deformation before reaching their maximum elongation and

resistance. Recently, Webber and co-workers incorporated dynamic boronate ester cross-links into flexible, non-filamentous networks to develop strain-stiffening hydrogels that could be adjusted by the composite concentration, pH and temperature).[57] Interestingly, in these hydrogels the critical stress exceeds the known range for most biological filaments (20 Pa).[58]

1.4.3. Viscoelasticity and plasticity

Viscoelasticity describes the ability of hydrogels to exhibit both viscous and elastic behavior under mechanical deformation while maintaining their structural integrity. The motion of entangled polymer chains, breaking of weak crosslinks or movement of fluid influences this property. [25] This property is found across tissues (e.g., skin, tendons, and muscles) and is related to the underlying collagen networks.[60] In synthetic hydrogels, this property is influenced by factors such as crosslinking density, polymer composition, polymer chain length and architecture and solvent conditions.[61] This property can be described by the Maxwell-Wiechert model that encompasses multiple parallel Maxwell elements to represent both elastic and viscous features.[62] Mooney and co-workers showed that physically crosslinked alginate hydrogels display rapid stress relaxation that influences mesenchymal stem cells (MSCs) spreading and osteogenic differentiation without the need for matrix degradation in 3D cell culture.[63] Anseth and co-workers further showed that myoblast cells spread rapidly on stress-relaxing polyethylene glycol (PEG) hydrogels crosslinked with hydrazone bonds.[64,65] These investigations indicate that stress relaxation is an key mechanical characteristic of the natural ECM that is needed in hydrogels to steer cell responses.

Viscoplasticity refers to the irreversible deformation of a material under applied stress, which is often accompanied by yielding or flow.[66] During rheometer measurements, the level of plasticity is determined by calculating the ratio between the permanent strain observed after stress removal and the total strain encountered during stress application in a creep and recovery test.[66,67] As viscoelastic substances undergo a time-dependent rise in strain when subjected to a constant stress, also known as creep, the plasticity of viscoelastic materials varies with time.[68,69] Studies indicate that viscoplasticity may affect cell behaviour in disease processes with cancer cells using this property to overcome the structural barriers imposed by the ECM to infiltrate tissues. In the disease process, the cells execute force-mediated remodeling and matrix metalloproteinase (MMP)-mediated degradation[70] resulting in realignment of matrix fibers and plastic remodeling.[66] This changes to the matrix in this process remain even after the cells are removed demonstrating a plastic response.

1.4.4. Poro(visco)elasticity

Poroelasticity refers to the elastic behavior of hydrated materials that arises from pore trapped water.[71] When the hydrogel matrix is compressed, the entrapped water is compelled to flow through the pores, leading to a decrease in water pressure due to friction with the matrix walls. This decrease in water pressure generates stress in response to compression. As water moves through the pores on compression, the water pressure decreases due to the frictional forces between the water molecules and the walls of the pores. This decrease in water pressure generates stress in response to compression. Features of the material that influence this property include porosity, pore size distribution, amount of water and mechanics.[72,73] Deguchi and co-workers studied the poroelasticity of a cellulose-based hydrogel dissolved in LiCl (8 wt%) or DMAc (92 wt%).[74] When subjected to gradual compression (0.05 mm/min), water was released at 70% strain without rupturing. In comparison, rapid compression (1.0 mm/min) resulted in a stiffer hydrogel with a steeper initial slope. At 25% strain, the hydrogel ruptured due to more rapid rate of water flow during fast compression. When polymer

materials that show both viscous and elastic properties are examined under compressive stress, they can show a poroviscoelastic response to compressive stress.[75] Monitoring of the stress relaxation process of viscoelastic materials in compression can yield this information.[76] Viscoelastic relaxation is first observed due to polymer chain and dynamic bond rearrangement, and then the poroelastic response arising from the gel microstructure and porosity.[76] Poroviscoelastic relaxation is observed in both biological tissues (e.g., cartilage) and synthetic materials (e.g., hydrogels), opening a new parameter to control and understand its influence on cell behaviour for application in areas such as tissue engineering and biomechanical studies.

1.4.5. Bioactive cue deposition in synthetic materials

While the ECM architecture and mechanics are critical to guide cell responses, engagement of a range of cell surface receptors is also critical.[77-79] Cell-adhesive proteins, such as selectins, laminin, and cadherins, bind to integrin receptors on the cell surface to promote cell adhesion and migration.[80] Growth factors and cytokines, such as TGF-β, regulate cell behavior, including proliferation and differentiation.[79] Proteoglycans, such as heparan sulfate proteoglycans, sequester and present growth factors, modulating their activity.[81] On the surface of synthetic materials, Ikada and co-workers found that a polymer film exhibiting a water contact angle ranging from 60° to 80° (moderately hydrophilic) in its dried state exhibited a higher preference for fibronectin adsorption and facilitated better growth of fibroblast cells, in comparison to films with contact angles ranging from 20° to 50° (highly hydrophilic).[82] Kawakami and co-workers incorporated phenol groups on to carboxymethylcellulose derivatives (CNC-Ph hydrogels) to obtain a hydrogel with high crosslinking speed and crosslinker density, showing that more L929 fibroblasts could adhere and grow on the hydrogel surface containing 15.4 phenol groups per 100 repeat units of uronic acid (with a 97% adhesion rate) compared to the gel with only 8.4 phenol groups (with a 62% adhesion rate). This cell behaviour was ascribed to the increased hydrophobicity of the gel resulting in the enhanced binding of cell-adhesive proteins (e.g., fibronectin, vitronectin).[83] Arinzeh and co-workers discovered that human mesenchymal stem cells (hMSCs) showed enhanced osteogenic differentiation when placed on a hydrophobic tyrosine-derived polyarylates and polycarbonates.[84] Overall, these studies point out the importance of hydrogel properties on the binding of proteins secret.

1.5. Synthetic hydrogels as ECM mimicking materials

Synthetic polymer hydrogels provide access to materials where precise control of their physical and chemical characteristic can be achieved. They can be synthesized from a range of synthetic polymers and combined with natural materials. [85,86] These synthetic polymers can be further subdivided into those that are covalent or supramolecular and will be discussed in detail below. Moreover, numerous possibilities abound when the multiple polymer networks when their own properties are combined and will also follow. This burgeoning research area that aims to emulate the ECM of various tissues and has provided a wealth of information on how cells behave in the context of a dynamic and static interfaces.[85,87,88]

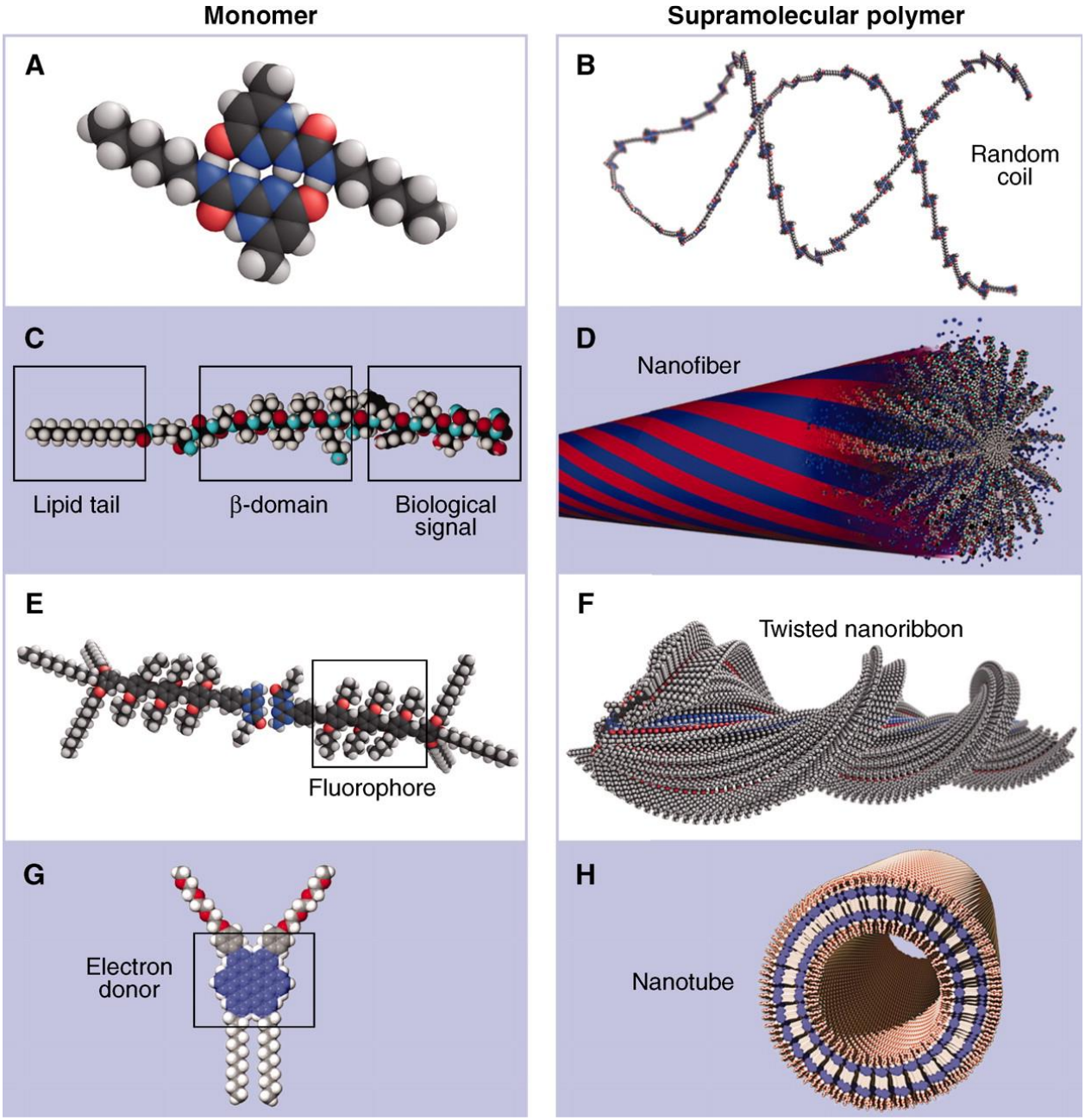

Figure 1.4. Four examples of monomers that can form supramolecular polymers. **A** and **B** The first example consists of a hydrogen bonding ureidopyrimidinone unit (left) that leads to a random-coil structure on polymerization (right). **C** and **D** The second set shows a peptide amphiphile (left) consisting of three segments: a biological cue, a β sheets forming domain, and a hydrophobic domain. The resulting supramolecular polymer (right) adopts a cylindrical structure with twisted β sheets. **E** and **F** A fluorophore oligo(phenylene vinylene) (left) modified with hydrophobic alkyl moieties and a chirality center forms stable dimers through quadruple hydrogen bonds at each monomer end leading to a chiral spiraled ribbon (right). **G** and **F** A hexabenzocoronene core (left) serving as an electron donor and adorned with phenyl triethylene glycol and dodecyl chains. The resulting shape of this supramolecular polymer is a nanotube (right), with thickness of the tube wall dictated by the dimensions of the individual building blocks.[89] Images adapted from references.

1.5.1. Supramolecular polymers

Supramolecular polymers are macromolecules held together by reversible, non-covalent interactions, exhibiting dynamic properties and functionalities with applications in diverse fields.[90] Supramolecular polymers mainly consist of two types based on the structures that are formed: random-coil supramolecular polymers without internal order that form random-coils and those that are shape-persistent nanostructure with a high degree of internal order.[89] The second type polymer is

different from covalent polymers and could achieve mechanical or biological functionalities depending on the monomers used.[89] Supramolecular polymerization can be described by one of three mechanisms: isodesmic (σ=1), cooperative (σ>1), and anti-cooperative (σ<1).[91] Random-coils usually polymerize according to an isodesmic polymerization while the ordered structures that polymerize result from an cooperative or anticooperative polymerization. The monomers that show cooperative polymerization include macrocycles, peptides and C3 symmetric monomers. Benzene-1,3,5-tricarboxamide (BTA) derivatives represent one of the most studied C3 symmetric cores in supramolecular chemistry,[92] with monomers prepared from them self-assembling into supramolecular polymers with a high level of cooperativity through π-π interactions and hydrogen bonding.[92-99] Moreover, when a critical concentration is surpassed, gel phase materials can be obtained.[94-99] Meijer and coworkers showed that supramolecular polymer hydrogels based on the 2-ureido-4[1H]-pyrimidinone (UPy) unit demonstrate mechanical properties relevant for biomedical applications. Dankers and coworkers designed a customizable single-component supramolecular transient network in water with unique nonlinear structure by modifying PEG with quadruple hydrogen bonding motifs that is shielded by a hydrophobic alkyl chain, which could incorporation of active proteins during gelation process and gradually releases the protein through the dissolution and stability of both the protein and polymer components after being implanted into the living organisms.[100] Sijbesma and co-workers demonstrated that diacetylene bis-urea bolaamphiphiles after light irradiation can show strain stiffening and self-healing attributes attributed to its semi-flexible fibers and dynamic properties.[101] Stupp and coworkers developed two different peptide amphiphiles that could self-assemble into supramolecular hydrogels with different stiffness, which could be applied to studied the influence in neuronal development.[102] These studies point out that supramolecular polymers can show relevant mechanical properties for biological application, but also the need for methods to modulate their mechanics as these non-covalent materials are often weak in mechanical character.

1.5.2. Squaramide-based supramolecular polymers and materials

The squaramide is a minimalistic ditopic hydrogen bonding synthon that consists of a cyclobutenedione ring with two N-H donor hydrogen bonding groups and two C=O acceptors. These groups positioned in an opposing manner on the ring, primes them to interact with another squaramide moiety as needed to facilitate the supramolecular monomer polymerization.[103] The squaramide unit has been widely used in molecular recognition, chemical catalysis, medicinal chemistry and self-assembly.[103,104] Our group first introduced squaramide units onto flexible amphiphilic monomers that polymerize into rigid filaments microns in length and nanometers in width.[105] Hydrogen bonds and hydrophobic effects drive the interaction of the monomer units when self-assembled in water. By systematically modifying the hydrophilic or hydrophobic domains present in the bolaamphiphiles, a transition from spherical aggregates to filamentous structures was induced.[105] Furthermore, co-assembly of a fluorescent monomer led to assessment of the biodistribution behaviour and potential for sequestration of the various nanoparticles by stabilin-2, a hepatic receptor in developing zebrafish embryos.[106] This investigation aimed to explore the impact of the morphology and dimensions of the supramolecular polymer nanoparticle on these biological mechanisms. Recently, our group reported a tripodal squaramide-based monomer that forms filamentous polymers and hydrogel materials above a critical concentration. The squaramide synthon was integrated into the hydrophobic domain of this tripodal amphiphile bearing a tris(2-aminoethyl)amine (TREN) core with peripheral tetra(ethylene glycol) chains. A series of

supramolecular monomers were designed by varying the aliphatic chain length, ranging from 6-12 methylene units. However, it was observed that only the monomers with 8 and 10 methylene units could form hydrogel materials.[107] Furthermore, our group also introduced 1,2-dithiolane (DT) onto the tripodal squaramide-based monomer to modulate the mechanics of the materials through the formation of dynamic covalent crosslinks in a light-mediated manner and an RGD peptide to guide cell adhesion and migration. This modified hydrogel exhibited strain stiffening, viscoelasticity, and plasticity, resembling the properties of biopolymer networks in the ECM and demonstrated the possibilities to tune the gel properties during cell culture.[108]

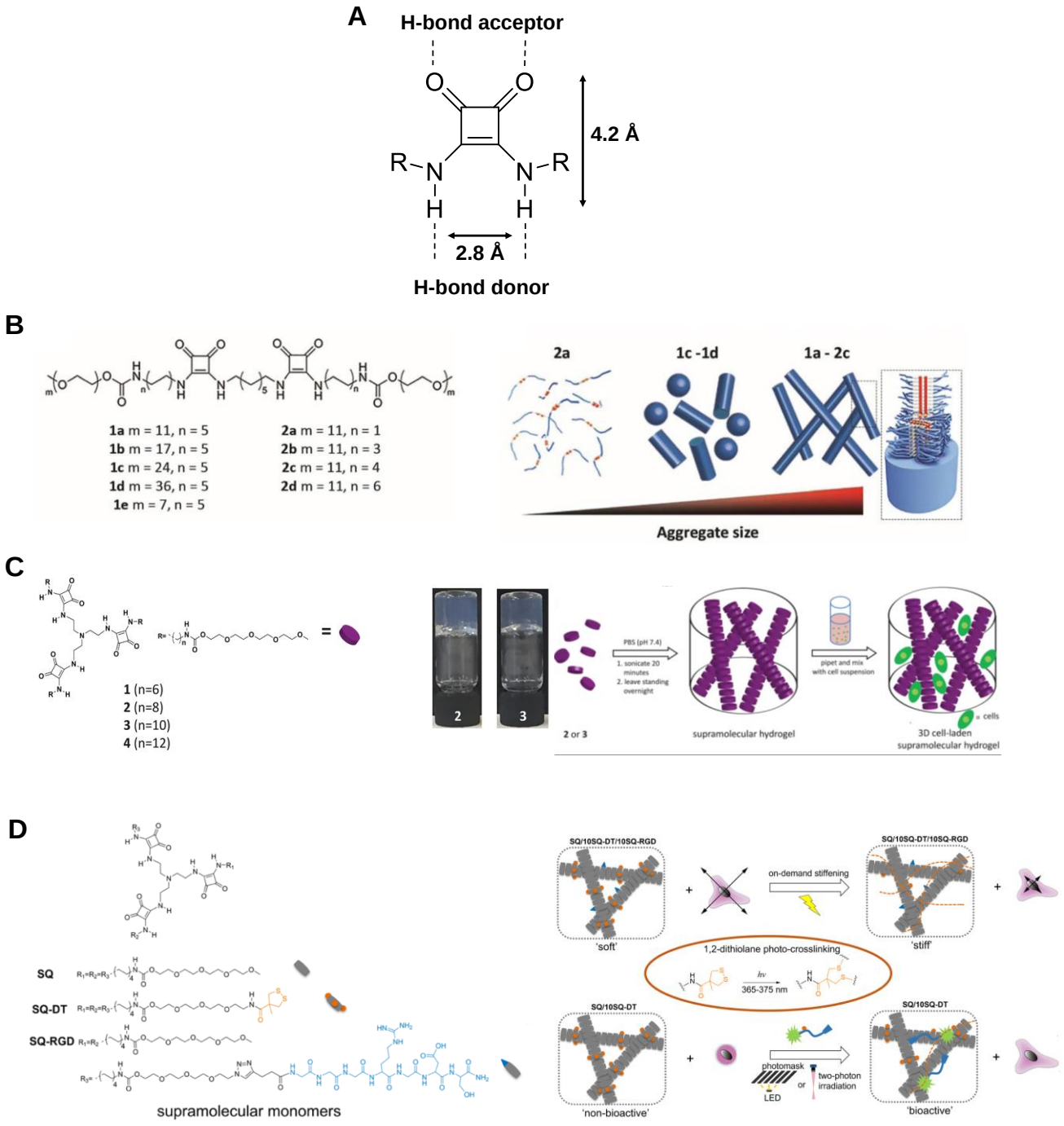

Figure 1.5. (A) Molecular structure of the squaramide.[109] (B) Chemical structures of squaramide-based bolaamphiphiles and a scheme of the observed structures of the supramolecular polymer in water as the ratio of hydrophilic to hydrophobic components was adjusted.[106] (C) Chemical structures of tripodal squaramide-based hydrogelators as the hydrophobic length was adjusted changed and a scheme of gelation process and cell culture study.[107] (D) Chemical structures of DT and RGD modified tripodal squaramide-based monomer, a scheme depicting mechanical modulation, and the controlled

arrangement over space and time of the biologically active RGD peptide (fluorescein)GK(DT)GGGRGDS within the hydrogel through DT cross-linking..[108] Images adapted from references.

1.5.3. Interpenetrated networks

Single network hydrogels (e.g., supramolecular and polymeric-based hydrogels) have been utilized widely in many biological applications. However, their weak and brittle character prevent them from mimicking load-bearing tissues. Several strategies have been explored to tackle these constraints including augmenting the monomer concentrations and cross-linking density.[110-112] To date, strategies based on semi-interpenetrating networks (IPNs) and double networks (DN), two common subclasses within this area, have also been employed to increase the mechanical properties of these gels bringing the needed mechanical characteristics to mimic these tissues in reach.[110,111] IPN hydrogels are individually cross-linked networks of multiple polymer chains that interpenetrate each other, providing access to properties such as enhanced thermal stability, mechanics, and chemical resistance.[113,114] Chaudhuri and co-workers developed an IPN hydrogel system consisting of hyaluronic acid (HA) and collagen I. The HA network chemically crosslinked through dynamic covalent bonds (hydrazine and aldehyde). This strategy aimed at replicating the viscoelastic and fibrillar properties of the ECM in native tissues. These IPN hydrogels showed distinguishable stress relaxation due to HA crosslinking within the network that can be modulated by varying the affinity of the crosslinkers, molecular weight or concentration of the HA network. This work showed that a faster stress relaxation process in the IPN hydrogels can permit cells to rearrange the fibers within the network, help to establish the focal adhesion sites, and accelerate their maturation.[115] Qin and co-workers developed a viscoelastic alginate-collagen hydrogel that shows both fast- and slow-relaxation supporting osteocyte viability within the hydrogel. They further discovered that a fast-relaxing environment could promote early cell spreading, while slow-relaxing hydrogels facilitate osteogenic differentiation, indicating a potential role in advancing 3D osteocyte models for bone mechanobiology research.[116] While IPN hydrogels do exhibit improved mechanical properties and retain the advantages of two polymer networks, they still fall short in terms of matching the toughness or loading capabilities found in certain native tissues (e.g., bone, cartilage), mainly due to the absence of crosslinking between the two networks. As a result, double network (DN) hydrogels have emerged as a response to overcome this limitation and enhance their suitability for biological applications.[117-119]

The DN hydrogel consists of a soft and ductile network (first network) as well as a rigid and brittle network (second network) that are covalently connected in between[117]. The soft and highly ductile is usually consists of long polymers that maintain the hydrogel integrity and tolerate high stress before break[120]. The second network serves as a “sacrificial network” that breaks first to dissipate energy when external stress is applied. Gong and coworkers[117,121,122] demonstrated the DN concept with the addition of poly(acrylamide) (PAAm) to a poly(2-acrylamido-2-methylpropanesulfonic acid) (PAMPS) and their crosslinking leading to hydrogels with exceptional mechanical strength (elastic modulus: 0.1-1 MPa; fracture tensile stress: 1-10 MPa, strain: 1000-2000%; tearing fracture energy of 100-1000 J/m^2) and the ability to sustain compressive pressure (fracture compressive stress 20-60 MPa, strain 90-95%) with an extremely low coefficient of friction.[117] DN hydrogels integrate many extraordinary properties in one network compared with traditional single hydrogel network and IPN hydrogel.[120,123,124] However, many DN hydrogels exhibit irreversible damage under external loading and could not totally recover to their original state after releasing the stimulations. Therefore, many sacrificial frameworks such as

ionic bonds[125,126], hydrophobic interactions[127,128], or crystallites[129,130], have been widely used to enhance the recovery of the network after the loading.

Filamentous supramolecular polymers have been applied into DN hydrogels for their self-healing capabilities, energy dissipation, and viscoelastic properties[131-133]. Jiang and coworkers developed a supramolecular-polymer DN hydrogel, combining acrylic acid functionalized EFK peptides (AA-EFK) and covalent polymer networks (a mixture of acrylamide, 4-arm PEG-acrylate and methacrylated hyaluronic acid (HAMA)) to exhibit remarkable mechanical properties (Young's modulus: ~209 kPa, compression limit: >70%, toughness: ~47 kJ/m^3) and rapid recovery. The DN hydrogel outperformed the single network hydrogels showing enhanced cell (SW1353) viability, differentiation in 2D culture. Subsequently, the crosslinked gel was implanted into rabbit models with cartilage defect. Successful regeneration of cartilage was observed, with regenerated tissues displaying native cartilage-like ECM and well organized cell arrangement after 12 weeks of *in vivo* study.[134] Heise and co-workers presented a synthetic polypeptide-based DN hydrogel that consisted of alkyne-functionalized polypeptides and azide-functionalized PEG, that could crosslink together through copper-catalyzed alkyne-azide cycloaddition. The resulting hydrogels demonstrated improved mechanical strength (ultimate compressive strength ~820kPa, strain ~30%) compared to conventional peptide-based hydrogels tunable and good cell compatibility (>68%), thus suggesting their suitability as scaffolds for soft tissue engineering.[135] Cao and coworkers introduced two peptides, acrylic acid-Ile-Ile-Ile-Lys-C (I_3K-AA) and acrylic acid-Ile-Ile-Ile-Thr-C (I_3T-AA), into a polymer network composed of polyacrylamide (PAM) and 4-arm PEG-acrylate (Mw: 20 kDa). Although both peptides could effectively enhance the mechanical strength of DN hydrogels, I_3T-AA exhibited 3-5 times higher values in all mechanical properties (e.g., Young's modulus: 107.4 kPa; fracture stress: 0.48 MPa; toughness: 0.38 MJ/m^3) compared to I_3K-AA. It also showed a better recovery rate of the dissipated energy (I_3T-AA: 93%; I_3K-AA: 86.6%) after 20 stretching-relaxation cycles without fracture.[136] These studies provide valuable insights into manipulating supramolecular network architectures to enhance the mechanical strength and rapid recovery of DN hydrogels. While DN hydrogels have garnered interest within the realm of biology because of their appealing properties, the protocols to prepare them are often bioincompatible and they lack the fibrillar structure of the extracellular matrix.

1.5.4. Nanoparticle-reinforced double networks

The introduction of nanoparticles into synthetic polymer materials opens the door to simultaneously modulate hydrogel mechanics as well as introduce new properties (e.g., electrical, magnetic).[138] Silica nanoparticles (SiO_2) were introduced into DN gels composed of poly(2-acrylamido-2-methylpropanesulfonic acid) (PAMPS) and poly(acrylamide) (PAAm) of as macro-crosslinkers. The hydrogels exhibited high compressive toughness, with no fracturing observed even under loading conditions of up to 73 MPa and a strain exceeding 98%.[139] Beyond silica, the remarkable optical and plasmonic characteristics exhibited by gold nanoparticles (AuNPs) and nanorods (GNRs) render them highly attractive additives to tune the mechanics of synthetic polymer materials and develop photo-thermo responsive hydrogels.[140]. Khademhosseini and co-workers[141] used gelatin methacrylate (GelMA) coated GNRs to crosslink a GelMA hydrogel with photoinitiator under UV irraditation to develop conductive bioinks for culturing cardiac cell culture. They found that the incorporated GNRs improved the electrical resistance of the material and cell coupling resulting in synchronized contraction of the bio-printed constructs.[142] Moreover, the photo-thermal responsiveness of GNRs has also been examined in single network hydrogels, presenting opportunities for their utilization of the

materials in photothermal therapy[143] and imaging applications.[144] Chen and co-workers developed an injectable thermosensitive hydrogel composed of β-glycerophosphate-bound chitosan (CGP), dopamine-modified alginate (Alg-DA), and polydopamine-coated GNRs (GNR-PDA) which could be used for efficient photothermal therapy. The strong interactions between the polymer (chitosan and alginate) and polydopamine (PDA) on the nanoparticles help to stabilize and immobilize GNR-PDA within the hydrogel uniformly. Both *in vitro* and *in vivo* studies demonstrated good biocompatibility and efficient tumor ablation, showing promise for long-term, repeated photothermal therapy for tumors.[137] Overall, incorporating nanoparticles into the hydrogel network is a practical approach for both introducing new functionalities and enhancing mechanical properties.

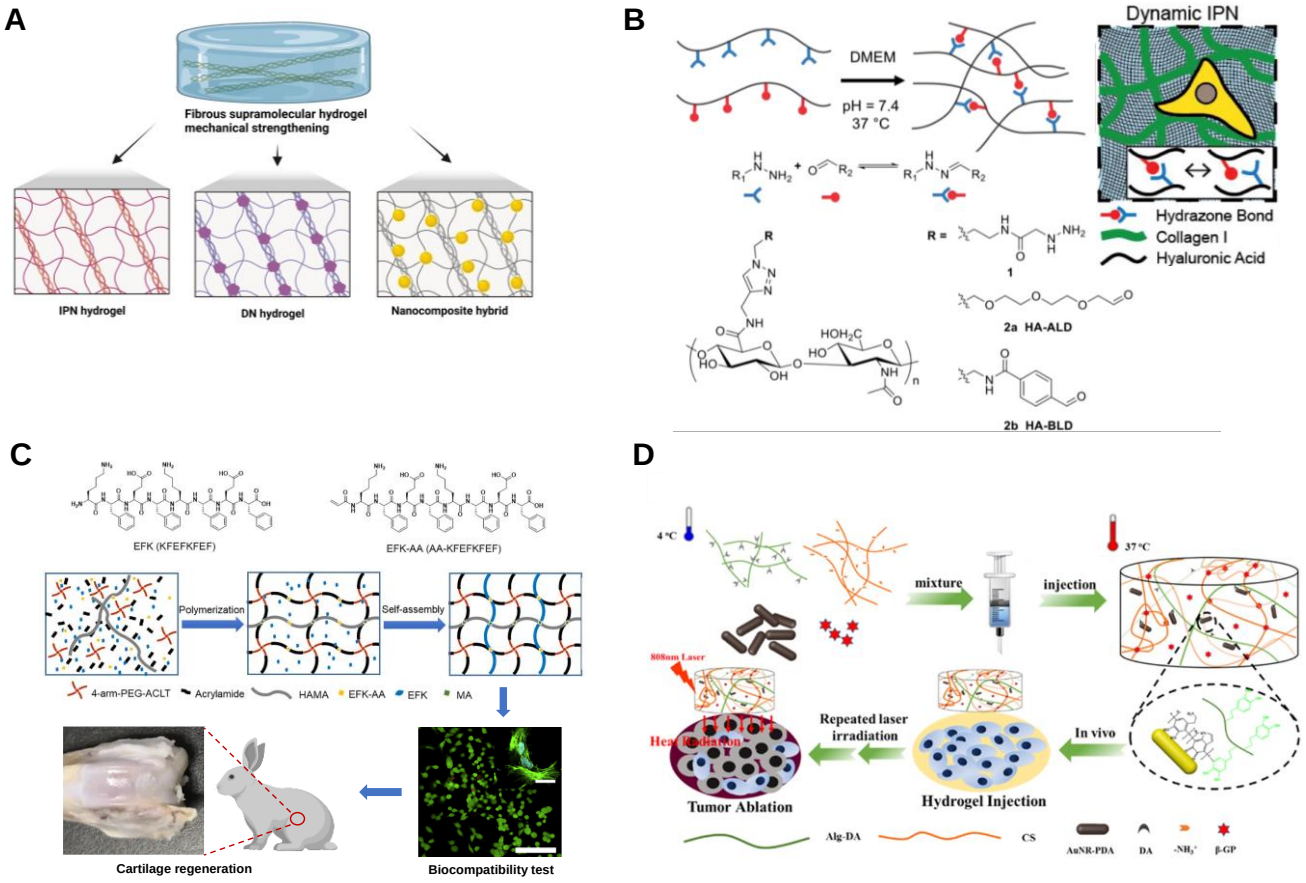

Figure 1.6. (A) Strategies to reinforce the mechanical characteristics of supramolecular hydrogels, figure made in biorender. (B) Molecular structures of hydrazine and aldehyde modified HA and their dynamic properties under physiological conditions and a scheme demonstrates that dynamic covalent interactions can regulate cell morphology in 3D cell culture.[115] (C) Molecular structures of EFK and EFK-AA peptides and their formation into a DN network, along with biocompatibility testing and cartilage regeneration in rabbits are presented.[134] (D) A GNRs-reinforced DN hydrogel that has potential applications in tumor ablation.[137] Images adapted from reference.

1.6. Aim and outline

This thesis first explores the squaramide-based supramolecular polymer properties by tuning the chemical structures, and further develop multiple synthetic hydrogels aiming at enhancing their mechanical strength and investigating their applications in 3D cell culture. A comprehensive range of chemical, biophysical, and biological studies are employed to analyze the impact of squaramide-based synthetic hydrogels on cell behavior.

Chapter 2 examines the relationship between the chemical structure of tripodal squaramide-based monomers and properties of the supramolecular polymer materials by tuning the hydrophilic-

hydrophobic ratio and hydrogen bonds within the monomers. Using a combination UV-Vis, cryo-TEM and oscillatory rheology experiments, it was demonstrated that the hydrophilic-hydrophobic ratio and hydrogen bonds can influence the thermal responsiveness of the polymers.

Chapter 3 discloses a mechanically enhanced DN hydrogel featuring a rapid ring-opening photopolymerization of DT and norbornene (NB) to prepare a DN hydrogel. The DN networks consist of supramolecular filaments and PEG polymers and show cartilage-like mechanical characteristics that can sustain dynamic compression in 3D cell culture. Furthermore, human primary articular chondrocytes (hPACs) were 3D seeded in these hydrogels and the composite could be applied for long-term loading to stimulate the production of cartilage ECM components (e.g. sGAGs).

Chapter 4 describes a novel DN hydrogel phenol-crosslinked hydrogel consisting of the filamentous squaramide-based supramolecular hydrogels from chapter 3 and modified 4-arm PEG network. The resulting hydrogel materials that are crosslinked by visible light show mechanical properties resembling cartilage and bone. Moreover, the ECM production by hPACs entrapped within this DN hydrogel highlights its applicability for cartilage-mimicking applications.

Chapter 5 discloses the use of gold nanoparticles (AuNPs) as crosslinkers in DN hydrogels that consists of a filamentous squaramide-based supramolecular polymers and a 4-arm PEG network. Crosslinking of these components results in improved compressive properties and enhanced energy dissipation levels of the DN hydrogels. Additionally, the incorporation of AuNPs provides the network with a photo-thermal effect that effectively eliminates MDA-MB-231-B1 cells (bone derived human breast cancer cells) showcasing its potential for bone cancer therapy.

Chapter 6 outlines the key findings of this thesis and explores potential avenues for future research of squaramide-based supramolecular materials that mimic the ECM for a wide variety of 3D cell culture aims.

Reference

(1) Bissell, M. J.; Hall, H. G.; Parry, G. How does the extracellular matrix direct gene expression? *Journal of theoretical biology* **1982,** *99* (1), 31.

(2) Langhans, S. A. Three-Dimensional *in Vitro* Cell Culture Models in Drug Discovery and Drug Repositioning. *Front Pharmacol* **2018,** *9*, 6.

(3) Antoni, D.; Burckel, H.; Josset, E.; Noel, G. Three-dimensional cell culture: a breakthrough *in vivo*. *Int J Mol Sci* **2015,** *16* (3), 5517.

(4) Bonev, B.; Mendelson Cohen, N.; Szabo, Q.; Fritsch, L.; Papadopoulos, G. L.; Lubling, Y.; Xu, X.; Lv, X.; Hugnot, J. P.; Tanay, A.et al. Multiscale 3D Genome Rewiring during Mouse Neural Development. *Cell* **2017,** *171* (3), 557.

(5) Garreta, E.; Kamm, R. D.; Chuva de Sousa Lopes, S. M.; Lancaster, M. A.; Weiss, R.; Trepat, X.; Hyun, I.; Montserrat, N. Rethinking organoid technology through bioengineering. *Nat. Mater.* **2021,** *20* (2), 145.

(6) Park, S. Y.; Hong, H. J.; Lee, H. J. Fabrication of Cell Spheroids for 3D Cell Culture and Biomedical Applications. *BioChip Journal* **2022,** *17* (1), 24.

(7) Cao, H.; Duan, L.; Zhang, Y.; Cao, J.; Zhang, K. Current hydrogel advances in physicochemical and biological response-driven biomedical application diversity. *Signal Transduct Target Ther* **2021,** *6* (1), 426.

(8) Baruffaldi, D.; Palmara, G.; Pirri, C.; Frascella, F. 3D Cell Culture: Recent Development in Materials with Tunable Stiffness. *ACS Applied Bio Materials* **2021,** *4* (3), 2233.

(9) Aisenbrey, E. A.; Murphy, W. L. Synthetic alternatives to Matrigel. *Nat Rev Mater* **2020,** *5* (7), 539.

(10) Kamatar, A.; Gunay, G.; Acar, H. Natural and Synthetic Biomaterials for Engineering Multicellular Tumor Spheroids. *Polymers (Basel)* **2020,** *12* (11), 2506.

(11) Kawase, E.; Nakatsuji, N. Development of substrates for the culture of human pluripotent stem cells. *Biomaterials Science* **2023**, *11*, 2974.

(12) Gjorevski, N.; Sachs, N.; Manfrin, A.; Giger, S.; Bragina, M. E.; Ordonez-Moran, P.; Clevers, H.; Lutolf, M. P. Designer matrices for intestinal stem cell and organoid culture. *Nature* **2016,** *539* (7630), 560.

(13) Benton, G.; Arnaoutova, I.; George, J.; Kleinman, H. K.; Koblinski, J. Matrigel: from discovery and ECM mimicry to assays and models for cancer research. *Adv Drug Deliv Rev* **2014,** *79-80*, 3.

(14) Walma, D. A. C.; Yamada, K. M. The extracellular matrix in development. *Development* **2020,** *147* (10).

(15) Naba, A.; Pearce, O. M. T.; Del Rosario, A.; Ma, D.; Ding, H.; Rajeeve, V.; Cutillas, P. R.; Balkwill, F. R.; Hynes, R. O. Characterization of the Extracellular Matrix of Normal and Diseased Tissues Using Proteomics. *J Proteome Res* **2017,** *16* (8), 3083.

(16) Dzamba, B. J.; DeSimone, D. W. Extracellular Matrix (ECM) and the Sculpting of Embryonic Tissues. *Curr Top Dev Biol* **2018,** *130*, 245.

(17) Lutolf, M. P.; Hubbell, J. A. Synthetic biomaterials as instructive extracellular microenvironments for morphogenesis in tissue engineering. *Nat. Biotechnol.* **2005,** *23* (1), 47.

(18) Adams, M. A.; Dolan, P. Spine biomechanics. *J Biomech* **2005,** *38* (10), 1972.

(19) Broders-Bondon, F.; Nguyen Ho-Bouldoires, T. H.; Fernandez-Sanchez, M. E.; Farge, E. Mechanotransduction in tumor progression: The dark side of the force. *J. Cell Biol.* **2018,** *217* (5), 1571.

(20) Souilhol, C.; Serbanovic-Canic, J.; Fragiadaki, M.; Chico, T. J.; Ridger, V.; Roddie, H.; Evans, P. C. Endothelial responses to shear stress in atherosclerosis: a novel role for developmental genes. *Nat Rev Cardiol* **2020,** *17* (1), 52.

(21) Wang, N.; Tytell, J. D.; Ingber, D. E. Mechanotransduction at a distance: mechanically coupling the extracellular matrix with the nucleus. *Nature reviews Molecular cell biology* **2009,** *10* (1), 75.

(22) Lee, S. E.; Chunsrivirot, S.; Kamm, R. D.; Mofrad, M. R. Molecular dynamics study of talin-vinculin binding. *Biophys. J.* **2008,** *95* (4), 2027.

(23) Nagy, P. Kinetics and mechanisms of thiol–disulfide exchange covering direct substitution and thiol oxidation-mediated pathways. *Antioxidants & redox signaling* **2013,** *18* (13), 1623.

(24) Mierke, C. T. Bidirectional Mechanical Response Between Cells and Their Microenvironment. *Frontiers in Physics* **2021,** *9*, 749830.
(25) Geiger, B.; Yamada, K. M. Molecular architecture and function of matrix adhesions. *Cold Spring Harb Perspect Biol* **2011,** *3* (5), a005033.
(26) Hall, M. S.; Alisafaei, F.; Ban, E.; Feng, X.; Hui, C. Y.; Shenoy, V. B.; Wu, M. Fibrous nonlinear elasticity enables positive mechanical feedback between cells and ECMs. *PNAS* **2016,** *113* (49), 14043.
(27) Han, Y. L.; Ronceray, P.; Xu, G.; Malandrino, A.; Kamm, R. D.; Lenz, M.; Broedersz, C. P.; Guo, M. Cell contraction induces long-ranged stress stiffening in the extracellular matrix. *Proc Natl Acad Sci U S A* **2018,** *115* (16), 4075.
(28) van Helvert, S.; Storm, C.; Friedl, P. Mechanoreciprocity in cell migration. *Nat Cell Biol* **2018,** *20* (1), 8.
(29) Holle, A. W.; Young, J. L.; Van Vliet, K. J.; Kamm, R. D.; Discher, D.; Janmey, P.; Spatz, J. P.; Saif, T. Cell-Extracellular Matrix Mechanobiology: Forceful Tools and Emerging Needs for Basic and Translational Research. *Nano Lett.* **2018,** *18* (1), 1.
(30) Yi, B.; Xu, Q.; Liu, W. An overview of substrate stiffness guided cellular response and its applications in tissue regeneration. *Bioact Mater* **2022,** *15*, 82.
(31) Saraswathibhatla, A.; Indana, D.; Chaudhuri, O. Cell–extracellular matrix mechanotransduction in 3D. *Nature Reviews Molecular Cell Biology* **2023**, 1, 495.
(32) Evans, N. D.; Gentleman, E. The role of material structure and mechanical properties in cell-matrix interactions. *J Mater Chem B* **2014,** *2* (17), 2345.
(33) Wells, R. G. The role of matrix stiffness in regulating cell behavior. *Hepatology* **2008,** *47* (4), 1394.
(34) Evans, N. D.; Gentleman, E. The role of material structure and mechanical properties in cell–matrix interactions. *J. Mater. Chem. B* **2014,** *2* (17), 2345.
(35) Xia, T.; Liu, W.; Yang, L. A review of gradient stiffness hydrogels used in tissue engineering and regenerative medicine. *J Biomed Mater Res A* **2017,** *105* (6), 1799.
(36) Pelham Jr, R. J.; Wang, Y.-l. Cell locomotion and focal adhesions are regulated by substrate flexibility. *PNAS* **1997,** *94* (25), 13661.
(37) Scott, R. A.; Robinson, K. G.; Kiick, K. L.; Akins, R. E. Human Adventitial Fibroblast Phenotype Depends on the Progression of Changes in Substrate Stiffness. *Adv Healthc Mater* **2020,** *9* (8), e1901593.
(38) Winkler, J.; Abisoye-Ogunniyan, A.; Metcalf, K. J.; Werb, Z. Concepts of extracellular matrix remodelling in tumour progression and metastasis. *Nat Commun* **2020,** *11* (1), 5120.
(39) Cox, T. R. The matrix in cancer. *Nat Rev Cancer* **2021,** *21* (4), 217.
(40) Legant, W. R.; Pathak, A.; Yang, M. T.; Deshpande, V. S.; McMeeking, R. M.; Chen, C. S. Microfabricated tissue gauges to measure and manipulate forces from 3D microtissues. *PNAS* **2009,** *106* (25), 10097.
(41) Lu, P.; Weaver, V. M.; Werb, Z. The extracellular matrix: a dynamic niche in cancer progression. *J. Cell Biol.* **2012,** *196* (4), 395.
(42) Mouw, J. K.; Ou, G.; Weaver, V. M. Extracellular matrix assembly: a multiscale deconstruction. *Nat Rev Mol Cell Biol* **2014,** *15* (12), 771.
(43) Pickup, M. W.; Mouw, J. K.; Weaver, V. M. The extracellular matrix modulates the hallmarks of cancer. *EMBO Rep* **2014,** *15* (12), 1243.
(44) Acerbi, I.; Cassereau, L.; Dean, I.; Shi, Q.; Au, A.; Park, C.; Chen, Y. Y.; Liphardt, J.; Hwang, E. S.; Weaver, V. M. Human breast cancer invasion and aggression correlates with ECM stiffening and immune cell infiltration. *Integr Biol (Camb)* **2015,** *7* (10), 1120.
(45) Wu, B.; Liu, D. A.; Guan, L.; Myint, P. K.; Chin, L.; Dang, H.; Xu, Y.; Ren, J.; Li, T.; Yu, Z.et al. Stiff matrix induces exosome secretion to promote tumour growth. *Nat Cell Biol* **2023,** *25* (3), 415.
(46) MacKintosh, F. C.; Kas, J.; Janmey, P. A. Elasticity of semiflexible biopolymer networks. *Phys. Rev. Lett.* **1995,** *75* (24), 4425.
(47) Storm, C.; Pastore, J. J.; MacKintosh, F. C.; Lubensky, T. C.; Janmey, P. A. Nonlinear elasticity in biological gels. *Nature* **2005,** *435* (7039), 191.

(48) Onck, P. R.; Koeman, T.; van Dillen, T.; van der Giessen, E. Alternative explanation of stiffening in cross-linked semiflexible networks. *Phys. Rev. Lett.* **2005,** *95* (17), 178102.
(49) Lieleg, O.; Claessens, M. M.; Heussinger, C.; Frey, E.; Bausch, A. R. Mechanics of bundled semiflexible polymer networks. *Phys. Rev. Lett.* **2007,** *99* (8), 088102.
(50) Licup, A. J.; Munster, S.; Sharma, A.; Sheinman, M.; Jawerth, L. M.; Fabry, B.; Weitz, D. A.; MacKintosh, F. C. Stress controls the mechanics of collagen networks. *Proc Natl Acad Sci U S A* **2015,** *112* (31), 9573.
(51) Wen, Q.; Basu, A.; Janmey, P. A.; Yodh, A. G. Non-affine deformations in polymer hydrogels. *Soft Matter* **2012,** *8* (31), 8039.
(52) Liu, K.; Mihaila, S. M.; Rowan, A.; Oosterwijk, E.; Kouwer, P. H. J. Synthetic Extracellular Matrices with Nonlinear Elasticity Regulate Cellular Organization. *Biomacromolecules* **2019,** *20* (2), 826.
(53) Xu, J.; Tseng, Y.; Wirtz, D. Strain hardening of actin filament networks. Regulation by the dynamic cross-linking protein alpha-actinin. *J. Biol. Chem.* **2000,** *275* (46), 35886.
(54) de Almeida, P.; Jaspers, M.; Vaessen, S.; Tagit, O.; Portale, G.; Rowan, A. E.; Kouwer, P. H. J. Cytoskeletal stiffening in synthetic hydrogels. *Nat Commun* **2019,** *10* (1), 609.
(55) Liu, K.; Veenendaal, T.; Wiendels, M.; Ruiz-Zapata, A. M.; van Laar, J.; Kyranas, R.; Enting, H.; van Cranenbroek, B.; Koenen, H.; Mihaila, S. M.et al. Synthetic Extracellular Matrices as a Toolbox to Tune Stem Cell Secretome. *ACS Appl. Mater. Interfaces* **2020,** *12* (51), 56723.
(56) Chen, W.; Kouwer, P. H. Combining mechanical tuneability with function: biomimetic fibrous hydrogels with nanoparticle crosslinkers. *Adv. Funct. Mater.* **2021,** *31* (47), 2105713.
(57) Ollier, R. C.; Xiang, Y.; Yacovelli, A. M.; Webber, M. J. Biomimetic strain-stiffening in fully synthetic dynamic-covalent hydrogel networks. *Chemical Science* **2023,** *14* (18), 4796.
(58) Wang, W.; Xiang, L.; Diaz-Dussan, D.; Zhang, J.; Yang, W.; Gong, L.; Chen, J.; Narain, R.; Zeng, H. Dynamic Flexible Hydrogel Network with Biological Tissue-like Self-Protective Functions. *Chem. Mater.* **2020,** *32* (24), 10545.
(59) Vernerey, F. J.; Lalitha Sridhar, S.; Muralidharan, A.; Bryant, S. J. Mechanics of 3D Cell-Hydrogel Interactions: Experiments, Models, and Mechanisms. *Chem Rev* **2021,** *121* (18), 11085.
(60) Shen, Z. L.; Kahn, H.; Ballarini, R.; Eppell, S. J. Viscoelastic properties of isolated collagen fibrils. *Biophys. J.* **2011,** *100* (12), 3008.
(61) Cuenot, S.; Gelebart, P.; Sinquin, C.; Colliec-Jouault, S.; Zykwinska, A. Mechanical relaxations of hydrogels governed by their physical or chemical crosslinks. *J Mech Behav Biomed Mater* **2022,** *133*, 105343.
(62) Rowe, R. A.; Pryse, K. M.; Elson, E. L.; Genin, G. M. Stable fitting of noisy stress relaxation data. *Mechanics of Soft Materials* **2019,** *1*, 1.
(63) Chaudhuri, O.; Gu, L.; Klumpers, D.; Darnell, M.; Bencherif, S. A.; Weaver, J. C.; Huebsch, N.; Lee, H. P.; Lippens, E.; Duda, G. N.et al. Hydrogels with tunable stress relaxation regulate stem cell fate and activity. *Nat. Mater.* **2016,** *15* (3), 326.
(64) McKinnon, D.; Domaille, D.; Brown, T.; Kyburz, K.; Kiyotake, E.; Cha, J.; Anseth, K. Measuring cellular forces using bis-aliphatic hydrazone crosslinked stress-relaxing hydrogels. *Soft matter* **2014,** *10* (46), 9230.
(65) McKinnon, D. D.; Domaille, D. W.; Cha, J. N.; Anseth, K. S. Biophysically defined and cytocompatible covalently adaptable networks as viscoelastic 3D cell culture systems. *Adv. Mater.* **2014,** *26* (6), 865.
(66) Nam, S.; Lee, J.; Brownfield, D. G.; Chaudhuri, O. Viscoplasticity Enables Mechanical Remodeling of Matrix by Cells. *Biophys. J.* **2016,** *111* (10), 2296.
(67) Tschoegl, N. W. *The phenomenological theory of linear viscoelastic behavior: Materials Chemistry and Physics,* **1990***, 26*, 417.
(68) Nam, S.; Hu, K. H.; Butte, M. J.; Chaudhuri, O. Strain-enhanced stress relaxation impacts nonlinear elasticity in collagen gels. *Proc Natl Acad Sci U S A* **2016,** *113* (20), 5492.
(69) Chaudhuri, O. Viscoelastic hydrogels for 3D cell culture. *Biomater Sci* **2017,** *5* (8), 1480.

(70) Ban, E.; Franklin, J. M.; Nam, S.; Smith, L. R.; Wang, H.; Wells, R. G.; Chaudhuri, O.; Liphardt, J. T.; Shenoy, V. B. Mechanisms of Plastic Deformation in Collagen Networks Induced by Cellular Forces. *Biophys. J.* **2018,** *114* (2), 450.
(71) Detournay, E.; Cheng, A. H.-D. In *Analysis and design methods*; Elsevier, 1993.
(72) Mason, T. G.; Ganesan, K.; van Zanten, J. H.; Wirtz, D.; Kuo, S. C. Particle tracking microrheology of complex fluids. *Phys. Rev. Lett.* **1997,** *79* (17), 3282.
(73) Crocker, J. C.; Valentine, M. T.; Weeks, E. R.; Gisler, T.; Kaplan, P. D.; Yodh, A. G.; Weitz, D. A. Two-point microrheology of inhomogeneous soft materials. *Phys. Rev. Lett.* **2000,** *85* (4), 888.
(74) Isobe, N.; Kimura, S.; Wada, M.; Deguchi, S. Poroelasticity of cellulose hydrogel. *Journal of the Taiwan Institute of Chemical Engineers* **2018,** *92*, 118.
(75) Sandino, C.; McErlain, D. D.; Schipilow, J.; Boyd, S. K. The poro-viscoelastic properties of trabecular bone: a micro computed tomography-based finite element study. *J Mech Behav Biomed Mater* **2015,** *44*, 1.
(76) Ed-Daoui, A.; Snabre, P. Poroviscoelasticity and compression-softening of agarose hydrogels. *Rheol. Acta* **2021,** *60* (6-7), 327.
(77) Unlu, G.; Levic, D. S.; Melville, D. B.; Knapik, E. W. Trafficking mechanisms of extracellular matrix macromolecules: insights from vertebrate development and human diseases. *Int. J. Biochem. Cell Biol.* **2014,** *47*, 57.
(78) Xin, T.; Greco, V.; Myung, P. Hardwiring Stem Cell Communication through Tissue Structure. *Cell* **2016,** *164* (6), 1212.
(79) Nicolas, J.; Magli, S.; Rabbachin, L.; Sampaolesi, S.; Nicotra, F.; Russo, L. 3D Extracellular Matrix Mimics: Fundamental Concepts and Role of Materials Chemistry to Influence Stem Cell Fate. *Biomacromolecules* **2020,** *21* (6), 1968.
(80) Yue, B. Biology of the extracellular matrix: an overview. *J Glaucoma* **2014,** *23* (8 Suppl 1), S20.
(81) Sarrazin, S.; Lamanna, W. C.; Esko, J. D. Heparan sulfate proteoglycans. *Cold Spring Harb Perspect Biol* **2011,** *3* (7), 1.
(82) Tamada, Y.; Ikada, Y. Effect of preadsorbed proteins on cell adhesion to polymer surfaces. *J. Colloid Interface Sci.* **1993,** *155* (2), 334.
(83) Ogushi, Y.; Sakai, S.; Kawakami, K. Phenolic Hydroxy Groups Incorporated for the Peroxidase‐Catalyzed Gelation of a Carboxymethylcellulose Support: Cellular Adhesion and Proliferation. *Macromolecular bioscience* **2009,** *9* (3), 262.
(84) Godbole, M.; Seyda, A.; Kohn, J.; Arinzeh, T. L. Surface properties of the substratum affect human mesenchymal stem cell differentiation. IEEE. 2004, 116.
(85) Huang, G.; Li, F.; Zhao, X.; Ma, Y.; Li, Y.; Lin, M.; Jin, G.; Lu, T. J.; Genin, G. M.; Xu, F. Functional and Biomimetic Materials for Engineering of the Three-Dimensional Cell Microenvironment. *Chem. Rev.* **2017,** *117* (20), 12764.
(86) Mahinroosta, M.; Farsangi, Z. J.; Allahverdi, A.; Shakoori, Z. Hydrogels as intelligent materials: A brief review of synthesis, properties and applications. *Materials Today Chemistry* **2018,** *8*, 42.
(87) Ullah, F.; Othman, M. B.; Javed, F.; Ahmad, Z.; Md Akil, H. Classification, processing and application of hydrogels: A review. *Mater Sci Eng C Mater Biol Appl* **2015,** *57*, 414.
(88) Mahinroosta, M.; Jomeh Farsangi, Z.; Allahverdi, A.; Shakoori, Z. Hydrogels as intelligent materials: A brief review of synthesis, properties and applications. *Materials Today Chemistry* **2018,** *8*, 42.
(89) Aida, T.; Meijer, E.; Stupp, S. Functional supramolecular polymers. *Science* **2012,** *335* (6070), 813.
(90) Krieg, E.; Bastings, M. M.; Besenius, P.; Rybtchinski, B. Supramolecular Polymers in Aqueous Media. *Chem Rev* **2016,** *116* (4), 2414.
(91) Herkert, L.; Droste, J.; Kartha, K. K.; Korevaar, P. A.; de Greef, T. F. A.; Hansen, M. R.; Fernandez, G. Pathway Control in Cooperative vs. Anti-Cooperative Supramolecular Polymers. *Angew Chem Int Ed Engl* **2019,** *58* (33), 11344.

(92) Cantekin, S.; de Greef, T. F. A.; Palmans, A. R. A. Benzene-1,3,5-tricarboxamide: a versatile ordering moiety for supramolecular chemistry. *Chemical Society Reviews* **2012,** *41* (18), 6125.
(93) Smulders, M. M. J.; Schenning, A. P. H. J.; Meijer, E. W. Insight into the Mechanisms of Cooperative Self-Assembly: The "Sergeants-and-Soldiers" Principle of Chiral and Achiral C3-Symmetrical Discotic Triamides. *Journal of the American Chemical Society* **2008,** *130* (2), 606.
(94) Stals, P. J. M.; Smulders, M. M. J.; Martín-Rapún, R.; Palmans, A. R. A.; Meijer, E. W. Asymmetrically Substituted Benzene-1,3,5-tricarboxamides: Self-Assembly and Odd–Even Effects in the Solid State and in Dilute Solution. *Chemistry – A European Journal* **2009,** *15* (9), 2071.
(95) Cantekin, S.; de Greef, T. F. A.; Palmans, A. R. A. Benzene-1,3,5-tricarboxamide: a versatile ordering moiety for supramolecular chemistry. *Chemical Society Reviews* **2012,** *41* (18), 6125.
(96) Howe, R. C.; Smalley, A. P.; Guttenplan, A. P.; Doggett, M. W.; Eddleston, M. D.; Tan, J. C.; Lloyd, G. O. A family of simple benzene 1,3,5-tricarboxamide (BTA) aromatic carboxylic acid hydrogels. *Chem Commun* **2013,** *49* (39), 4268.
(97) Leenders, C. M.; Albertazzi, L.; Mes, T.; Koenigs, M. M.; Palmans, A. R.; Meijer, E. W. Supramolecular polymerization in water harnessing both hydrophobic effects and hydrogen bond formation. *Chem Commun* **2013,** *49* (19), 1963.
(98) Leenders, C. M. A.; Mes, T.; Baker, M. B.; Koenigs, M. M. E.; Besenius, P.; Palmans, A. R. A.; Meijer, E. W. From supramolecular polymers to hydrogel materials. *Mater. Horiz.* **2014,** *1* (1), 116.
(99) Leenders, C. M. A.; Baker, M. B.; Pijpers, I. A. B.; Lafleur, R. P. M.; Albertazzi, L.; Palmans, A. R. A.; Meijer, E. W. Supramolecular polymerisation in water; elucidating the role of hydrophobic and hydrogen-bond interactions. *Soft Matter* **2016,** *12* (11), 2887.
(100) Dankers, P. Y.; Hermans, T. M.; Baughman, T. W.; Kamikawa, Y.; Kieltyka, R. E.; Bastings, M. M.; Janssen, H. M.; Sommerdijk, N. A.; Larsen, A.; Van Luyn, M. J. Hierarchical formation of supramolecular transient networks in water: a modular injectable delivery system. *Adv. Mater.* **2012,** *24* (20), 2703.
(101) Fernandez-Castano Romera, M.; Lafleur, R. P.; Guibert, C.; Voets, I. K.; Storm, C.; Sijbesma, R. P. Strain stiffening hydrogels through self-assembly and covalent fixation of semi-flexible fibers. *Angew. Chem.* **2017,** *129* (30), 8897.
(102) Shantanu S., Christina J. N., Matthew J., Webber c, Samuel I. S. Tuning supramolecular mechanics to guide neuron development. *Biomaterial*. **2013**, *34* (20), 4749.
(103) Wurm, F. R.; Klok, H. A. Be squared: expanding the horizon of squaric acid-mediated conjugations. *Chem. Soc. Rev.* **2013,** *42* (21), 8220.
(104) Marchetti, L. A.; Kumawat, L. K.; Mao, N.; Stephens, J. C.; Elmes, R. B. P. The Versatility of Squaramides: From Supramolecular Chemistry to Chemical Biology. **2019,** *5* (6), 1398.
(105) Saez Talens, V.; Englebienne, P.; Trinh, T. T.; Noteborn, W. E.; Voets, I. K.; Kieltyka, R. E. Aromatic Gain in a Supramolecular Polymer. *Angew Chem Int Ed Engl* **2015,** *54* (36), 10502.
(106) Saez Talens, V.; Makurat, D. M. M.; Liu, T.; Dai, W.; Guibert, C.; Noteborn, W. E. M.; Voets, I. K.; Kieltyka, R. E. Shape modulation of squaramide-based supramolecular polymer nanoparticles. *Polymer Chemistry* **2019,** *10* (23), 3146.
(107) Tong, C.; Liu, T.; Saez Talens, V.; Noteborn, W. E. M.; Sharp, T. H.; Hendrix, M.; Voets, I. K.; Mummery, C. L.; Orlova, V. V.; Kieltyka, R. E. Squaramide-Based Supramolecular Materials for Three-Dimensional Cell Culture of Human Induced Pluripotent Stem Cells and Their Derivatives. *Biomacromolecules* **2018,** *19* (4), 1091.
(108) Tong, C.; Wondergem, J. A. J.; van den Brink, M.; Kwakernaak, M. C.; Chen, Y.; Hendrix, M.; Voets, I. K.; Danen, E. H. J.; Le Devedec, S.; Heinrich, D.et al. Spatial and Temporal Modulation of Cell Instructive Cues in a Filamentous Supramolecular Biomaterial. *ACS Appl. Mater. Interfaces* **2022,** *14* (15), 17042.
(109) Storer, R. I.; Aciro, C.; Jones, L. H. Squaramides: physical properties, synthesis and applications. *Chem. Soc. Rev.* **2011,** *40* (5), 2330.

(110) Dragan, E. S. Design and applications of interpenetrating polymer network hydrogels. A review. *Chemical Engineering Journal* **2014,** *243*, 572.
(111) Gu, Z.; Huang, K.; Luo, Y.; Zhang, L.; Kuang, T.; Chen, Z.; Liao, G. Double network hydrogel for tissue engineering. *Wiley Interdiscip Rev Nanomed Nanobiotechnol* **2018,** *10* (6), e1520.
(112) Means, A. K.; Grunlan, M. A. Modern Strategies To Achieve Tissue-Mimetic, Mechanically Robust Hydrogels. *ACS Macro Letters* **2019,** *8* (6), 705.
(113) Zoratto, N.; Matricardi, P. Semi-IPNs and IPN-based hydrogels. *Polymeric gels* **2018**, 91.
(114) Dhand, A. P.; Galarraga, J. H.; Burdick, J. A. Enhancing biopolymer hydrogel functionality through interpenetrating networks. *Trends Biotechnol.* **2021,** *39* (5), 519.
(115) Lou, J.; Stowers, R.; Nam, S.; Xia, Y.; Chaudhuri, O. Stress relaxing hyaluronic acid-collagen hydrogels promote cell spreading, fiber remodeling, and focal adhesion formation in 3D cell culture. *Biomaterials* **2018,** *154*, 213.
(116) Bernero, M.; Zauchner, D.; Müller, R.; Qin, X.-H. Interpenetrating network hydrogels for studying the role of matrix viscoelasticity in 3D osteocyte morphogenesis. *Biomaterials Science* **2024,** *12*, 919.
(117) Gong, J. P.; Katsuyama, Y.; Kurokawa, T.; Osada, Y. Double-Network Hydrogels with Extremely High Mechanical Strength. *Adv. Mater.* **2003,** *15* (14), 1155.
(118) Na, Y.-H.; Kurokawa, T.; Katsuyama, Y.; Tsukeshiba, H.; Gong, J. P.; Osada, Y.; Okabe, S.; Karino, T.; Shibayama, M. Structural characteristics of double network gels with extremely high mechanical strength. *Macromolecules* **2004,** *37* (14), 5370.
(119) Haque, M. A.; Kurokawa, T.; Gong, J. P. Super tough double network hydrogels and their application as biomaterials. *Polymer* **2012,** *53* (9), 1805.
(120) Nonoyama, T.; Gong, J. P. Double-network hydrogel and its potential biomedical application: A review. *Proc Inst Mech Eng H* **2015,** *229* (12), 853.
(121) Gong, J. P. Why are double network hydrogels so tough? *Soft Matter* **2010,** *6* (12), 2583.
(122) Sun, J. Y.; Zhao, X.; Illeperuma, W. R.; Chaudhuri, O.; Oh, K. H.; Mooney, D. J.; Vlassak, J. J.; Suo, Z. Highly stretchable and tough hydrogels. *Nature* **2012,** *489* (7414), 133.
(123) Nakayama, A.; Kakugo, A.; Gong, J. P.; Osada, Y.; Takai, M.; Erata, T.; Kawano, S. High Mechanical Strength Double-Network Hydrogel with Bacterial Cellulose. *Adv. Funct. Mater.* **2004,** *14* (11), 1124.
(124) Chen, Q.; Chen, H.; Zhu, L.; Zheng, J. Fundamentals of double network hydrogels. *J Mater Chem B* **2015,** *3* (18), 3654.
(125) Liu, S.; Oderinde, O.; Hussain, I.; Yao, F.; Fu, G. Dual ionic cross-linked double network hydrogel with self-healing, conductive, and force sensitive properties. *Polymer* **2018,** *144*, 111.
(126) Li, D.; Chen, K.; Tang, H.; Hu, S.; Xin, L.; Jing, X.; He, Q.; Wang, S.; Song, J.; Mei, L. A Logic‐Based Diagnostic and Therapeutic Hydrogel with Multistimuli Responsiveness to Orchestrate Diabetic Bone Regeneration. *Adv. Mater.* **2022,** *34* (11), 2108430.
(127) Chang, X.; Geng, Y.; Cao, H.; Zhou, J.; Tian, Y.; Shan, G.; Bao, Y.; Wu, Z. L.; Pan, P. Dual-Crosslink Physical Hydrogels with High Toughness Based on Synergistic Hydrogen Bonding and Hydrophobic Interactions. *Macromol. Rapid Commun.* **2018,** *39* (14), e1700806.
(128) Yu, F.; Yang, P.; Yang, Z.; Zhang, X.; Ma, J. Double-network hydrogel adsorbents for environmental applications. *Chem. Eng. J.* **2021,** *426*, 131900.
(129) Zhao, D.; Huang, J.; Zhong, Y.; Li, K.; Zhang, L.; Cai, J. High-Strength and High-Toughness Double-Cross-Linked Cellulose Hydrogels: A New Strategy Using Sequential Chemical and Physical Cross-Linking. *Adv. Funct. Mater.* **2016,** *26* (34), 6279.
(130) Xu, X.; Jerca, V. V.; Hoogenboom, R. Bioinspired double network hydrogels: from covalent double network hydrogels via hybrid double network hydrogels to physical double network hydrogels. *Mater Horiz* **2021,** *8* (4), 1173.
(131) Sun, W.; Xue, B.; Li, Y.; Qin, M.; Wu, J.; Lu, K.; Wu, J.; Cao, Y.; Jiang, Q.; Wang, W. Polymer-Supramolecular Polymer Double-Network Hydrogel. *Adv. Funct. Mater.* **2016,** *26* (48), 9044.

(132) Li, H.; Wang, H.; Zhang, D.; Xu, Z.; Liu, W. A highly tough and stiff supramolecular polymer double network hydrogel. *Polymer* **2018,** *153*, 193.
(133) Bovone, G.; Guzzi, E. A.; Bernhard, S.; Weber, T.; Dranseikiene, D.; Tibbitt, M. W. Supramolecular reinforcement of polymer–nanoparticle hydrogels for modular materials design. *Adv. Mater.* **2022,** *34* (9), 2106941.
(134) Li, L.; Zhang, K.; Wang, T.; Wang, P.; Xue, B.; Cao, Y.; Zhu, L.; Jiang, Q. Biofabrication of a biomimetic supramolecular-polymer double network hydrogel for cartilage regeneration. *Materials & Design* **2020,** *189*, 108492.
(135) O'Brien, S.; Brannigan, R. P.; Ibanez, R.; Wu, B.; O'Dwyer, J.; O'Brien, F. J.; Cryan, S.-A.; Heise, A. Biocompatible polypeptide-based interpenetrating network (IPN) hydrogels with enhanced mechanical properties. *J. Mater. Chem. B* **2020,** *8* (34), 7785.
(136) Wang, T.; Zhang, Y.; Gu, Z.; Cheng, W.; Lei, H.; Qin, M.; Xue, B.; Wang, W.; Cao, Y. Regulating mechanical properties of polymer‐supramolecular double‐network hydrogel by supramolecular self‐assembling structures. *Chin. J. Chem .* **2021,** *39* (10), 2711.
(137) Zeng, J.; Shi, D.; Gu, Y.; Kaneko, T.; Zhang, L.; Zhang, H.; Kaneko, D.; Chen, M. Injectable and near-infrared-responsive hydrogels encapsulating dopamine-stabilized gold nanorods with long photothermal activity controlled for tumor therapy. *Biomacromolecules* **2019,** *20* (9), 3375.
(138) Chen, Q.; Chen, H.; Zhu, L.; Zheng, J. Engineering of tough double network hydrogels. *Macromol. Chem. Phys.* **2016,** *217* (9), 1022.
(139) Wang, Q.; Hou, R.; Cheng, Y.; Fu, J. Super-tough double-network hydrogels reinforced by covalently compositing with silica-nanoparticles. *Soft Matter* **2012,** *8* (22), 6048.
(140) Turner, J. G.; Og, J. H.; Murphy, C. J. Gold nanorod impact on mechanical properties of stretchable hydrogels. *Soft Matter* **2020,** *16* (28), 6582.
(141) Zhu, K.; Shin, S. R.; van Kempen, T.; Li, Y. C.; Ponraj, V.; Nasajpour, A.; Mandla, S.; Hu, N.; Liu, X.; Leijten, J.et al. Gold Nanocomposite Bioink for Printing 3D Cardiac Constructs. *Adv. Funct. Mater.* **2017,** *27* (12), 1605352.
(142) Ding, F.; Zhang, L.; Chen, X.; Yin, W.; Ni, L.; Wang, M. Photothermal nanohybrid hydrogels for biomedical applications. *Frontiers in bioengineering and biotechnology* **2022,** *10*, 1066617.
(143) Huang, X.; El-Sayed, M. A. Gold nanoparticles: Optical properties and implementations in cancer diagnosis and photothermal therapy. *Journal of Advanced Research* **2010,** *1* (1), 13.
(144) Wahid, F.; Zhao, X.-J.; Jia, S.-R.; Bai, H.; Zhong, C. Nanocomposite hydrogels as multifunctional systems for biomedical applications: Current state and perspectives. *Composites Part B: Engineering* **2020,** *200,* 108208.

Chapter 2

Modulation of Thermally Driven Transitions in Squaramide-based Supramolecular Hydrogels

Temperature is a potent stimulus that can build and transform supramolecular materials from the molecular to the macroscopic scales. In this work, we designed a small library of squaramide-based monomers to delineate the structural modifications necessary to tune the formation of fibrillar aggregates and gel phase materials that respond to temperature. We found that the substitution of carbamate linkages with an ether bonds results in the formation of a 4-fold less stiff hydrogel relative to the native tripodal squaramide monomer, whereas a hydrogel still form at high concentrations even when lacking a squaramide moiety. Importantly, these structural modifications alter the response of the gels to temperature. After heating to 130°C and cooling them back to room temperature, we observed that hydrogels composed of molecules with symmetrical tripodal squaramide-based structures can retain their original shapes as gels but underwent shrinkage, eventually transforming into materials with a high degree of internal order. Understanding the effect of temperature on supramolecular hydrogels constructed from small molecule monomers opens the door to a range of applications in the biomedical field.

This chapter was prepared as a research article: Ying Chen, Francesca Lauria, Thomas J.F. Kock, Goutam Ghosh, Marco M. R. M. Hendrix, Ilja K. Voets, Gustavo Fernandez, Roxanne E. Kieltyka*

2.1 Introduction

Supramolecular polymers have sparked much interest for their unique properties that arise from the inherent dynamic character of the interactions that hold them together.[1-5] The delicate balance of noncovalent interactions, such as hydrogen bonding, hydrophobic-hydrophilic interactions, van der Waals forces, and π-π interactions in the monomer, permit tuning of their structural and functional of the resultant polymers and materials. As hydrogels, altering their molecular structures opens the door to tune their mechanics and responsiveness to a diverse range of physical and chemical stimuli.[4,6,7] However, the rational design of supramolecular materials starting from small molecule monomers and prediction of their final properties and behaviours remains challenging. This holds especially in water, where the hydrophobic effect has a major influence on supramolecular polymerization and hydrogelation process, and ultimately their final properties, such as their mechanics and thermoreponsiveness.[8-12]

Thermo-responsive polymers are being extensively investigated due to their broad applicability for use in the biomedical field (e.g., drug delivery, sensors and tissue engineering) that comes from their capacity to undergo physical changes in response to temperature.[13-17] There is a particular interest in exploring the lower critical solution temperature (LCST), where a distinct phase shift occurs due to dehydration of the polymer chains above a given temperature, in such materials. To access this property in the supramolecular materials, an often used strategy involves the tethering of molecular recognition units to water soluble polymers that exhibit this behaviour.[18,19] Moreover, filamentous supramolecular polymers that are constructed from the assembly of small molecule monomers respond distinctly to temperature in line with their specific chemistries. For example, in peptide-based systems often disruption of the assemblies is observed with increasing temperature leading to gel-to-sol transitions whereas in small molecule monomers with oligo(ethylene glycol) chains LCST behaviour can be detected within the assemblies. In these monomers, the hydrophobic core of the gelator remains shielded from water maintaining the assembly, while the hydrophilic part (e.g., oligoethylene glycol) that is thermo-responsive enables nanophase segregation and further regulates material properties.[24,25] Therefore, balancing hydrophobicity with the appropriate hydrogen bond design and the hydrophilic peripheral parts that interact with water molecules is critical to facilitate thermo-responsive behavior.[20-23]

We previously reported a tripodal squaramide-based monomer capable of self-assembling into supramolecular polymers and forming gel-phase materials in water.[34] In a first approach, we varied the aliphatic chain length (ranging from 6 to 12 methylene units) in the hydrophobic region of a tripodal amphiphile, resulting in hydrogel materials for 8 to 10 carbons whereas highlighting the importance of hydrogen bonding and a balance of the hydrophilic and hydrophobic domains on the gelation of the monomer. Inspired by these results, we designed a library of tripodal squaramide-based monomers to further understand the impact of a range of chemical modifications to the tripodal squaramide-based gelator evaluating their mechanics and thermal behaviour in the assembled state. It was envisaged that the non-uniform changes to the monomer geometry and hydrophobic content, as well as the number of squaramides and the presence of the carbamate moiety, will affect the supramolecular polymerization, gelation, and thermo-responsive properties in aqueous solution.

2.2 Result and Discussion

Tripodal Squaramide-Based Amphiphile Design and Synthesis

We sought first to understand the features (e.g., hydrophilicity, hydrogen bonds, etc.) of the tripodal squaramide-based monomers that enable them to form supramolecular hydrogels and the tuning of their physical properties (Scheme 1, Figure S1-S5).[18] We synthesized **5** according to an earlier method reported by our group[18] and evaluated the influence of the carbamate moiety in **5** by preparing **4** with an ether moiety.[19] We first conjugated tetraethylene glycol monomethyl ether and 1,10-dibromodecane in the presence of sodium hydride. We then converted the resultant amphiphilic monomer that containing a halide into a primary amine by the Gabriel synthesis and coupled 3,4-dibutoxy-3-cyclobutene-1,2-dione to obtain the squaramide-based amphiphile. In the last step, we reacted tris(2-aminoethylamine) (TREN) with the squaramide amphiphile to obtain the final tripodal supramolecular monomer **4**.

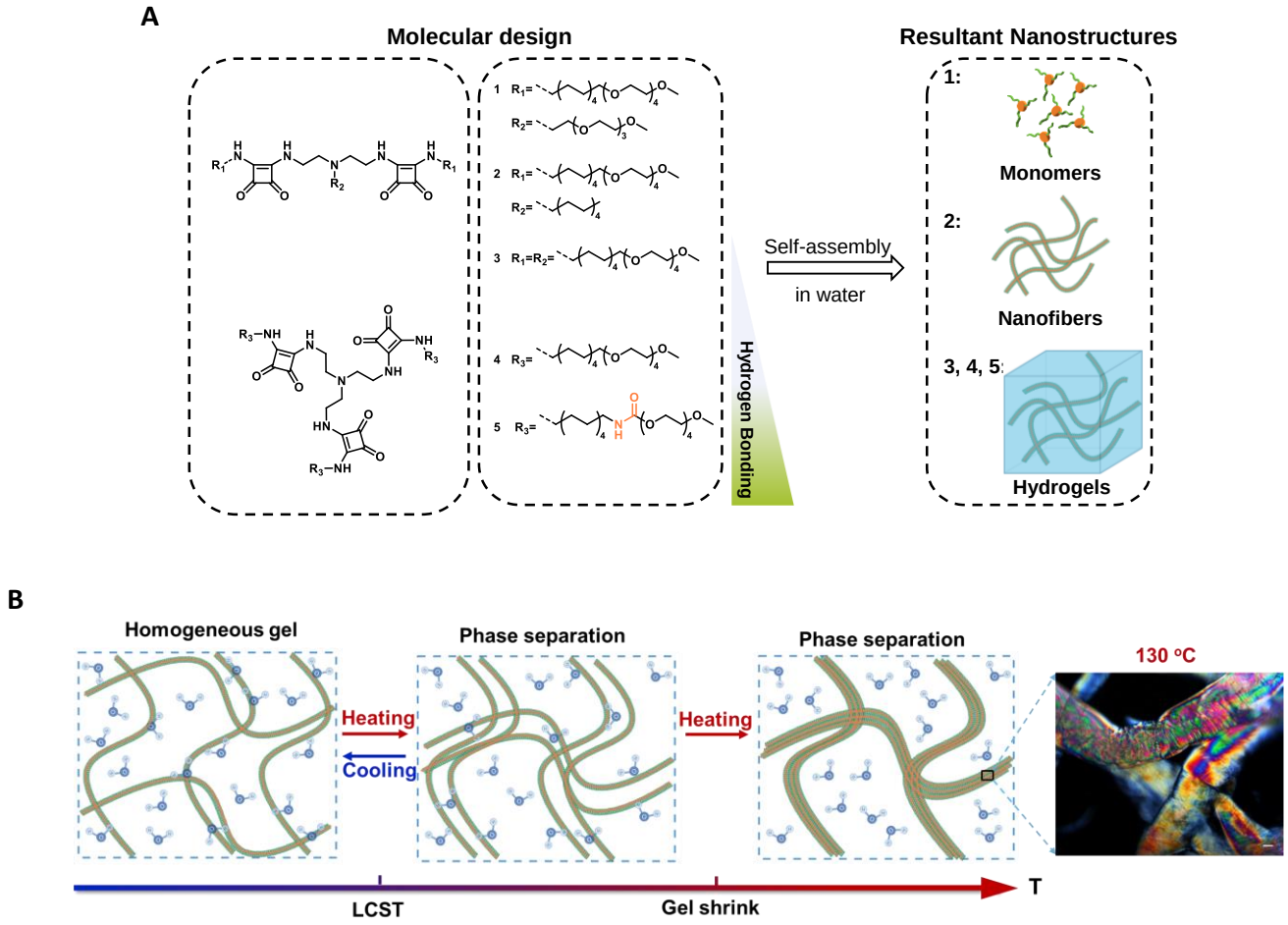

Scheme 1. (A) Squaramide-based tripodal supramolecular monomers **1**-**5** used in this study, and their self-assembly into supramolecular polymers and gel-phase materials. (B) Schematic of thermal transitions in the supramolecular network of **4** with increasing temperature.

We further explored a second set of monomers (**1**-**3**) to understand the effect of reducing the number of squaramide moieties and modifying the hydrophilic-hydrophobic balance within the monomer. We implemented this alteration to investigate the impact of aliphatic spacers linked to the oligo(ethylene glycol) chains and the carbamate bonds on the supramolecular polymerization of squaramide moieties. Monomers **1**-**3** consisted of two squaramide amphiphiles arms that contain ester bonds like **4**, and we coupled a third arm with either an oligoethylene glycol chain (**1**, ωTEG = 0.55), a

shorter alkyl chain (**2**, ωTEG = 0.53), or a chain consisting of alkyl and oligoethylene glycol segments (**3**, ωTEG = 0.46) directly attached to the nitrogen of the TREN core (Scheme S1). We synthesized monomers **1**-**3** starting from reacting benzyl alcohol with diethylenetriamine to obtain N,N″-di-Z-diethylenetriamine followed by coupling of oligoethylene glycol (**12a**), a short alkyl chain (**12b**) or a chain with alkyl and oligoethylene glycol domains (**12c**) onto the N,N'-di-Z-diethylenetriamine core. After in situ catalytic hydrogenation with triethylsilane and palladium on carbon to remove the carboxybenzyl-protecting group, the core was further coupled with two squaramide-based amphiphiles (**9**) to obtain the monomers **1**-**3**.

Evaluation of supramolecular polymer and gel properties at ambient temperature

We first investigated the ability of the tripodal squaramide-based monomers **1**-**5** to form gels in water by the gel inversion method and oscillatory rheology. Sonication of the various monomers in water led to gels for monomers **3** – **5** (Figure S6-S9). Monomer **5**[18] exhibited a critical gelation concentration (CGC) of 1.5-2 mM, whereas **4** containing the ester moiety showed a higher CGC of 2-2.5 mM consistent with the formation of fewer hydrogen bonds (Figure S8-S9). Further removal of one of the squaramide moieties in **3** showed an even higher CGC value (4-5 mM) and longer gelation time (Figure S7). These results suggest that both the importance of the number of hydrogen bonds both in the core and on the periphery of the amphiphile to tune the hydrogel storage modulus. Further removal of the alkyl chain from **3** leaving only an oligoethylene glycol chain (**1**) resulted in excellent water solubility with no gel being formed up to 6 mM. In contrast, exchange of one of the amphiphile arms for a hydrophobic group as in **2** resulted in visible precipitation at concentrations as low as 0.75 mM (Figure S6).

We then quantified the mechanical properties of hydrogels **3** - **5** by oscillatory rheology to understand the impact of the various structural substitutions of the hydrogelators (Figure 1A-C, S10-S11). We performed time sweep measurements on the hydrogels to gain insight into the time for the hydrogels to recover after their dispensing on the rheometer plate and to understand if their properties continue to change over time. We then determined the linear viscoelastic regime (LVE) of the hydrogels though an amplitude sweep measurement. Hydrogel **5** (5 mM) exhibited constant storage (G') and loss (G'') moduli until 3% strain, while hydrogels **3** (5 mM) and **4** (5 mM) showed less brittle behaviour showing constant moduli until strains of 10% and 7%, respectively. Frequency sweep experiments showed that hydrogels **4** and **5** exhibited a G' nearly 10 times higher than the G'' and showed frequency independent behavior within the measured range and more elastic character. Conversely, hydrogel **3** displayed a G' only 2 times higher than G'' and showed weak frequency dependence, suggestive of more viscoelastic behavior. More specifically, hydrogel **5** showed the greatest storage modulus of 100 Pa whereas **4** and **5** showed a significant decrease to 19 and 8 Pa, respectively, consistent with a decrease in the number of hydrogen bonds that can be formed between the various monomers. Because of the supramolecular nature of the gels, we evaluated their capacity to self-recover by performing a step-strain test. Here, a large strain outside the LVE is applied to the supramolecular hydrogel and then removed evaluating its response throughout the process. Subjecting the hydrogels to a large amplitude strain (300%) resulted in a decrease of the G' values of **3**-**5** with an inversion of their moduli (G'' > G'). Withdrawal of the large amplitude strain, all hydrogels formed gels again (G' > G'') though with a slight decrease in G' to a similar extent between monomers.

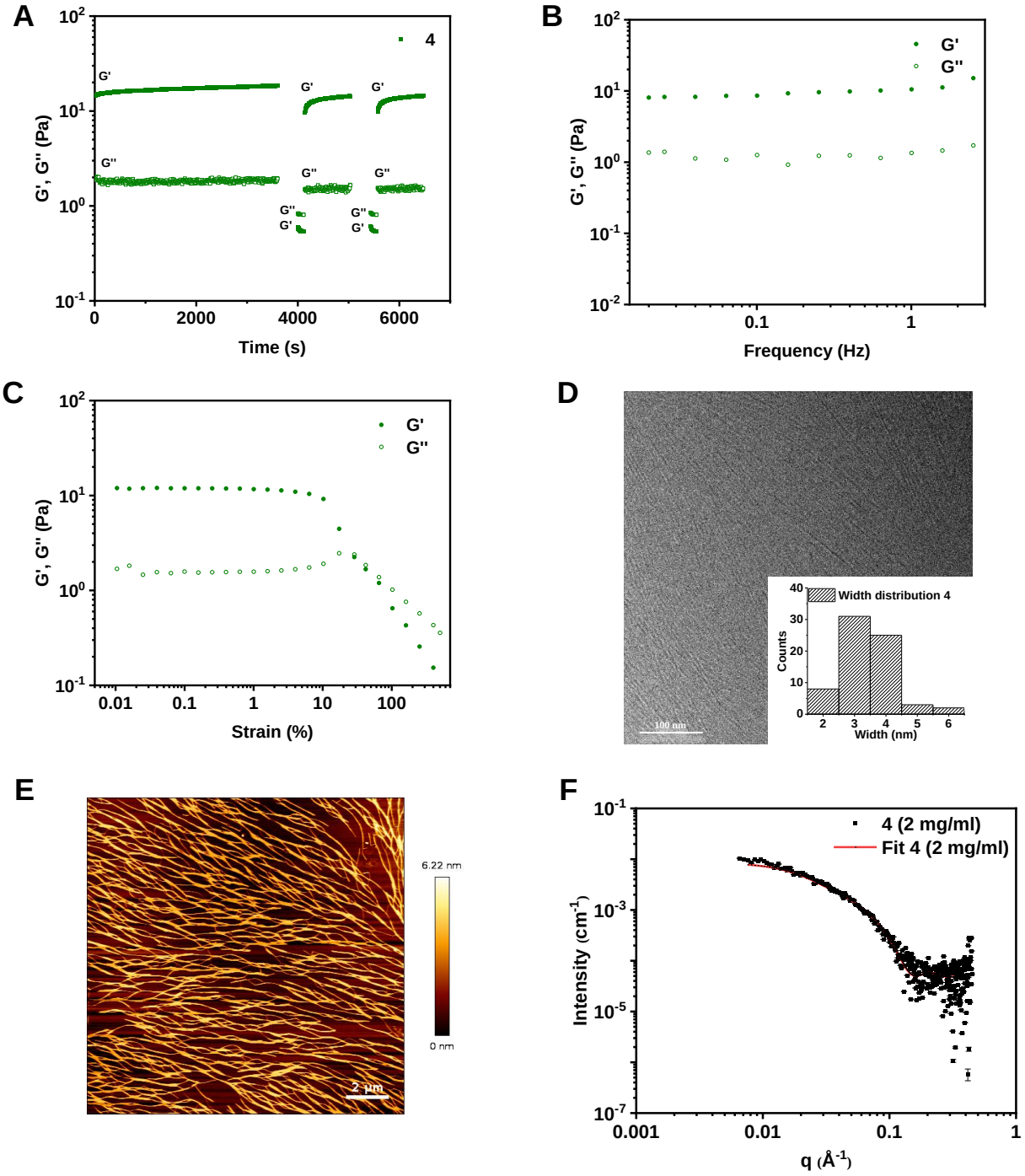

Figure 1. Oscillatory rheology measurements of hydrogels **4** (5 mM) in MilliQ water at RT: (A) Time sweep measurements (ƒ = 1 Hz, γ = 0.05%) and self-recovery process of hydrogel **4** (5 mM) in MilliQ water at RT. (B) Frequency sweep (γ = 0.05%). (C) Amplitude sweep (ƒ = 1 Hz). (D) Cryo-TEM images of **4** (0.5 mM) in Milli Q water. Insert Histograms of fiber width distribution for a sample size of N ≥ 50. Scale bar: *100 nm*. (E) AFM height image of **4** (0.25 mM) by spinning coating (2000 rpm, 2 min) and deposited on mica overnight after dissolution. (F) Small-angle X-ray scattering profiles of fibers **4** (2 mg/mL). Black dots represent experimental data; the red line represents fit with a form factor for flexible cylinders.

To understand the origin of the distinct mechanical properties of hydrogels **2**-**5**, we performed studies that permit insight into the morphological aspect of the assembled structures. Monomers **3**-**5** formed high-aspect ratio fibers on assembly reaching several micrometers in length by cryo-TEM imaging (Figure 1D, S12). Monomer **4** exhibited thicker supramolecular polymer fibers (4 nm) compared to **3** (3 nm) that contained an increased number of squaramide units, while **5** showed the

thickest fibers (5 nm) bearing the maximum number of squaramides and the carbamate group in place of the ether. Most likely, the weak mechanical properties measured by oscillatory rheology originate from the dense and entangled presentation of filamentous structures with the differences in moduli arising due to the differences in fibrillar diameter. Recorded AFM images of **3**, **4** and **5** further support the cryo-EM findings (Figure 1E, S13). Moreover, we found for monomer **2** (0.25 mM) sheet-like structures instead of fibers consistent with its lower solubility due to the introduction of an alkyl chain. Small-angle X-ray scattering (SAXS) further supported the differences in morphology of the supramolecular polymers **3**-**5** in water. The scattering profiles revealed the presence of elongated one-dimensional aggregates with high aspect ratios of solutions **3**-**5** (Figure 1F, S14). A form factor appropriate for flexible cylinders best described the obtained scattering profiles, yielding cross-sectional radii of 1.8 nm (**3**), 2.3 nm (**4**), and 2.4 nm (**5**) for the various monomers in line with earlier trends measured from cryoTEM images. These findings indicate that altering the hydrophilic and hydrogen bonding domains of the squaramide-based tripodal monomers can modulate the fiber properties.

We then probed the impact of supramolecular polymerization on monomers **1**-**5** at the molecular level by spectroscopic (UV, IR) methods. Monomer **5** displayed two distinct peaks at 270 and 323 nm in the UV spectra, corresponding to HOMO-LUMO and HOMO-LUMO+1 transitions of the squaramide moiety when polymerized in a head-to-tail hydrogen bonding arrangement (Figure 2A). Replacement of the carbamate moieties with ethers in the monomer **4** yielded a similar spectral profile to that of **5**, with red- and blue-shifted transitions observed at 271 nm and 321 nm but with reduced absorption intensity. Monomer **3** showed a distinct spectral profile with a sharp peak 324 nm and a plateau-like shoulder at 274 nm pointing out a distinct conformation of the squaramides within the monomer due to the alteration in their number and the hydrophobic and hydrophilic domains. The introduction of an alkyl chain in the third position of **2** to yield a more hydrophobic structure, led to a UV-Vis profile displaying two broad peaks at 257 nm and 318 nm with a lower intensity compared to **3**. Monomer **1** that lacked one squaramide moiety and one aliphatic spacer, exhibited a single band at 289 nm, suggesting a lack of polymerization due to the imbalance between the hydrophilic and hydrophobic domains and an insufficient number of hydrogen bonds. These results demonstrate that chemical modifications to the squaramide-based monomers at the periphery do not impact the orientation of the squaramides in the resulting supramolecular polymers, whereas those at the center result in distinct modes of monomer assembly. These UV-Vis studies can further benefit from computation to unravel the conformation of the monomers that lead to the observed polymer structures.

To gain further insight into the polymerization mechanism of the monomers **1**-**5**, we evaluated the effect of changes in concentration or addition of a co-solvent to the supramolecular polymers. Concentration-dependent UV-Vis absorption studies revealed that monomers **1**-**5** retained their peak shifts even with decreasing their concentration down to the sub-micromolar range (Figure 2B, S15). Because of the insensitivity of the formed supramolecular polymers to concentration changes, we used a co-solvent approach to depolymerize **1**-**5**. We titrated acetonitrile (MeCN) to supramolecular polymers of **3**-**5** in water. For all monomers, a H_2O-MeCN volume ratio of 6:4 yielded a single absorbance band at 293 nm consistent with depolymerization (Figure S16-S17). In solely MeCN, monomers **1**-**3** exhibited a single band in the same range as the other. Interestingly, monomers **4** and **5** in MeCN displayed two peaks at 290 and 321 nm and 294 and 323 nm, respectively, consistent with

head-to-tail squaramide assembly of the monomer similarly to water. The depolymerization of the monomers with a co-solvent opens the door to unravel the mechanism of the polymerization of the monomers and the influence of their distinct chemical structures on this process.

We then evaluated the changes in chemical structure on the hydrophobic domains presented by the aggregates on assembly by the Nile Red dye assay. Nile Red is a solvatochromic dye that shows a blue shift and an increase in the intensity of its fluorescence emission when embedded within a hydrophobic environment relative to water.[35,36] We observed a highly intense, blue-shifted emission band at 615 nm for **5**, whereas the emission maxima of **4** and **3** shifted to lesser extent at 623 nm and 621 nm, respectively, when we exchanged the carbamate moieties with ethers and further removed a squaramide unit (Figure 1C). The replacement of the third arm for an alkyl chain in monomer **2** resulted in a very low intensity emission band at 621 nm. Monomer **1** that lacked one squaramide moiety and one alkyl spacer showed a fluorescence emission profile as the dye in water in line with UV-Vis studies that suggest a lack of polymerization. These differences in emission maxima and intensity align with the changes in the hydrophobic and hydrophilic domains of the monomers and their distinctive modes of aggregation.[37-40]

We next examined the interactions between the monomers through Fourier Transform Infrared (FTIR) Spectroscopy on lyophilized samples and solutions. Lyophilized samples of **5** exhibited two distinct bands for the N-H stretch of the carbamate (3315 cm^{-1}) and squaramide units (3166 cm^{-1}), while the exchange of the carbamate for an ether bond in **2**-**4** displayed only one band for the squaramide unit (3169 - 3165 cm^{-1}) (Figure 2D, Table S1). Additionally, **5** displayed two extra C=O bands at 1719 cm^{-1} and 1689 cm^{-1} due to the carbamate moieities. The C-H stretches (both antisymmetric and symmetric) shifted slightly to a lower wavenumber because of the additional squaramide unit and carbamate groups in the monomer (Figure 2D, inset), and suggests a closer packing of the aliphatic chains within the supramolecular polymer.[41,42] We recorded a small independent ring breathing band at 1797 - 1799 cm^{-1} for monomers **2**-**5** consistent with the squaramide moiety. In the amide I region, all monomers possessed multiple C=O stretches originating from the carbamates and squaramides, that suggested the presence of several monomer packing modes in the polymerized state.

We performed infrared spectroscopy on monomers **3**-**5** in the solution state to probe the effect of adding a co-solvent to the polymers. The N-H stretch of the squaramide progressively moved to lower wavenumbers in **3**-**5** in D_2O (**3**: 3170 cm^{-1}, **4**: 3162 cm^{-1}, **5**: 3141 cm^{-1}), in line with stronger hydrogen bonds being formed by the squaramide moiety likely due to a more optimal packing of the monomers (Figure S18, Table S2). Alternatively, these peaks shifted to higher wavenumbers (**3**: 3174 cm^{-1}, **4**: 3166 cm^{-1}, **5**: 3155 cm^{-1}) when the solvent was changed to D_2O-CD_3CN (v/v-6:4) maintaining the same trend, pointing out that their depolymerization occurred. Furthermore, monomer **5** showed an extra band (1674 cm^{-1}) corresponding to the carbamate that shifted to a higher wavenumber (1692 cm^{-1}) on assembly in D_2O which aligns with our prior findings.[43] These results suggest that the squaramides play an important role in the assembly in the solid and solution state and solvents that compete with the association of the monomers trigger depolymerization affecting key interactions.

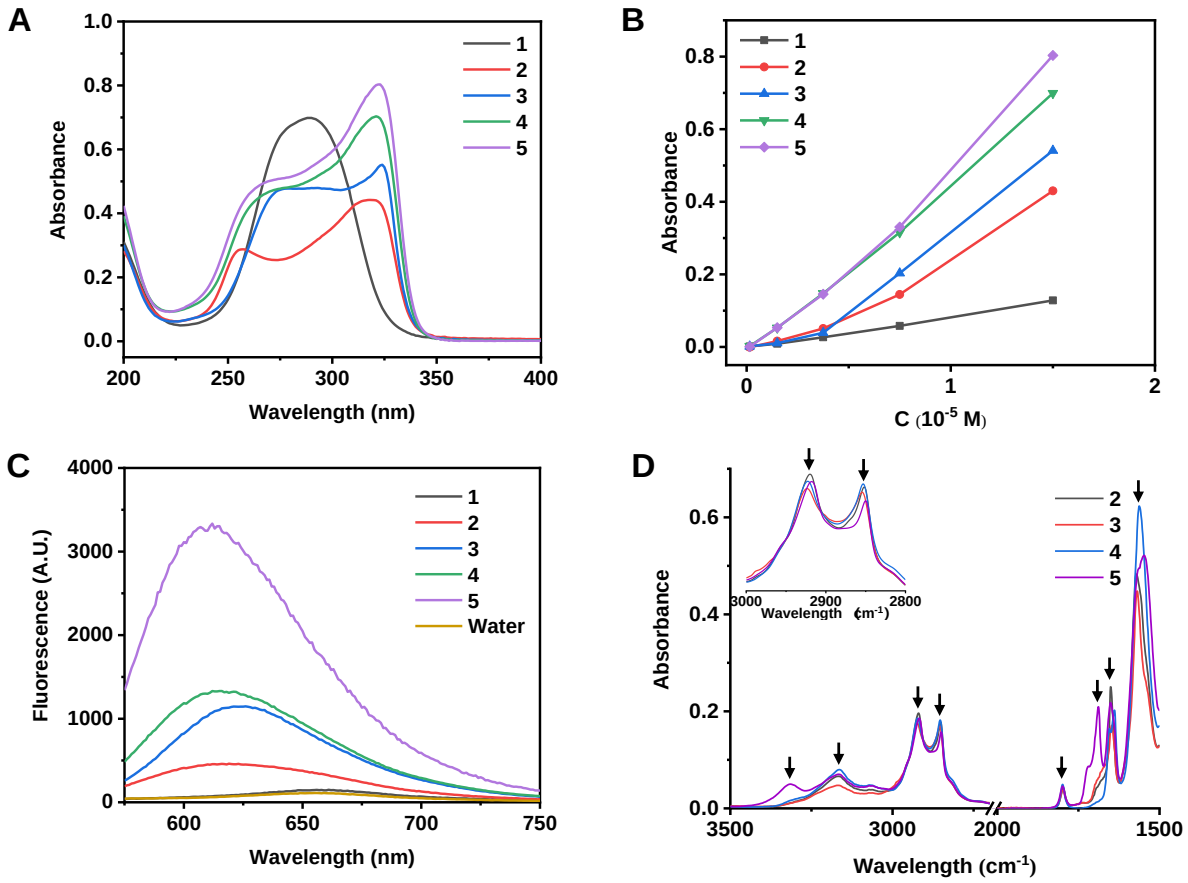

Figure 2. Spectroscopic studies of tripodal squaramide-based molecules: (A) UV-Vis spectra of **1**-**5** (15 µM) in water. (B) Concentration varied UV absorbance of **1**-**5** plotted at 322nm. (C) Fluorescence spectra (15 µM) of Nile Red dye embedded tripodal molecules **1**-**5**: ($c_{NileRed}$=0.005 mg/mL, λ_{exc} = 550 nm., λ_{em} = 560-750 nm), Nile red in water is used as a control. (D) FTIR spectra of **2**-**5** in the solid state (samples lyophilized from water (5 mM), arrows highlight peaks considered).

Squaramide-based hydrogels show thermal responsiveness and shape memory

Once insight into the various assembly modes of the monomers and their capacity to prepare gel phase materials was assessed we then evaluated their response to temperature. We first considered the effect of temperature on the supramolecular assemblies by UV-Vis thermal ramping experiments. Increasing the temperature of the various assembled monomer solutions in water resulted dehydration of oligoethylene glycol chains with a concomitant increase in turbidity of the samples due to their phase separation at a particular temperature, otherwise known as the lower critical solution temperature (LCST) (Figure S19). We recorded a LCST of ~52.5°C for **3** at 1 mM, whereas **4** with one additional squaramide unit showed a slightly higher value at ~60.5°C, and **5** demonstrated the highest LCST at ~69.0°C when the ether was replaced with the carbamate. These results illustrate that the LCST values of **3**, **4**, and **5** can be modulated according to the structural modification. Furthermore, when the decreasing the concentration to 0.2 mM, the LCST values increased to ~73.5°C for **5**, ~63.5°C for **4** and ~51.5°C for **3**, with **4** and **5** showing a higher sensitivity to concentration changes compared to **3** that showed a less significant variation, which is in line with similar studies for temperature-responsive polymers.[44,45] These results are likely due to the stronger interactions between the supramolecular polymer chain and water molecules due to the addition of squaramide unit and carbamate in **4** and **5**, which resulted in a more noticeable change in LCST compared with **3** has the minimal hydrogen bonds.[14,16,46] Strikingly, after heating **4** and **5** up to 90°C

in the cuvette and returning to room temperature the original state of the solution is retained (Figure S19B, insert). On the other hand, **3** appeared as a membrane-like precipitate after the heating process.

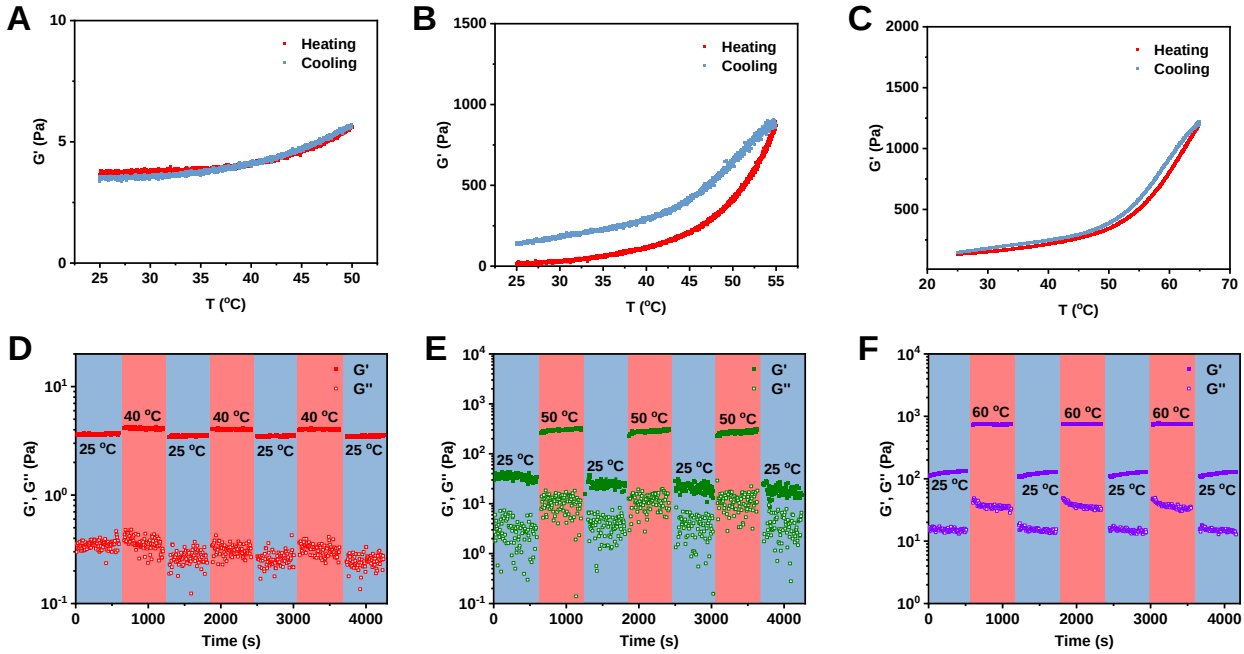

Figure 3. Self-healing properties of hydrogels (5 mM) (A) **3**, (B) **4**, (C) **5** in H_2O at different temperatures. Heating and cooling of hydrogels (5 mM) in various temperature ranges (D) **3** (25°C – 50°C), (E) **4** (25°C – 55°C), (F) **5** (25°C – 65°C) in H_2O.

We probed the mechanical response of the hydrogels **3**-**5** (5 mM) to temperature by conducting cyclic temperature sweep measurements on the rheometer. On the heating run, we observed an abrupt increase in the storage modulus (G') indicative of an LCST transition and thermal stiffening process for hydrogel **3** at 44.6°C, for gel **4** at 48.2°C and for hydrogel **5** at 71°C (Figure 3A-C), which showed the same trend as UV results with the increase in hydrogen bond number. Hydrogels **3** and **5** demonstrated nearly identical profiles during the heating and cooling process, indicating a high degree of recovery while hydrogel **4** showed hysteresis and did not fully recover after one temperature ramp. The cyclic temperature sweep measurements results demonstrated the reversible nature[47] of the thermal stiffening process in hydrogels **3**-**5**, as evidenced by the fully reversible storage modulus G' that could be reproduced over multiple cycles when kept at temperatures near the LCST of each monomer (Figure 3D-F). We then performed differential scanning calorimetry (DSC) measurements on the samples to further probe the phase-transition properties and thermal stability of hydrogels **3**-**5** (5 mM) (Figure S20). The recorded DSC profiles showed an endothermic shift at the same inflection point corresponding to the LCST transition in the rheological data. These findings are further consistent with the UV results and the structural variations of monomers **3**-**5**, indicating that the incorporation of squaramide units and an increase the number of hydrogen bonds result in an elevated LCST and a more significant release of energy during the LCST transition process.

To further explore the thermal behavior of hydrogel **3**-**5** above the LCST range, we subsequently heated hydrogels **3**-**5** in NMR tubes from RT to 90°C in an oil bath to monitor the macrophase separation process. During this process, hydrogels **3**-**5** transformed from transparent gels to opaque solids after reaching a certain temperature (**3**: ~41 °C, **4**: ~51 °C, **5**: ~68 °C) while maintaining a constant volume (Figure 4A). This onset of this transition in the sample aligned with the LCST transitions in the rheometer. Further heating caused the gels to shrink and become whiter. Reaching 130 °C resulted in

the white substance breaking apart due to boiling water inside the NMR tube. Upon cooling back to room temperature, the white substance regained transparency but could not recover to its original state.

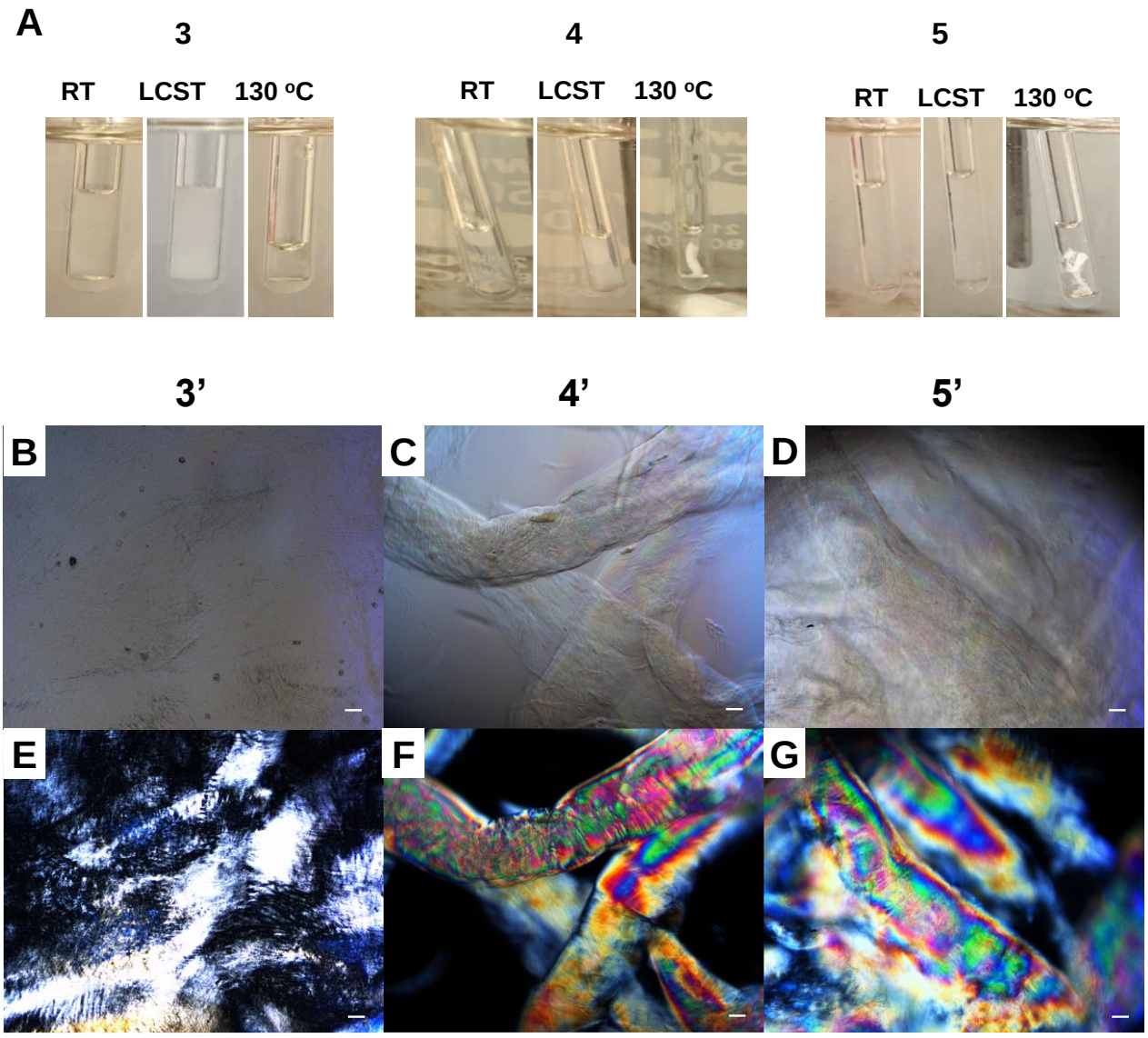

Figure 4. (A) Digital photos of hydrogel **3**-**5** (5 mM) during the heating process. Optical microscopy pictures and polarized optical microscopy (POM) of squaramide-based hydrogel prepared with H_2O after heating to 130°C and cooled back to RT: visible picture of **3'** (B), **4'** (C) and **5'** (D). POM micrographs of **3'** (E), **4'**(F), and **5'**(G). Scale bar: *100μm*.

Next, we employed polarizing microscopy (POM) to examine the optical properties of the annealed samples (**3'**, **4'**, **5'**) through exploring the birefringence of the substances. The POM images revealed that even after the heating process, the distinct shapes of **4'** and **5'** remained intact while **3'** was incomplete fragments, and we can observe the formation of colorful highly aligned substances with strong birefringence in **4'** and **5'**, while **3'** only displays slight birefringence (Figure 4B-G). Before heating, POM images of hydrogels **3**-**5** displayed a slight birefringence that is in line with cryo-TEM and AFM images showing alignment of some fibers after the self-assembly process (Figure S21). Scanning electron microscopy (SEM) images confirmed the presence of densely aligned fibers in **4** and **5**, while **3** exhibited a membrane-like morphology (Figure S22-S23). These structural differences among the hydrogels can be attributed to the alignment of fibers in hydrogels **4** and **5**, as observed in earlier cryo-

TEM images, that further consolidated during the heating process and lacked irreversibility upon cooling. However, monomer **3** lacked this behaviour, possibly due to the relatively weaker interactions between monomers with fewer hydrogen bonds that allowed disruption of its structure during the heating process.

We then examined the differences between the annealed samples at the molecular scale through X-ray diffraction (XRD) analysis. The low position peaks (**3'**: 4.36°, **4'**: 4.16°, **5'**: 3.83°) indicated an ordered structure of single fiber width while the peak around 21° signifies the presence of hydrophobic alkyl substituents (Figure S24). Additionally, the annealed samples (**3'**, **4'**, **5'**) showed reflections with a significantly stronger intensity compared to the non-annealed samples, indicating a higher orientation in the annealed fibers, and further explaining the difference in birefringence between samples.

In general, tripodal squaramide monomers **3**-**5** showed an organized fiber arrangement upon self-assembly in water, as observed through cryo-TEM, AFM and POM techniques. Upon heating, the water is removed from the oligo(ethylene glycols) between the supramolecular structures. It is hypothesized that **3**, with weaker and fewer molecular interactions between monomers, is more susceptible to a loss of stability when subjected to the removal of water molecules from the chains during the heating process. On the other hand, monomers **4** and **5**, with stronger molecular/fiber interactions due to the presence of the additional squaramide unit and carbamate, retain their stability, aggregating the fibers when exposed to a higher temperature above the LCST. We hypothesize that the greater orientation in the annealed fibers stems from the aggregation and fusion during the dehydration process.[48]

2.3 Conclusion

In this study, we performed systematic chemical modifications of the tripodal squaramide monomer reading out their effect on supramolecular polymerization and mechanical and thermal responsive properties of the hydrogels. The exchange of the carbamate for an ether linkage resulted in a reduction in hydrogel stiffness, whereas a reduction in the number of squaramide units and hydrophilic and hydrophobic properties still permitted the formation of gel phase materials that required a higher concentration of monomer and showed decreased stiffness. The observed effects on gelation likely result from the reduced degrees of polymerization of the squaramide monomers that affect supramolecular polymer entanglement. Additionally, thermo-responsive behaviors of hydrogels **3**-**5** varied according to their distinct hydrophilicity and hydrogen bonding units. After heating the hydrogels to 130°C and cooling them back to room temperature, we observed that the hydrogels **4** and **5** retained their original shapes but underwent shrinkage, eventually transforming into highly aligned materials. Cumulatively, these results point out the necessary structural features to guide gelation and tune thermal responsive properties of tripodal squaramide-based monomers in water, but also their hints at their tolerance to structural modifications for future works that involve their use as functional supramolecular biomaterials.

Reference

(1) Aida, T.; Meijer, E. W.; Stupp, S. I. Functional Supramolecular Polymers. *Science* **2012,** *335* (6070), 813.

(2) Yang, L.; Tan, X.; Wang, Z.; Zhang, X. Supramolecular Polymers: Historical Development, Preparation, Characterization, and Functions. *Chemical Reviews* **2015,** *115* (15), 7196.

(3) Dou, X.; Mehwish, N.; Zhao, C.; Liu, J.; Xing, C.; Feng, C. Supramolecular Hydrogels with Tunable Chirality for Promising Biomedical Applications. *Acc. Chem. Res.* **2020,** *53* (4), 852.

(4) Du, X.; Zhou, J.; Shi, J.; Xu, B. Supramolecular Hydrogelators and Hydrogels: From Soft Matter to Molecular Biomaterials. *Chem Rev* **2015,** *115* (24), 13165.

(5) Cheng, J.; Amin, D.; Latona, J.; Heber-Katz, E.; Messersmith, P. B. Supramolecular Polymer Hydrogels for Drug-Induced Tissue Regeneration. *ACS Nano* **2019,** *13* (5), 5493.

(6) Li, L.; Sun, R.; Zheng, R. Tunable morphology and functionality of multicomponent self-assembly: A review. *Materials & Design* **2021,** *197,* 109209.

(7) de Marco, A. L.; Bochicchio, D.; Gardin, A.; Doni, G.; Pavan, G. M. Controlling Exchange Pathways in Dynamic Supramolecular Polymers by Controlling Defects. *ACS Nano* **2021,** *15* (9), 14229.

(8) Bruckner, E. P.; Stupp, S. I. Designing supramolecular polymers with nucleation and growth processes. *Polym. Int.* **2022,** *71* (5), 590.

(9) Lotz, B.; Miyoshi, T.; Cheng, S. Z. 50th anniversary perspective: Polymer crystals and crystallization: Personal journeys in a challenging research field. *Macromolecules* **2017,** *50* (16), 5995.

(10) De Greef, T. F.; Smulders, M. M.; Wolffs, M.; Schenning, A. P.; Sijbesma, R. P.; Meijer, E. Supramolecular polymerization. *Chem. Rev.* **2009,** *109* (11), 5687.

(11) Sen, S. K.; Mukhopadhyay, R. D.; Choi, S.; Hwang, I.; Kim, K. Spatiotemporal segregation of chiral supramolecular polymers. *Chem* **2023,** *9* (3), 624.

(12) Leenders, C. M.; Albertazzi, L.; Mes, T.; Koenigs, M. M.; Palmans, A. R.; Meijer, E. W. Supramolecular polymerization in water harnessing both hydrophobic effects and hydrogen bond formation. *Chem Commun (Camb)* **2013,** *49* (19), 1963.

(13) Chassenieux, C.; Tsitsilianis, C. Recent trends in pH/thermo-responsive self-assembling hydrogels: from polyions to peptide-based polymeric gelators. *Soft Matter* **2016,** *12* (5), 1344.

(14) Zhang, Q.; Dong, S.; Zhang, M.; Huang, F. Supramolecular control over thermo-responsive systems with lower critical solution temperature behavior. *Aggregate* **2021,** *2* (1), 35.

(15) Yan, X.; Wang, F.; Zheng, B.; Huang, F. Stimuli-responsive supramolecular polymeric materials. *Chem. Soc. Rev.* **2012,** *41* (18), 6042.

(16) Xian, S.; Webber, M. J. Temperature-responsive supramolecular hydrogels. *J. Mater. Chem. B* **2020,** *8* (40), 9197.

(17) Lu, W.; Le, X.; Zhang, J.; Huang, Y.; Chen, T. Supramolecular shape memory hydrogels: a new bridge between stimuli-responsive polymers and supramolecular chemistry. *Chem. Soc. Rev.* **2017,** *46* (5), 1284.

(18) Lu, H.; Xing, Z.; Chen, M.; Yu, K.; Fu, Y. Q. Solvent-aided phase separation in hydrogel towards significantly enhanced mechanoresponsive strength. *Acta Mechanica Sinica* **2021,** *37*, 757.

(19) Chen, H.; Li, Y.; Tao, G.; Wang, L.; Zhou, S. Thermo- and water-induced shape memory poly(vinyl alcohol) supramolecular networks crosslinked by self-complementary quadruple hydrogen bonding. *Polymer Chemistry* **2016,** *7* (43), 6637.

(20) Zhang, G.; Chen, Y.; Deng, Y.; Ngai, T.; Wang, C. Dynamic Supramolecular Hydrogels: Regulating Hydrogel Properties through Self-Complementary Quadruple Hydrogen Bonds and Thermo-Switch. *ACS Macro Lett* **2017,** *6* (7), 641.

(21) Hao, L.; Yegin, C.; Talari, J. V.; Oh, J. K.; Zhang, M.; Sari, M. M.; Zhang, L.; Min, Y.; Akbulut, M.; Jiang, B. Thermo-responsive gels based on supramolecular assembly of an amidoamine and citric acid. *Soft Matter* **2018,** *14* (3), 432.

(22) Naya, M.; Kokado, K.; Landenberger, K. B.; Kanaoka, S.; Aoshima, S.; Sada, K. Supramolecularly designed thermoresponsive polymers in different polymer backbones. *Macromol. Chem. Phys.* **2020,** *221* (5), 1900455.
(23) Wang, F.; Gillissen, M. A.; Stals, P. J.; Palmans, A. R.; Meijer, E. W. Hydrogen bonding directed supramolecular polymerisation of oligo(phenylene-ethynylene)s: cooperative mechanism, core symmetry effect and chiral amplification. *Chemistry* **2012,** *18* (37), 11761.
(24) Hendricks, M. P.; Sato, K.; Palmer, L. C.; Stupp, S. I. Supramolecular Assembly of Peptide Amphiphiles. *Acc. Chem. Res.* **2017,** *50* (10), 2440.
(25) Jiang, Z. C.; Xiao, Y. Y.; Kang, Y.; Pan, M.; Li, B. J.; Zhang, S. Shape Memory Polymers Based on Supramolecular Interactions. *ACS Appl. Mater. Interfaces* **2017,** *9* (24), 20276.
(26) Merino, D. H.; Slark, A. T.; Colquhoun, H. M.; Hayes, W.; Hamley, I. W. Thermo-responsive microphase separated supramolecular polyurethanes. *Polymer Chemistry* **2010,** *1* (8), 1263.
(27) Zhang, G.; Chen, Y.; Deng, Y.; Ngai, T.; Wang, C. Dynamic supramolecular hydrogels: regulating hydrogel properties through self-complementary quadruple hydrogen bonds and thermo-switch. *ACS Macro Letters* **2017,** *6* (7), 641.
(28) Lugger, S. J. D.; Houben, S. J. A.; Foelen, Y.; Debije, M. G.; Schenning, A.; Mulder, D. J. Hydrogen-Bonded Supramolecular Liquid Crystal Polymers: Smart Materials with Stimuli-Responsive, Self-Healing, and Recyclable Properties. *Chem Rev* **2022,** *122* (5), 4946.
(29) Guo, M.; Pitet, L. M.; Wyss, H. M.; Vos, M.; Dankers, P. Y.; Meijer, E. W. Tough stimuli-responsive supramolecular hydrogels with hydrogen-bonding network junctions. *J. Am. Chem. Soc.* **2014,** *136* (19), 6969.
(30) Feng, Z.; Zuo, H.; Gao, W.; Ning, N.; Tian, M.; Zhang, L. A Robust, Self-Healable, and Shape Memory Supramolecular Hydrogel by Multiple Hydrogen Bonding Interactions. *Macromol. Rapid Commun.* **2018,** *39* (20), e1800138.
(31) Leenders, C. M.; Baker, M. B.; Pijpers, I. A.; Lafleur, R. P.; Albertazzi, L.; Palmans, A. R.; Meijer, E. W. Supramolecular polymerisation in water; elucidating the role of hydrophobic and hydrogen-bond interactions. *Soft Matter* **2016,** *12* (11), 2887.
(32) Taylor, M. J.; Tomlins, P.; Sahota, T. S. Thermoresponsive gels. *Gels* **2017,** *3* (1), 4.
(33) Xin, F.; Lyu, Q. A Review on Thermal Properties of Hydrogels for Electronic Devices Applications. *Gels* **2022,** *9* (1), 7.
(34) Tong, C.; Liu, T.; Saez Talens, V.; Noteborn, W. E. M.; Sharp, T. H.; Hendrix, M.; Voets, I. K.; Mummery, C. L.; Orlova, V. V.; Kieltyka, R. E. Squaramide-Based Supramolecular Materials for Three-Dimensional Cell Culture of Human Induced Pluripotent Stem Cells and Their Derivatives. *Biomacromolecules* **2018,** *19* (4), 1091.
(35) Haidekker, M. A.; Nipper, M.; Mustafic, A.; Lichlyter, D.; Dakanali, M.; Theodorakis, E. A. Dyes with segmental mobility: molecular rotors. *Advanced fluorescence reporters in chemistry and biology I: fundamentals and molecular design* **2010**, 267.
(36) Martinez, V.; Henary, M. Nile red and nile blue: applications and syntheses of structural analogues. *Chemistry–A European Journal* **2016,** *22* (39), 13764.
(37) Mako, T. L.; Racicot, J. M.; Levine, M. Supramolecular luminescent sensors. *Chem. Rev.* **2018,** *119* (1), 322.
(38) Wang, Y.; Wu, H.; Hu, W.; Stoddart, J. F. Color-Tunable Supramolecular Luminescent Materials. *Adv. Mater.* **2022,** *34* (22), 2105405.
(39) Rajdev, P.; Ghosh, S. Fluorescence resonance energy transfer (FRET): a powerful tool for probing amphiphilic polymer aggregates and supramolecular polymers. *The Journal of Physical Chemistry B* **2018,** *123* (2), 327.
(40) Hu, Y. X.; Li, W. J.; Jia, P. P.; Wang, X. Q.; Xu, L.; Yang, H. B. Supramolecular Artificial Light-Harvesting Systems with Aggregation-Induced Emission. *Advanced Optical Materials* **2020,** *8* (14), 2000265.
(41) Yang, M.; Zhang, Z.; Yuan, F.; Wang, W.; Hess, S.; Lienkamp, K.; Lieberwirth, I.; Wegner, G. Self-assembled structures in organogels of amphiphilic diblock codendrimers. *Chemistry–A European Journal* **2008,** *14* (11), 3330.

(42) Nebot, V. J.; Armengol, J.; Smets, J.; Prieto, S. F.; Escuder, B.; Miravet, J. F. Molecular hydrogels from bolaform amino acid derivatives: A structure–properties study based on the thermodynamics of gel solubilization. *Chemistry–A European Journal* **2012,** *18* (13), 4063.
(43) Saez Talens, V.; Davis, J.; Wu, C. H.; Wen, Z.; Lauria, F.; Gupta, K.; Rudge, R.; Boraghi, M.; Hagemeijer, A.; Trinh, T. T.et al. Thiosquaramide-Based Supramolecular Polymers: Aromaticity Gain in a Switched Mode of Self-Assembly. *J. Am. Chem. Soc.* **2020,** *142* (47), 19907.
(44) Chen, F.; Lu, G.; Yuan, H.; Li, R.; Nie, J.; Zhao, Y.; Shu, X.; Zhu, X. Mechanism and regulation of LCST behavior in poly (hydroxypropyl acrylate)-based temperature-sensitive hydrogels. *Journal of Materials Chemistry A* **2022,** *10* (35), 18235.
(45) Kojima, H. Studies on the phase transition of hydrogels and aqueous solutions of thermosensitive polymers. *Polym. J.* **2018,** *50* (6), 411.
(46) Liu, H.; Prachyathipsakul, T.; Koyasseril-Yehiya, T. M.; Le, S. P.; Thayumanavan, S. Molecular bases for temperature sensitivity in supramolecular assemblies and their applications as thermoresponsive soft materials. *Materials horizons* **2022,** *9* (1), 164.
(47) Wei, Y.; Zheng, L.; Xie, X.; Yang, X.; Liao, J. Recent advances in stimuli responsive hydrogels for oral disease treatment. *Materials & Design* **2024**, 112817.
(48) Zhang, S.; Greenfield, M. A.; Mata, A.; Palmer, L. C.; Bitton, R.; Mantei, J. R.; Aparicio, C.; de la Cruz, M. O.; Stupp, S. I. A self-assembly pathway to aligned monodomain gels. *Nat. Mater.* **2010,** *9* (7), 594.

Supporting Information

S2.1 Materials and methods

Materials

O-methyl-undecaethylene glycol was obtained from polypure and Broadpharm. Compounds **5** and **10** were synthesized as previously reported.[1] Potassium phthalimide, hydrazine monohydrate, sodium and all other commercially available chemicals were purchased from Sigma Aldrich and used without further purification. Lacey carbon 200 mesh grids were purchased from Electron Microscopy Sciences. Deuterated solvents for NMR experiments were obtained from Euriso-top. Milli-Q water (H_2O) was employed for all the experiments. All the compounds were stored at -20^oC until further usage.

Methods

^{1}H-NMR and ^{13}C-NMR spectra were recorded on a Bruker DMX-300. All the final compounds were purified by high performance liquid chromatography (HPLC) on a Shimadzu system equipped with two LC-20AR pumps, an SPD-20A UV-Vis detector and Phenomenex Kinetex EVO C18 column. The mobile phase used consisted of CH_3CN and H_2O with 0.1% trifluoroacetic acid and the purity of the compounds was assessed by LC-MS. LC-MS analysis was performed on a Finnigan Surveyor HPLC system equipped (UV detection from 200-600 nm) with a Gemini C18 50 x 4.60 mm reverse phase column coupled to Finnigan LCQ Advantage Max mass spectrometer with ESI. For the mobile phase, a gradient of 10-90% of CH_3CN/H_2O with 0.1% trifluoroacetic acid over 13.5 minutes was used. High resolution mass spectra (HR-MS) were collected on Q-Exactive HF Orbitrap mass spectrometer from Thermo Scientific that equipped with an electrospray ion source (ESI). The spectra were collected by direct injection of a 2 µL aliquot of the sample solution (1 µM) into Ultimate 3000 nano UPLC (Dionex) with an external calibration using source voltage of 3.5kV, capillary temperature 275˚C, resolution = 240000 at *m/z* = 400, mass range *m/z* = 160-2000 or until a maximum of 6000. Eluents used: CH_3CN:H_2O (1:1 v/v) supplemented with 0.1% formic acid. UV absorption spectra were acquired at room temperature (RT) on a Cary 300 UV-Vis spectrophotometer from 400 to 800 nm using a quartz cuvette with a path length of 1 cm equipped with a temperature control system. Fluorescence spectra were recorded on a TECAN Infinite M1000 PRO fluorescence plate reader. FTIR spectra in the solid state were recorded on a PerkinElmer Spectrum Two UATR FT-IR spectrometer with a resolution of 4 cm^{-1}. Fourier transform infrared spectroscopy (FTIR) spectra in the solution state were obtained on a Bruker Tensor 27 IR spectrometer with a resolution of 1 cm^{-1} averaged over 128 scans at RT. The supramolecular fiber morphologies were imaged on a Talos L120C cryogenic electron microscope (cryo-EM) operating at 120 kV, samples were plunge frozen on a Vitrobot Mark IV, both from Thermo Fisher Scientific. Atomic force (AFM) micrographs were recorded on a JPK Nanowizard Ultra AFM using silicon cantilever tips with a 70 kHz resonance frequency and 2 N/m force constant. The surface morphology and annealed hydrogels were imaged by scanning electron microscope (SEM). The critical gelation concentration (CGC) was determined from the gel inversion method. Oscillatory rheology experiments were performed on a Discovery Hybrid Rheometer purchased from TA Instruments with a temperature controller using a parallel plate geometry (40 mm diameter) with a fixed gap (0.6 mm). Differential scanning calorimetry (DSC) test were measured in a nano DSC purchased from TA Instruments to determine the endothermic and exothermic curves. X-Ray diffraction (XRD) analysis were performed using a Bruker D8 Advance diffractometer with a Bragg-Brentano geometry and

equipped with a Cu-Kα X-ray source that has a wavelength of 1.54 Å in 2θ ranging from 2.5 to 30˚. Polarized optical images (POM) were probed on an Olympus BH-2 microscope. Small angle X-ray scattering measurements (SAXS) were carried out on a SAXSLAB GANESHA 300 XL SAXS system equipped with a GeniX 3D Cu ultralow divergence microfocus sealed tube source producing X-rays with a wavelength λ = 1.54 Å at a flux of $1x10^8$ ph/s, and a Pilatus 300K silicon pixel detector with 487 x 619 pixels of 172 µm x172 µm in size, which is placed at two sample-to-detector distances of 713 and 1513 mm respectively to access a q-range of $0.009 \leq q \leq 0.456$ $Å^{-1}$, where $q = 4\pi/\lambda(\sin \theta/2)$. The calibration of the beam center and q-range was achieved by using silver behenate. Samples were prepared on a Branson 2510 Ultrasonic Cleaner ice bath for ~20 minutes.

Synthetic Procedures

Synthetic routes of monomers 1-4

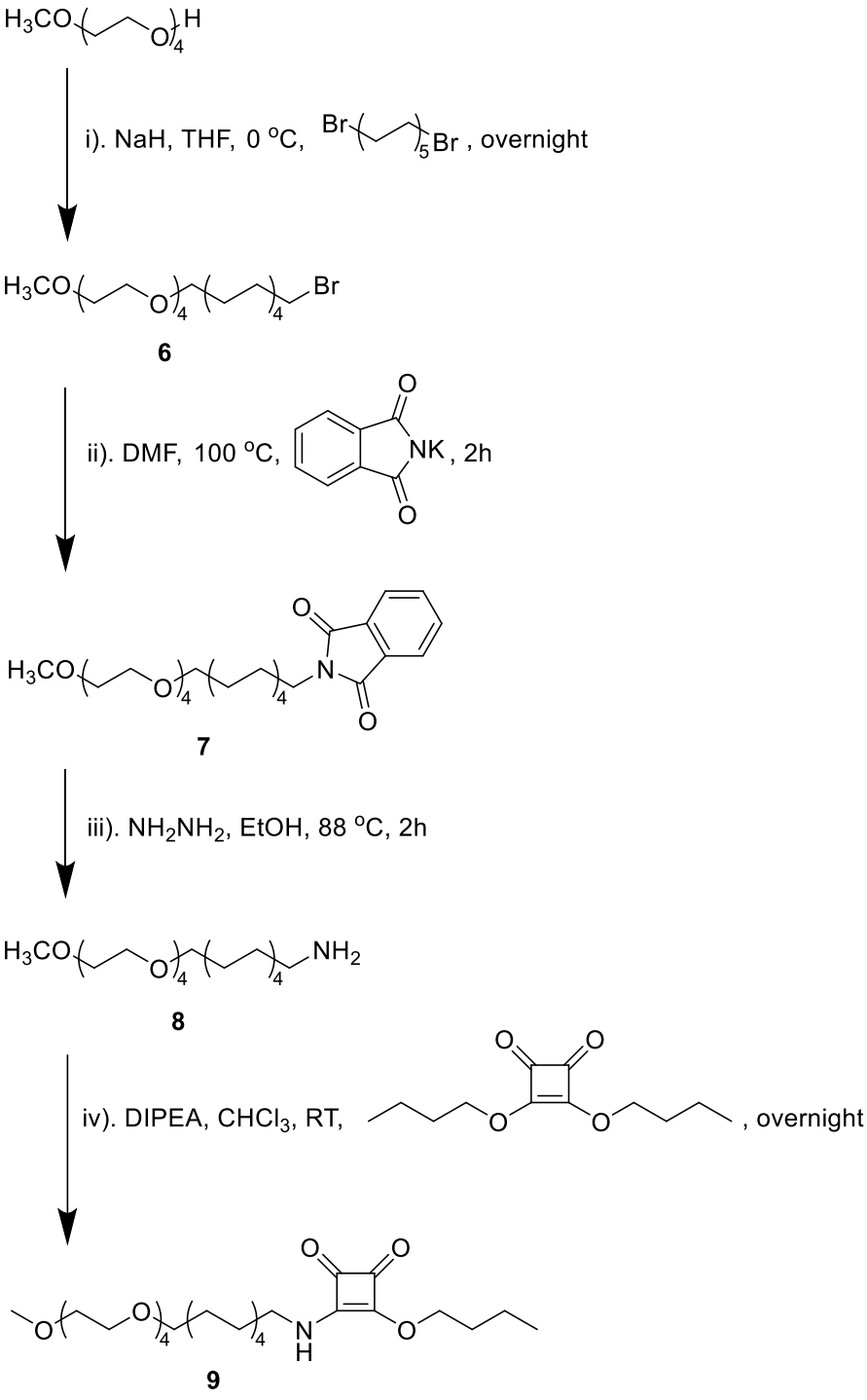

Figure S1. Synthetic route of monomer **9**.

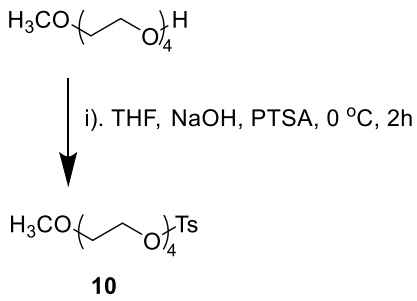

Figure S2. Synthetic route of monomer **10**.

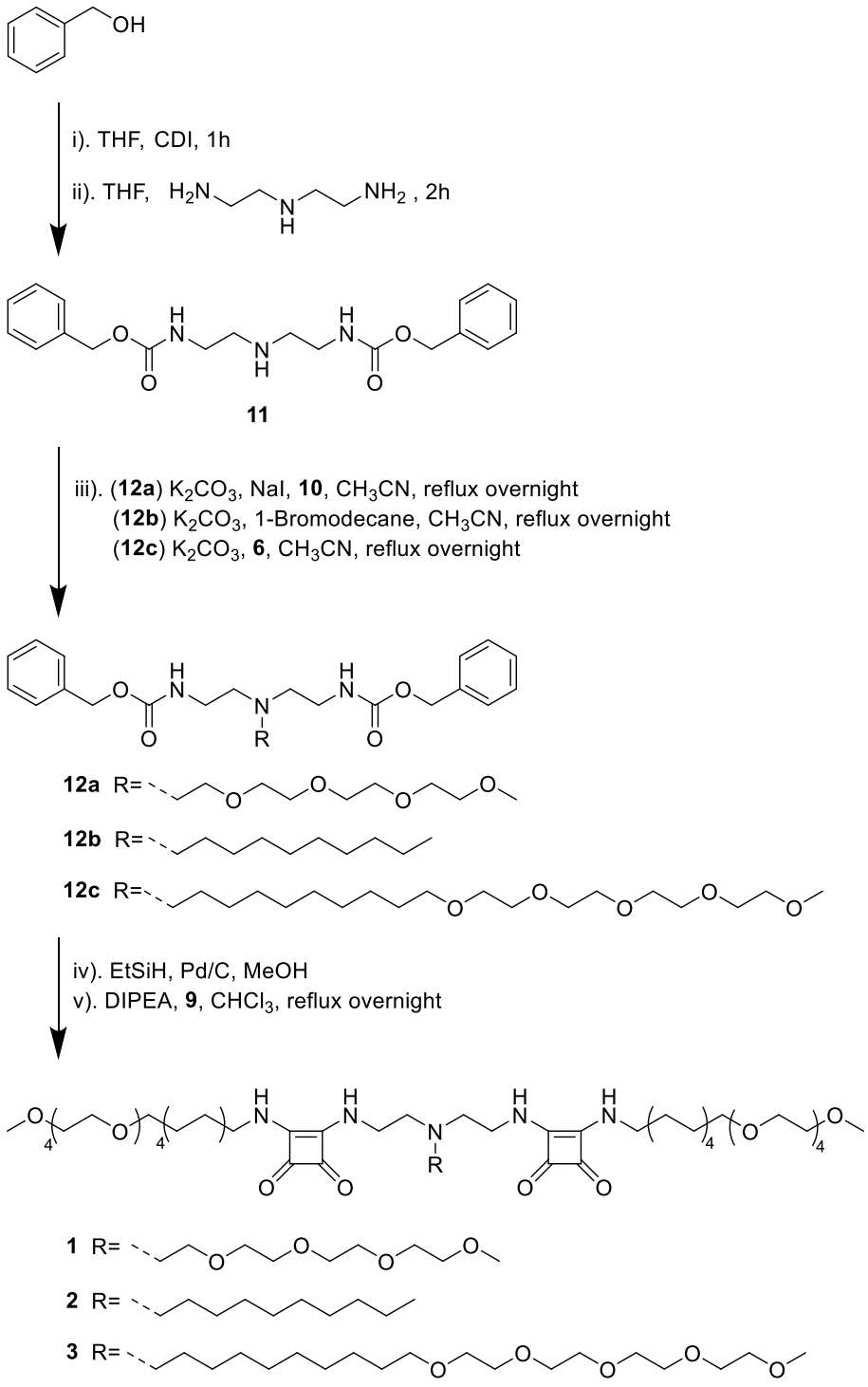

Figure S3. Synthetic route of monomers **1**-**3**.

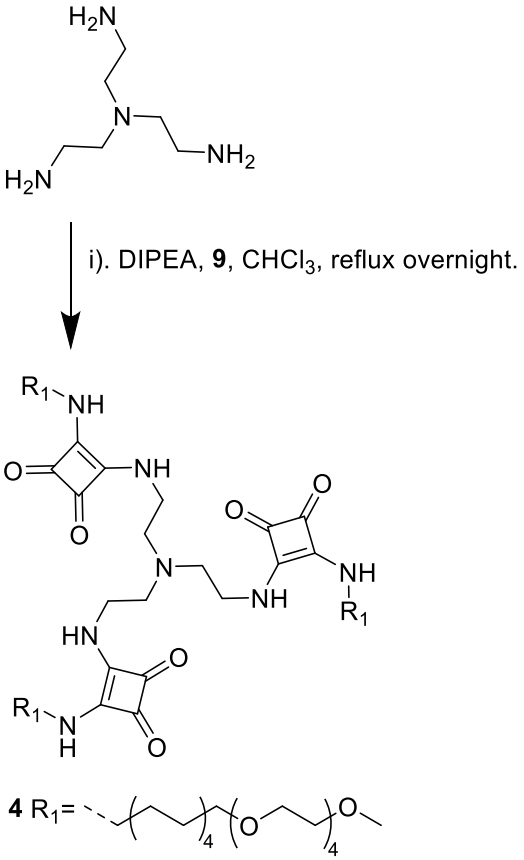

Figure S4. Synthetic route of monomer **4**.

Structure of monomer 5

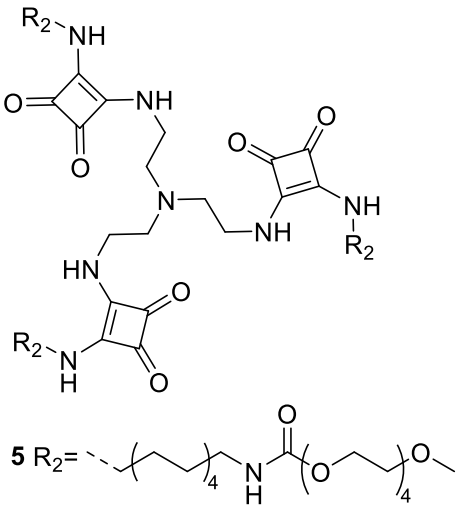

Figure S5. Structure of tripodal squaramide-based monomer **5**.

Synthesis of 6

A dispersion of sodium hydride in mineral oil (60%) (0.77 g, 19.23 mmol) was added in small portions to a stirring solution of tetraethylene glycol monomethyl ether (4.0 g, 19.23 mmol) in dry THF (40 mL) at 0°C, resulting in a foaming grey solution. The ice bath was removed once the foam ceased. Subsequently, 1,10-dibromodecane (11.56 g, 38.46 mmol) was added and the reaction mixture was stirred overnight at RT. H_2O was added to the reaction mixture (20 mL) and extracted with Et_2O (3 x 40 mL). The combined organic layers were collected, dried with Na_2SO_4, filtered, and concentrated in vacuum. The crude was purified by silica column chromatography (EtOAc/Pet ether: 10/90 - 30/70) to obtain the product as a colorless oil.

Yield = 5.27 g, 64.3 %. ^{1}H NMR (300 MHz, $CDCl_3$): δ (ppm) = 3.58-3.46 (m, 16H), 3.39-3.30 (m, 5H), 1.79-1.72 (t, 2H), 1.52-1.47 (t, 2H), 1.35-1.22 (d, 14H). ^{13}C NMR (75 MHz, $CDCl_3$): δ (ppm) = 71.87, 71.38, 70.53, 70.45, 70.01, 58.94, 33.87, 33.74, 32.72, 29.56, 29.38, 29.35, 29.29, 28.99, 28.83, 28.66, 28.08, 26.00. HRMS (ESI) *m/z*: $[M+H]^+$ calcd. for $C_{19}H_{40}O_5Br$: 427.20536; found: 427.20391. LC-MS: *t* = 8.95 min, *m/z*: 448.38 $[M+Na]^+$.

Synthesis of 7

6 (4.04 g, 9.45 mmol) and potassium phthalimide (2.45 g, 13.23 mmol) were dissolved in dry DMF (30 mL) and the mixture was heated to reflux for 2 hours. After the removal of the solvent by rotary evaporation, the residue was redissolved in CH_2Cl_2 (50 mL), washed with 1M HCl (2 x 30 mL), dried with Na_2SO_4, filtered, and concentrated in vacuum. The crude was purified by silica column chromatography (EtOAc/Pet ether: 10/90 – 30/70) to obtain the product as a colorless oil.

Yield = 4.18 g, 85.7 %. ^{1}H NMR (300 MHz, $CDCl_3$): δ (ppm) = 7.84-7.68 (d, 4H), 3.68-3.56 (m, 18H), 3.56-3.42 (m, 2H), 3.36 (s, 3H), 1.67-1.50 (m, 4H), 1.24 (m, 14H). ^{13}C NMR (75 MHz, $CDCl_3$): δ (ppm) = 168.43, 134.27, 132.16, 123.18, 71.92, 71.50, 70.60, 70.58, 70.55, 70.50, 70.03, 58.76, 38.04, 29.60, 29.47, 29.40, 29.14, 28.57, 26.83, 26.03. HRMS (ESI) *m/z*: $[M+H]^+$ calcd. for $C_{27}H_{44}NO_7$, 494.31123; found, 494.31392. LC-MS: t =8.51 min, *m/z*: 515.34 $[M+H]^+$.

Synthesis of 8

Hydrazine monohydrate (3.81 mL, 78.34 mmol) was added to a stirring solution of **7** (2.69 g, 5.45 mmol) in ethanol (50 mL) and the mixture was refluxed overnight. The solvent was removed by rotary evaporation and the mixture was dissolved in $CHCl_3$ (100 mL), extracted with 1M NaOH (3 x 100 mL) and the organic layers were collected and dried with Na_2SO_4, filtered, and concentrated in vacuum. The product was obtained as a colorless oil and used for the next step without any further purification.

Yield = 1.64 g, 82.9 %. ^{1}H NMR (300 MHz, $CDCl_3$): δ (ppm) = 3.53-3.40 (m, 16H), 3.34-3.29 (t, 2H), 3.25 (s, 3H), 2.57-2.53 (t, 2H), 1.46-1.15 (m, 18H). ^{13}C NMR (75 MHz, $CDCl_3$): δ (ppm) = 71.83, 71.39, 70.51, 70.48, 70.46, 70.40, 69.96, 58.81, 41.99, 33.42, 29.53, 29.45, 29.43, 29.36, 26.78, 25.98. HRMS (ESI) *m/z*: $[M+H]^+$ calcd. for $C_{19}H_{42}NO_5$, 364.30575; found, 364.30517. LC-MS: t =4.56 min, *m/z*: 363.52 $[M]^+$.

Synthesis of 9

8 (1.18 g, 3.26 mmol), 3,4-dibutoxy-3-cyclobutene-1,2-dione (0.87 mL, 3.91 mmol), and DIPEA (0.85 mL, 4.89 mmol) were dissolved in $CHCl_3$ (50 mL) and were stirred at RT for 2 h. The crude washed with H_2O (2 x 50 mL), dried with Na_2SO_4, filtered, and concentrated in vacuum. The crude was purified by silica column chromatography (EtOAc/Pet ether: 10/90 – 30/70) to obtain the final product as a light yellow oil.

Yield = 1.07 g, 63.9 %. ^{1}H NMR (300 MHz, $CDCl_3$): δ (ppm) = 7.26-7.24 (m, 1H), 4.71-4.62 (t, 2H), 3.60-3.47 (m, 16H), 3.41-3.32 (t, 6H), 1.78-1.68 (m, 2H), 1.58-1.22 (m, 18H), 0.94-0.89 (t, 3H). ^{13}C NMR (75 MHz, $CDCl_3$): δ (ppm) = 189.7, 172.37, 137.88, 73.30, 71.85, 71.41, 70.54, 70.51, 70.49, 70.42, 58.98, 44.84, 31.96, 30.61, 29.55, 29.42, 29.36, 29.07, 26.33, 26.00, 18.59, 13.74. HRMS (ESI) *m/z*: $[M+H]^+$ calcd. for $C_{27}H_{50}NO_8$, 516.35309; found, 516.35249. LC-MS: t =7.73 min, *m/z*: 515.62 $[M]^+$.

Synthesis of 10

10 was prepared according to a previously published protocol.[1] A solution of NaOH (0.88 g in 3 mL H_2O) was added to a stirring solution of tetraethylene glycol monomethyl ether (2.50g, 12.00 mmol) in THF (3.5 mL) at 0°C. After 15 minutes, 4-toluenesulfonyl chloride (2.25 g in 5 mL THF) was added dropwise and the reaction was allowed to stir at RT for 30 minutes. The solvent was removed by rotary evaporation and the reaction mixture was dissolved in H_2O (25 mL) and extracted with Et_2O (3 x 25 mL). The organic layers were collected and dried with Na_2SO_4, filtered, and concentrated in vacuum. The product was obtained as a colorless oil and used for the next step without any further purification.

Yield = 3.08 g, 70.7%. ^{1}H NMR (300 MHz, $CDCl_3$): δ (ppm) = 7.59-7.57 (d, 2H), 7.17-7.15 (d, 2H), 3.96-3.93 (t, 2H), 3.48-3.31 (m, 14H), 3.15 (s, 3H), 2.24 (s, 3H). 13C NMR (75 MHz, $CDCl_3$): δ (ppm) = 144.67, 132.84, 129.73, 127.71, 71.69, 70.40, 70.33, 70.27, 70.23, 69.29, 68.38, 58.68, 21.37. HRMS (ESI) *m/z*: $[M+H]^+$ calcd. for $C_{16}H_{27}O_7S$, 363.14720; found: 363.14720. LC-MS: t =7.82 min, *m/z*: 362.14 $[M]^+$.

Synthesis of 11

Benzyl alcohol (1.67 g, 15.42 mmol) and carbonyldiimidazole (3.0 g, 12.85 mmol) were dissolved in THF (50 mL) and stirred at RT for 30 minutes. Diethylenetriamine (0.6 mL, 5.77 mmol) was slowly added and stirred overnight at RT. The reaction mixture was extracted using EtOAc (3 x 50 mL) and the combined organic layers were collected and dried with Na_2SO_4, filtered, and concentrated in vacuum. The crude was purified by silica column chromatography (EtOAc/Pet ether: 50/50 – 100/0) to obtain the final product as a white solid.

Yield = 1.64 g, 76.5%. ^{1}H NMR (300 MHz, $CDCl_3$): δ (ppm) = 7.33 (s, 10H), 5.33 (s, 2H), 5.10 (s, 4H), 3.28-3.26 (t, 4H), 2.75-2.73 (t, 4H), 1.33 (s, 1H). ^{13}C NMR (75 MHz, $CDCl_3$): δ (ppm) = 156.69, 136.56, 128.50, 128.09, 66.71, 48.62, 40.74. HRMS (ESI) *m/z*: $[M+H]^+$ calcd. for $C_{20}H_{26}N_3O_4$, 372.19178; found, 372.19154. LC-MS: t = 5.11 min, *m/z*: 371.43 $[M]^+$.

Synthesis of 12a

10 (0.42 g, 1.15 mmol), **11** (0.23 g, 0.62 mmol), K_2CO_3 (0.12 g, 0.88 mmol), and sodium iodide (0.096 g, 0.64 mmol) were dissolved in dry CH_3CN (15 mL) and refluxed for 36 hours. The solvent was removed by rotary evaporation and the reaction mixture was redissolved in CH_2Cl_2 (25 mL), extracted with 1M NaOH (3 x 25 mL). The organic layers were collected and dried with Na_2SO_4, filtered, and concentrated in vacuum. The crude was purified by silica column chromatography (EtOAc/PE: 20/80 – 0/100) to obtain the final product as a colorless oil.

Yield = 0.31 g, 88.5%. ^{1}H NMR (300 MHz, $CDCl_3$): δ (ppm) = 7.29 (s, 10H), 5.91 (t, 2H), 5.05 (s, 4H), 3.64-3.40 (s, 14H), 3.33 (s, 3H), 3.22-3.16 (q, 4H), 2.61 (t, 6H). ^{13}C NMR (75 MHz, $CDCl_3$): δ (ppm) = 156.81, 136.87, 128.48, 128.05, 127.90, 71.77, 70.49, 70.46, 70.35, 70.32, 70.16, 69.99, 66.33, 58.71, 54.24, 53.20, 39.04. HRMS (ESI) *m/z*: $[M+H]^+$ calcd. for $C_{29}H_{44}N_3O_8$, 562.31229; found, 562.31153. LC-MS: t =5.46 min, 561.31 *m/z*: $[M]^+$.

Synthesis of 1

Triethylsilane (4.5 mL, 26.50 mmol) was added dropwise to a stirring solution of **12a** (243.50 mg, 0.43 mmol) and palladium on carbon (80 mg, 0.72 mmol) in dry CH_3OH (10 mL) under a N_2 atmosphere. The reaction was kept stirring overnight and then was filtered over celite, concentrated, and dissolved in $CHCl_3$ (50 mL). Subsequently, **1** (492.16 mg, 0.95 mmol) and DIPEA (0.33 mL, 1.90 mmol) were added to the reaction mixture and kept at reflux overnight. The solvent was removed by rotary evaporation and the residue was redissolved in CH_2Cl_2 (20 mL), washed with 1M HCl (3 x 10 mL). The combined organic fractions were collected and dried with $MgSO_4$, filtered, and concentrated in vacuum. The crude was purified by silica column chromatography (EtOAc: 100% – CH_3OH/ CH_2Cl_2: 10/90) to obtain the final product as a yellow oil. The compound was further purified by HPLC and lyophilized to obtain a yellow sticky solid.

Yield = 0.122 g, 40.6 %.^{1}H NMR (300 MHz, $CDCl_3$): δ (ppm) = 3.59 (m, 50H), 3.42 (t, 8H), 3.35 (s, 6H), 3.31 (s, 3H), 2.68 (m, 6H), 1.58 (m, 12H), 1.24 (s, 20H). ^{13}C NMR (75 MHz, $CDCl_3$): δ (ppm) = 183.25, 181.50, 168.98, 168.81, 72.26, 71.82, 71.67, 71.49, 70.87, 70.53, 70.49, 70.44, 70.36, 69.92, 58.98, 57.15, 53.89, 44.61, 43.52, 31.14, 29.55, 29.51, 29.44, 29.25, 26.50, 26.03. HRMS (ESI) *m/z*: $[M+H]^+$ calcd. for $C_{59}H_{110}N_5O_{18}$, 1176.78404; found, 1176.78445. LC-MS: t = 6.19 min, *m/z*: 1175.43 $[M]^+$.

Synthesis of 12b

11 (0.21 g, 0.58 mmol), 1-bromodecane (0.14 mL, 0.67 mmol) and K_2CO_3 (0.37 g, 2.69 mmol) were dissolved in dry CH_3CN (30 mL) and was relfluxed overnight. The solvent was removed by rotary evaporation and the reaction mixture was dissolved in CH_2Cl_2 (25 mL) and extracted with 1M NaOH (3 x 25 mL). The organic layers were collected and dried with Na_2SO_4, filtered, and concentrated in vacuum. The crude was purified by silica column chromatography (EtOAc/Pet ether: 10/90 – 50/50) to obtain the final product as a white solid.

Yield = 0.24 g, 81.1 %. ^{1}H NMR (300 MHz, $CDCl_3$): δ (ppm) = 7.32 (s, 10H), 5.08 (s, 4H), 3.45-3.19 (t, 2H), 3.30-3.19 (m, 4H), 2.62-2.43 (m, 4H), 1.39-1.26 (d, 16H), 0.93-0.88 (t, 3H). ^{13}C NMR (75 MHz, $CDCl_3$): δ (ppm) = 156.68, 136.72, 128.44, 128.01, 127.98, 66.56, 54.03, 53.51, 38.86, 34.01, 31.93, 31.90, 29.71, 29.62, 29.53, 29.36, 29.30, 27.39, 26.89, 22.71, 14.16. HRMS (ESI) *m/z*: $[M+H]^+$ calcd. for $C_{30}H_{46}N_3O_4$, 512.34381; found, 512.34726. LC-MS: t = 7.68 min, 511.70 *m/z*: $[M]^+$.

Synthesis of 2

Triethylsilane (4.0 mL, 25.21 mmol) was added dropwise to a stirring mixture solution of **12b** (215.2 mg, 420.6 mmol) and palladium on carbon (80 mg, 0.72 mmol) in dry CH_3OH (10 mL) under a N_2 atmosphere and kept at RT for overnight. The solution was filtered over celite, concentrated and dissolved in $CHCl_3$ (50 mL). **1** (477.1 mg, 0.93 mmol) and DIPEA (0.32 mL, 1.85 mmol) were added to the reaction mixture and heated to reflux overnight. The solvent was removed by rotary evaporation and the residue was redissolved in CH_2Cl_2 (20 mL) and washed with 1M HCl (3 x 10 mL). The combined organic fractions were collected and dried with $MgSO_4$, filtered, and concentrated in vacuum. The crude was purified by silica column chromatography (EtOAc: 100% – CH_3OH/CH_2Cl_2: 10/90) to obtain the final product as a yellow oil. The compound was further purified by HPLC and lyophilized to obtain a white solid.

Yield = 0.17 g, 47.1%. ^{1}H NMR (300 MHz, $CDCl_3$): δ (ppm) = 8.28 (s, 4H), 3.65-3.40 (m, 44H), 3.37 (s, 6H), 2.87-2.73 (t, 6H), 1.64-1.53 (m, 12H), 1.30-1.23 (m, 36H), 0.88-0.84 (m, 3H). ^{13}C NMR (75 MHz, $CDCl_3$): δ (ppm) = 181.81, 168.79, 167.18, 71.85, 71.53, 70.57, 70.53, 70.46, 70.38, 70.01, 69.94, 59.01, 57.41, 54.76, 44.68, 31.91, 31.07, 29.63, 29.59, 29.54, 29.50, 29.35, 29.29, 26.57, 26.07, 22.68, 14.13.

HRMS (ESI) *m/z*: $[M+H]^+$ calcd. for $C_{60}H_{112}N_5O_{14}$, 1126.82003; found, 1126.81981. LC-MS: t = 7.68 min, 1125.55 $[M]^+$.

Synthesis of 12c

11 (0.20 g, 0.54 mmol), **6** (0.29 g, 0.67 mmol) and K_2CO_3 (0.37 g, 2.69 mmol) were dissolved in dry CH_3CN (30 mL) and heated to reflux overnight. The solvent was removed by rotary evaporation and the reaction mixture was dissolved in CH_2Cl_2 (25 mL) and extracted with 1M NaOH (3 x 25 mL). The organic layers were collected and dried with $MgSO_4$, filtered, and concentrated in vacuum. The crude was purified by silica column chromatography (EtOAc/Pet ether: 10/90 – 60/40) to obtain the title product as a colorless oil.

Yield = 0.26 g, 66.3 %. ^{1}H NMR (300 MHz, $CDCl_3$): δ (ppm) = 7.38-7.30 (m, 10H), 5.08 (s, 4H), 3.67-3.63 (m, 16H), 3.59-3.57 (m, 4H), 3.48-3,45 (m, 2H), 3.42-3.36 (d, 3H), 3.26 (s, 2H), 2.60-2.45 (d, 4H), 1.58 (t, 2H), 1.27 (m, 16H). ^{13}C NMR (75 MHz, $CDCl_3$): δ (ppm) = 156.57, 136.64, 128.48, 128.02, 71.98, 71.52, 70.62, 70.59, 70.52, 70.06, 66.63, 58.99, 54.09, 53.50, 38.81, 29.64, 29.55, 29.47, 27.35, 26.09. HRMS (ESI) *m/z*: $[M+H]^+$ calcd. for $C_{39}H_{64}N_3O_9$, 718.46371; found, 718.46250. LC-MS: t = 6.49 min, 717.32 *m/z*: $[M]^+$.

Synthesis 3

Triethylsilane (4.0 mL, 25.21 mmol) was added dropwise to a stirring solution of **7c** (239 mg, 0.33 mmol) and palladium on carbon (80 mg, 0.72 mmol) in dry CH_3OH (10 mL) under a N_2 atmosphere and kept at RT overnight. The solution was filtered over celite, concentrated, and dissolved in $CHCl_3$ (50 mL). **1** (378.48 mg, 0.73 mmol) and DIPEA (0.26 mL, 1.47 mmol) were added to the reaction mixture and refluxed overnight. The solvent was removed by rotary evaporation and the residue was redissolved in CH_2Cl_2 (20 mL) and washed with 1M HCl (3 x 10 mL). The combined organic fractions were collected and dried with $MgSO_4$, filtered, and concentrated in a vacuum. The crude was purified by silica column chromatography (EtOAc: 100% - CH_3OH/CH_2Cl_2: 10/90) to obtain the final product as a yellow oil. The compound was further purified by HPLC and lyophilized to obtain a white solid.

Yield = 0.11 g, 21.5%. ^{1}H NMR (300 MHz, $CDCl_3$): δ (ppm) = 3.69-3.40 (m, 62H), 3.37 (s, 9H), 2.64 (s, 4H), 2.56 (s, 2H), 1.40 (m, 48H). ^{13}C NMR (75 MHz, $CDCl_3$): δ (ppm) = 185.16, 168.88, 167.07, 71.87, 71.52, 70.53, 70.49, 70.44, 70.36, 69.98, 69.93, 59.00, 44.66, 31.10, 29.61, 29.53, 29.31, 26.56, 26.08. HRMS (ESI) *m/z*: [M+H]+ calcd. for $C_{69}H_{130}N_5O_{19}$, 1332.93545; found, 1332.94272. LC-MS: t = 6.90 min, 1331.65 *m/z*: $[M]^+$.

Synthesis of 4

Tris(2-aminoethyl)amine (33.99 mg, 0.23 mmol), **1** (395.04 g, 0.77 mmol), and DIPEA (0.27 mL, 1.53 mmol) were dissolved in $CHCl_3$ (30 mL) and kept at reflux overnight. The solvent was removed by rotary evaporation and the residue was redissolved in CH_2Cl_2 (20 mL) and washed with 1M HCl (3 x 10 mL). The combined organic fractions were collected and dried with $MgSO_4$, filtered, and concentrated in vacuum. The crude was purified by silica column chromatography (EtOAc: 100% – CH_3OH/CH_2Cl_2: 10/90) to obtain the final product as a yellow solid. The compound was further purified by HPLC and lyophilized to obtain a white solid.

Yield = 0.131 g, 86.9%.^{1}H NMR (300 MHz, $CDCl_3$): δ (ppm) = 7.65 (s, 4H), 3.72-3.60 (m, 60H), 3.59-3.45 (m, 6H), 3.37 (s, 9H), 2.62 (s, 6H), 1.64-1.53 (m, 12H), 1.39-1.29 (m, 6H), 1.25 (s, 30H). ^{13}C NMR (75 MHz, $CDCl_3$): δ (ppm) = 182.66, 168.50, 167.17, 71.66, 71.52, 70.31, 70.19, 70.16, 70.11, 70.04,

69.71, 59.01, 56.69, 55.65, 44.50, 31.08, 29.51, 29.44, 29.24, 26.46, 25.96. HRMS (ESI) *m/z*: $[M+H]^+$ calcd. for $C_{75}H_{136}N_7O_{21}$, 1470.97838; found, 1470.97865. LC-MS: t = 6.96 min, 1469.76 *m/z*: $[M]^+$.

Gel inversion test

The critical gelation concentration (CGC) is defined as the minimum concentration of a given compound to form a hydrogel. A concentration series of **2-5** were prepared with H_2O in 2 mL glass vials before sonicating for 20 minutes. All the samples were left to equilibrate overnight prior to imaging the inverted vials. All hydrogels for the following tests were prepared in H_2O.

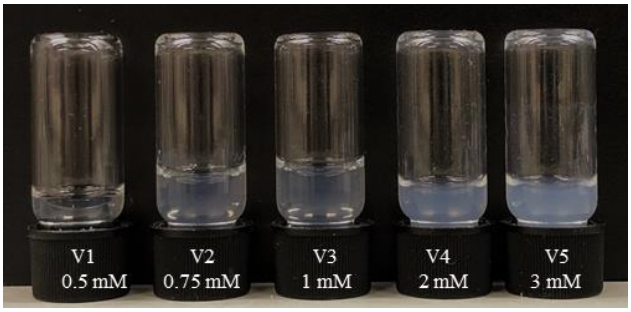

Figure S6. Gel inversion test of **2** in H_2O at various concentration of 0.5 mM (V1), 0.75 mM (V2), 1 mM (V3), 2.0 mM (V4) and 3.0 mM (V5) in glass vials.

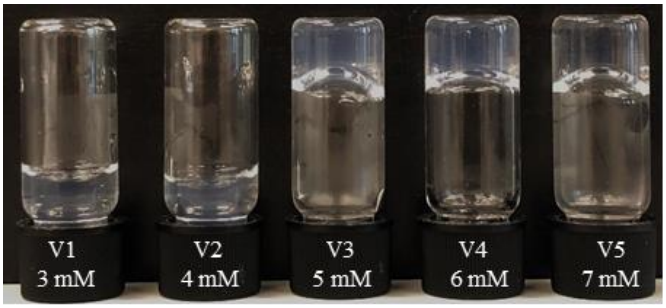

Figure S7. Gel inversion test of **3** in H_2O at concentration 3.0 mM (V1), 4.0 mM (V2), 5.0 mM (V3), 6.0 mM (V4) and 7.0 mM (V5) in glass vials.

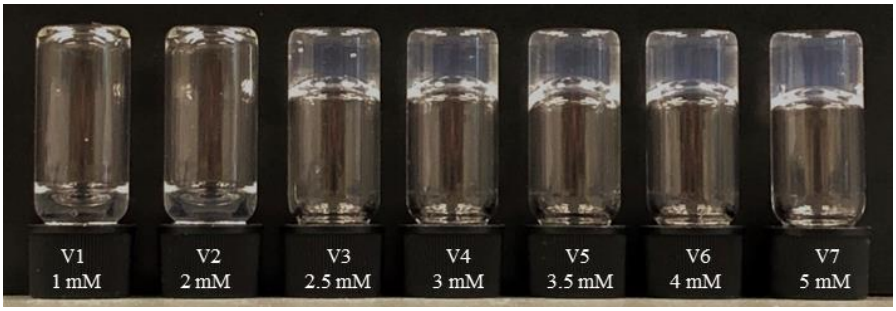

Figure S8. Gel inversion test of **4** in H_2O at concentration 1.0 mM (V1), 2.0 mM (V2), 2.5 mM (V3), 3.0 mM (V4), 3.5 mM (V5), 4.0 mM (V6) and 5.0 mM (V7) in glass vials.

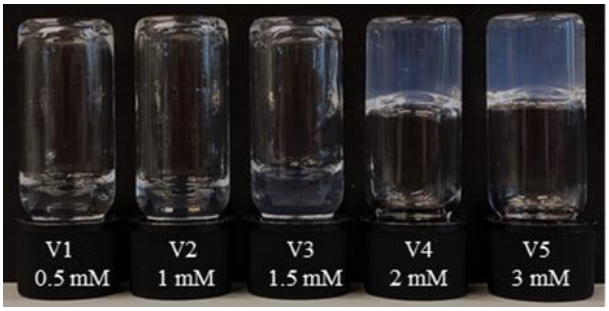

Figure S9. Gel inversion test of **5** in H_2O at concentration 0.5 mM (V1), 1.0 mM (V2), 1.5 mM (V3), 2.0 mM (V4) and 3.0 mM (V5) in glass vials.

Oscillatory rheology

Hydrogels of **3-5** (5 mM) were prepared as described above. Time sweep measurements were performed at a strain amplitude (γ) of 0.05% and at a frequency (ƒ) of 1 Hz. Strain sweeps were conducted in a range of strain amplitudes of 0.01 - 500% at a fixed frequency (ƒ=1 Hz). Frequency sweeps were executed over a frequency range from 0.01 - 3 Hz at a constant strain amplitude (γ=0.05%). A step-strain measurement was performed to estimate the self-recovery of the hydrogel. The measurement started with a time sweep (3600 s, f = 1.0 Hz, γ = 0.05%) and was followed by a frequency sweep (ƒ = 0.01 - 3 Hz, γ = 0.05%). Once a plateau in the storage modulus (G') was reached, a strain of 300% was applied to the sample for 120 s and was then left to recover while measuring at a low strain percentage (ƒ = 1 Hz, γ = 0.05%) for 800s. The process was repeated in this manner for two cycles. Temperature sweep tests were performed by applying a temperature ramp at 0.1 °C/min between 25 to 85°C under a fixed strain (γ = 0.05%) and frequency (ƒ = 1 Hz) with mineral oil placed around the geometry to prevent the drying of the hydrogels during the experiment. Storage modulus (G') and loss moduli (G'') were recorded during the process.

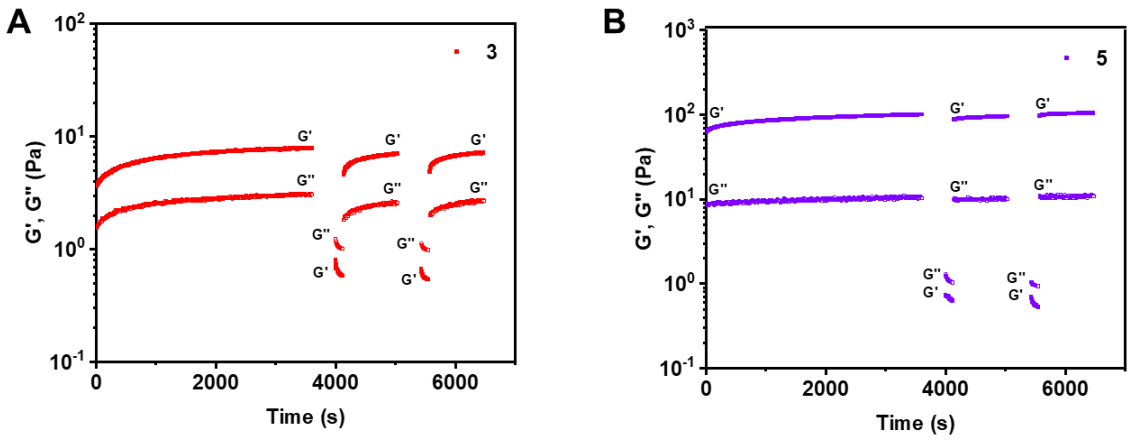

Figure S10. Time sweep measurements (ƒ = 1 Hz, γ = 0.05%) and self-recovery process of hydrogels **3** (A) and **5** (B) (5 mM) in H_2O at 25 °C. The absence of data before the application of high strain is due to the acquisition of a frequency sweep (ƒ = 0.01 to 3 Hz, γ = 0.05%).

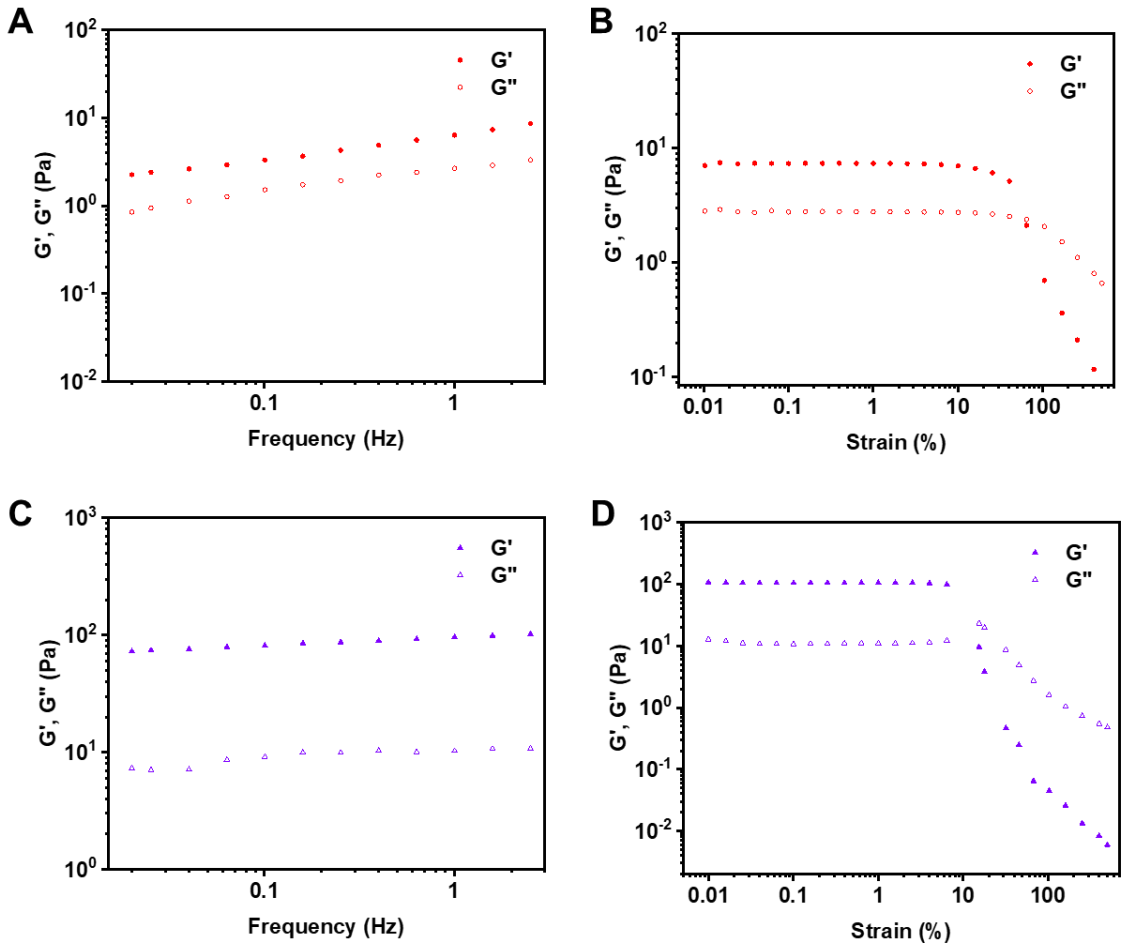

Figure S11. Oscillatory rheology measurements of hydrogels **3** and **5** (5 mM) in H_2O at 25 °C: Amplitude sweep (ƒ = 1 Hz) for hydrogels **3** (B) and **5** (D). Frequency sweep (γ = 0.05% strain) of hydrogels **3** (A) and **5** (C).

Cryogenic Transmission Electron microscopy (cryo-TEM)

Hydrogels (5 mM) of **3**-**5** were prepared as described before and diluted to the imaging concentration (0.5 mM). Subsequently, the samples (3 µL, 0.5 mM) were applied to a freshly glow-discharged carbon 200 mesh Cu grid. The excess liquid was blotted off (3 s) at 100% humidity and plunge-frozen in liquid ethane using a Vitrobot plunge-freezer. The images were recorded on a BM-Ceta (4k x 4k) at a nominal magnification of 73000x (1.34 Ångstrom per pixel) and defocus of -2.0 to -3.0 µm. The length and width of the fibers were measured using Fiji software. The size distribution was obtained by measuring the length and the width of at least 50 fibers per sample.

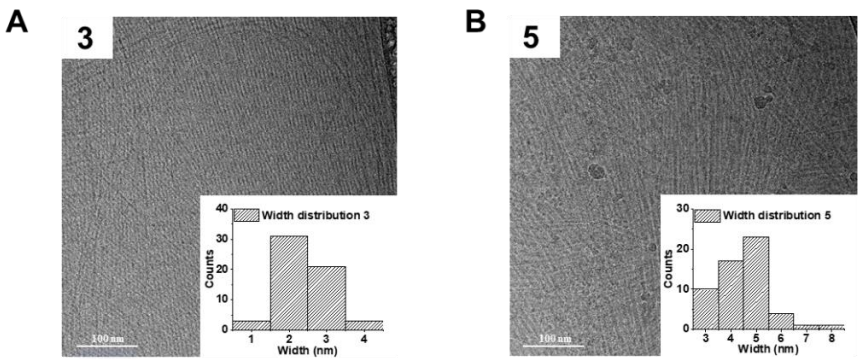

Figure S12. Cryo-TEM images of (A) **3** and (B) **5** at (0.5 mM in H_2O). Insert: Histograms of fiber width distribution for a sample size of N ⩾ 50. Scale bar: *100 nm*.

Atomic force microscopy (AFM)

Compounds **1-5** were dissolved in H_2O (0.25 mM) and equilibrated overnight. The samples were prepared by dropping solutions (10 µL) on a 1 cm^{-2} piece of mica with spin coating (2 min, 2000 rpm). The samples were dried overnight at RT prior to imaging. The obtained images were processed using the Nanoscope software.

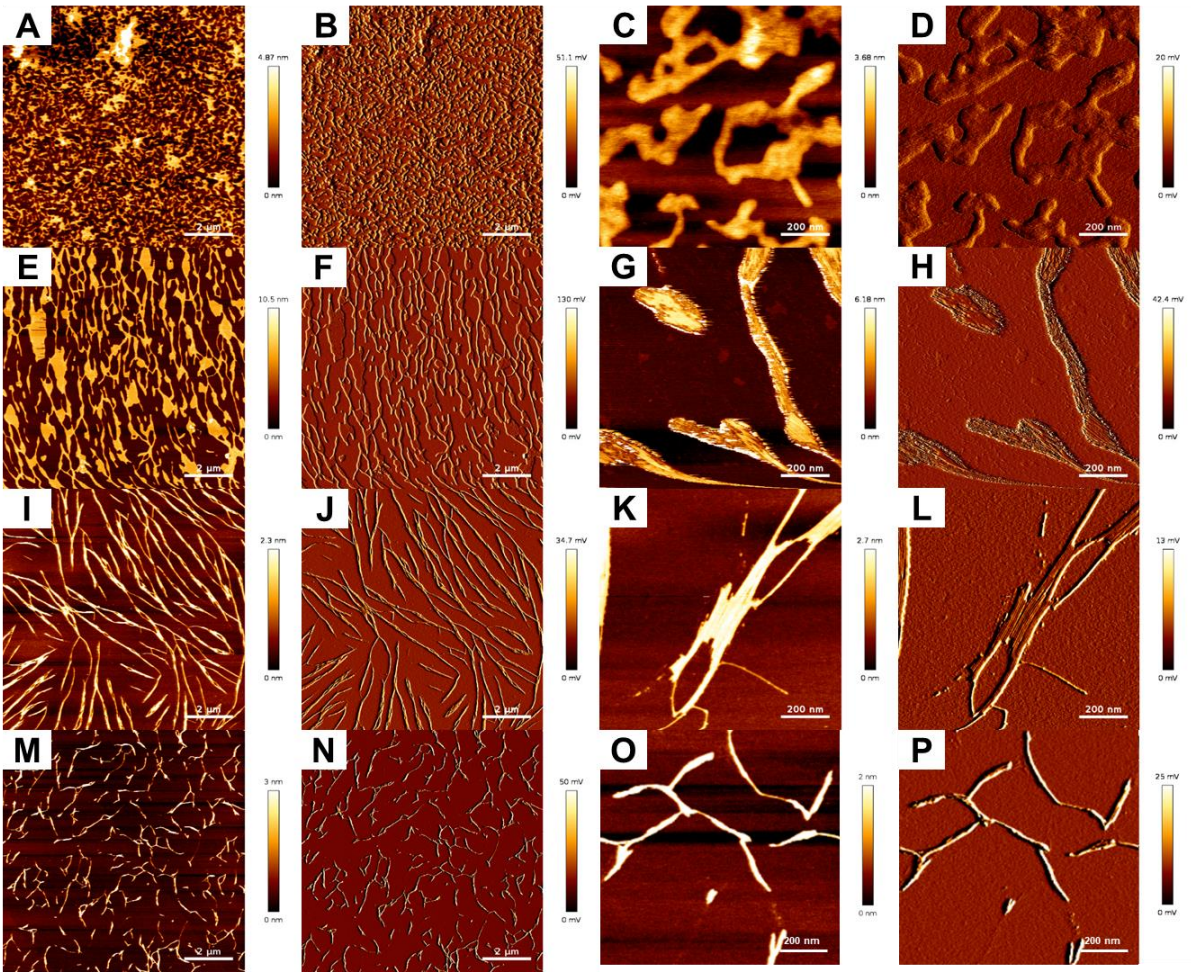

Figure S13. AFM height and amplitude phase images of **2-5** by spinning coating and deposited on mica overnight after dissolution. AFM height images at low magnification: (A) **2**, (B) **3**, (C) **4**, (D) **5**. Scale bar: *2 µm.* AFM phase images at low magnification: (E) **2**, (F) **3**, (G) **4**, (H) **5**. Scale bar: *2 µm.* AFM height images at high magnification: (I) **2**, (J) **3**, (K) **4**, (L) **5**. Scale bar: *200 nm*. AFM phase images at high magnification: (M) **2**, (N) **3**, (O) **4**, (P) **5**. Scale bar: *200 nm.*

Small angle X-ray scattering (SAXS)

Samples **3**-**5** (2 mg/mL) were prepared in H_2O before measurement as previously described and pipetted into 2 mm quartz capillaries before the measurements. The SAXS patterns were adjusted utilizing the calibrated detector response function to establish an absolute intensity scale, along with known sample-to-detector distance, measured incident, and transmitted beam intensities. These patterns were then azimuthally averaged, yielding one-dimensional SAXS profiles. To isolate the scattering curves specific to the self-assembled fibers, the scattering contribution of the solvent and quartz cell was subtracted using the SAXS utilities within the software package available at http://www.sztucki.de/SAXSutilities/. The resulting SAXS profiles were further analyzed using the software package SASview, accessible at http://www.sasview.org/.

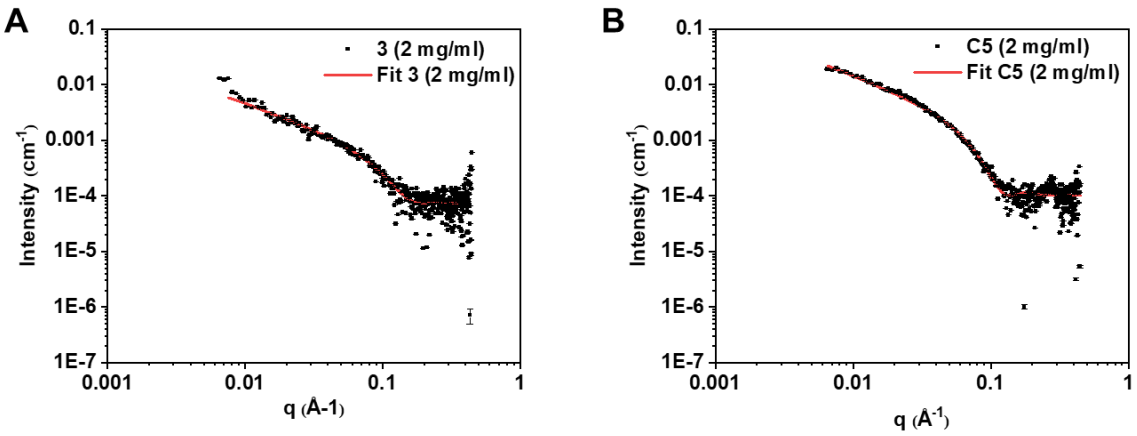

Figure S14. Small-angle X-ray scattering profiles of fibers (A) **3** and (B) **5** collected at a concentration of 2 mg/mL. Black dots represent experimental data; red line represents fit with a form factor for flexible cylinders.

UV-Vis spectroscopy

Stock solutions of **1-5** (1 mM) were prepared with H_2O in glass vials (2 mL) and subsequently diluted to the measured concentrations or solvent mixtures. The individual samples were left to equilibrate overnight at RT prior to UV-Vis measurements.

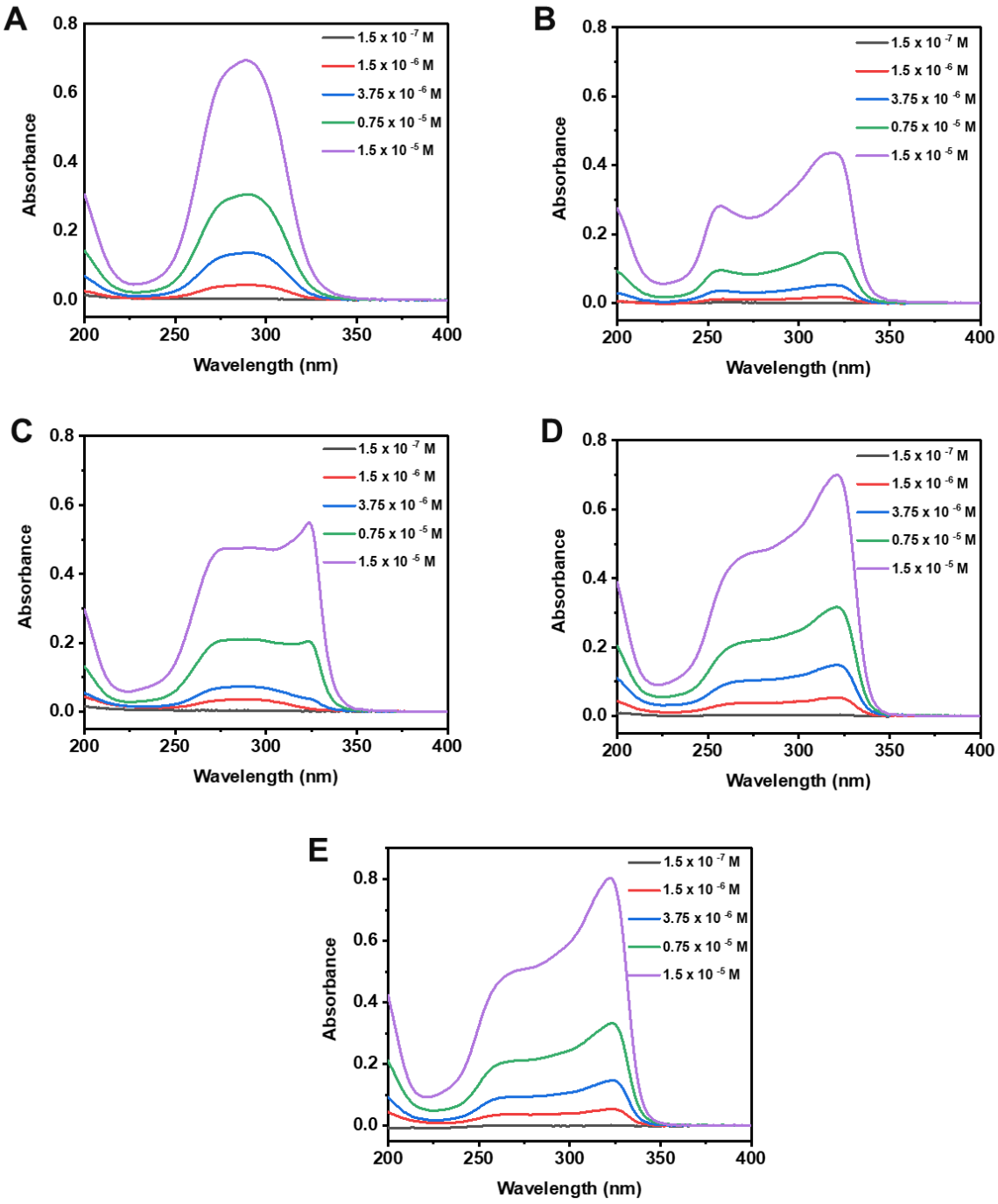

Figure S15. Concentration-dependent UV-Vis spectra of **1** (A), **2** (B), **3** (C), **4** (D) and **5** (E) in H_2O.

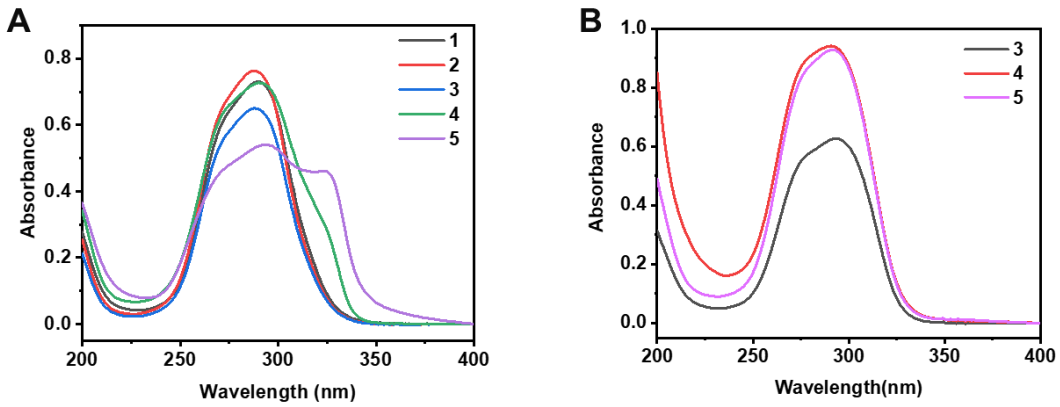

Figure S16. UV-Vis spectra of (A) **1-5** (1.5×10^{-5} M) in CH_3CN and (B) **3-5** in CH_3CN-H_2O (v/v, 6:4).

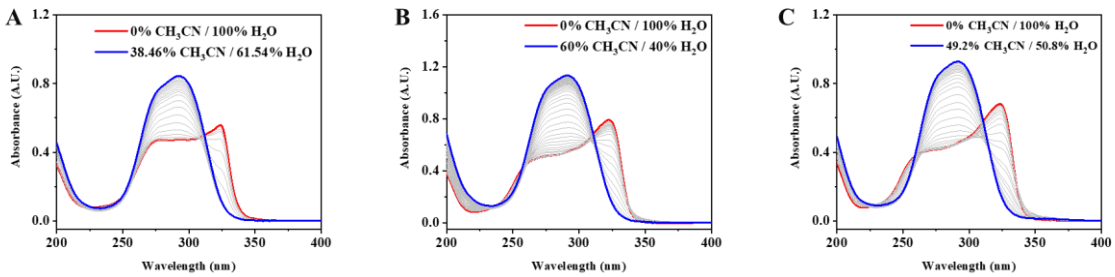

Figure S17. UV-Vis titration spectra of 3-5 (1.5×10^{-5} M) in CH_3CN and in CH_3CN-H_2O (v/v, 6:4). (A) **3**, (B) **4**, (C) **5**.

Fluorescence spectroscopy

Stock solutions of **1-5** (1 mM) were prepared in H_2O by sonication for 20 min, diluted to the desired concentration (1.5×10^{-5} M) and left to equilibrate overnight at RT prior to measurement. A Nile red dye solution (5×10^{-3} mg/mL) was prepared in methanol before being pipetted (12 µL) into the individual wells of a black 96-well plate. The methanol was removed in a vacuum oven at 25°C for 4 hours. Subsequently, an aliquot (200 µL) from the stock solutions of **1-5** was pipetted into a 96-well plate containing the Nile red dye and equilibrated overnight before measurement. An excitation wavelength of 520 nm was used and emission data was recorded from 575 to 750 nm. The Nile red dye in H_2O (200 µL) was also measured as a negative control.

Fourier Transform Infrared (FTIR) Spectroscopy

Compounds **2-5** were prepared in H_2O (200 µL, 8 mM) as previously described and left to equilibrate overnight at RT. The samples were then lyophilized prior to the acquisition of FTIR spectra.

A liquid transmission cell consisting of CaF_2 windows was cleaned carefully with D_2O or CD_3CN before use. Compounds **3-5** (500 µL, 5 mM) were first sonicated in D_2O for 20 min and then lyophilized. This process was repeated 3 times to remove traces of H_2O from the samples. **3-5** (5 mM) were then prepared in D_2O and 4:6 D_2O/CD_3CN individually by sonication for 20 min. The samples were sealed and left to equilibrate overnight at RT prior to measurement. The recorded IR spectra were plotted with respect to absorbance and appropriate background subtracted.

Table S1 Infrared spectrum assignment of vibrational modes from 3500-1500 cm^{-1} for the various peaks indicated in Figure 2D of freeze-dried samples **2-5**.

	2	**3**	**4**	**5**
v (N-H)	3166 cm^{-1} (squaramide)	3169 cm^{-1} (squaramide)	3165 cm^{-1} (squaramide)	3315 cm^{-1} (carbamate) 3164 cm^{-1} (squaramide)
v (C-H)	2920 cm^{-1} (antisym) 2852 cm^{-1} (sym)	2924 cm^{-1} (antisym) 2855 cm^{-1} (sym)	2923 cm^{-1} (antisym) 2854 cm^{-1} (sym)	2918 cm^{-1} (antisym) 2851 cm^{-1} (sym)
Ring Breathing	1797 cm^{-1}	1799 cm^{-1}	1799 cm^{-1}	1799 cm^{-1}
v (C=O)	1654 and 1639 cm^{-1} (squaramide)	1654 and 1639 cm^{-1} (squaramide)	1654 and 1639 cm^{-1} (squaramide)	1719 and 1689 cm^{-1} (carbamate) 1654 and 1639 cm^{-1} (squaramide)

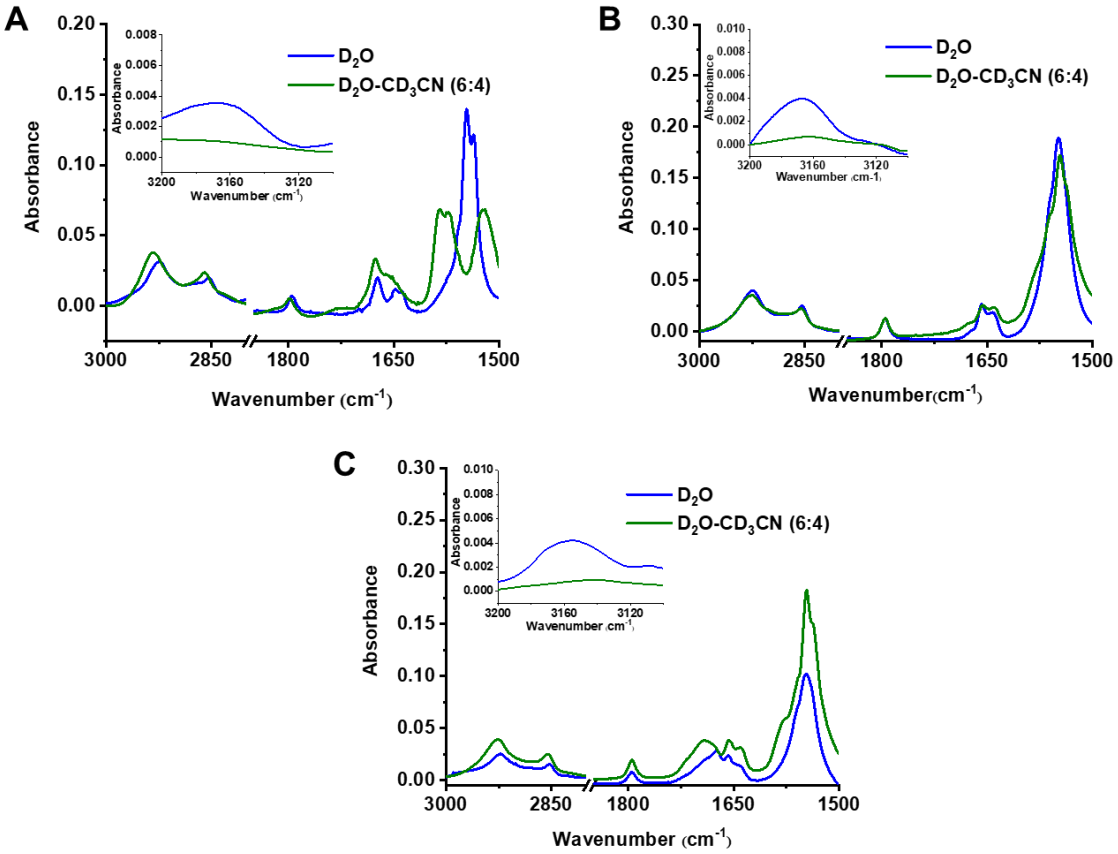

Figure S18. IR spectrum recorded in the N-H region (inset), amide I and amide II regions in D_2O and CD_3CN-D_2O (v/v, 6:4) at 5 mM for **3** (A),**4** (B) and **5** (C).

Table S2 Infrared spectrum assignment of vibrational modes from 3000-1500 cm^{-1} for the various peaks indicated in Figure **S18** of **3-5** in self-assembly state and monomer state.

	3		**4**		**5**	
	D_2O	**D_2O-CD_3CN (v/v, 6:4)**	**D_2O**	**D_2O-CD_3CN (v/v, 6:4)**	**D_2O**	**D_2O-CD_3CN (v/v, 6:4)**
v (N-H)	3174 cm^{-1} (squaramide)	3170 cm^{-1} (squaramide)	3166 cm^{-1} (squaramide)	3162 cm^{-1} (squaramide)	3155 cm^{-1} (squaramide)	3140 cm^{-1} (squaramide)
v (C-H)	2923 cm^{-1} (antisym) 2854 cm^{-1} (sym)	2933 cm^{-1} (antisym) 2860 cm^{-1} (sym)	2924 cm^{-1} (antisym) 2854 cm^{-1} (sym)	2926 cm^{-1} (antisym) 2855 cm^{-1} (sym)	2923 cm^{-1} (antisym) 2853 cm^{-1} (sym)	2926 cm^{-1} (antisym) 2855 cm^{-1} (sym)
Ring Breathing	1795 cm^{-1}	1798 cm^{-1}	1795 cm^{-1}	1795 cm^{-1}	1795 cm^{-1}	1794 cm^{-1}
v (C=O)	1648 cm^{-1}, 1638 cm^{-1} (squaramide)	1652 cm^{-1}, 1635 cm^{-1} (squaramide)	1658 cm^{-1}, 1642 cm^{-1} (squaramide)	1656 cm^{-1}, 1640 cm^{-1} (squaramide)	1674 cm^{-1} (carbamate) 1658 cm^{-1}, 1642 cm^{-1} (squaramide)	1692 cm^{-1} (carbamate) 1657 cm^{-1}, 1641 cm^{-1} (squaramide)

Lower critical solution temperature (LCST) measurements

Samples of **3-5** (0.2 mM and 1 mM) in H_2O were prepared as previously described and equilibrated overnight prior to measurement. Samples (2 mL) were placed into UV cuvettes, equilibrated at 20°C for 10 minutes before heating at 0.1°C / min to 90°C. The cuvettes were sealed with high-temperature-resistant tape to prevent evaporation.

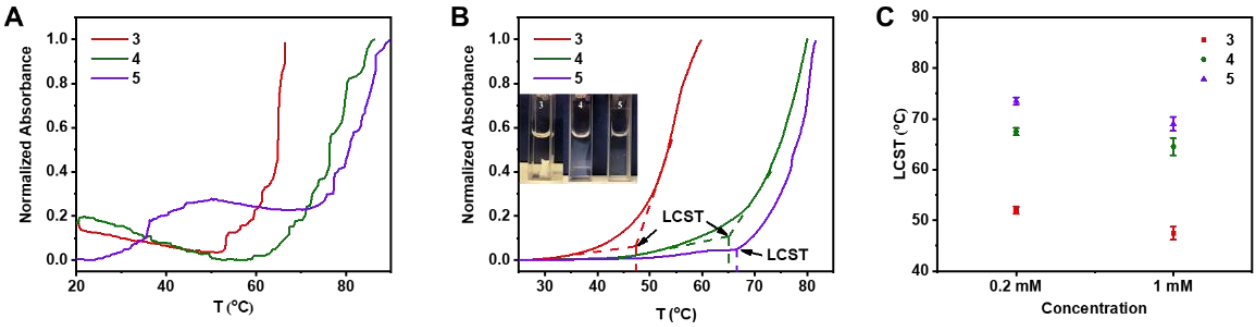

Figure S19. Turbidity measurements from UV-Vis absorbance spectra at 450 nm of **3-5** with increasing temperature from 20°C to 90°C at 0.1°C/min: (A) 0.2 mM; (B) 1 mM (Insert: digital picture of **3-5** after the test and cooled back to RT). (C) LCST of **3-5** at 0.2 mM and 1mM.

Differential scanning calorimetry (DSC) measurements

Hydrogels of **3-5** (5 mM) in H_2O were prepared as previously described and equilibrated overnight prior to measurement. Hydrogels (200 µL) were first placed into platinum capillary tubes, for every experiment, the samples were cooled to 0°C and equilibrated for 10 minutes before heating at 2°C / min to130°C under N_2 flow, followed by a cooling process at the same speed. The thermograms recorded were analyzed with the NanoAnalyze 2.0 software. T_1 and T_2 was determined as the peak1 and peak2 temperature values, ΔH corresponded to enthalpy and ΔS corresponded to entropy. The H_2O baseline underwent a minimum of 5 heating/cooling cycles until consistent heating was achieved, subsequently, it was subtracted from the sample data.

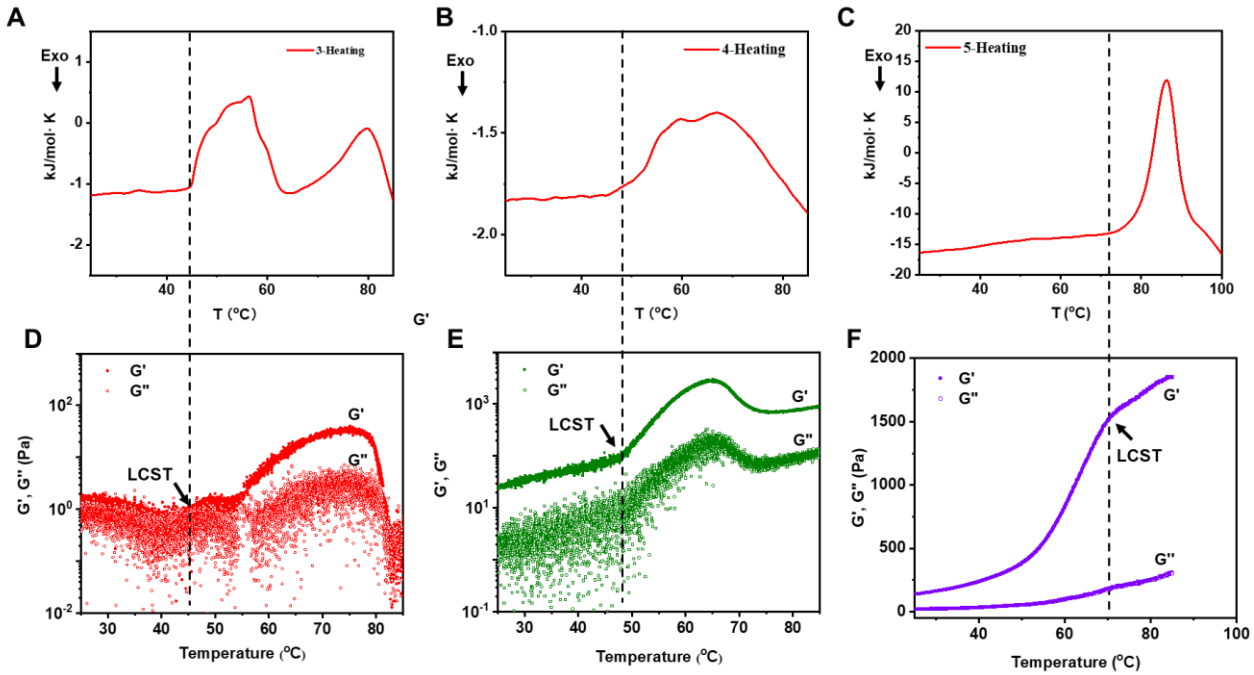

Figure S20. DSC curves measured for hydrogels of **3-5** (5 mM) heating from 20°C to 100°C: (A) **3**, (B) **4**, (C) **5**. Temperature sweeps for hydrogels (5 mM) (D) **3**, (E) **4** and (F) **5** in H_2O heating 20°C to 85°C at a rate of 0.1°C/min.

Hydrogel heating process

Hydrogels of **3-5** (5mM) were prepared as previously described and equilibrated overnight prior to the heating experiment. The hydrogels were put into NMR tubes and heated from RT to 130°C at a rate of ~2°C / min and then cooled back to RT. The heating process was imaged using a digital camera at different time points.

Polarized optical microscopy (POM)

Hydrogels of **3-5** (5 mM, 200 µL) were prepared, heated in NMR tubes and cooled down to RT as described before. The samples (100 µL) were carefully drop-casted onto a glass slide before imaging.

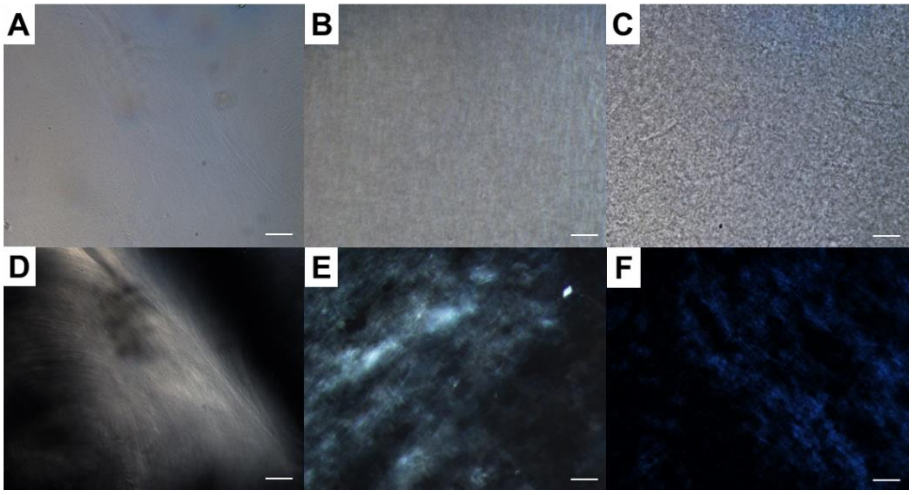

Figure S21. Optical and polarized optical microscopy (POM) images of squaramide-based hydrogels **3-5** (5 mM): (A) **3**, (B) **4,** (C) **5** in optical mode. (D) **3**, (E) **4,** (F) **5** in polarized mode. Scale bar: *100µm*.

Scanning electron microscopy (SEM)

The surface morphology of the heated hydrogels of **3-5** and **3'-5'** were examined by SEM. Samples of **3'-5'** (5 mM, 500 µL) were prepared, heated in NMR tubes, and cooled down to RT as described before. Afterwards, each sample (100 µL) was drop-casted on a desiccator with double-sided carbon tape on it, and dried in a 25°C vacuum overnight. The samples were sputter-coated with 2 mm gold–palladium (Au/Pd) prior to SEM imaging.

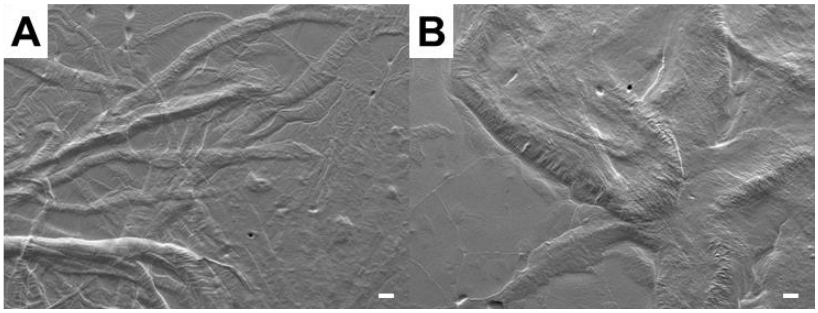

Figure S22. SEM pictures of hydrogels (5 mM) after heating process: (A) **4'**, (B) **5'**. Scale bar: *100µm*.

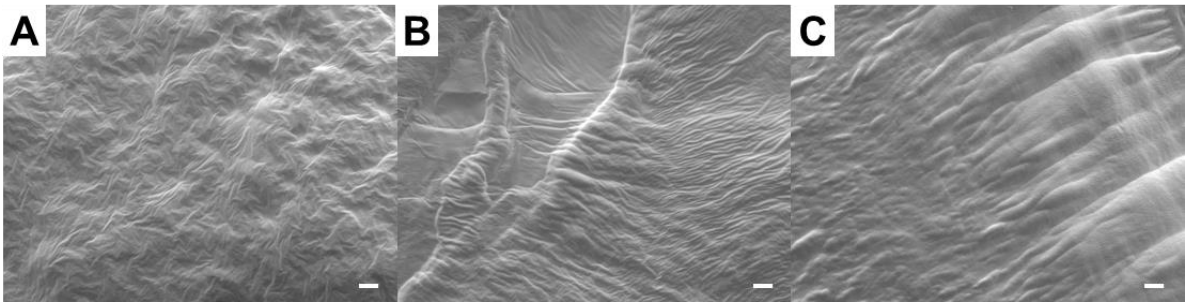

Figure S23. SEM pictures of hydrogels **3'-5'** (5 mM) after heating process: (A) **3**. (B) **4**. (C) **5**. Scale bar: *10µm.*

X-ray diffraction analysis (XRD)

Hydrogels of **3-5** (5 mM, 500 µL) were prepared, heated in NMR tubes, and cooled down to RT as described before. Afterwards, samples were lyophilized and directly loaded onto a rectangular glass sample holder, and then scans were carried out immediately and after prescribed times at a scan rate of 0.5°/min. Samples without heating process were lyophilized and measured in the same manner.

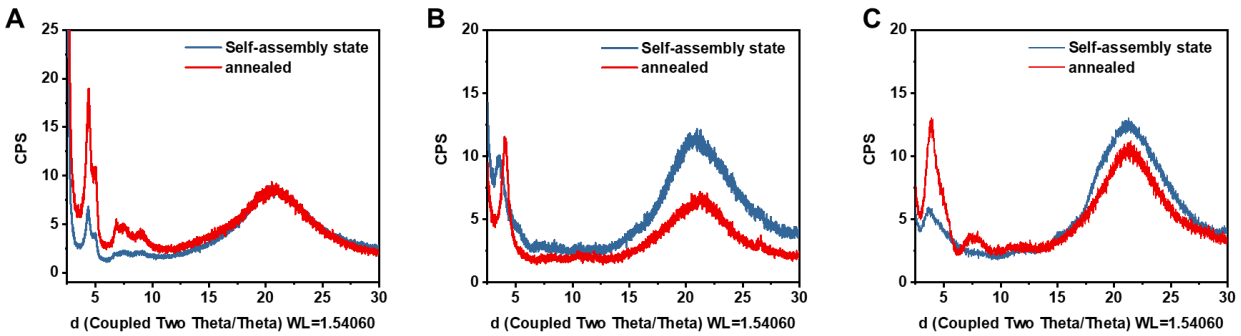

Figure S24. XRD of lyophilized hydrogels **3**-**5** and their heated samples **3'**-**5'**. (A) **3** and **3'**. (B) **4** and **4'**. (C) **5** and **5'**.

Reference

(1) Tong, C.; Liu, T.; Saez Talens, V.; Noteborn, W. E. M.; Sharp, T. H.; Hendrix, M.; Voets, I. K.; Mummery, C. L.; Orlova, V. V.; Kieltyka, R. E. Squaramide-Based Supramolecular Materials for Three-Dimensional Cell Culture of Human Induced Pluripotent Stem Cells and Their Derivatives. Biomacromolecules 2018, 19 (4), 1091.

Chapter 3

Dithiolane-ene Photopolymerization of Covalent and Supramolecular Networks Permits Cyclic Compressive Loading in 3D Cell Culture

Filamentous supramolecular polymers provide a modular synthetic platform that emulates the biopolymers of the extracellular matrix in their structure and function. However, the materials are mechanically weak and challenged to mimic the properties of tissues that undergo cyclic compressive loading like cartilage. Herein, we explore the use of light-mediated chain growth polymerization of dithiolane and dithiolane-ene to simultaneously crosslink a network of nanoscale supramolecular filaments with covalent polymer macromonomers, yielding hybrid double network hydrogels that can sustain dynamic compression in 3D cell culture. Benefitting from the energy dissipation mechanisms accessible to supramolecular materials, they show cartilage-like mechanical characteristics, such as biomimetic stress responses to compression and relaxation that can be tuned according to component ratios and concentrations using light. 3D culture of human primary articular chondrocytes in the photocrosslinked hydrogels displayed increased deposition of sulfated-glycosaminoglycans. Exploiting the photoreactive macromonomers, we mechanically pattern the materials at cell relevant length scales and apply cyclic compressive loads up to 14 days. The enclosed covalent network fortification strategy combined with bioorthogonal light-mediated crosslinking provides a base to tune the mechanics of filamentous supramolecular biomaterials in both space and time for 3D cell culture to mimic tissues under compressive loads in development and disease.

This chapter was prepared as a research article: Ying Chen,[+] Dr. Ciqing Tong,[+] Merel L. Janssen, Isabel Sariol, Joeri A. J. Wondergem, Marijn van den Brink, Prof. Dr. Rob G. H. H. Nelissen, Prof. Dr. Doris Heinrich, Dr. Yolande F. M. Ramos* and Dr. Roxanne E. Kieltyka*

[+] These authors contributed equally to this work.

3.1 Introduction

Synthetic hydrogels that mimic features of the natural extracellular matrix (ECM) are essential to promote *in vivo* cell behaviors for applications in tissue engineering and regenerative medicine. In the ECM, matrix proteins (e.g., collagens, proteoglycans) create an environment where numerous biochemical, architectural, and mechanical cues change in both space and time.[1–3] While hydrogel stiffness is a widely recognized mechanical cue that has been examined extensively in shear, others that are strain- and time-dependent (e.g., strain-stiffening or viscoelasticity) are being increasingly shown to influence cell behaviors in complex developmental and disease processes.[4–7] Moreover, cell cultures within these hydrogels are studied in absence of external mechanical loads, yet numerous tissues (e.g., cardiovascular, musculoskeletal, cartilage) are subjected to them (e.g., compression, tension).[8] As an example, the mechanical loading of cartilage starts before birth, influencing chondrocyte proliferation, maturation, and synthesis of ECM proteins, ultimately providing a stiff and tough tissue that maintains the joint biomechanical properties throughout life.[9,10] Hence, synthetic polymer hydrogels that can sustain a range of mechanical loads and respond in a biomimetic manner are urgently needed to not only unravel cell behaviour in health and disease (e.g., osteoarthritis (OA)),[11] but also for the development of more effective cellular therapies.

The exceptional mechanical properties of cartilage tissue, namely its capacity to bear a wide range of compressive loads up to 18 MPa[12] with a low coefficient of friction is enabled by its extensive ECM proteins[13,14] synthesized by chondrocytes. Cartilage ECM is presented differentially across the tissue being subdivided into three zones, from the superficial and middle to the deep zone, and exhibiting distinct structure and mechanics.[13,15] A critical player is the pericellular matrix (PCM) that is immediately adjacent to the chondrocyte cell membrane, consisting of fibrillar and network type collagens (i.e., collagens II/VI/IX), fibronectin and proteoglycans (e.g., aggrecan), transducing both mechanical and biochemical signals from the tissue to the cell.[16] Together with the chondrocyte they form the chondron, that has distinct mechanical properties from the surrounding cartilage ECM with a Young's modulus of 40 kPa – 70 kPa versus 1 MPa, respectively.[11] The PCM changes in its presentation around the chondrocyte during development, in diseases such as OA, and synthetic hydrogel materials based on their mechanics can alter its presentation only a few hours after seeding.[11,17,18] As cartilage mechanics and architecture vary across the tissue, hydrogel materials that span this range in their properties can enrich the growing knowledge of chondrocyte biology providing opportunities to direct their behavior for tissue engineering applications.

Supramolecular polymers bear analogy to ECM proteins, such as collagens, based on their filamentous nanostructures and functions that emerge from the non-covalent assembly of small molecules.[19–24] Above a critical monomer concentration gel phase materials with complex mechanics (e.g., viscoelasticity, strain stiffening, plasticity) can be prepared and drive cell responses when decorated with the appropriate chemical and bioactive cues.[25,26] Despite the modular and flexible approach to their preparation, the resulting materials show low storage moduli (10 Pa – 100 Pa) due to the entanglement of the filaments.[27,28] Consequently, such supramolecular networks alone cannot be applied for *in vitro* culture applications where dynamic mechanical loads are used. One strategy in

synthetic hydrogels that can permit access to the mechanics of load bearing tissues, such as cartilage, involves the use of double networks.[29,30] Two polymers that are juxtaposed in their properties are combined, one that is brittle and the other ductile (e.g., acrylates, acrylamides), with chemical and/or physical crosslinks between them leading to stiff (E ~ 0.1- 1 MPa) and tough materials (toughness ~ 0.01 - 1 MJ/m^{-3}).[31,32] The brittle network dissipates the energy on deformation by fracturing easily whereas the ductile network provides support to yield high toughness. However, the exclusive use of covalent bonds in both networks limits recovery of the material because of their irreversible character. While the use of supramolecular filaments can overcome this challenge, their preparation protocols lack cytocompatibility (e.g., high temperature, solvents) hampering opportunities to study their biomimetic structure and mechanics on cell behaviour in 3D culture.[33–36]

In this study, we explore a bioorthogonal strategy involving ring opening photopolymerization of 1,2-dithiolane (DT) and norbornene (NB) to prepare double networks (**DN**) based on supramolecular filaments consisting of squaramide[37–39] monomers and covalent poly(ethylene glycol) polymers for their 3D cell culture under compressive mechanical loads. While the thiol-norbornene reaction is a widely used photo-click reaction to prepare hydrogels through a step-growth mechanism, we demonstrated that exchange of thiol for DT, that provides two thiyl radicals on UV exposure at 365 nm, can lead to polymer networks (**PN**) through a chain-growth mechanism based on thioether linkages from linear poly(ethylene glycol) macromonomers showing similar cell viabilities.[40] Moreover, this dithiolane-ene photopolymerization strategy was recently used to fabricate granular hydrogels.[41] We therefore became interested to apply this covalent network to supramolecular filaments (**SN**) to form and fortify the materials with UV exposure at the same wavelength through the simultaneous photopolymerization of DT and DT-NB. Because a chain-growth polymerization approach is taken, several covalent and supramolecular polymers can be involved in a crosslink permitting simultaneous formation of the covalent network and its crosslinking to the supramolecular filaments. We then leverage these hybrid supramolecular and covalent materials for the 3D cell culture of human primary articular chondrocytes under cyclic mechanical loads and read out nascent matrix deposition, gaining insight into the potential of this biomimetic materials class tune their behavior. Finally, we show that this photopolymerization strategy can be used to engineer spatially distinct mechanical domains, stiff and soft, within these supramolecular biomaterials opening the door to mimic developmental and disease conditions that evolve in space and time.

3.2 Results and Discussion

Design and preparation of the squaramide-based supramolecular and covalent polymer double network hydrogels

To prepare the DN hydrogels based on supramolecular and covalent polymers, we co-assembled tripodal squaramide-based supramolecular polymers with 10 mol% 1,2-dithiolane (DT) monomer (5

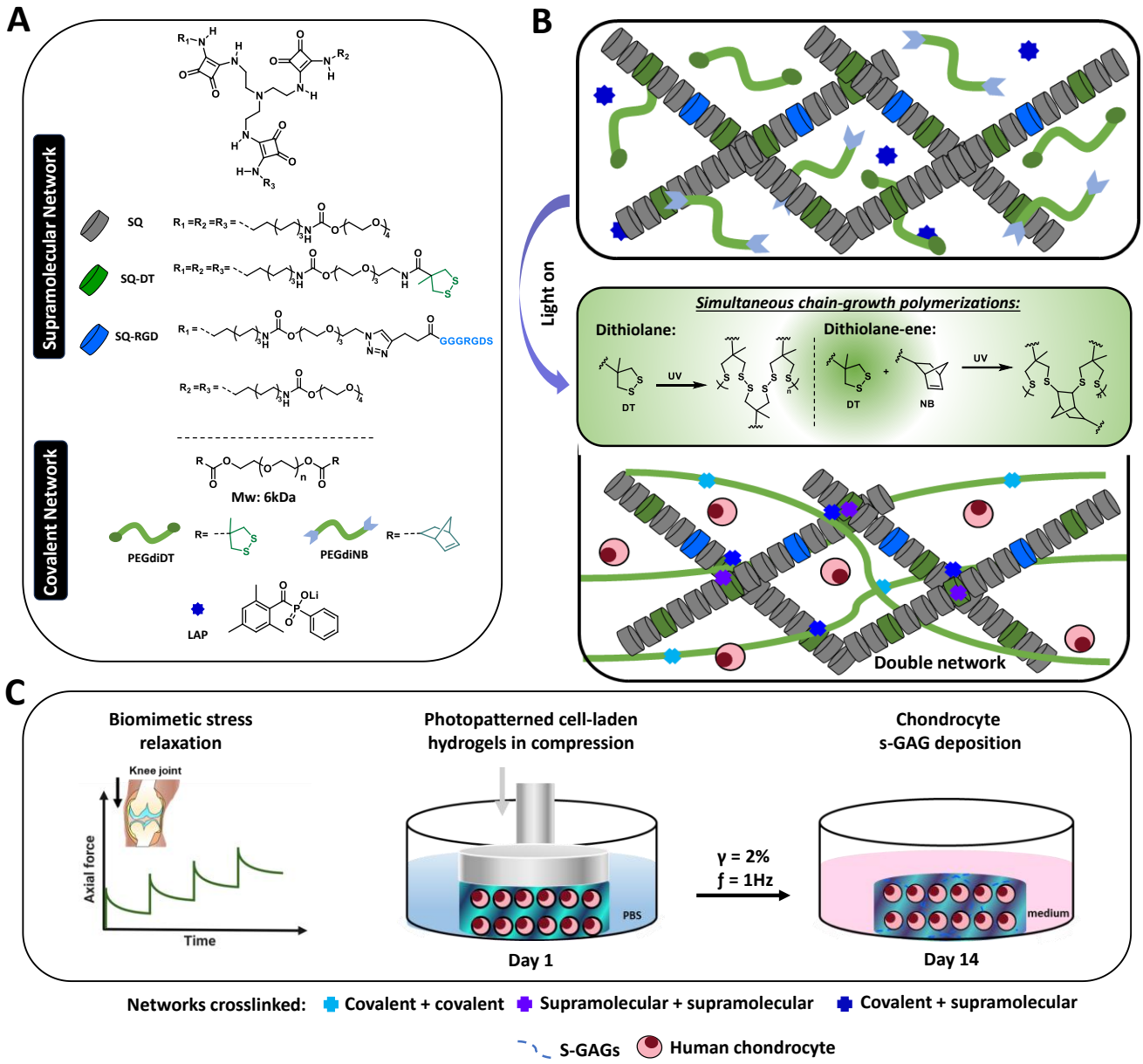

Scheme 1. (A) Supramolecular filament (**SN**: SQ, SQ-DT, and SQ-RGD) and covalent polymer (**PN**: PEGdiDT and PEGdiNB) components (*left*) to prepare **DN** hydrogels. (B) Mixing of components, DT and DT-NB photopolymerization to form **DN** hydrogels. (C) Biomimetic cartilage mechanical properties can be achieved in compression and release (*left*). The bioorthogonal photopolymerization approach in the **DN** hydrogel permits 3D human chondrocyte culture with cyclic compression leading to increased s-GAGs deposition (*middle and right, respectively*).

mM) (SN)[42] and linear 2-arm poly(ethylene glycol) (PEG) macromonomer (in total 3.6 wt%) end-functionalized with DT or NB (PN). More specifically, after sonication of a solution of the supramolecular filaments in phosphate buffered saline (pH 7.4) on ice, we added the DT and NB macromonomers and then brought them to room temperature (RT) to result in a hydrogel. Subsequently, photopolymerization of the soft hydrogel with UV light at 365-375 nm simultaneously formed a covalent network and crosslinked with the supramolecular filaments (SN) at the above component ratios. This result is supported by our earlier demonstrations that double addition of DT occurs across NB in the presence of LAP on covalent macromonomers[41] and poly(disulfide)s are formed on supramolecular polymers with UV exposure.[43] The hydrogels remained transparent (Figure S1) even after photopolymerization as observed in gel inversion tests; a feature that is needed for the eventual imaging of 3D cell cultures (Scheme 1).

Photocrosslinking of supramolecular and covalent polymer networks shows mechanical characteristics that outperform either component

We probed the effect of adding a second covalent network to the filamentous supramolecular network and DT-NB photopolymerization on hydrogel mechanical properties using oscillatory rheology. In time sweep measurements after 10 min UV exposure, we recorded **DN** storage moduli (G') greater than the individual components (Figure 1A). For the single network hydrogels, the **PN** (3.6 wt%) consisting of PEGdiDT (1.8 wt%) and PEGdiNB (1.8 wt%) with LAP (1.0 mM) showed a storage modulus of ~1 kPa, and the DT-crosslinked supramolecular polymer network **SN** reached ~3 kPa. For the double network material **DN**, mixing of the supramolecular **SN** and covalent **PN** networks resulted in a storage modulus of ~10 kPa (Figure 1A). The rise in the storage modulus is an order of magnitude greater than the sum of the **SN** and **PN**, and significantly greater than the pre-UV exposed hydrogel (~10 Pa), highlighting the synergy of mixing these two networks and their photocrosslinking. Additionally, the rate required to a reach a maximum in the storage modulus was reduced to 3 min for the **DN** as compared to the **SN** hydrogel that required ~10 min due to the absence of NB that rapidly undergoes photopolymerization with DT in the presence of **LAP** (Figure S2-S3). We then evaluated the change in hydrogel stiffness with short bursts of UV light in a sequential manner. The storage modulus increased in a stepwise manner rapidly with each step highlighting the rapid kinetics of the photopolymerization reaction, reaching equivalent values to the **DN** exposed for longer durations (e.g., 3 and 10 min). The response and duration of light used opens possibilities to modulate their mechanical properties in space and time as encountered in numerous complex biological process that occur in native tissues (Figure 1B).

We further examined different network compositions to deconvolute the origin of the dramatic increase in storage modulus on combining **SN** and **PN** (Figure S3). A semi-interpenetrating network **IPN** prepared at the same concentration as the **DN** without 10 mol% SQ-DT in the **SN** to crosslink both polymers gave a storage modulus of ~4 kPa. This result highlights the importance of the crosslinking of both **SN** and **PN** in the **DN** on the measured mechanical properties. On the other hand, incorporation of 10 mol% SQ-DT into the **SN** and exchange of the PEGdiDT for a PEG dithiol in the **PN** resulted in a storage modulus of ~3 kPa (Figure S4). As the DT unit is a bifurcated cross-linking unit that yields two

disulfides on ring opening with light leading to polymerization, its replacement with a thiol in the **PN** components abrogates opportunities for its formation and simultaneous crosslinking with the **SN**. To understand the contribution of the covalent network on the mechanical properties of the **DN**, we prepared a sample where only crosslinking of the **SN** would be possible by adding equivalent amounts of SQ-DT and PEG-NB without PEG-DT. Crosslinking of the supramolecular filaments alone did not yield the earlier recorded **DN** storage moduli (~2 kPa) (Figure S5). Overall, both the *in-situ* formation of the second **PN** and the crosslinking to the **SN** through the chain-growth photopolymerization of both networks is required to attain the stiffness of the **DN**.

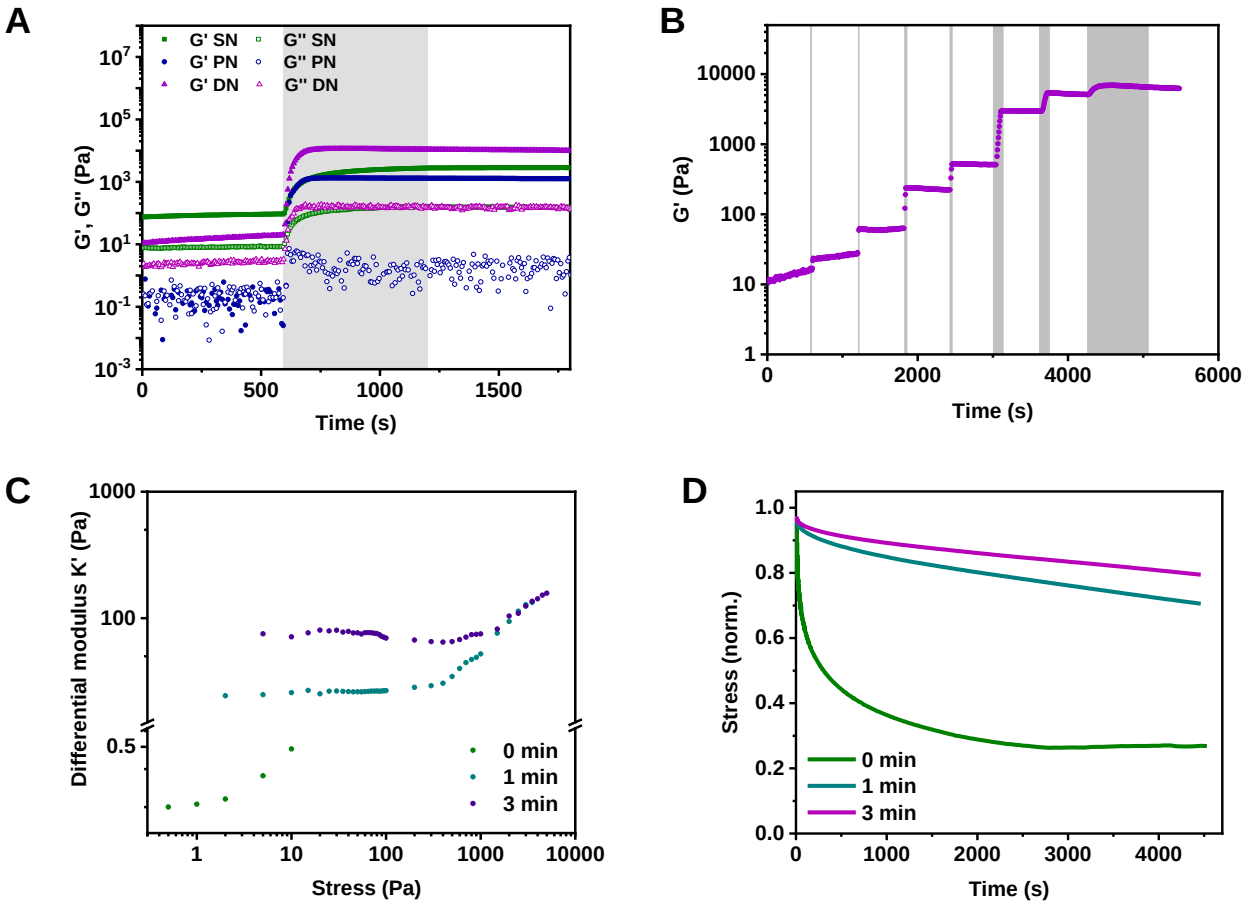

Figure 1. Oscillatory rheology data of hydrogels at RT: (A) Averaged (N=3 independent samples) time sweeps showing storage (G') and loss moduli (G") of **DN**, **PN** and **SN** with 10 min UV exposure. (B) Averaged (N=2 independent samples) time sweep showing storage modulus (G') with stepwise UV exposure of the **DN**. (C) Normalized stress relaxation behavior (σ/σ_0) (strain = 10%) of **DN** after different UV exposure times (0 min, 1 min, and 3 min). (D) Strain-stiffening behavior as indicated by differential modulus (K') of **DN** with different UV exposure times (0 min, 1 min and 3 min) measured using a pre-stress protocol. Light source parameters: ~10 mW/cm^2, λ = 320-500 nm, primary peak: 365 nm. Grey regions indicate UV exposure.

We then examined the range by which stiffness of the **DN** can be tuned by altering the reaction conditions. We modified the molar percentage of SQ-DT in **SN**, the total polymer concentration of the **DN**, and light source parameters while keeping the supramolecular polymer concentration constant (Table S1, Figure S6-S7). Increasing the concentration of the SQ-DT monomer from 0 to 10 mol% in the

supramolecular filament network resulted in an increase in storage modulus from ~4 kPa to ~10 kPa of the **DN** (Figure S6) pointing out that a small amount of co-assembled photoreactive monomer can significantly impact materials properties. Further increasing the covalent polymer concentration in the **DN** from 3.6 to 9.6 wt% resulted in an even greater increase in network stiffness raising the storage modulus up to ~21 kPa (Figure S7). Moreover, doubling the SQ concentration from 5 to 10 mM and reducing SQ-DT from 10 to 5 mol% resulted in similar storage moduli pointing out the salience of the covalent crosslinks and showcasing the modularity of the materials.

Since (dynamic) covalent bonds are made simultaneously between the **SN** and **PN** on photopolymerization, we evaluated their consequence on the **DN**s to self-recover after imposing a large strain (Figure S8-S9) in a cyclic manner through a step-strain test. After removal of a high strain (500%) from the **DN**, the initial storage modulus recovered ~51% as compared to the **SN** (8 mM) that reached 60% after two cycles. The extent of recovery of the **DN** increased to 64% when the **PN** increased to 7.2 wt%. This result confirms the formation of covalent bonds between both networks, but also highlights that the supramolecular interactions between filaments still contribute to the recovery of the materials at large strains on short timescales.

Covalent character is gained in the hydrogels complex mechanical characteristics

Native tissues show complex mechanical character in response to load that is time- and strain-dependent regulating cell processes such as long-distance communication, differentiation, and morphogenesis.[5–7,44,45] We therefore evaluated incorporation of the **PN** and its photopolymerization on the **DN** viscoelastic, viscoplastic and strain-stiffening properties in response to their shear deformation as supramolecular network filaments provide access to these properties. On subjecting the **DN** to 10% strain, the extent and rate of stress (σ) relaxation decreased with the UV exposure time. UV exposure for 1 min reduced the relaxed stress by ~44% after 75 minutes as compared to the non-UV exposed control. Increasing UV exposure to 3 min decreased relaxation by an additional ~10 % consistent with the increased covalent crosslinking through photopolymerization (Figure 1C). When compared against a **PN** (7.2 wt%) of equivalent storage modulus, the **DN** showed stress relaxation over the measuring period whereas the **PN** did not (Figure S10). This result demonstrates that the **SN** endows the **DN** with stress relaxation behavior through its entangled filament network.

Photopolymerization of both networks also resulted in changes to their susceptibility to plastic deformation in response to a constant shear stress in a creep and recovery test. UV exposure for 1 minute largely nullified the viscoplastic response of the **DN** to stress (300 Pa) as compared to the non-UV exposed control (Figure S11). We then examined the strain stiffening behavior of the **DN** using by a pre-stress method.[46] Non-linear responses were observed for all samples on comparison of the differential modulus (K') with increasing stress. The stress value at which the response of the sample deviates from linearity otherwise known as the critical stress, σ_c, increased significantly over several orders of magnitude for the supramolecular and covalent networks after UV exposure from 2.3 Pa (0 min) to 0.35 kPa (1 min) and 1 kPa (3 min) (Figure 1D, S12). Overall, the addition of the covalent polymer network and its chain-growth photopolymerization with the supramolecular filaments results in hydrogel mechanical properties that tend towards their covalent counterparts, but still retain features

that are inherently associated with those that are non-covalent and essential to mimic the mechanics of ECM proteins.

Highly compressive mechanical properties of DN hydrogels

Articular cartilage is a tissue that is subjected to cyclic compressive loading,[47] therefore understanding the mechanical behaviour of the covalent and supramolecular double network gels in compression is crucial. Axial force compression tests in the rheometer (Figure 2A) revealed significant differences in mechanical behaviour between the various networks from the collected compressive stress-strain profiles (Table S2). Compression of the **SN** hydrogel to ~2% of its initial height resulted in fracture at a stress of ~0.5 kPa (Figure 2B) demonstrating its brittle character and could not be characterized further. On the other hand, the **PN** endured up to ~40% strain (γ) prior to fracture with a stress increase of ~84 kPa consistent with formation of the covalent network and stable covalent crosslinks between the two networks. Addition of the **PN** to the **SN** forming the **DN**, boosted the compressive stress (~164 kPa) of the **DN** due to the supramolecular filaments albeit with a lower fracture strain (~20%) consistent with their mixing. For comparison, exchange of PEGdiDT for PEG dithiol or altering the ratio of NB in the **DN** (NB:DT ratio 1:1 or 1:2) only resulted in a slight improvement in compressive properties relative to **SN** (Figure S4 and S5) in line with earlier shear experiments. In the **IPN**, where the SQ-DT monomer that enables crosslinking of both networks is removed from the **SN**, a lower stress (~74 kPa) at fracture is recorded despite a similar fracture strain (~22%). Compression of the **DN** and **PN** hydrogels to 10% of their original height with a larger diameter geometry (20 mm), culminated in fracture of the **PN** (3.6 wt%) (Figure 2A) whereas the **DN** hydrogel maintained its form and removal of the compressive stress led to restoration of the initial shape. Importantly, the **DN** showed the most rapid increase in stress on compression of hydrogel with a greater compressive modulus (E) (~614 kPa) as compared to the **IPN** (~216 kPa) and **PN** (~62 kPa) (Figure 2C). The step-wise increase in compression modulus with the addition of the supramolecular filaments to the **PN** and their crosslinking through photopolymerization highlights the salient contribution of both features to the **DN** compressive properties. When compared to cartilage ECM, the compressive moduli obtained for these double networks is most like the PCM that envelops and aids to transduce mechanical signals from the surrounding ECM to the chondrocyte.

Compression relaxation cycles with increasing strains were performed to confirm the **SN**'s role as a sacrificial network and the influence of crosslinking on energy dissipation. With larger imposed strains, the hysteresis loops of the **DN** grew in area, indicating energy dissipated (E_D), from ~0.08 kJ/m^3 at 5% to ~3.93 kJ/m^3 at 20% strain (Figure 2D) validating the sacrificial contribution of the **SN**. In contrast, the **IPN** showed hysteresis loops with smaller areas (e.g., 1 kJ/m^3 at 20% strain) signaling that covalent crosslinks between the **SN** and **PN** are needed to enhance energy dissipation in the **DN**. In contrast, the **PN** showed a linear profile lacking hysteresis loops even at 40% strain (Figure 2D, S13-S14). As the toughening of the **DN** relies on the fracture of the **SN** as an energy dissipation mechanism, we compared the fracture energies of the various networks. The toughness of the **DN** (~13 kJ/m^3) was greater than the **SN** (4 J/m^3), pointing out the importance of the **PN** on its mechanical strength (Figure S15-S16). The **PN** (~10 kJ/m^3) showed decreased toughness relative to the **DN** due to the absence of the sacrificial

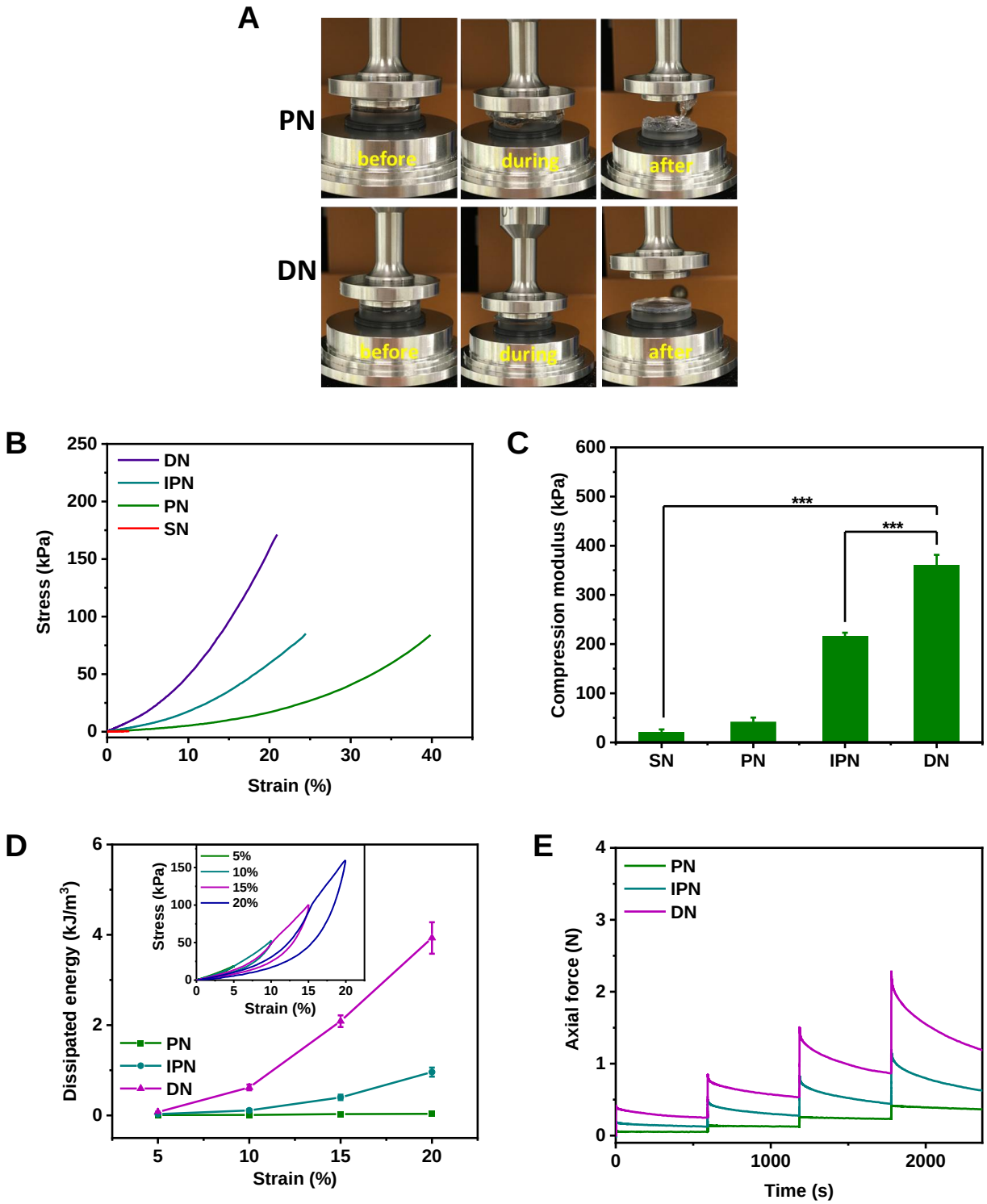

Figure 2. Compression behavior of the **SN**, **PN, IPN** and **DN** hydrogels: (A) Optical images displaying the photocrosslinked **PN** and **DN** before/during/after the compression experiments on the rheometer. (B) Uniaxial stress-strain (σ - γ) curves. (C) Measured compression moduli (E). *P*-values: ***<0.001, mean ± SD, N ≥ 3. (D) Measured dissipated energy (E_D) with increasing maximum strain (insert: uniaxial compression relaxation cycles of the **DN** at different maximum strains), Mean ± SD, N≥3. (E) Step-stress relaxation experiment with increasing strain (5%) at the start of each loading cycle.

network. However, its measured fracture energy was still greater than the **IPN** (~8 kJ/m^3) highlighting the contribution of the **PN** mechanical strength to the semi-interpenetrated network and the need for covalent crosslinking between both networks to reach the **DN** values (Figure S13-S14).

Rapid stress relaxation is a key feature of cartilage tissue that protects the joint from damage by dampening the mechanical load. Compressive loads were rapidly applied to the hydrogels and released monitoring their capacity to relax stress in a cyclic manner with increasing strain at the start of each loading cycle. The **DN** efficiently and promptly relaxed the stress in response to axial force (F) during each cycle (~36% – 48%) in a similar manner to cartilage,[48,49] whereas the **PN** hydrogel (Figure 2E) completely lacked this response profile. The **IPN** also relaxed the applied stress (44% - 46%) to a similar extent as the **DN** under identical conditions, but with a reduced axial force response to the applied load at the start of the cycle. This shows that the filamentous supramolecular polymers are important to guide this biomimetic stress relaxation behaviour within the **DN**, and crosslinking of both **SN** and **PN** through their photopolymerization provides a means to boost the axial force generated with cyclic compressive loading of the hydrogels.

Material characterizations of diverse DN hydrogels

To better understand the structural aspects of the gel that lead to the observed mechanical characteristics and influence their application for eventual 3D cell culture, we performed several imaging and equilibrium swelling assays. Cryo-TEM imaging of the **DN** before UV exposure confirmed that the supramolecular filaments remain present after the addition of poly(ethylene glycol) polymer. We observed flexible and micron-long entangled supramolecular filaments after incorporation of the **PN** (Figure S17). The retention of the **SN** after **PN** addition provides access to the biomimetic mechanical responses on compressive loading.

We further examined the hydrogels at the microscale after UV exposure by scanning electron microscopy (SEM). The pore size of the **DN** is smaller (~15 μm) than the **IPN** (~54 μm) that lacks crosslinking between the two networks through photopolymerization or that of the **PN** (~88 μm) (Figure S18). This finding supports the trends in the rheological data that show addition of a second network and its crosslinking result in increased storage and compressive moduli. We conducted an equilibrium swelling assay to determine the hydrogel stability and equilibrium water content (EWC) for their subsequent application in 3D cell culture. The **DN** showed consistent and minimal changes in swelling percentage after 3 minutes of UV exposure with maintenance in PBS or cell culture medium (DMEM) at 37 °C for more than 21 days, showing suitability for long-term cell culture experiments (Figure 3A). At the same time, the EWC values were measured for the various hydrogels after 3 minutes UV exposure (Figure 3B). While all hydrogels showed a EWC values above 95%, the **DN** showed a slightly lower EWC relative to the **SN** and **PN** that would be consistent with the increased network density and decreased pore sizes as measured in SEM. As the EWC value is well above 75% for the **DN**, transport of nutrients, and other biomolecules is expected[50] and through introduction of the second network and its crosslinking, stability for longer term culture periods can also be achieved.

To further quantify transport through the **PN** and **DN** after photopolymerization, we performed fluorescence recovery after photobleaching (FRAP) of fluorescently-labeled polymers through the

hydrogels. We compared diffusion of fluorescein isothiocyanate (FITC)-dextran (10 kDa and 70 kDa) against a small molecule fluoresceinamine (347 Da) for the various compositions at two different UV exposure times (0 and 3 min). All polymer sizes diffused at a sufficient rate in all the tested hydrogels in line with the length and time scales of nutrient diffusion and waste exchange involved in culturing encapsulated cells (Figure 3C). The diffusion coefficients (23.7, 6.5 and 2.0 $\mu m^2 s^{-1}$) of all FITC-dextran variants (347 Da, 10 kDa and 70 kDa) in the non-photopolymerized **DN** ((Figure S19A, Table S3) were comparable to the native squaramide-based hydrogels.[22] As the molecular weight of the polymers increased, their diffusion within the hydrogels and fluorescence recovery slowed down. After photopolymerization, the rate of diffusion in **DN** decreased (5.1, 3.5 and 0.7 $\mu m^2 s^{-1}$), but polymer exchange remained unblocked. For a **PN** (7.2 wt%) of similar stiffness to the **DN**, the diffusion of the fluorescent probes decreased further (1.6, 1.1 and 0.2 $\mu m^2 s^{-1}$) pointing at differences in architecture of the two materials (Figures S19B). The recovery half-times for all the measured hydrogels and fluorescent probes (Figure 3D) supported that diffusion slows down after photopolymerization but are within the same range as commonly used 3D culture substrates.[51]

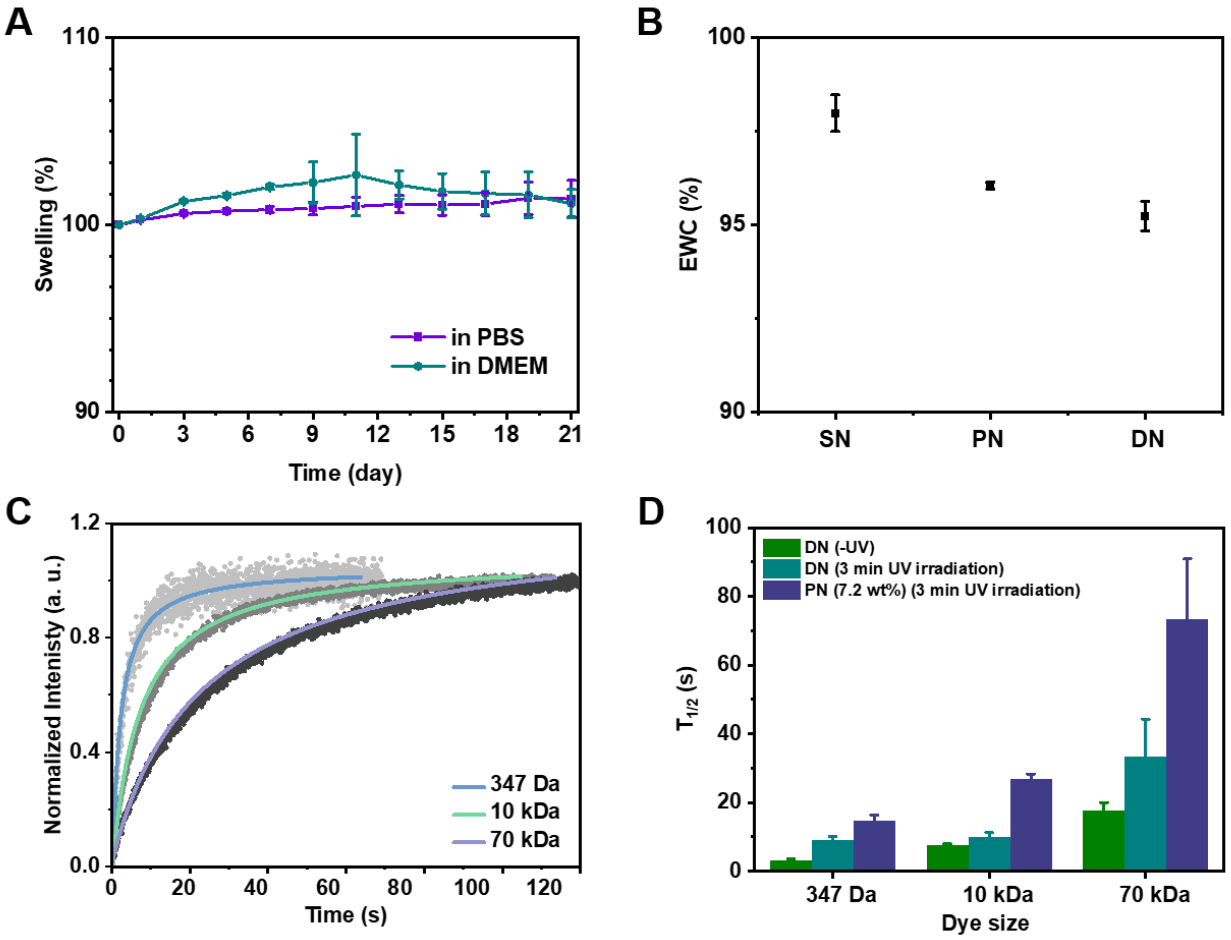

Figure 3. (A) Averaged (N = 3 independent samples) swelling percentage of **DN** hydrogel in PBS and cell culture medium DMEM containing 20% serum at 37 °C. (B) Averaged (N = 3) equilibrium water content (EWC) data for the different hydrogel networks. (C) FRAP characterization of **DN** hydrogel for three fluorescent probes of increasing molecular weight. Grey dots: Normalized intensity in the bleached spot; Lines: diffusion constant fit. (D) Extracted fluorescence recovery half-times of

different hydrogel compositions with and without 3 min UV irradiation using different sized fluorophores. Fluorophores: fluoresceinamine (347 Da); FITC-dextran (10 kDa); and FITC-dextran (70 kDa), mean ± SD, N≥3.

Mechanical loading effect the matrix growth in 3D culture

Cyclic compressive loading of the synthetic hydrogels *in vitro* provides unique opportunities to mimic the biomechanical environment that chondrocytes residing in cartilage are exposed to *in vivo*. Compressive loading of chondrocytes is known to prompt production of cartilaginous matrix proteins when in the physiological range, whereas excessive or hyperphysiological loading can lead to increased catabolic activity and decreased tissue production.[47,52] Therefore, we examined the potential to cyclically compress the chondrocyte-laden **DN** hydrogels using strains from 2-20% that mimic physiological to excessive loads in the joint.

Before performing cyclic loading experiments, we first evaluated the **DN** crosslinking chemistry on the 3D encapsulation of human primary articular chondrocytes (hPACs). We observed high viability (>80% / 5 d) of the hPACs after seeding and crosslinking of the **DN** using UV light (e.g., 0, 1 and 3 min) (Figure S20-S22). We then sought to understand hydrogel stiffness, inclusion of RGD and culture medium composition under free swelling (unloaded) conditions on hPACs viability and ECM production. We probed the effect of increased crosslinking and stiffness of the **DN** on their behaviour by varying the UV exposure times from 0 min (5 Pa) to 3 min (7.8 kPa) with SQ-RGD monomers co-assembled in the supramolecular filaments of the **DN** providing a handle for integrin targeting and chondrocyte mechanosensing of the hydrogels.[47] In the stiffer **DN** hydrogels, the chondrocytes appeared round whereas in softer hydrogels the cells were more spindle-like with less Alcian Blue staining reflecting a reduced sulphated-glycosaminoglycans (s-GAGs) deposition. When maintained in chondrogenic media with TGF-β1, all tested hydrogel conditions showed cartilaginous matrix surrounding the cells denoted by its intense Alcian Blue staining (Figure S23-S25). Hydrogels with greater stiffness (3 min UV, 7.8 kPa) displayed increased s-GAGs deposition as further quantified by the dimethylmethylene blue (DMMB) assay (Figure S26-S27). This finding is consistent with previous reports showing increased matrix deposition by chondrocytes in matrices of comparable stiffness.[53,54] Conversely, the culture of hPACs-laden **DN**s in chondrogenic expansion medium lacking TGF-β1 displayed minimal s-GAGs deposition, highlighting the relevance of both matrix stiffness and chondrogenic stimuli in triggering ECM deposition by hPACs (Figure S28). Subsequent removal of the RGD peptide showed limited effects on s-GAGs deposition suggesting that integrin engagement may not be necessary for matrix production under the tested culture conditions (Figure S27, S29). However, as earlier reports involving PEG-based covalent hydrogels showed that the presence of RGD ligands enhances matrix synthesis when mechanically stimulated,[55] we included them in the **DN** hydrogels to undergo dynamic mechanical loading with chondrocytes.

At this stage, we also exploited the photopolymerization chemistry to mechanically pattern the hydrogels with the aim of mimicking cartilage in development and disease. Alcian Blue staining of the photopatterned hydrogels revealed increased s-GAGs deposition by the hPACs in crosslinked areas (UV exposure 3 min) as compared to areas that were shielded from UV exposure by a striped photomask

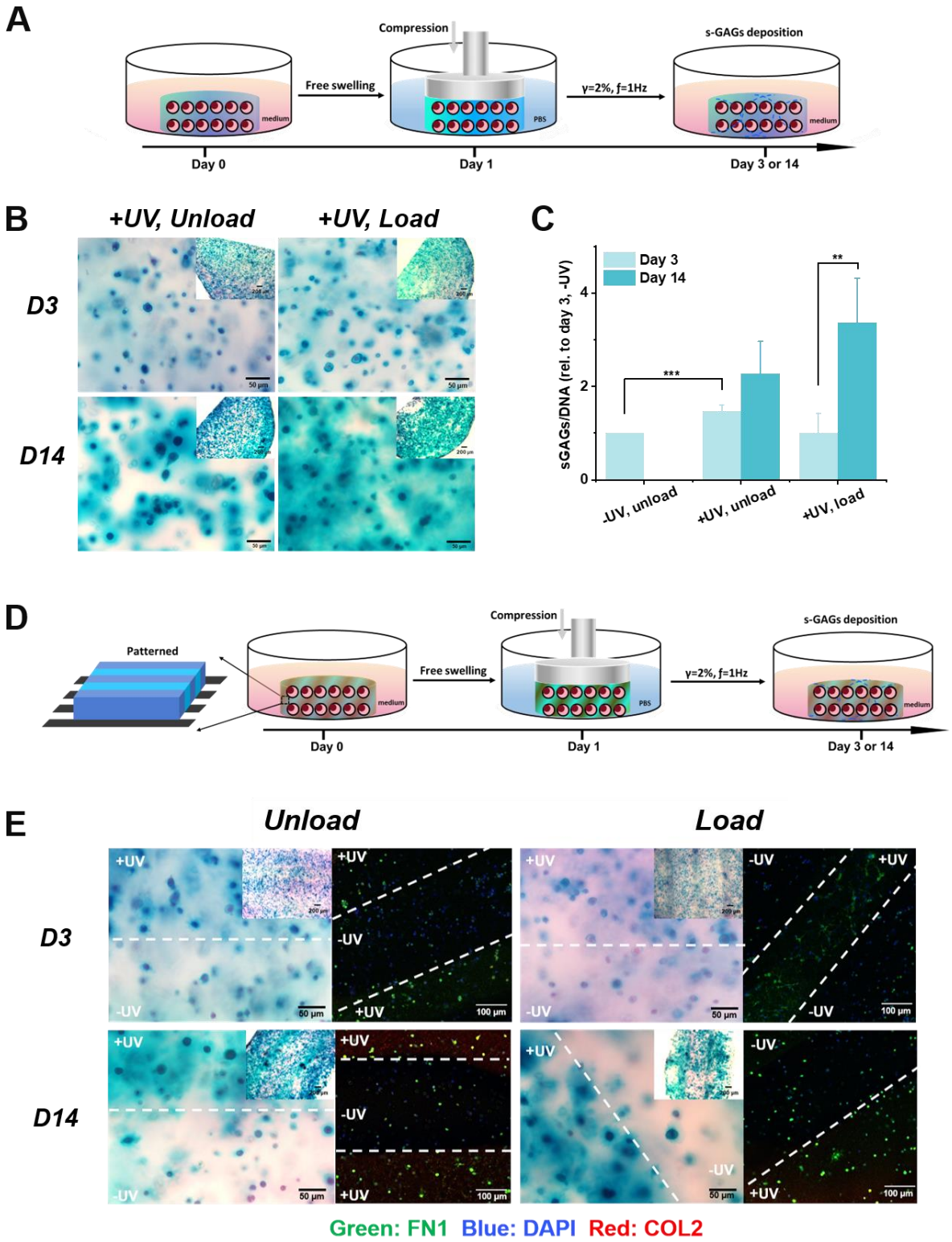

Figure 4. Cyclic compression of hPACs-laden **DN** hydrogels with SQ-RGD. (A) Scheme for dynamic mechanical loading during 3D chondrocyte culture. (B) Representative images for Alcian Blue and nuclear fast red staining after dynamic compression or in free swelling controls. (C) s-GAGs deposition, quantified by DMMB assay and normalized to DNA content, relative to day 3, -UV sample (5 donors total, 3-4 donors per condition). Mean + SEM; *P*-values Ttest: ** <0.01; *** <0.001. (D) Scheme for dynamic mechanical loading on 3D photopatterned hPACs-laden **DN** hydrogels. (E) Representative images for Alcian Blue

and nuclear fast red staining of s-GAGs deposition and overlay for immunofluorescence staining of fibronectin I and collagen II of photopatterned **DN**s after dynamic compression or in free swelling controls.

(Figure S24). To interrogate the capacity of the hPAC-laden **DN** hydrogels (UV exposure 3 min) to withstand physiological and excessive compressive loading, we performed dynamic mechanical compression experiments in a Mach-1 mechanical tester. Soft (2% strain, 1Hz) and heavy-loaded (20% strain, 5Hz) hPACs both displayed increased s-GAGs production compared to free swelling controls after 2 days (Figure S30) pointing out the ability of hydrogel matrices to transfer mechanical forces to the encapsulated cells. We observed little difference between soft and heavy loading regimes on s-GAGs deposition. However, as excessive loading using high strains is known to have detrimental effects on cartilage constructs over longer periods,[52] we selected a soft loading regime to investigate the effect of longer periods (e.g., 14 days) of dynamic compression on chondrocyte behaviour within the hydrogels.

DN hydrogels laden with hPACs were dynamically compressed for 14 days, with an intermediate sample being collected after 3 days of loading (Figure 4A). After 3 days, photocrosslinked samples (3 min UV) showed a consistent and significant increase in s-GAGs deposition when compared to non-crosslinked free swelling controls (Figure 4B-C) (0 min UV; 1.5-fold, P=7.3x10^{-5}). Loaded hydrogel constructs (3 min UV) compared to free swelling controls tend to deposit less s-GAGs at this time point (3 min UV; 0.6-fold, P=7.7x10^{-2}) (Figure 4B-C, S25, S31-S33, Table S4). After 14 days, photocrosslinked samples showed a general trend towards increased s-GAGs deposition compared to day 3 (3 min UV), with a larger increase for loaded (3.4-fold, P=6.3x10^{-3}) samples than for unloaded hydrogels (2.3-fold, P=6x10^{-2}), with some donor variation. Importantly, the s-GAGs deposited after the culture period extend beyond the cell surface, highlighting the contribution of the **SN** mechanics in accommodating deposited matrix despite the increased crosslink density[56] of the **DN** after UV exposure. Notably, photopatterned **DN** hydrogels possessing soft (0 min UV exposure) and stiff (UV exposure 3 min) regions in a single construct sustained dynamic mechanical loading, while the hydrogels without UV exposure were unstable. In line with the unloaded materials, higher levels of s-GAGs deposition can be observed in stiff regions against soft regions (Figure 4D). Pursuant to the previous findings, the differences became more evident after 14 days with more intense s-GAGs staining in the stiffer regions of the **DN**. Immunofluorescence staining of essential components of cartilaginous matrix fibronectin I (green) and collagen II (red) in photopatterned **DN**s showed higher fluorescence intensities in stiff regions in contrast to soft, especially for fibronectin I (Figure 4E), highlighting the contribution of matrix stiffness and culture duration on the production of cartilaginous matrix under dynamic mechanical compression. Taken together, these findings demonstrate the potential of the **DN** hydrogels to preserve chondrogenic characteristics of hPACs while stimulating the production and deposition of cartilaginous matrix under dynamic mechanical loading conditions.

3.3 Conclusion

We herein report a crosslinking strategy involving the photopolymerization of 1,2-dithioloane and norbornene to simultaneously crosslink and prepare supramolecular filament and covalent polymer networks in situ for 3D cell culture with cyclic compressive loading. The simultaneous chain-growth polymerizations of the DT and DT-NB groups provides access to the enhanced stiff and tough mechanical properties in compression not observed in either network on their own after photopolymerization. Strikingly, the use of filamentous supramolecular polymers in the **IPN** and **DN** yields hydrogels that display biomimetic cartilage-like mechanical responses to compression and release. The cytocompatible light-based crosslinking strategy and mechanical characteristics of the material permit cyclic compressive loading of 3D human primary articular chondrocytes for a two-week culture period that is challenging to achieve for single supramolecular networks as they as they unstable on their own and current double network preparation methods lack cytocompatibility for cell encapsulation. Within these hydrogels, the cells produce and deposit nascent matrix proteins that increase on compressive loading during the culture period providing insight into the consequence of **DN**s containing supramolecular filaments on chondrocyte behaviour. Further exploiting this photocrosslinking strategy, we demonstrate the patterning of soft and stiff domains in the hydrogels and their resultant loading in compression leads to contrasting cell responses. Importantly, this latent strategy involving 1,2-dithiolane and norbornene photopolymerization is a valuable addition to the commonly used polymerization chemistries to generate supramolecular and covalent double network hydrogels as it provides opportunities to spatiotemporally augment the mechanics of this biomimetic materials class to study and direct cell behaviour in 3D culture.

Reference

(1) Yamada, K. M.; Doyle, A. D.; Lu, J. Cell–3D Matrix Interactions: Recent Advances and Opportunities. *Trends in Cell Biology*. **2022**, 32 (10), 883.

(2) Qazi, T. H.; Blatchley, M. R.; Davidson, M. D.; Yavitt, F. M.; Cooke, M. E.; Anseth, K. S.; Burdick, J. A. Programming Hydrogels to Probe Spatiotemporal Cell Biology. *Cell Stem Cell* **2022**, *29* (5), 678.

(3) Huang, G.; Li, F.; Zhao, X.; Ma, Y.; Li, Y.; Lin, M.; Jin, G.; Lu, T. J.; Genin, G. M.; Xu, F. Functional and Biomimetic Materials for Engineering of the Three-Dimensional Cell Microenvironment. *Chem Rev* **2017**, *117* (20), 12764.

(4) Rizwan, M.; Ling, C.; Guo, C.; Liu, T.; Jiang, J.-X.; Bear, C. E.; Ogawa, S.; Shoichet, M. S. Viscoelastic Notch Signaling Hydrogel Induces Liver Bile Duct Organoid Growth and Morphogenesis. *Adv Healthc Mater* **2022**, *11* (23), 2200880.

(5) Chaudhuri, O.; Cooper-White, J.; Janmey, P. A.; Mooney, D. J.; Shenoy, V. B. Effects of Extracellular Matrix Viscoelasticity on Cellular Behaviour. *Nature* **2020**, *584* (7822), 535.

(6) Chaudhuri, O.; Gu, L.; Klumpers, D.; Darnell, M.; Bencherif, S. A.; Weaver, J. C.; Huebsch, N.; Lee, H.; Lippens, E.; Duda, G. N.; Mooney, D. J. Hydrogels with Tunable Stress Relaxation Regulate Stem Cell Fate and Activity. *Nat Mater* **2016**, *15* (3), 326.

(7) Storm, C.; Pastore, J. J.; MacKintosh, F. C.; Lubensky, T. C.; Janmey, P. A. Nonlinear Elasticity in Biological Gels. *Nature* **2005**, *435* (7039), 191.

(8) Guimarães, C. F.; Gasperini, L.; Marques, A. P.; Reis, R. L. The Stiffness of Living Tissues and Its Implications for Tissue Engineering. *Nat Rev Mater* **2020**, *5* (5), 351.

(9) Shea, C. A.; Rolfe, R. A.; Murphy, P. The Importance of Foetal Movement for Co-Ordinated Cartilage and Bone Development in Utero. *Bone Joint Res* **2015**, *4* (7), 105.

(10) Lee, H.-Y.; Han, L.; Roughley, P. J.; Grodzinsky, A. J.; Ortiz, C. Age-Related Nanostructural and Nanomechanical Changes of Individual Human Cartilage Aggrecan Monomers and Their Glycosaminoglycan Side Chains. *J Struct Biol* **2013**, *181* (3), 264.

(11) Guilak, F.; Nims, R. J.; Dicks, A.; Wu, C. L.; Meulenbelt, I. Osteoarthritis as a Disease of the Cartilage Pericellular Matrix. *Matrix Biology*. **2018**, *71*, 40.

(12) Hodge, W. A.; Fijan, R. S.; Carlson, K. L.; Burgess, R. G.; Harris, W. H.; Mann, R. W. Contact Pressures in the Human Hip Joint Measured in Vivo. *Proc Natl Acad Sci U S A* **1986**, *83* (9), 2879.

(13) Liu, M.; Zeng, X.; Ma, C.; Yi, H.; Ali, Z.; Mou, X.; Li, S.; Deng, Y.; He, N. Injectable Hydrogels for Cartilage and Bone Tissue Engineering. *Bone Res* **2017**, *5* (1), 17014.

(14) Fox, A. J. S.; Bedi, A.; Rodeo, S. A. The Basic Science of Articular Cartilage: Structure, Composition, and Function. *Sports Health* **2009**, *1* (6), 461.

(15) Antons, J.; Marascio, M. G. M.; Nohava, J.; Martin, R.; Applegate, L. A.; Bourban, P. E.; Pioletti, D. P. Zone-Dependent Mechanical Properties of Human Articular Cartilage Obtained by Indentation Measurements. *Journal of Materials Science: Materials in Medicine*. **2018**, *29* (5), 57.

(16) Wilusz, R. E.; Sanchez-Adams, J.; Guilak, F. The Structure and Function of the Pericellular Matrix of Articular Cartilage. *Matrix Biology*. **2014**, *39*, 25.

(17) Loebel, C.; Kwon, M. Y.; Wang, C.; Han, L.; Mauck, R. L.; Burdick, J. A. Metabolic Labeling to Probe the Spatiotemporal Accumulation of Matrix at the Chondrocyte–Hydrogel Interface. *Adv Funct Mater* **2020**, *30* (44), 1.

(18) Alexopoulos, L. G.; Williams, G. M.; Upton, M. L.; Setton, L. A.; Guilak, F. Osteoarthritic Changes in the Biphasic Mechanical Properties of the Chondrocyte Pericellular Matrix in Articular Cartilage. *J Biomech* **2005**, *38* (3), 509.

(19) Hafeez, S.; Decarli, M. C.; Aldana, A.; Ebrahimi, M.; Ruiter, F. A. A.; Duimel, H.; van Blitterswijk, C.; Pitet, L. M.; Moroni, L.; Baker, M. B. In Situ Covalent Reinforcement of a Benzene-1,3,5-Tricarboxamide Supramolecular Polymer Enables Biomimetic, Tough, and Fibrous Hydrogels and Bioinks. *Adv Mater* **2023**, *35* (35), 2301242.

(20) Kuang, Y.; Yao, Z.-F.; Lim, S.; Ngo, C.; Rocha, M. A.; Fishman, D. A.; Ardoña, H. A. M. Biomimetic Sequence-Templating Approach toward a Multiscale Modulation of Chromogenic Polymer Properties. *Macromolecules* **2023**, *56* (12), 4526.

(21) Zhu, Y.; Shmidov, Y.; Harris, E. A.; Theus, M. H.; Bitton, R.; Matson, J. B. Activating Hidden Signals by Mimicking Cryptic Sites in a Synthetic Extracellular Matrix. *Nat Commun* **2023**, *14* (1), 3635.

(22) Monti, M.; Scarel, E.; Hassanali, A.; Stener, M.; Marchesan, S. Diverging Conformations Guide Dipeptide Self-Assembly into Crystals or Hydrogels. *Chem Comm* **2023**, *59* (73), 10948.

(23) Sikder, A.; Sarkar, J.; Barman, R.; Ghosh, S. Directional Supramolecular Assembly of π-Amphiphiles with Tunable Surface Functionality and Impact on the Antimicrobial Activity. *J Phys Chem B* **2019**, *123* (33), 7169.

(24) Gruschwitz, F. V; Hausig, F.; Schüler, P.; Kimmig, J.; Hoeppener, S.; Pretzel, D.; Schubert, U. S.; Catrouillet, S.; Brendel, J. C. Shear-Thinning and Rapidly Recovering Hydrogels of Polymeric Nanofibers Formed by Supramolecular Self-Assembly. *Chemistry of Materials* **2022**, *34* (5), 2206.

(25) Liu, T.; van den Berk, L.; Wondergem, J. A. J.; Tong, C.; Kwakernaak, M. C.; Braak, B. ter; Heinrich, D.; van de Water, B.; Kieltyka, R. E. Squaramide-Based Supramolecular Materials Drive HepG2 Spheroid Differentiation. *Adv Healthc Mater* **2021**, *10* (11), e2001903.

(26) Diba, M.; Spaans, S.; Hendrikse, S. I. S.; Bastings, M. M. C.; Schotman, M. J. G.; van Sprang, J. F.; Wu, D. J.; Hoeben, F. J. M.; Janssen, H. M.; Dankers, P. Y. W. Engineering the Dynamics of Cell Adhesion Cues in Supramolecular Hydrogels for Facile Control over Cell Encapsulation and Behavior. *Adv Mater* **2021**, *33* (37), 2008111.

(27) Chivers, P. R. A.; Smith, D. K. Shaping and Structuring Supramolecular Gels. *Nat Rev Mater* **2019**, *4* (7), 463.

(28) Tong, C.; Liu, T.; Saez Talens, V.; Noteborn, W. E. M.; Sharp, T. H.; Hendrix, M. M. R. M.; Voets, I. K.; Mummery, C. L.; Orlova, V. V.; Kieltyka, R. E. Squaramide-Based Supramolecular Materials for Three-Dimensional Cell Culture of Human Induced Pluripotent Stem Cells and Their Derivatives. *Biomacromolecules* **2018**, *19* (4), 1091.

(29) Aldana, A. A.; Houben, S.; Moroni, L.; Baker, M. B.; Pitet, L. M. Trends in Double Networks as Bioprintable and Injectable Hydrogel Scaffolds for Tissue Regeneration. *ACS Biomater Sci Eng* **2021**, *7* (9), 4077.

(30) Means, A. K.; Grunlan, M. A. Modern Strategies To Achieve Tissue-Mimetic, Mechanically Robust Hydrogels. *ACS Macro Lett* **2019**, *8* (6), 705.

(31) Gong, J. P. Why Are Double Network Hydrogels so Tough? *Soft Matter* **2010**, *6* (12), 2583.

(32) Gong, J. P.; Katsuyama, Y.; Kurokawa, T.; Osada, Y. Double-Network Hydrogels with Extremely High Mechanical Strength. *Adv Mater* **2003**, *15* (14), 1155.

(33) Yasui, T.; Zheng, Y.; Nakajima, T.; Kamio, E.; Matsuyama, H.; Gong, J. P. Rate-Independent Self-Healing Double Network Hydrogels Using a Thixotropic Sacrificial Network. *Macromolecules* **2022**, *55* (21), 9547.

(34) Sun, W.; Xue, B.; Li, Y.; Qin, M.; Wu, J.; Lu, K.; Wu, J.; Cao, Y.; Jiang, Q.; Wang, W. Polymer-Supramolecular Polymer Double-Network Hydrogel. *Adv Funct Mater* **2016**, *26* (48), 9044.

(35) Wei, Q.; Chang, Y.; Ma, G.; Zhang, W.; Wang, Q.; Hu, Z. One-Pot Preparation of Double Network Hydrogels via Enzyme-Mediated Polymerization and Post-Self-Assembly for Wound Healing. *J Mater Chem B* **2019**, *7*, 6195.

(36) Liang, Y.; Wang, K.; Li, J.; Wang, H.; Xie, X. Q.; Cui, Y.; Zhang, Y.; Wang, M.; Liu, C. Sen. Low-Molecular-Weight Supramolecular-Polymer Double-Network Eutectogels for Self-Adhesive and Bidirectional Sensors. *Adv Funct Mater* **2021**, *31* (45), 2104963.

(37) Bujosa, S.; Doncel-Giménez, A.; Bäumer, N.; Fernández, G.; Ortí, E.; Costa, A.; Rotger, C.; Aragó, J.; Soberats, B. Thermoreversible Polymorph Transitions in Supramolecular Polymers of Hydrogen-Bonded Squaramides. *Angewandte Chemie International Edition* **2022**, *61* (47), e202213345.

(38) Ramos, J.; Arufe, S.; Martin, H.; Rooney, D.; Elmes, R. B. P.; Erxleben, A.; Moreira, R.; Velasco-Torrijos, T. Glycosyl Squaramides, a New Class of Supramolecular Gelators. *Soft Matter* **2020**, *16* (34), 7916.

(39) Saez Talens, V.; Davis, J.; Wu, C. H.; Wen, Z.; Lauria, F.; Gupta, K. B. S. S.; Rudge, R.; Boraghi, M.; Hagemeijer, A.; Trinh, T. T.; Englebienne, P.; Voets, I. K.; Wu, J. I.; Kieltyka, R. E. Thiosquaramide-Based Supramolecular Polymers: Aromaticity Gain in a Switched Mode of Self-Assembly. *J Am Chem Soc* **2020**, *142* (47), 19907.

(40) Tong, C.; Wondergem, J. A. J.; Heinrich, D.; Kieltyka, R. E. Photopatternable, Branched Polymer Hydrogels Based on Linear Macromonomers for 3D Cell Culture Applications. *ACS Macro Lett* **2020**, *9* (6), 882.

(41) Nelson, B. R.; Kirkpatrick, B. E.; Miksch, C. E.; Davidson, M. D.; Skillin, N. P.; Hach, G. K.; Khang, A.; Hummel, S. N.; Fairbanks, B. D.; Burdick, J. A.; Bowman, C. N.; Anseth, K. S. Photoinduced Dithiolane Crosslinking for Multiresponsive Dynamic Hydrogels. *Adv Mater* **2023**, 3, e2211209.

(42) Tong, C.; Wondergem, J. A. J.; van den Brink, M.; Kwakernaak, M. C.; Chen, Y.; Hendrix, M. M. R. M.; Voets, I. K.; Danen, E. H. J.; Le Dévédec, S.; Heinrich, D.; Kieltyka, R. E. Spatial and Temporal Modulation of Cell Instructive Cues in a Filamentous Supramolecular Biomaterial. *ACS Appl Mater Interfaces* **2022**, *14* (15), 17042.

(43) Tong, C.; Wondergem, J. A. J.; van den Brink, M.; Kwakernaak, M. C.; Chen, Y.; Hendrix, M. M. R. M.; Voets, I. K.; Danen, E. H. J.; Le Dévédec, S.; Heinrich, D.; Kieltyka, R. E. Spatial and Temporal Modulation of Cell Instructive Cues in a Filamentous Supramolecular Biomaterial. *ACS Appl Mater Interfaces* **2022**, *14* (15), 17042.

(44) Hall, M. S.; Alisafaei, F.; Feng, X.; Hui, C.-Y.; Shenoy, V. B.; Wu, M.; Weitz, D. A. Fibrous Nonlinear Elasticity Enables Positive Mechanical Feedback between Cells and ECMs. *Proceedings of the National Academy of Science* **2016**, *113* (49), 14043.

(45) Rudnicki, M. S.; Cirka, H. A.; Aghvami, M.; Sander, E. A.; Wen, Q.; Billiar, K. L. Nonlinear Strain Stiffening Is Not Sufficient to Explain How Far Cells Can Feel on Fibrous Protein Gels. *Biophys J* **2013**, *105* (1), 11.

(46) Broedersz, C. P.; Kasza, K. E.; Jawerth, L. M.; Münster, S.; Weitz, D. A.; MacKintosh, F. C. Measurement of Nonlinear Rheology of Cross-Linked Biopolymer Gels. *Soft Matter* **2010**, *6* (17), 4120.

(47) Sanchez-Adams, J.; Leddy, H. A.; McNulty, A. L.; O'Conor, C. J.; Guilak, F. The Mechanobiology of Articular Cartilage: Bearing the Burden of Osteoarthritis. *Curr Rheumatol Rep* **2014**, *16* (10), 451.

(48) Shao, X.; Goh, J. C. H.; Hutmacher, D. W.; Lee, E. H.; Zigang, G. Repair of Large Articular Osteochondral Defects Using Hybrid Scaffolds and Bone Marrow-Derived Mesenchymal Stem Cells in a Rabbit Model. *Tissue Eng* **2006**, *12* (6), 1539.

(49) Li, L. P.; Herzog, W.; Korhonen, R. K.; Jurvelin, J. S. The Role of Viscoelasticity of Collagen Fibers in Articular Cartilage: Axial Tension versus Compression. *Med Eng Phys* **2005**, *27* (1), 51.

(50) Harrass, K.; Krüger, R.; Möller, M.; Albrecht, K.; Groll, J. Mechanically Strong Hydrogels with Reversible Behaviour under Cyclic Compression with MPa Loading. *Soft Matter* **2013**, *9* (10), 2869.

(51) Urciuolo, A.; Giobbe, G. G.; Dong, Y.; Michielin, F.; Brandolino, L.; Magnussen, M.; Gagliano, O.; Selmin, G.; Scattolini, V.; Raffa, P.; Caccin, P.; Shibuya, S.; Scaglioni, D.; Wang, X.; Qu, J.; Nikolic, M.; Montagner, M.; Galea,

G. L.; Clevers, H.; Giomo, M.; De Coppi, P.; Elvassore, N. Hydrogel-in-Hydrogel Live Bioprinting for Guidance and Control of Organoids and Organotypic Cultures. *Nat Commun* **2023**, *14* (1), 3128.
(52) Houtman, E.; Tuerlings, M.; Riechelman, J.; Suchiman, E. H. E. D.; van der Wal, R. J. P.; Nelissen, R. G. H. H.; Mei, H.; Ramos, Y. F. M.; Coutinho de Almeida, R.; Meulenbelt, I. Elucidating Mechano-Pathology of Osteoarthritis: Transcriptome-Wide Differences in Mechanically Stressed Aged Human Cartilage Explants. *Arthritis Res Ther* **2021**, *23* (1), 215.
(53) Tan, Y.; Huang, H.; Ayers, D. C.; Song, J. Modulating Viscoelasticity, Stiffness, and Degradation of Synthetic Cellular Niches via Stoichiometric Tuning of Covalent versus Dynamic Noncovalent Cross-Linking. *ACS Cent Sci* **2018**, *4* (8), 971.
(54) Lee, H.; Gu, L.; Mooney, D. J.; Levenston, M. E.; Chaudhuri, O. Mechanical Confinement Regulates Cartilage Matrix Formation by Chondrocytes. *Nat Mater* **2017**, *16* (12), 1243.
(55) Villanueva, I.; Weigel, C. A.; Bryant, S. J. Cell–Matrix Interactions and Dynamic Mechanical Loading Influence Chondrocyte Gene Expression and Bioactivity in PEG-RGD Hydrogels. *Acta Biomater* **2009**, *5* (8), 2832.
(56) Loebel, C.; Kwon, M. Y.; Wang, C.; Han, L.; Mauck, R. L.; Burdick, J. A. Metabolic Labeling to Probe the Spatiotemporal Accumulation of Matrix at the Chondrocyte–Hydrogel Interface. *Adv Funct Mater* **2020**, *30* (44), 1909802.

Supporting information

3.1. Materials and methods

Materials

All chemicals and reagents for synthesis were obtained from Sigma Aldrich and directly used without further purification. Deuterated solvent for NMR experiments were obtained from Euriso-top. Water was deionized before use. Lacey carbon 200 mesh grids were purchased from Electron Microscopy Sciences. Dulbecco's phosphate buffered saline (DPBS, pH=7.4) was purchased from Sigma Aldrich. Dulbecco's modified Eagle medium (DMEM) was received from Gibco, Life Technologies. Fetal bovine serum (FBS) was procured from Biowest. The antibiotics penicillin and streptomycin were purchased from Gibco. Collagenase Type I was obtained from Worthington Biochemical Corporation. Calcein AM, Propidium Iodide (PI), Alcian Blue 8-GX, Nuclear fast red-aluminum sulfate, and normal goat serum were purchased from Sigma Aldrich. The goat anti-mouse Alexa Fluor 647 and goat anti-rabbit Alexa Fluor 488 were obtained from Abcam. µ-Slide 15 Well 3D chambered coverplates were purchased from Ibidi. Polydimethylsiloxane (PDMS) (Sylgard 184 Silicon Elastomer Kit, Dow Corning), silicon wafers and fluorosilane (1H,1H,2H,2H-perfluorooctyltrichlorosilane) from VWR chemicals, Siegert Wafers and Sigma-Aldrich, respectively. Monomers SQ, SQ-DT, SQ-RGD, PEGdiNB (6 kDa), and PEGdiDT (6 kDa) were synthesized as previously described.[1] All compounds were stored at -20°C prior to further use.

Methods

^{1}H-NMR and ^{13}C-NMR spectra were collected at room temperature (RT) on a Bruker DMX-400 (400 MHz). Oscillatory rheology experiments were performed at RT on a Discovery Hybrid Rheometer (DHR-2) from TA Instruments on a quartz lower plate (20 mm) and a aluminum upper plate (20 mm) using a fixed gap of 300 µm. UV light (λ = 320-500 nm, primary peak: 365 nm) was applied through an Omnicure S2000 high-pressure mercury light source from Excelitas connected to the rheometer through a UV light guide accessory (5 mm diameter). The UV intensity was calibrated using a Silverline radiometer sensor (20 mm) designed for the quartz parallel plate. Compression experiments were performed on this setup using aluminum upper plates with different diameters (8 mm and 20 mm) at a fixed gap of 1.2 mm and a maximum axial force of 50 N. Cryogenic electron microscope (cryo-EM) images were taken on a Talos L120C operating at 120 kV, samples were plunge frozen on a Vitrobot Mark IV, both from Thermo Fisher Scientific. Scanning electron micrographs (SEM) were collected on a JSM-7600F microscope from JEOL under high vacuum with an acceleration voltage of 2.0 kV. FRAP experiments were performed on an Eclipse Ti confocal microscope from Nikon Instruments, with a Yokogawa confocal spinning disk unit operated at 10,000 rpm, equipped with a Plan Fluor objective, and recorded with an Andor iXon Ultra 897 high speed EM-CCD camera. Human primary articular chondrocytes (hPACs) were counted on NucleoCounter NC-200 from ChemoMetec. Images for cell viability assessment in 3D cultures were captured on a LSM 710 confocal laser scanning microscope from Zeiss. Compressive mechanical loading of the 3D cell cultures was performed continuously in cycles on a MACH-1 mechanical tester from Biomomentum at RT. Confocal fluorescent images of

immunostained 3D cell cultures were acquired on a Stellaris 8 confocal laser scanning microscope from Leica with a supercontinuum white light laser (440-790 nm) and Power HyD detectors. Alcian Blue stained images were taken in brightfield on a light microscope from Olympus. The DNA concentration extracted from the hydrogels was measured on a NanoDrop from Thermo Scientific. A microplate reader from BioTek Synergy HT was used to quantitate sulfated glycosaminoglycan (s-GAGs) content through the dimethylmethylene blue (DMMB) assay using measured absorbance values at 525 and 595 nm. A benchtop LED light (~10 mW/cm², 375 nm) was employed to initiate crosslinking in all other samples except for the ones on the rheometer.

Hydrogel preparation

Preparation of supramolecular hydrogels (SN)

The preparation of the supramolecular hydrogels with different molar ratios of SQ-DT and SQ-RGD was executed according to an earlier published protocol[1b]. Briefly, SQ, SQ-DT and SQ-RGD stock solutions (10.0 mM) were prepared by adding dimethyl sulfoxide (DMSO) to each component with 2 min of vortexing. To acquire **SN** hydrogels with different total monomer concentrations or varied SQ-DT and SQ-RGD molar percentages, a pre-determined volume of the DMSO stock solutions containing the necessary components were pipetted into a glass vial (2 mL) followed by 30 s of gentle vortexing to obtain homogeneous solutions. The DMSO was then removed using a stream of N_2 overnight. Afterwards, the required volume of PBS was added to reach the desired concentration and sonicated in an ultrasonic ice-water bath for 10 to 30 min (0 °C - 4 °C) yielding a clear solution; the necessary sonication time depended on the monomer concentration and the power of sonication bath. The clear solutions were then incubated for 15 min in a 37 °C oven to form gels. The transparent **SN** hydrogels were further equilibrated at RT overnight and photopolymerized prior to other measurements. The **SN** hydrogel is composed largely of the native monomer SQ and SQ-DT and can include SQ-RGD depending on the experiment.

Preparation of PEG-based hydrogels (PN)

PEG-based polymeric hydrogels (**PN**) were prepared according to an earlier published protocol.[1a] The preparation of a **PN** with 3.6 wt% PEG network, containing 1.8 wt% PEGdiDT (6 kDa), 1.8 wt% PEGdiNB (6 kDa) and 1 mM photoinitiator lithium phenyl-2,4,6-trimethylbenzoylphosphinate (LAP) is used here as an example. First, stock solutions of PEGdiDT (3.9 wt%), PEGdiNB (3.9 wt%), and LAP (15 mM) were prepared separately by dissolving each component in PBS in a vial (2 mL) with 30 s of vortexing. Hereafter, PEGdiDT (70 µL), PEGdiNB (70 µL) and LAP (10 µL) stock solutions were pipetted into a new vial (2 mL) followed with another 30 s of vortexing to obtain a homogeneous precursor solution (150 µL). The volume ratio of PEGdiDT, PEGdiNB and LAP was always kept at 7:7:1 and were photopolymerized prior to other measurements.

Preparation of hybrid hydrogels (IPN and DN)

A simple one-pot strategy was used to prepare the **IPN** and **DN** hydrogels prior to photopolymerization. For example, to obtain the **IPN** (3.6 wt% **PN** and 5 mM **SN** (SQ)) and **DN** (3.6 wt% **PN** and 5 mM **SN** (SQ with 10 mol% SQ-DT)) hydrogels, pre-determined volumes of the PEG stock solutions (PEGdiDT: 3.9 wt%, PEGdiNB: 3.9 wt%) were dissolved in water, pipetted into (PEGdiDT: 70

µL and PEGdiNB: 70 µL) a new vial (2 mL) and gently pipetted up and down (10 times). The PEGdiDT/PEGdiNB solution was lyophilized overnight to obtain a white solid. Aliquots of PBS (20 µL) and LAP stock solutions (15mM, 10µL) were added to re-dissolve the above PEGdiDT/PEGdiNB solid. Then, the **SN** (120 µL, 6.25 mM (SQ) or 6.25 mM (SQ with 10 mol% SQ-DT)) after sonication in an ice bath was kept on ice and pipetted into the polymeric stock solution **PEG** (30 µL), followed by gentle pipetting up and down (10 times) to mix both polymers (150 µL). The obtained supramolecular and covalent polymer mixture was equilibrated at 37°C for 15 min to trigger supramolecular hydrogel formation and was stored at RT overnight. The preparation of all other **IPN** and **DN** hydrogels before photopolymerization followed this procedure. Finally, various UV exposure times (1 - 10 min) were used to crosslink the hybrid hydrogels (Figure S1). During this UV step, the covalent polymer network, and crosslinks in and with the supramolecular network are made simultaneously. Parameters such as total supramolecular monomer concentration, the molar percentage of SQ-DT in the supramolecular mixture, the total polymer concentration of PEGdiDT/PEGdiNB and UV exposure time were examined on the **DN** properties.

Table S1. Plateau storage moduli of the various hydrogels (**SN**, **PN**, **IPN** and **DN**) with different compositions (e.g., supramolecular monomer concentration, SQ-DT mol% in **SN**, total polymer concentration) and UV exposure times. Averaged storage moduli are presented (N ≥ 3).

System name	Composition				UV exposure time (min)	Storage modulus before UV exposure (Pa)	Storage modulus after UV exposure (Pa)
	SN (mM)	**SQ** (mol%)	**SQ-DT** (mol%)	**PEG** (wt%)			
SN	5.0	100	0	-	10	5 ± 1	8 ± 1
	5.0	99	1	-	10	9 ± 3	196 ±114
	5.0	95	5	-	10	44 ± 10	1392 ± 541
	5.0	90	10	-	10	91 ± 15	2816 ± 519
PN	-	-	-	1.8	10	S	VS
	-	-	-	2.4	10	S	177 ± 32
	-	-	-	3.6	10	S	1284 ± 56
IPN	5.0	100	-	1.8	10	VS	473 ± 118
	5.0	100	-	1.8	3	VS	239 ± 90
	5.0	100	-	2.4	10	VS	1093 ± 283
	5.0	100	-	3.6	10	VS	3704 ± 243
	5.0	100	-	3.6	3	VS	4193 ± 2351
DN	5.0	99	1	3.6	10	VS	7833 ± 583
	10.0	90	10	3.6	10	71 ± 2	11606 ± 553
	5.0	90	10	1.8	10	10 ± 8	3028 ± 129
	5.0	90	10	1.8	3	22 ± 9	2182 ± 350
	5.0	90	10	2.4	10	15 ± 12	4994 ± 370
	5.0	90	10	3.6	10	16 ± 7	10391 ± 541
	5.0	90	10	3.6	3	10 ± 5	9371 ± 213
	5.0	90	10	4.8	10	10 ± 10	11815 ± 351
	5.0	90	10	7.2	10	4 ± 2	17307 ± 4273
	5.0	90	10	9.6	10	VS	21072 ± 5071

[S]: Solution; [VS]: Viscous Solution.

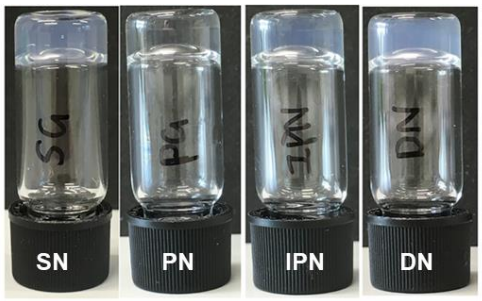

Figure S1. Gel inversion experiments of hydrogels after 3 min UV exposure using a LED at RT: **SN** (5 mM SQ with 10 mol% SQ-DT); **PN** (3.6 wt% PEG); **IPN** (3.6 wt% **PN** and 5 mM **SN** (SQ)); and **DN** (3.6 wt% **PN** and 5 mM **SN** (SQ with 10 mol% SQ-DT).

Oscillatory Rheology

The prepared hydrogels (**SN**, **IPN**, **DN**) (110 µL) and **PN** solutions (104 µL) prior to photopolymerization were gently pipetted on to the quartz plate of the rheometer. The upper plate was then lowered to a gap distance of 300 µm. The samples were then exposed to UV light for 10 min. Time sweeps (frequency = 1.0 Hz, strain = 0.05%), frequency sweeps from 0.01 to 10 Hz (strain = 0.05%), and strain sweeps from 0.01 to 1000% (frequency = 1.0 Hz) were collected. The self-recovery properties were measured using a step-strain experiment. After the above strain experiment, a time-dependent recovery measurement was applied at low strain (0.05%) for 300 s. Once the storage modulus reached its plateau, a high strain (500%) was applied for 300 s. The application of high- and low strain in an alternating fashion was repeated for two cycles. The recovery rate[2] of the hydrogels were calculated by collecting the storage modulus before (G_0') and after (G_t') the large strain was applied. The recovery rate (%) was determined as following: recovery rate (%) = (G_t'/G_0')*100%.

The strain stiffening behaviour of hydrogels with different UV exposure times were evaluated in the rheometer applying the pre-stress method. The hyhdrogels were subjected to a constant pre-stress (from 0.5 Pa) upon which a small oscillatory stress was superimposed, $\delta\sigma(t) = \delta\sigma e^{iwt}$, up to a maximum of 10% of the prestress at a fixed frequency (1.0 Hz). The stress relaxation behaviour of the hydrogels with different UV exposure times were measured at a constant strain of 10%. The stress (σ) was normalized to the average stress (σ_0) during the first two seconds at the beginning of data collection. The creep and recovery behavior of the hydrogels with different UV exposure times were performed after a time sweep of 1200 s with a fixed strain (0.01%) and frequency (1.0 Hz). The strain in response to a constant stress (1 Pa for **DN** hydrogel with 0 min UV exposure, 0.3 kPa for **DN** hydrogel with 1 min and 3 min photoirradiation) was measured for 3600 s, after which the stress was removed, and the strain was measured for another 5000 s. Water was added on top of the cover surrounding the upper plate to reduce drying of the hydrogels during the measurement.

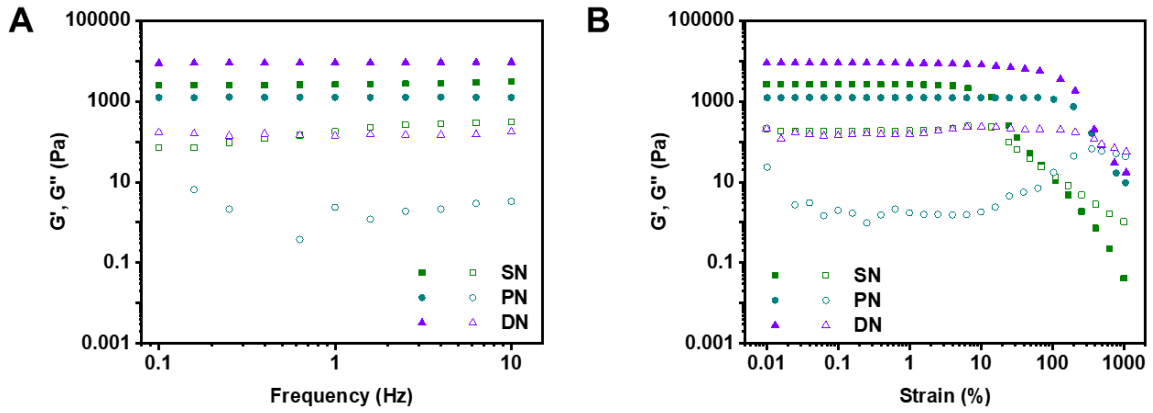

Figure S2. Averaged (N = 3) (A) frequency (0.1-10 Hz) and (B) strain (0.01-1000%) sweeps of hydrogels at RT: **SN** (5 mM (SQ with 10 mol% SQ-DT), **PN** (3.6 wt%) and **DN** (3.6 wt% **PN** network and 5 mM **SN** (SQ with 10% mol SQ-DT)). The frequency sweep experiment was performed at a fixed strain (0.05%) and the strain experiment was collected at fixed frequency (1.0 Hz).

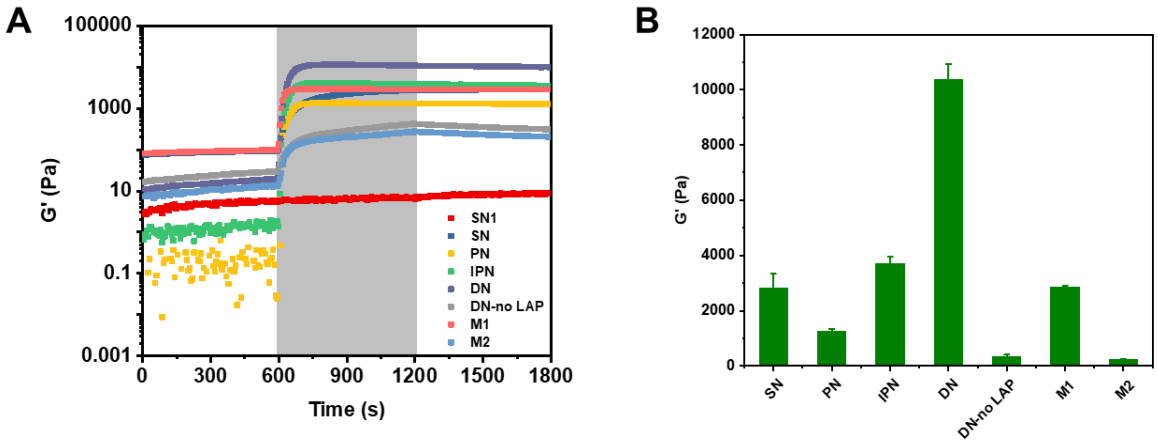

Figure S3. (A) Averaged (N = 3) time sweep experiment and (B) Plateau storage moduli of the various hydrogels after 10 min UV exposure measured at a fixed frequency (1.0 Hz) and strain (0.05%) at RT: (1) **SN** (5 mM (SQ with 10 mol% SQ-DT)); (2) **SN1** (5 mM SQ); (2) **PN** (3.6 wt%); (3) **IPN** (3.6 wt% **PN** network and 5 mM **SN** (SQ)); (4) **DN** (3.6 wt% **PN** network and 5 mM **SN** (SQ with 10 mol% SQ-DT)); (5) **DN-no LAP** (3.6 wt% **PN** network and 5 mM **SN** (SQ with 10 mol% SQ-DT)) (6) **M1** (5 mM **SN** (SQ with 10 mol% SQ-DT) and 1.8 wt% PEGdiNB with 1.0 mM LAP); and (7) **M2** (5 mM **SN** (SQ with 10 mol% SQ-DT) and 1.8 wt% PEGdiDT with 1.0 mM LAP). Grey regions indicate UV exposure. The standard deviation was calculated according to the average of repeat independent measurements (N ≥

3).

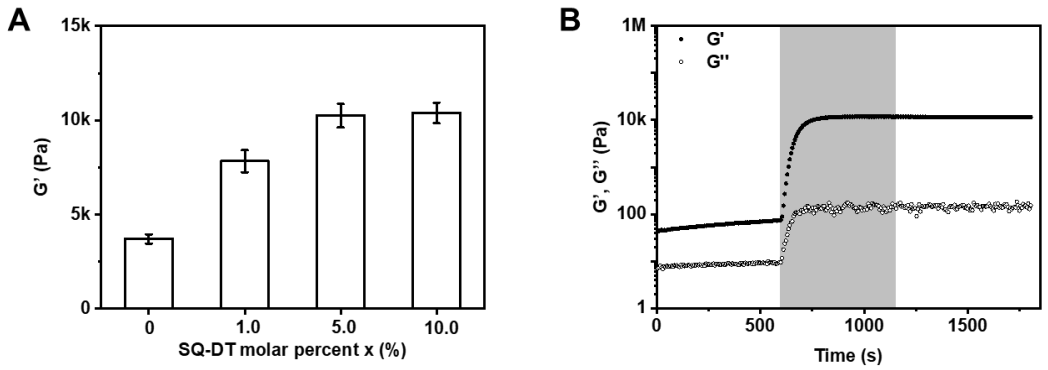

Figure S4. (A) Plateau storage moduli of **DN** (3.6 wt% **PN** network and 5 mM **SN** (SQ with 0-10 mol% SQ-DT)), (B) Averaged (N = 2) time sweep experiment of **DN** (3.6 wt% **PN** network and 10 mM **SN** with 5 mol% SQ-DT) with 10 min UV exposure. The measurement was performed under fixed frequency (1.0 Hz) and strain (0.05%). Grey regions indicate UV exposure. The standard deviation was calculated according to the average of repeat independent measurements (N ≥ 3).

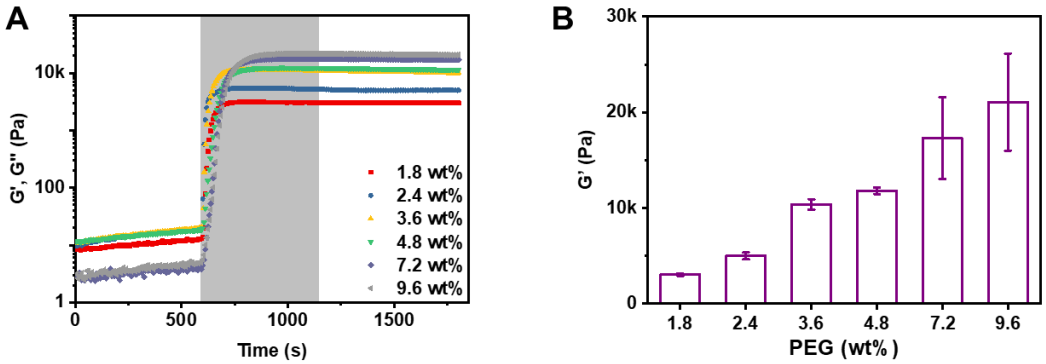

Figure S5. (A) Averaged (N = 3) time sweep experiment and (B) the plateau storage moduli of various **DN** with 5 mM **SN** (SQ with 10 mol% SQ-DT) and different **PN** concentrations after 10 min UV exposure. The measurement was performed under fixed frequency (1.0 Hz) and strain (0.05%). Grey regions indicate UV exposure. The standard deviation was calculated according to the average of repeat independent measurements (N ≥ 3).

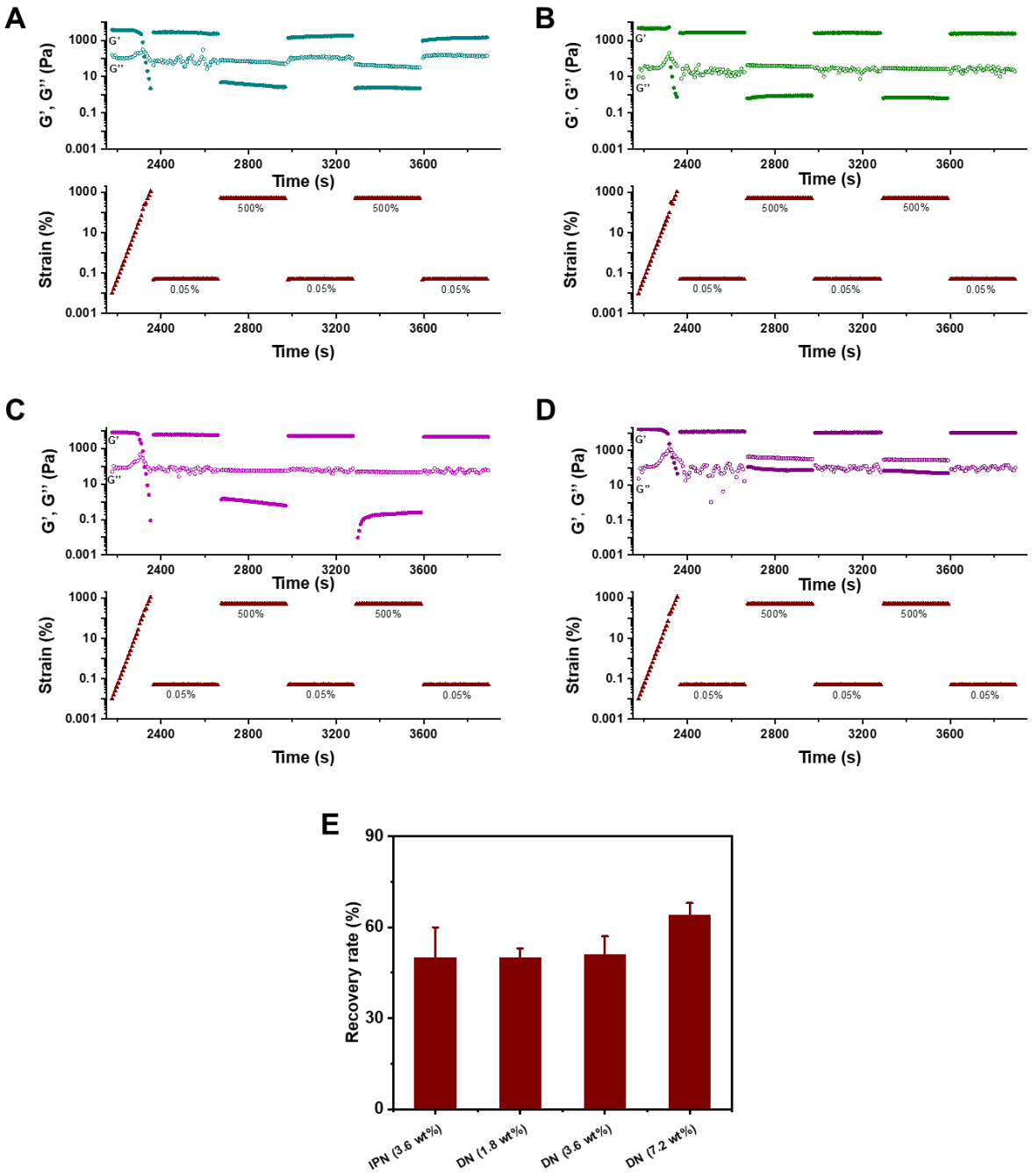

Figure S6. Averaged (N = 3) step-strain experiments of the various **IPN** and **DN** hydrogels: (A) **IPN** (3.6 wt% **PN** network and 5 mM **SN** (SQ)) (B) **DN** (1.8 wt% **PN** network and 5 mM **SN** (SQ with 10 mol% SQ-DT)). (C) **DN** (3.6 wt% **PN** network and 5 mM **SN** (SQ with 10 mol% SQ-DT)). (D) **DN** (7.2 wt% **PN** network and 5 mM **SN** (SQ with 10 mol% SQ-DT)) (E) The averaged (N = 3) storage recovery rate of **IPN** hydrogels (5 mM **SN** (SQ)) and various **DN** hydrogels (5 mM **SN** (SQ with 10 mol% SQ-DT) with different **PN** concentrations.

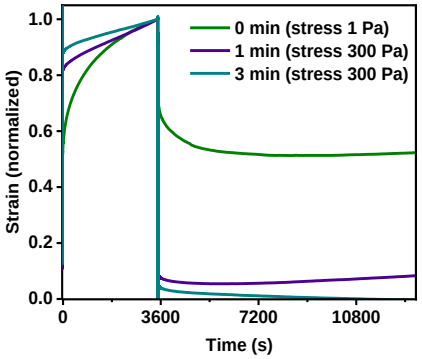

Figure S7. Creep and recovery test of **DN** (3.6 wt% **PN** network and 5 mM **SN** (SQ with 10 mol% SQ-DT) after different UV exposure times (0 min, 1 min and 3 min). A constant stress of 1 Pa was applied to the sample with 0 min UV exposure, whereas 0.3 kPa was applied to the samples with 1 min and 3 min.

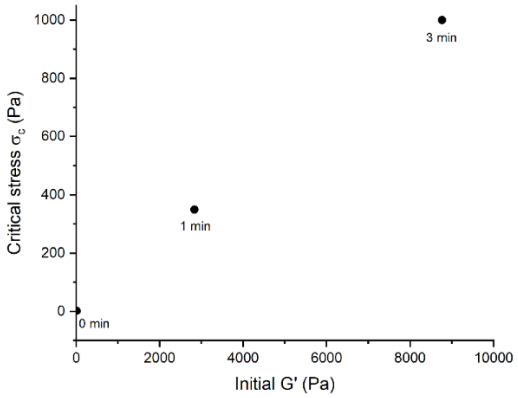

Figure S8. Critical stress (σ_c) as a function of initial storage modulus of **DN** hydrogels (3.6 wt% **PN** network and 5 mM **SN** (SQ with 10 mol% SQ-DT)) with various UV exposure times (0 min, 1 min and 3 min) at RT.

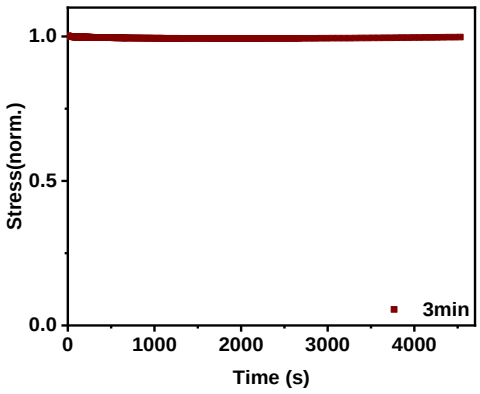

Figure S9. Stress relaxation behavior (10% strain) of the **PN** (7.2 wt%, 3 min).

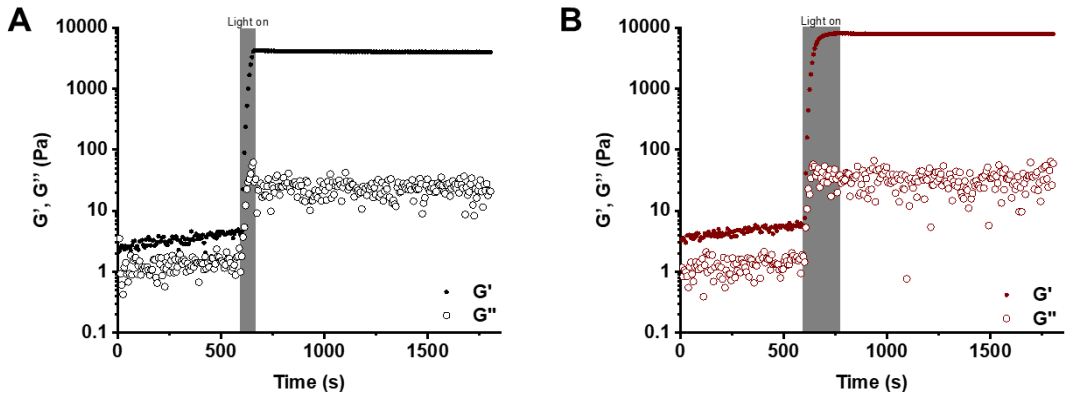

Figure S10. Averaged (N = 2) time sweep experiment of **DN** hydrogels (3.6 wt% **PN** network and 5 mM **SN** (SQ with 10 mol% SQ-DT and 5 mol% SQ-RGD)) with different UV exposure times measured at fixed frequency (1.0 Hz) and strain (0.05%) at RT: (A) 1 min and (B) 3 min. Grey regions indicate UV exposure.

Compression test

The prepared samples before photopolymerization (20 mm geometry: 400 µL; 8 mm geometry: 75 µL) were gently pipetted on to the quartz plate of the rheometer and the upper plate was lowered to 1.2 mm. The samples were equilibrated for 5 min before data collection. After a time sweep experiment of 60 s, the samples were UV exposed for 10 min to reach a plateau in storage modulus. PBS was carefully placed around the samples immediately after the samples were fully crosslinked to prevent evaporation during the measuring period. Afterwards, an axial compression test was set up to compress the sample ~80 % of its initial height (0.2 mm gap) at a rate of 10 µm/s. The compression modulus was calculated from the slope of the linear region of the compressive stress-strain curve (**SN**: strain = 0-2%, other samples: strain = 5-10%). Cyclic axial compression (loading and unloading) tests were performed on the UV exposed hydrogels by compressing them to 2% of their initial heights at a rate of 10 µm/s and then removing the load. The next compression cycle was started immediately after release of the load. Energy dissipation within the gels were probed under the same conditions as the cyclic axial compression test using increasing strain percentages from 5% to 50%. Compressive stress relaxation test on the UV exposed hydrogels were performed starting with applying 5% strain to the sample at a rate of 50 µm/s. The hydrogels were compressed for 10 min at this strain percentage and stress relaxation was monitored. Steps of 5% strain were then applied to the material in sequence for the same amount of time until a maximum of 20% strain was achieved. The curves were plotted until the hydrogel fractured.

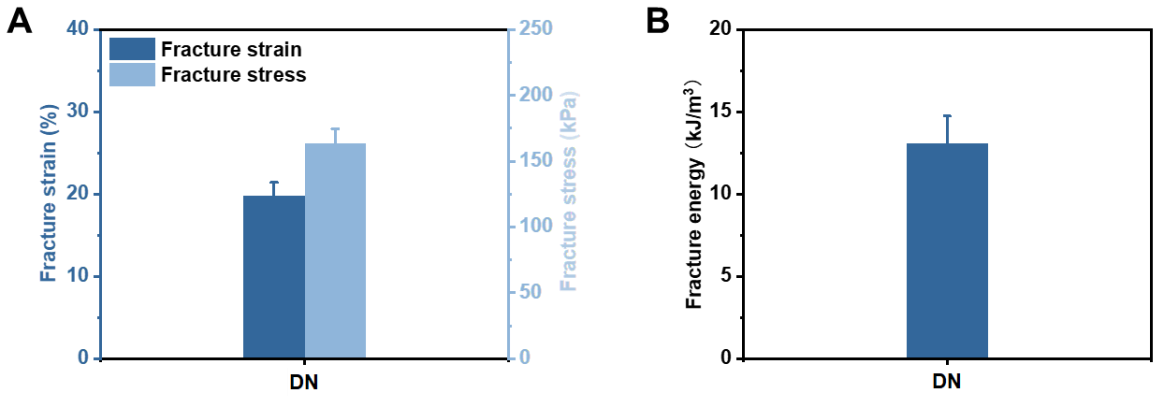

Figure S11. Mechanical properties of **DN** (3.6 wt% **PN** and 5 mM **SN** (SQ with 10 mol% SQ-DT) at fracture: (A) Compressive fracture strain and compressive fracture stress, (B) Fracture energy. The sample was compressed at a speed of 10 μm/s. Mean ± SD, N≥3.

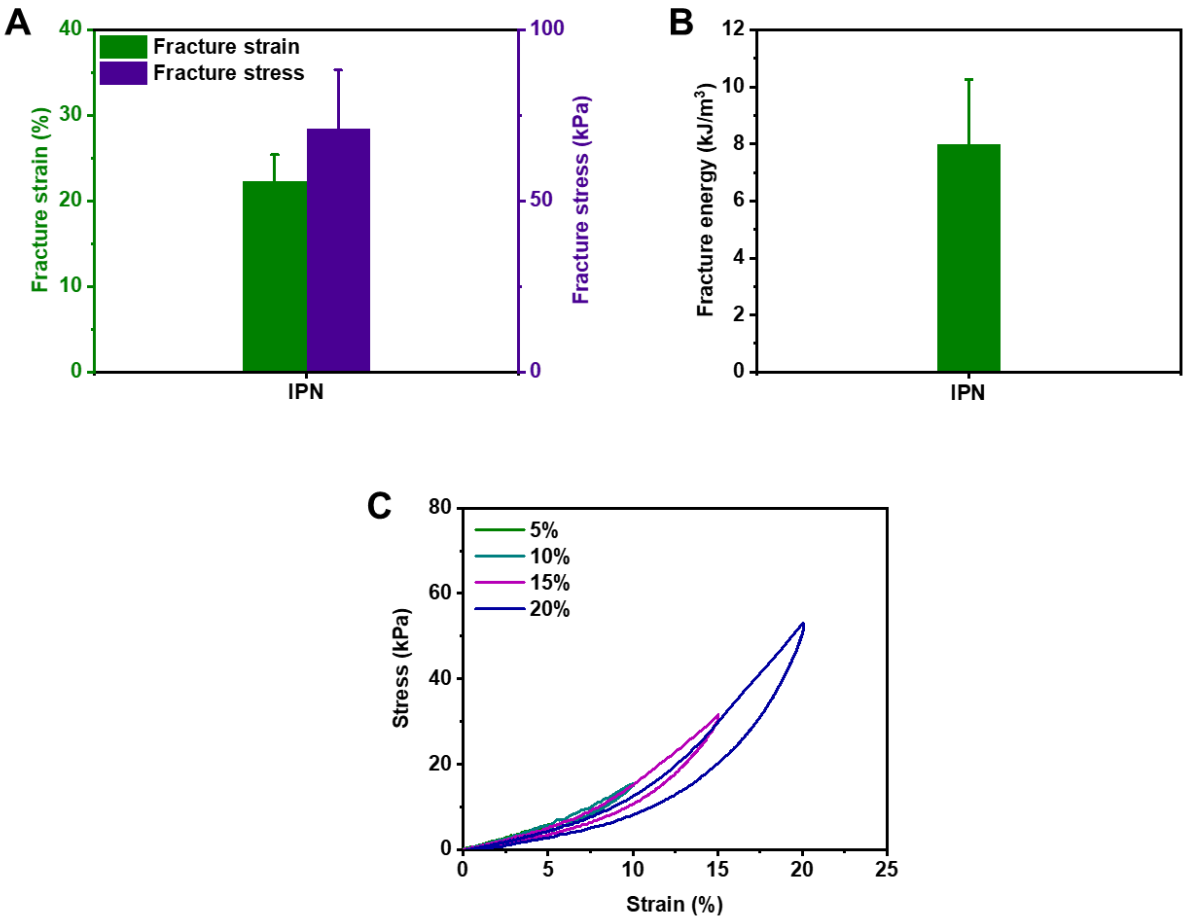

Figure S12. Mechanical properties of **IPN** hydrogels (3.6 wt% **PN** network and 5 mM **SN** (SQ)) at fracture: (A) Compressive fracture strain and compressive fracture stress, (B) Fracture energy. (C) Uniaxial compression cycles at different maximum strains. The sample was compressed at a speed of 10 μm/s. Mean ± SD, N≥3.

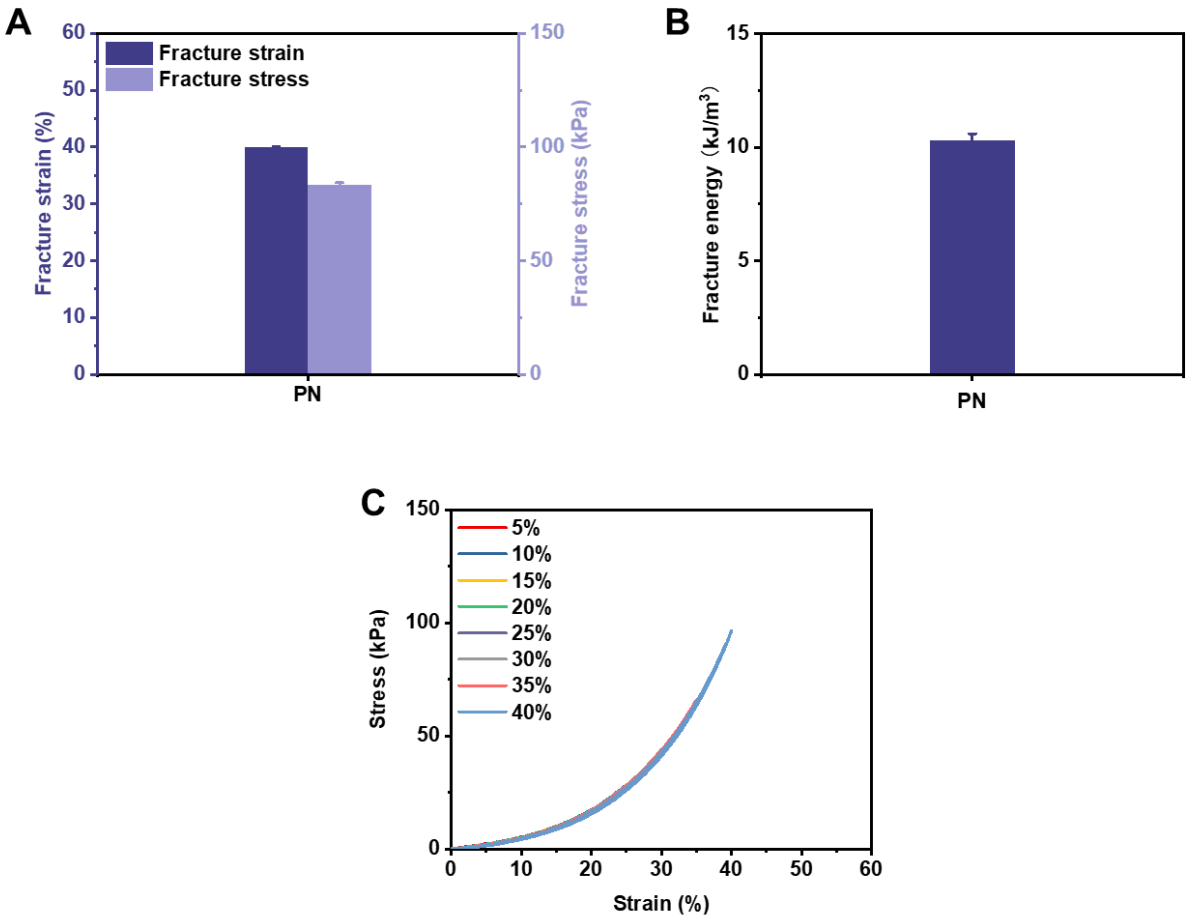

Figure S13. Mechanical properties of **PN** (3.6 wt% PEG) at fracture: (A) Compressive fracture strain and compressive fracture stress, (B) Fracture energy. (C) Uniaxial compression cycles at different maximum strains. The sample was compressed at a speed of 10 μm/s. Mean ± SD, N≥3.

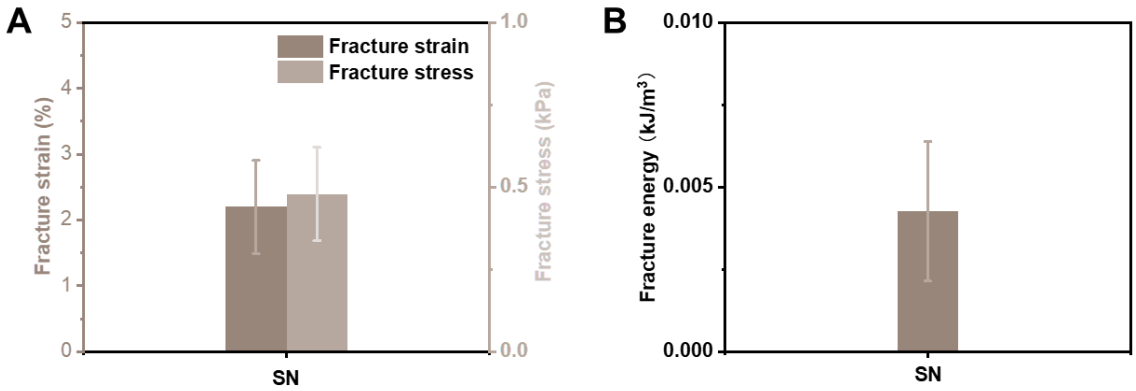

Figure S14. Mechanical properties of **SN** hydrogels (5 mM SQ with 10 mol% SQ-DT)) at fracture: (A) Compressive fracture strain and compressive fracture stress, (B) Fracture energy. The sample was compressed at a speed of 10 μm/s. Mean ± SD, N≥3.

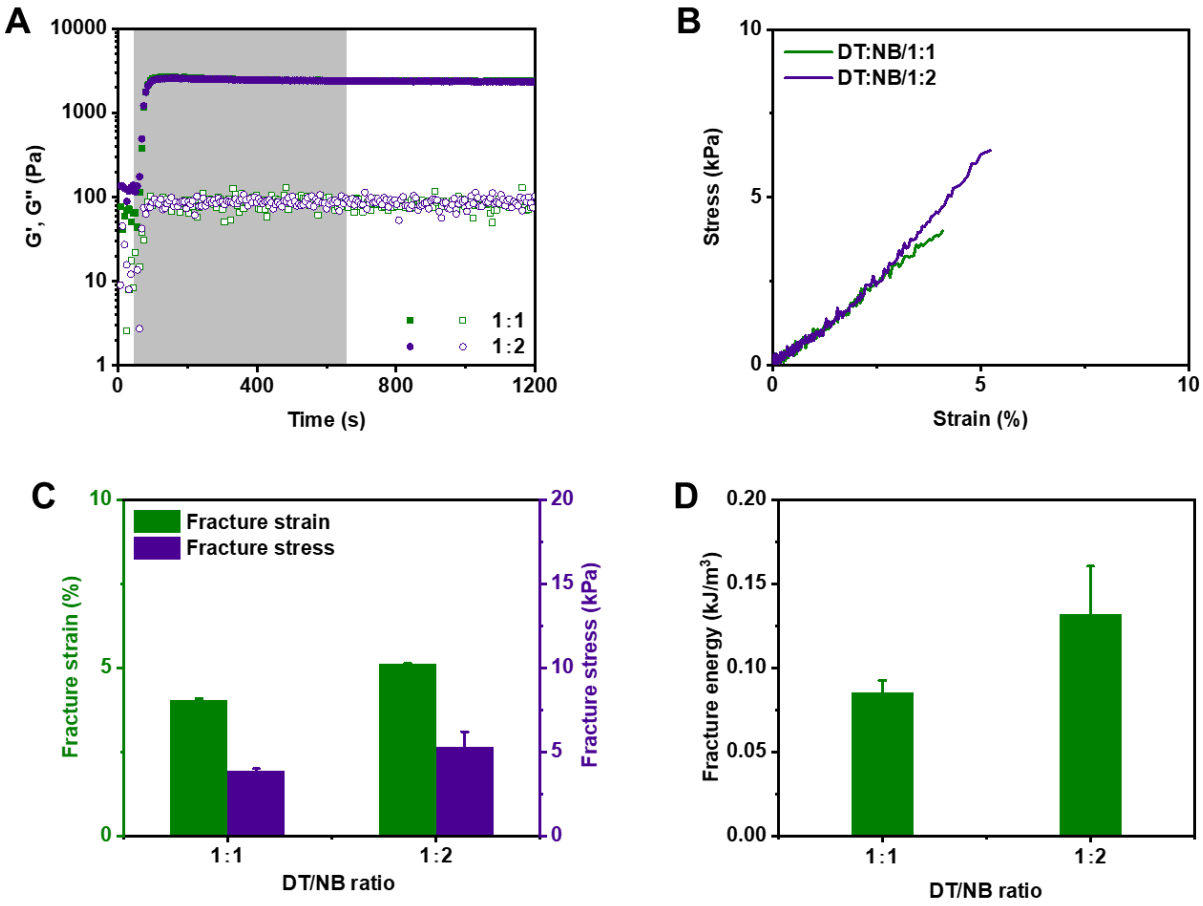

Figure S15. Mechanical properties of **SN** hydrogels **1:1** (5 mM **SN** (SQ with 10 mol% SQ-DT) and 0.45 wt% PEGdiNB, DT to NB molar ratio is 1:1) and **1:2** (5 mM **SN** (SQ with 10 mol% SQ-DT) and 0.9 wt% PEGdiNB, DT to NB molar ratio is 1:2). (A) Time sweep experiment after 10 min UV exposure. (B) Uniaxial stress-strain curves at a constant compression speed (10 µm/s). (C) Compressive fracture strain, fracture stress and (D) fracture energy. The sample was compressed at a speed of 10 µm/s. Mean ± SD, N≥3.

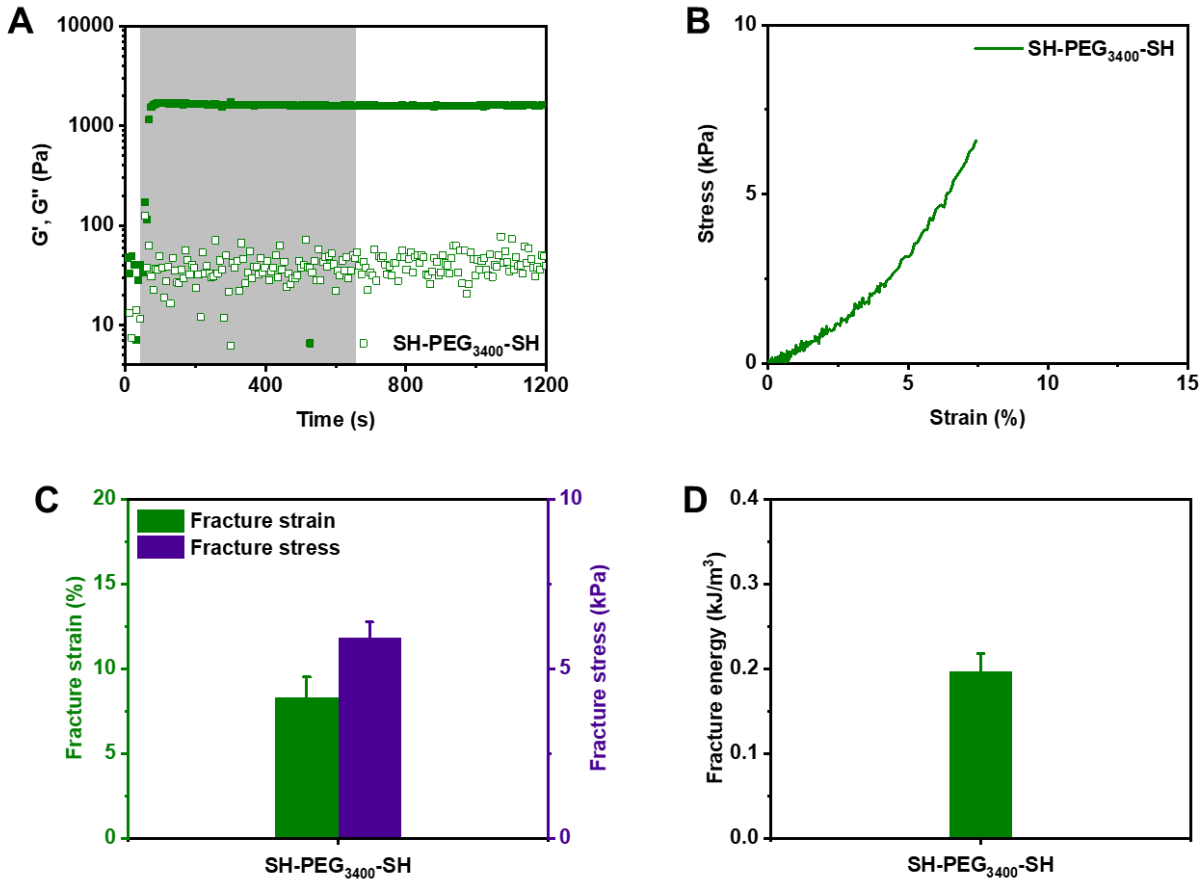

Figure S16. Mechanical properties of **DN** (5 mM **SN** (SQ with 10 mol% SQ-DT), and 1.8 wt% PEGdiNB and 1.0 wt% SH-PEG3400-SH). (A) Time sweep experiment of **DN** after 10 min UV exposure. (B) Uniaxial stress-strain curves under a constant compression speed (10 µm/s). (C) Compressive fracture strain, fracture stress and (D) fracture energy. The sample was compressed at a speed of 10 µm/s. Mean ± SD, N≥3.

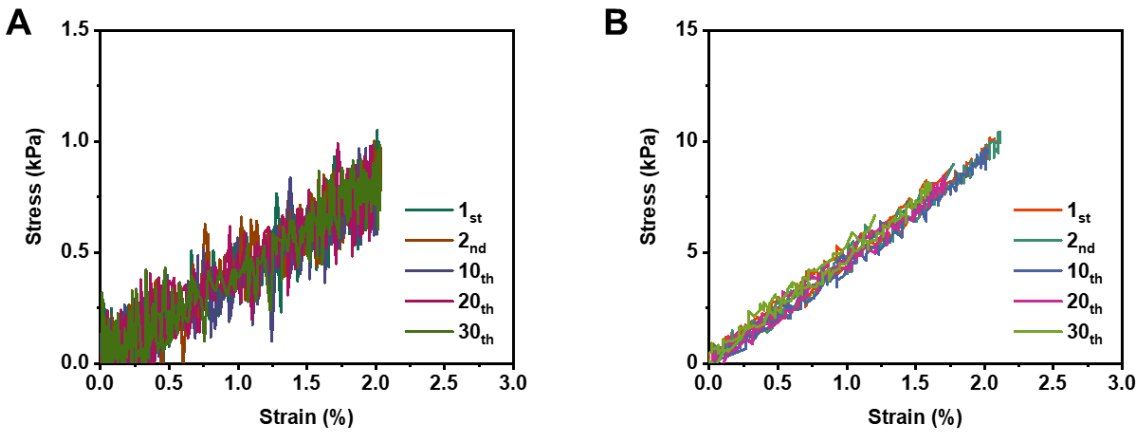

Figure S17. Representative loading-unloading curves of (A) **PN** (3.6 wt%) and (B) **DN** (3.6 wt% **PN** network and 5 mM **SN** (SQ with 10 mol% SQ-DT)). A strain of 2% was applied at a constant compression speed (10 µm/s).

Table S2. Fracture strain and stress, fracture energy, compression modulus and stress relaxation extent (axial) of the various hydrogels **SN**, **PN**, **IPN** and **DN** after 10 min UV exposure. (N ≥ 3).

Sample name	Fracture strain (%)	Fracture stress (kPa)	Fracture energy (kJ/m^3)	Compression modulus (kPa)	Stress relaxation extent (axial)
SN	2.20 ± 0.71	0.48 ± 0.14	0.00427 ± 0.00006	21.46 ± 5	/
PN	39.92 ± 0.11	83.52 ± 0.74	10.32 ± 0.2687	42.2 ± 8.4	~0
IPN	22.28 ± 3.09	71.10 ± 17.07	8.00 ± 2.26	216.01 ± 7.14	44% - 46%
DN	19.82 ± 1.59	163.66 ± 10.75	13.10 ± 1.65	360.61 ± 20.9	36% – 48%

SN: SQ with 10 mol% SQ-DT. **PN:** 3.6 wt%. **IPN:** 3.6 wt% **PN** and 5 mM **SN** (SQ with 10 mol% SQ-DT). **DN**: 3.6 wt% **PN** network and 5 mM **SN** (SQ with 10 mol% SQ-DT).

Cryogenic transmission electron microscopy (Cryo-TEM)

The **DN** samples prior to UV exposure were prepared as described above.[1b] The **DN** (3 µL) was applied to a freshly glow-discharged carbon 200 mesh Cu grid (Lacey carbon film) and the excess liquid was blotted off (3 s) at 100% humidity and plunge-frozen in liquid ethane prior to imaging.

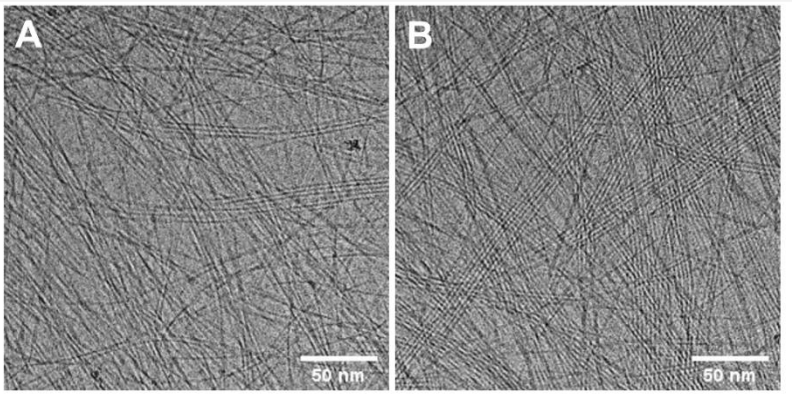

Figure S18. Cryo-TEM images of the **DN** with 5 mM **SN** (SQ with 10 mol% SQ-DT) and increasing **PN** concentration: (A) 3.6 wt% **PN** (B) 7.2 wt% **PN** without UV exposure. Scale bar: *50 nm*.

Scanning electron microscopy (SEM)

The **PN**, **IPN** and **DN** hydrogels (300 µL) were prepared as described above and exposed to UV light for 3 min by LED. The hydrogels were subsequently freeze-dried overnight and then, fractured after briefly dipping the solids in liquid nitrogen using tweezers. The fractured pieces were directly applied on to two-sided adhesive tape attached to an aluminum stub and coated for 2 min by a thin layer of gold (under vacuum) before imaging.

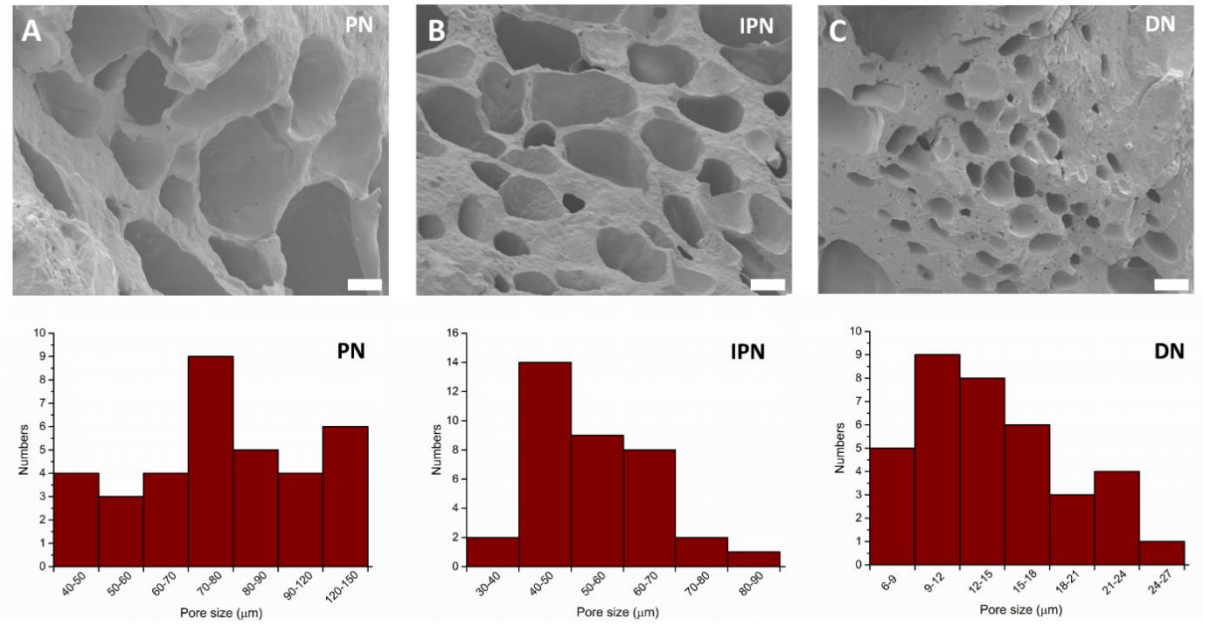

Figure S19. SEM images of the various hydrogels (A) **PN** (3.6 wt%), (B) **IPN** hydrogel (3.6 wt% **PN** and 5 mM **SN** (SQ with 10 mol% SQ-DT); (C) **DN** hydrogel (3.6 wt% **PN** network and 5 mM **SN** (SQ with 10 mol% SQ-DT)) and the relative distribution of measured pore sizes by the Image J software. Scale bar: *20 μm*.

Fluorescence recovery after photobleaching (FRAP) diffusion measurements

The hydrogel-fluorophore mixtures were prepared as previously described.[1b] The **SN** and **PN** mixtures were independently mixed prior to UV exposure with stock solutions of fluoresceinamine (Mw: 347 Da, 1.0 mM), FITC-dextran (Mw: ~10 kDa, 0.5 mM), and FITC-dextran (Mw: ~70 kDa, 0.15 mM) in PBS in a volume ratio of 9:1 (gel:fluorophore/fluorophore-labelled dextran). The hydrogel-fluorophore mixtures contained **DN** hydrogel (3.6 wt% **PN** network and 5 mM **SN** (SQ with 10% mol% SQ-DT) with either fluoresceinamine (347 Da, 100 µM), FITC-dextran (10 kDa, 50 µM), or FITC-dextran (70 kDa, 15 µM). Then, the mixtures (12 µL) were gently pipetted into a µ-Slide 15 well plate and were UV exposed for different durations (0 min, and 3 min) using a benchtop LED source (~10 mW/cm^2, 375 nm). The control **PN** (7.2 wt%) with either fluoresceinamine (347 Da, 100 µM), FITC-dextran (10 kDa, 50 µM), or FITC-dextran (70 kDa, 15 µM) was prepared following the same procedure above. The PEG-fluorophore hydrogel mixtures were exposed to UV light for 3 min using a benchtop LED source (~10 mW/cm^2, 375 nm). A well plate containing the various hydrogel-fluorophore mixtures were then loaded on a confocal microscope and samples were recorded with an Andor iXon Ultra 897 high speed EM-CCD camera to obtain 512 x 512 images with a resolution of 0.33 µm/pix using a 40x NA 0.8 plan fluor objective lens from Nikon. Prior to bleaching, the hydrogel-fluorophore mixtures were imaged for 2s with a 40 ms framerate. Then, a circular bleaching ROI (r = 12 µm), 40 µm into the hydrogel, was excited for 5 seconds (2 ms/pix dwell time) using a 488 nm Argon laser through an Andor FRAPPA unit. After bleaching, recovery images were recorded with a frame rate of 40 ms. All imaging was done at low laser excitation (1-10% of maximum intensity) to prevent bleaching and reference ROIs were used to normalize the recorded intensities at the bleaching spot.

Diffusion measurement

Figure S20A-B shows example recovery signals recorded for the hydrogel mixtures with fluoresceinamine (*light-grey*), 10 kDa FITC-dextran (*grey*) and 70 kDa FITC-dextran (*dark-grey*). The intensities were normalized by:

$$f_r(t) = \frac{f_{ROI}(t)/f_{ref}(t) - f_{ROI}(0)/f_{ref}(0)}{f_{ROI}(\infty)/f_{ref}(\infty) - f_{ROI}(0)/f_{ref}(0)}$$

Here $f_r(t)$ is the recovery signal, $f_{ROI}(t)$ the intensity of the bleached region and $f_{ref}(t)$ the intensity of the ROI, following Liu et al.[6] The recovery curves are well fit by a single exponential:

$$f_r(t) = A\left(1 - e^{-\frac{t}{t_0}}\right)$$

where t_0 can be used to determine the half-time of recovery by . . The averaged (n > 5) half times show that cell-culture associated biomolecules, like nutrients and growth factors, can adequately diffuse through the hydrogel.

Next to extracting the half-time of recovery, the diffusion constant was estimated by fitting the normalized recovery curves to:

$$f(t) = \sum_{n=0}^{\infty} \frac{-K^n}{n!} \frac{1}{1 + n\left[1 + \left(\frac{2t}{\tau_D}\right)\right]}$$

where τ_D is the 2-D characteristic diffusion time and K is the bleaching constant that depends on the experimental system.[7] For a Gaussian laser beam the diffusion constant is related to τ_D by $D = \omega^2/4\tau_D$, where ω is half the width of Gaussian laser profile determined at e^{-2} of the profile height. The radius was determined by fitting a Gaussian to the bleach spot (identical settings and depth to supramolecular hydrogels) of dried-out agar (2%)-fluoresceinamine (100 µM) samples and found to be $\omega = 17.1 \pm 1.6$. The diffusion constants are shown in **Table S3**. All calculations were performed in Matlab 2019a, using the curve-fitting and image-processing toolboxes.

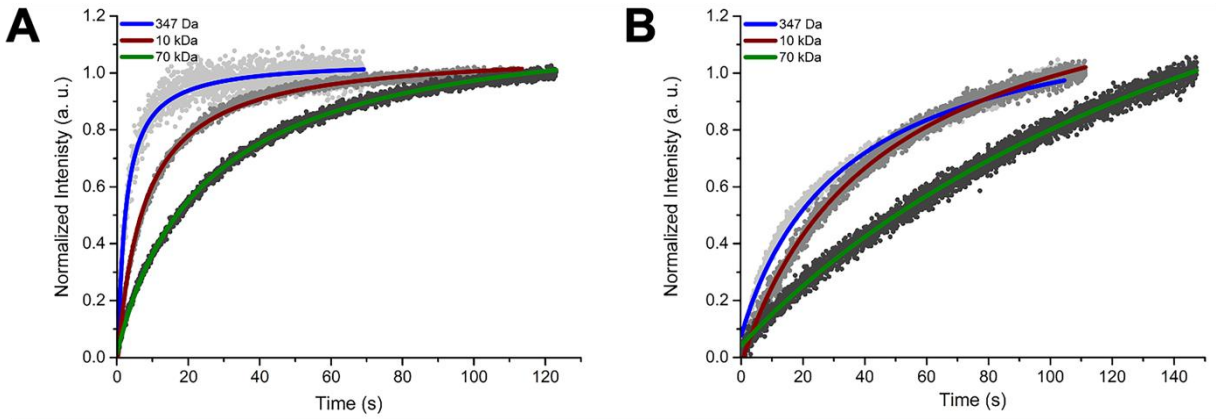

Figure S20. FRAP characterization of the **PN** and **DN** hydrogels with three different fluorescent probes (A) **DN** (3.6 wt% **PN** and 5 mM **SN** (SQ with 10 mol% SQ-DT)) without UV exposure and (B) **PN** (7.2 wt%) with 3 min UV exposure using different sized fluorophores (Fluoresceinamine (347 Da), and FITC-dextran (10 kDa and 70 kDa)). Grey dots: Normalized intensity in the bleached spot; Lines: fit of the diffusion constant.

Table S3. Effect of hydrogel composition and dye size on the diffusion coefficient (D) ($\mu m^2/s$).

Hydrogel composition	UV exposure time (min)	Fluorophore dye size 347 Da	10 kDa	70 kDa
DN (3.6 wt% **PN** network and 5 mM **SN** (SQ with 10 mol% SQ-DT))	0	23.66 ± 5.40	6.49 ± 1.48	2.01 ± 0.46
DN (3.6 wt% **PN** network and 5 mM **SN** (SQ with 10 mol% SQ-DT))	3	5.12 ± 1.17	3.52 ± 0.80	0.73 ± 0.17
PN (7.2 wt%)	3	1.57 ± 0.36	1.10 ± 0.25	0.18 ± 0.04

Equilibrium water content (EWC)

DN hydrogels (150 µL) were prepared in a glass vial (2.0 mL) as previously described and exposed to UV light for 3 min. To determine the equilibrium water content (EWC), they were first allowed to swell in PBS (600 µL) at 37 °C in an incubator for 24 h to reach equilibrium. Prior to measuring the hydrogel weight (W_s), the excess PBS was removed with a micropipet and blotted with a soft tissue paper. The hydrogels were then lyophilized overnight, and the weight was recorded (W_d). For all samples, three independent replicate experiments were performed. The EWC for each hydrogel was calculated using: EWC (%) = $(W_s-W_d)/W_s*100\%$.

Swelling and degradation assays

The swelling percentage of hydrogels were determined according to a previously published method.[3] Individual hydrogels (150 µL) were first prepared in a glass vial (2.0 mL) as described above and exposed to UV light for 3 min. The original weight (W_0) of each hydrogel prior to swelling was measured. Subsequently, each hydrogel was covered either with PBS or DMEM (high glucose) (600 µL), and then incubated at 37 °C. The weight (W_t) of all hydrogels was then collected at pre-determined time points, after complete removal of PBS or DMEM from the surface. The fresh PBS and DMEM were changed every two days during swelling. Three independent replicates were performed for each hydrogel condition. The swelling ratio was determined as $100\% * W_t/W_0$.

hPAC culture

Collection and expansion of hPACs from the ongoing Research Arthritis and Articular Cartilage (RAAK) study was performed as earlier described.[4] In short, within 2 hours following joint replacement surgery of osteoarthritis patients, cartilage of the macroscopically unaffected (preserved) region of the joint was sampled in DMEM (high glucose) supplemented with 10% FBS, antibiotics penicillin (100 units/mL) and streptomycin (100 µg/mL) and collagenase Type I (2 mg/mL); and were incubated overnight under standard conditions. Subsequently, isolated chondrocytes were expanded for 2 passages in DMEM supplemented with 10% FBS, antibiotics (100 units/mL penicillin and 100 µg/mL streptomycin) and FGF-2 (0.5 ng/mL) prior to encapsulation into the hydrogel materials.

3D cell encapsulation

3D cell encapsulation of hPACs in the **DN** (3.6 wt% **PN** network and 5 mM **SN** (SQ with 10 mol% SQ-DT without and with 5 mol% SQ-RGD) was explored. The hPAC suspension in the hydrogels were seeded at a density of 5 x 10^6 cells/mL. Different UV exposure times (0 min, 0.5 min, 1 min, and 3 min) were applied using a benchtop LED to crosslink the hydrogels and yield different mechanical properties. Afterwards, 3D constructs were covered with chondrogenic differentiation medium (500 µL) (DMEM high glucose supplemented with ascorbate (50 µg/mL), Dexamethasone (0.1 µM), L-proline (40 µg/mL), sodium pyruvate (100 µg/mL), ITS-plus, antibiotics, and TGF-β1 (10 ng/mL) and cultured under standard conditions. Cell media was refreshed 3 times every 15 min after seeding and was changed daily during the experiment.

Cell viability test

The LIVE/DEAD (calcein AM/propidium iodide (PI)) assay was used to assess cell viability after 3D encapsulation of the cells within the hydrogel. The mixed staining solutions of calcein AM (2.0 µM) and PI (1.5 µM) were prepared by diluting pre-prepared stock solutions of calcein AM (2.5 mM in DMSO) and PI (1.5 mM in PBS) with PBS (pH 7.4). At pre-determined time points (e.g., day 1 and 5), the medium was removed from the top of the hydrogel, the cell-laden hydrogels were washed with PBS (2 x 48 µL). The hydrogel was covered with the staining solution (48 µL) for 30 min at 37 °C and then removed from the top of hydrogel, and further washed with PBS (2 x 48 µL). An additional volume of PBS (48 µL) was pipetted on top of the hydrogel to prevent drying during imaging. Fluorescent Z-stack images were obtained using a 488 nm laser for excitation of calcein AM and a 532 nm laser for excitation of the PI dye. The Image J software package was used to process the collected raw images and count cell viability. LIVE/DEAD staining of hPACs was performed after 1 day and 5 days culture within hydrogels.

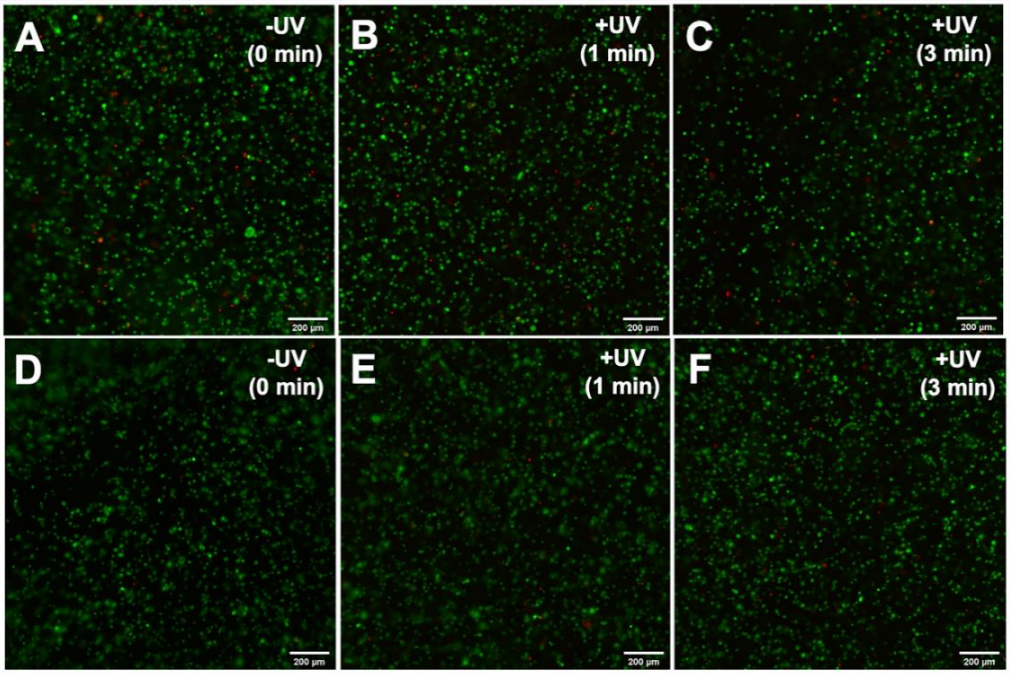

Figure S21. Confocal microscopy images of calcein AM/PI stained hPACs cells after culture day 1 in the **DN** hydrogels (3.6 wt% **PN** and 5 mM **SN** (SQ with 10 mol% SQ-DT without and with 5 mol% SQ-RGD) and different UV exposure times: (1) **DN**

without SQ-RGD at (A) 0 min; (B) 1 min; (C) 3 min; (2) **DN** with 5 mol% SQ-RGD at (D) 0 min; (E) 1 min; (F) 3 min. Viable cells are green and dead cells are red. Scale bar: *200 μm*.

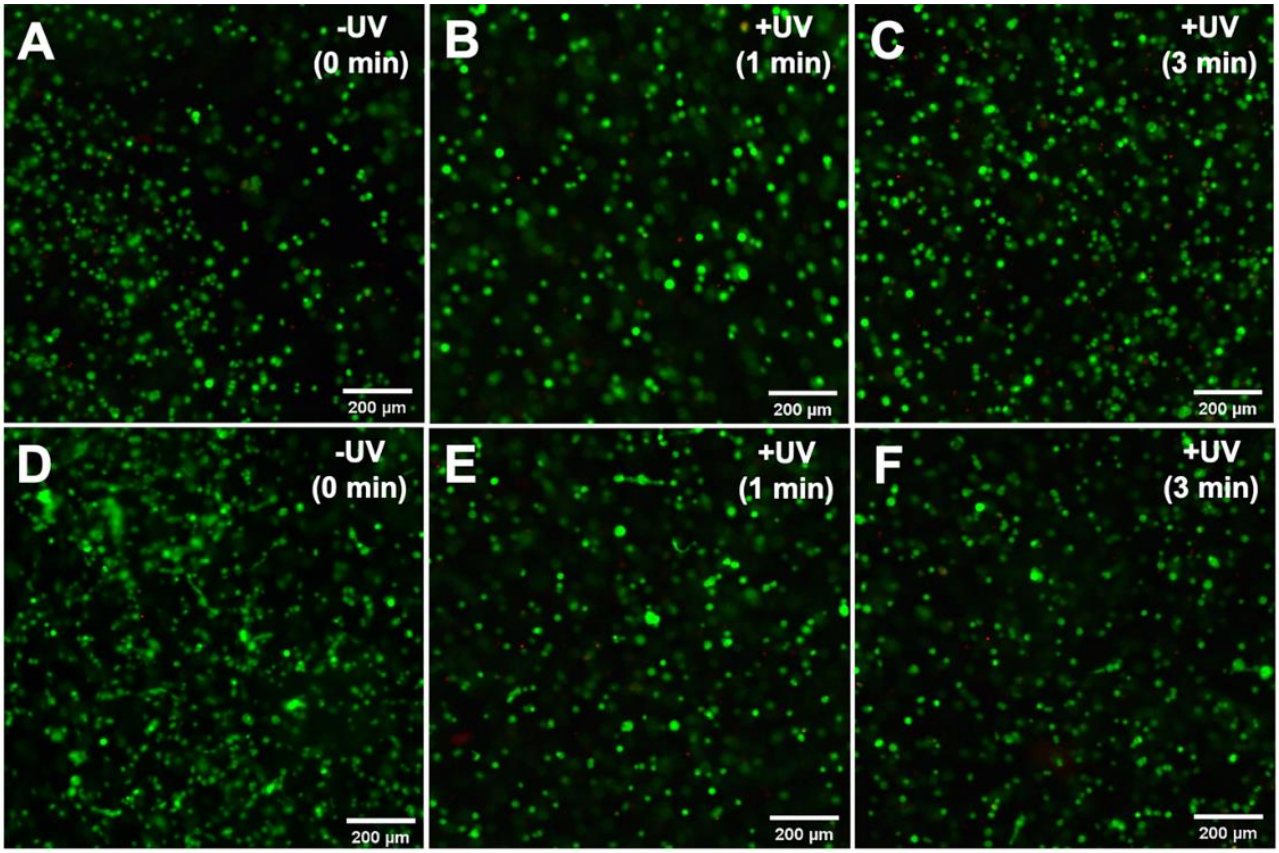

Figure S22. Confocal microscopy images of calcein AM/PI stained hPACs cells after culture day 5 in the **DN** hydrogels (3.6 wt% **PN** and 5 mM **SN** (SQ with 10 mol% SQ-DT without and with 5 mol% SQ-RGD) and different UV exposure times: (1) **DN** without SQ-RGD at (A) 0 min; (B) 1 min; (C) 3 min; (2) **DN** with 5 mol% SQ-RGD at (D) 0 min; (E) 1 min; (F) 3 min. Viable cells are green and dead cells are red. Scale bar: *200 μm*.

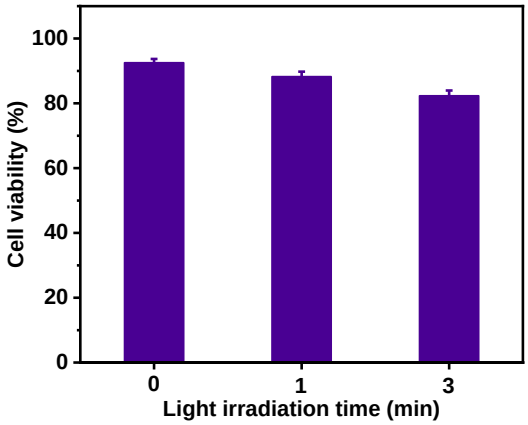

Figure S23. LIVE/DEAD counting of cells after 3D encapsulation of hPACs cell viability in **DN** hydrogels (3.6 wt% **PN** network and 5 mM **SN** (SQ with 10 mol% SQ-DT) with distinct UV exposure after 24h.

Compressive loading in 3D cell culture

Agarose culture wells with a diameter of 4 mm and a height of 1 mm were prepared by putting agarose (350 µL, 3%) in each well of a 24-well flat-bottom plate, using a 4 mm metal punch to create a small hole in the middle of the solidified agarose. The cell-laden hydrogel **DN** (20 µL) before UV exposure was gently pipetted into agarose wells. Then the cell-laden constructs were UV exposed (3 min) using a benchtop LED. Chondrogenic differentiation media (500 µL) with TGF-β1 (10 ng/ml) was carefully pipetted on top of construct. The plate was cultured under standard cell culture conditions. Cell media was refreshed 3 times every 15 min after seeding and was changed daily during the experiment.

For short-term (2 days) loading, the cell culture medium was carefully removed from the culture plate and the hydrogels were washed once with PBS before covering with the same buffer. The hydrogels were mechanically loaded independently for 10 minutes with a strain amplitude of 2% and fixed frequency of 1.0 Hz as soft loading, and a larger strain (20%) amplitude at a higher frequency (5.0 Hz) as heavy loading. After loading, the hydrogels were covered with chondrogenic differentiation media and further cultured under standard cell culture conditions. The control hydrogels were placed at the RT for 10 min in PBS.

For long-term (14 days) loading, the cell-laden hydrogels were exposed following the conditions for soft loading (2% strain amplitude at a fixed frequency (1.0 Hz)) for 45 minutes each day. Compressive loads were applied on days 1-3, 6-10 and 13-14.

Alcian Blue staining

To perform Alcian Blue staining of sulphated glycosaminoglycans (s-GAGs), the hPACs encapsulated in hydrogels were first fixed by applying formaldehyde (4%) for 15 min at RT. The hydrogels were washed with PBS (3 x 500 µL) and incubated with HCl (0.1N, 500 µL) for 10 min. To detect s-GAGs, the hydrogels were incubated with Alcian Blue 8-GX (1%) in HCl (0.1N) for 3 h and with HCl (0.1N, 3 x 500 µL), followed by adding HCl (0.1N, 500 µL) and incubated at RT overnight to totally remove the excess Alcian Blue. The hydrogels were washed with Milli-Q water (3 x 500 µL) before adding Nuclear Fast Red (0.1% in 5% aluminum sulfate) to stain the cell nuclei and incubated for 10 min before washing with MilliQ water (3 x 500 µL) before imaging.

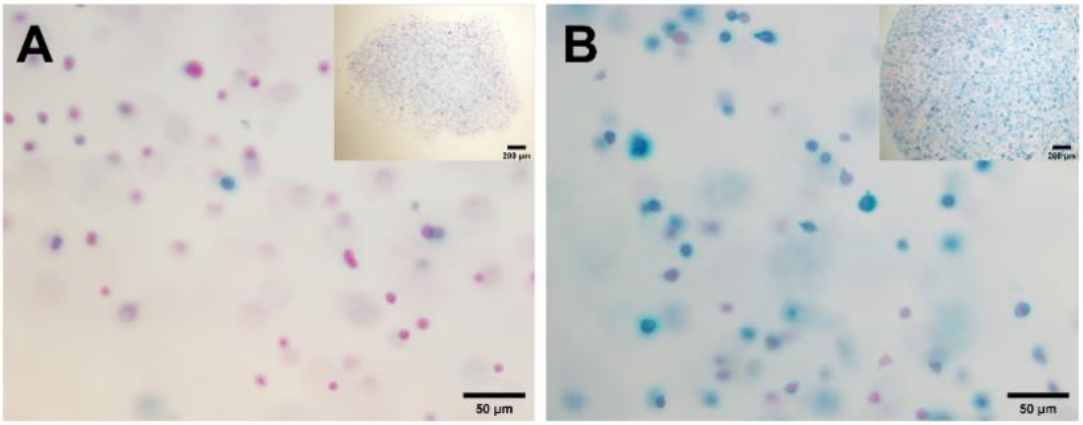

Figure S24. At day 5, Alcian Blue staining for s-GAGs with nuclear fast red counterstaining of hPACs in cell-laden **DN** hydrogels (7.2 wt% **PN** and 5 mM **SN** (SQ with 10 mol% SQ-DT) without SQ-RGD with UV exposure times: (A) 0 min and (B) 3 min. All cell-laden hydrogels were maintained in chondrogenic media containing TGF-β1.

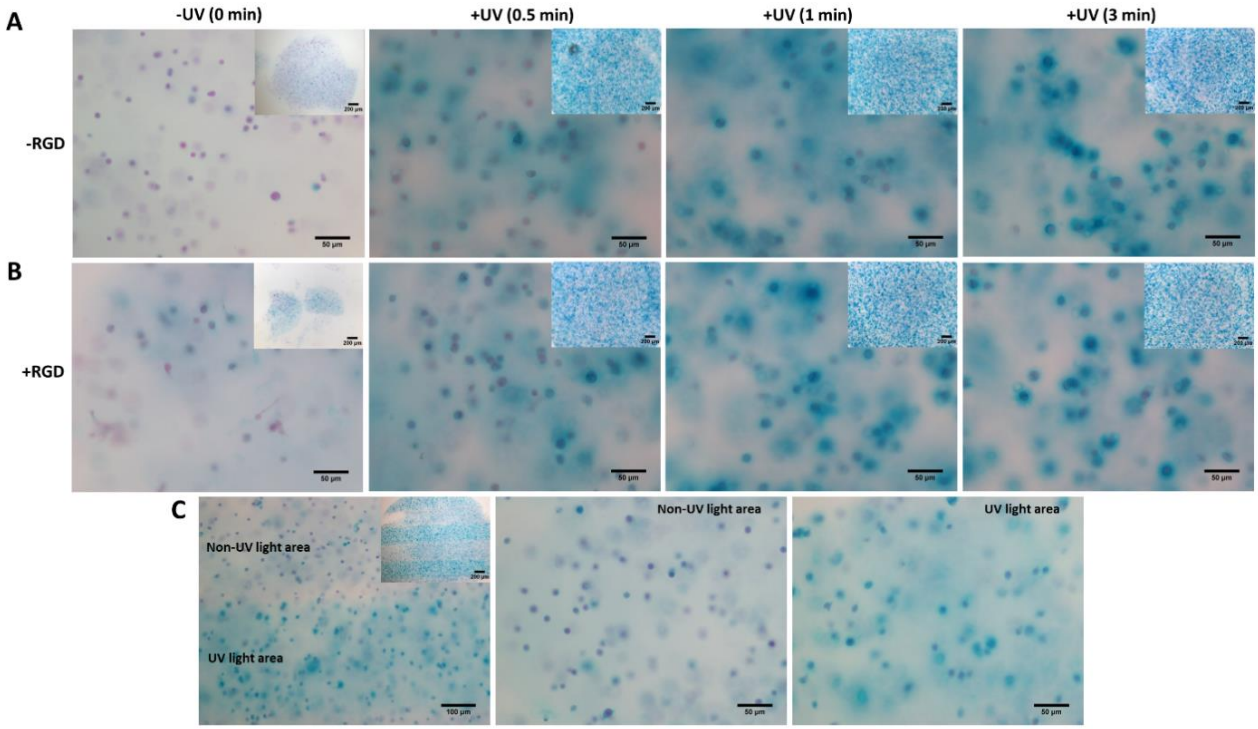

Figure S25. At day 5, Alcian Blue staining for s-GAGs with nuclear fast red counterstaining of hPACs in cell-laden hydrogels with varying UV exposure times (0 min, 0.5 min, 1 min and 3 min): (A) **DN** (3.6 wt% **PN** and 5 mM **SN** (SQ with 10% molar SQ-DT) without SQ-RGD and B) with 5 mol% SQ-RGD. (C) hPACs cell-laden **DN** hydrogels (3.6 wt% **PN** network and 5 mM **SN** with 10% mol SQ-DT) patterned with 3 min UV exposure using a photomask. All the cell laden hydrogels were maintained in chondrogenic media containing TGF-β1.

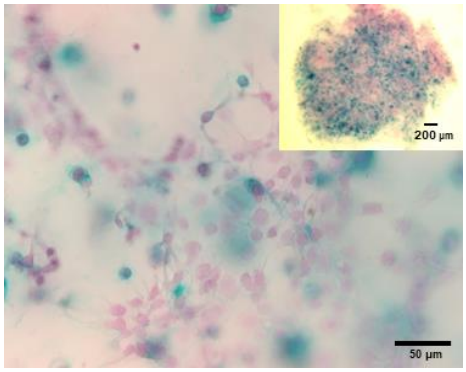

Figure S26. Representative Alcian Blue staining images with nuclear fast red counterstaining of hPACs cell-laden **DN** hydrogels (3.6 wt% **PN** and 5 mM **SN** (SQ with 10% mol SQ-DT and 5 mol% SQ-RGD)) without UV exposure and mechanical loading after culture day 3 in chondrogenic media containing TGF-β1.

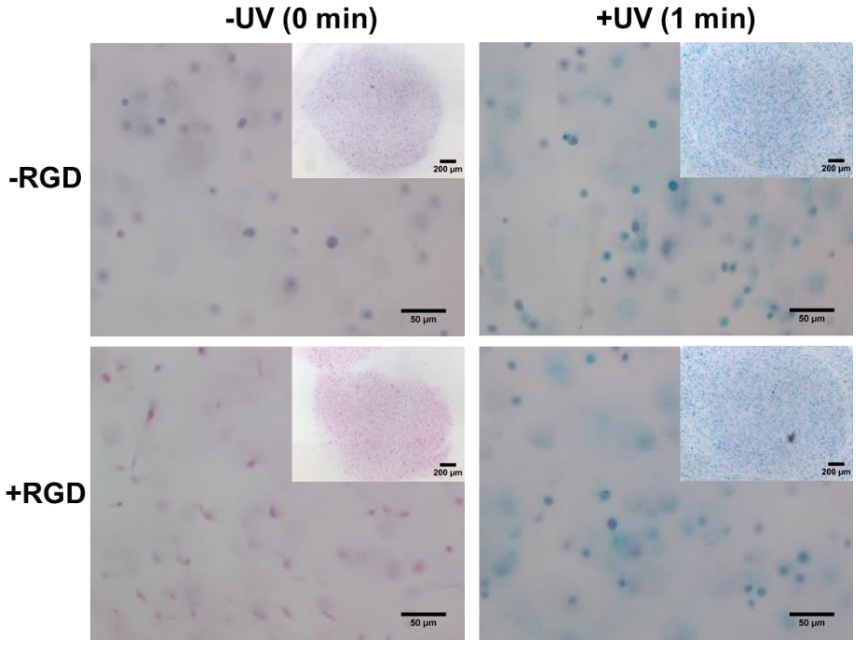

Figure S27. At day 5, Alcian Blue staining for s-GAGs with nuclear fast red counterstaining of hPACs in cell-laden **DN** hydrogels (3.6 wt% **PN** and 5 mM **SN** (SQ with 10 mol% SQ-DT) with/without 5 mol% SQ-RGD with varying UV exposure times (0 min, 1 min). All cell-laden hydrogels were maintained in chondrogenic media without TGF-β1.

DMMB assay and DNA content analysis

The s-GAGs and DNA content at indicated time points was quantified using biochemical analysis. The wet cell-hydrogel constructs were first weighed, lyophilized and digested overnight at 60 °C by a papain digestion solution in PBS-EDTA (pH 7.1). The s-GAGs concentration was measured by using DMMB assay[5] with Shark chondroitin sulfate in PBS-EDTA (pH 7.1) as a reference. The obtained solution was diluted 30x before performing measuring DMMB absorption at 525 and 595 nm. The concentration of DNA from the digested hydrogel samples were measured on a NanoDrop.

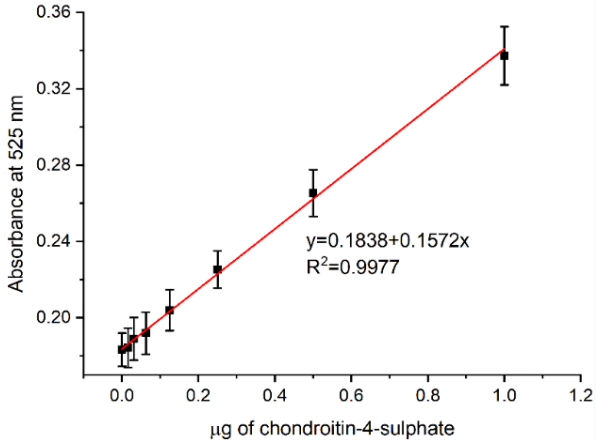

Figure S28. Standard solution curve for DMMB assay using chondroitin-4-sulfate.

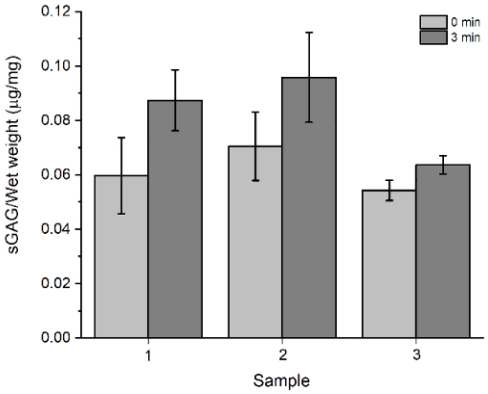

Figure S29. Results of the biochemical analysis of s-GAGs after 5 days culture of hPACs in cell-laden hydrogels with different UV exposure times (0 min and 3 min): sample 1: **DN** (3.6 wt% **PN** and 5 mM **SN** (SQ with 10 mol% SQ-DT)) without SQ-RGD. Sample 2: **DN** (3.6 wt% **PN** and 5 mM **SN** (SQ with 10 mol% SQ-DT)) with 5 mol% SQ-RGD. Sample 3: **DN** (7.2 wt% **PN** and 5 mM **SN** (SQ with 10 mol% SQ-DT)) without SQ-RGD. All cell laden hydrogels were maintained in chondrogenic media containing TGF-β1.

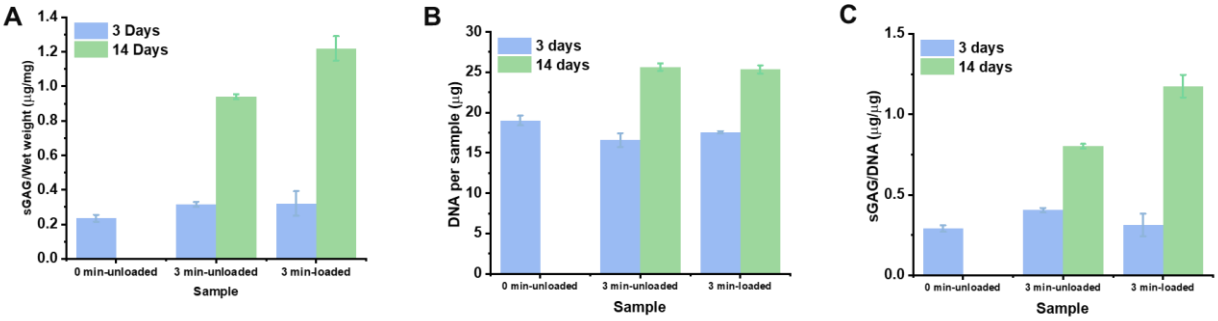

Figure S30. Results of biochemical analysis of s-GAGs, wet cell-laden hydrogel weight and DNA content after culture days 3 and 14 of hPACs (donor 1) in cell-laden **DN** hydrogels (3.6 wt% **PN** and 5 mM **SN** (SQ with 10 mol% SQ-DT and 5 mol% SQ-RGD)) and different UV exposure times (0 min and 3 min) and with/without mechanical loading (strain: 2%, frequency: 1Hz). (A) s-GAGs content normalized to wet cell-laden hydrogel weight. (B) Quantification of extracted DNA. (C) s-GAGs content normalized to the DNA content. All the cell laden hydrogels were maintained in chondrogenic media containing TGF-β1.

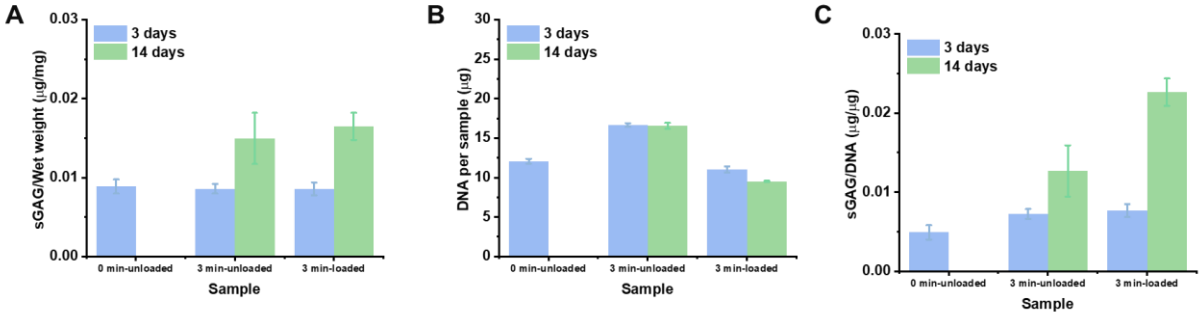

Figure S31. Results of biochemical analysis of s-GAGs, wet cell-laden hydrogel weight and DNA content after culture days 3 and 14 of hPACs (donor 2) in cell-laden **DN** hydrogels (3.6 wt% **PN** and 5 mM **SN** (SQ with 10 mol% SQ-DT and 5 mol% SQ-RGD)) and different UV exposure times (0 min and 3 min) and with/without mechanical loading (strain: 2%, frequency: 1Hz).

(A) s-GAGs content normalized to wet cell-laden hydrogel weight. (B) Quantification of extracted DNA. (C) s-GAGs content normalized to the DNA content. All the cell laden hydrogels were maintained in chondrogenic media containing TGF-β1.

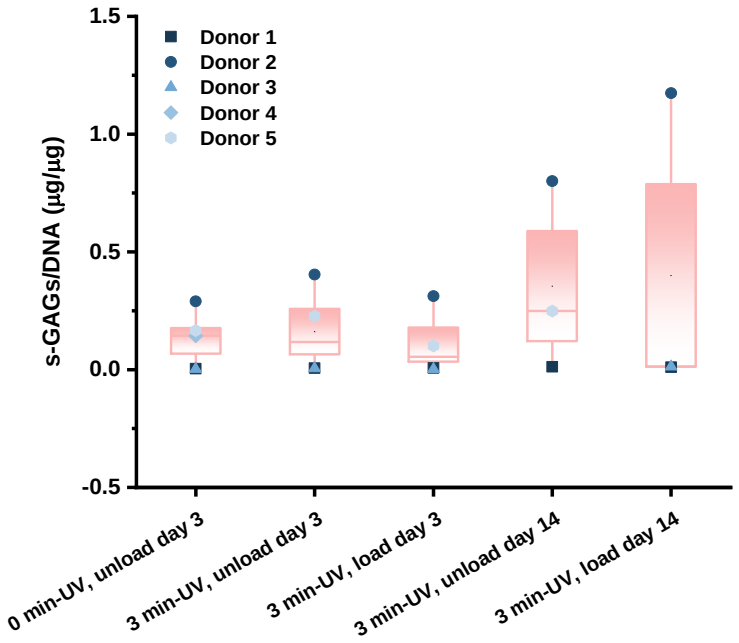

Figure S32. Results of biochemical analysis of s-GAGs content normalized to the DNA content after culture days 3 and 14 of hPACs (donor 1-5) in cell-laden **DN** hydrogels (3.6 wt% **PN** and 5 mM **SN** (SQ with 10 mol% SQ-DT and 5 mol% SQ-RGD)) and different UV exposure times (0 min and 3 min) and with/without mechanical loading (strain: 2%, frequency: 1Hz). All the cell laden hydrogels were maintained in chondrogenic media containing TGF-β1.

Table S4. Normalized s-GAGs per DNA relative to the control (0 min-UV, unload on day 3) of the different donors.

	Donor 1	Donor 2	Donor 3	Donor 4	Donor 5	AVG	SD	*P*-value	*P*-value
				Relative change GAG/DNA					
0 min-UV, unload day 3	1.0	1.0	1.0	1.0	1.0	1.0	0.0		
3 min-UV, unload day 3	1.5	1.4	1.7	/	1.4	1.5	0.1	[a]7.3×10^{-5}	
3 min-UV, load day 3	1.6	1.1	0.8	/	0.6	1.0	0.4	[b]7.7×10^{-2}	
3 min-UV, unload day 14	2.58	2.76	/	/	1.50	2.28	0.6825	/	[d]6.3×10^{-2}
3 min-UV, load day 14	2.28	4.04	3.79	/	/	3.37	0.9547	[c]1.8×10^{-1}	[e]6.3×10^{-3}

[a]: *P*-value of 3 min-UV, unload day 3 *vs.* 0 min-UV, unload day 3.
[b]: *P*-value of 3 min-UV, load day 3 *vs.* 3 min-UV, unload day 3.
[c]: *P*-value of 3 min-UV, load day 14 *vs.* 3 min-UV, unload day 14.
[d]: *P*-value of 3 min-UV, unload day 14 *vs.* 3 min-UV, unload day 3.
[e]: *P*-value of 3 min-UV, load day 14 *vs.* 3 min-UV, load day 3.

Immunocytochemical staining

To visualize collagen type II and fibronectin 1 after culture day 5, the cell-laden hydrogels were first fixed with paraformaldehyde (4%) at RT for 15 min. After washing the hydrogels for 3 times with

PBS, the cells were permeabilized using Triton X-100 solution (0.5%) in PBS at RT for 10 min. The cell-laden hydrogels were washed with PBS (3 x 500 µL) at RT for 5 min. Antigen retrieval was accomplished with Proteinase K treatment (5 µg/mL) at 37°C for 10 min, followed by hyaluronidase treatment (5 mg/mL) at 37°C for 30 min. After washing with PBS (3 x 500µL) for 5 min and blocking of non-specific binding with normal goat serum (NGS, 5%) in PBS at RT for 1 h, the hydrogels were incubated overnight at 4°C with the mixed primary antibodies containing anti-COL II mouse MAB1330 Millipore (1:100) and anti-FN (ab2413, Abcam, 1:100) in the blocking solution (5% NGS in PBS). Then the hydrogels were washed with PBS (3 x 500µL) and incubated at RT for 1 hour with secondary antibodies containing goat anti-mouse Alexa Fluor 647 (1:500) and goat anti-rabbit Alexa Fluor 488 (1:500) in block solution (5% NGS in PBS). After 3 times washing PBS, the hydrogels were covered with VECTASHIELD Antifade Mounting Medium with DAPI at RT for 5 min prior to imaging.

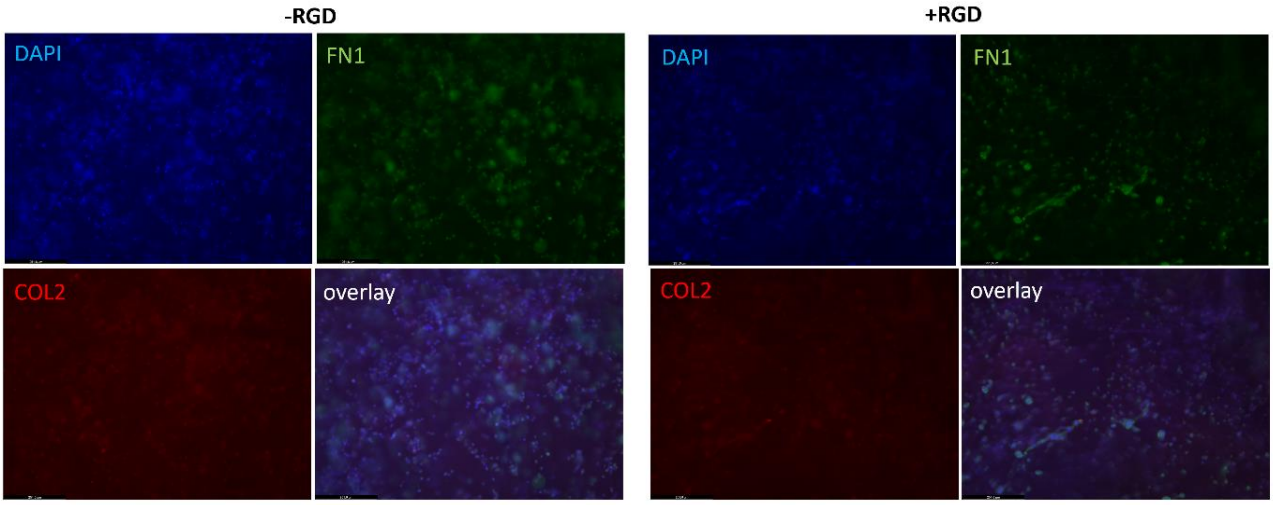

Figure S33. Representative immunofluorescent staining images of hPAC cell-laden **DN** hydrogels (3.6 wt% **PN** and 5 mM **SN** (SQ with 10 mol% SQ-DT) with and without 5 mol% SQ-RGD after 5 days in culture in chondrogenic media containing TGF-β1 with 3 min UV exposure (DAPI for blue, FN1 for green, Type II collagen for red and its overlay). Scale bar: *100 µm*.

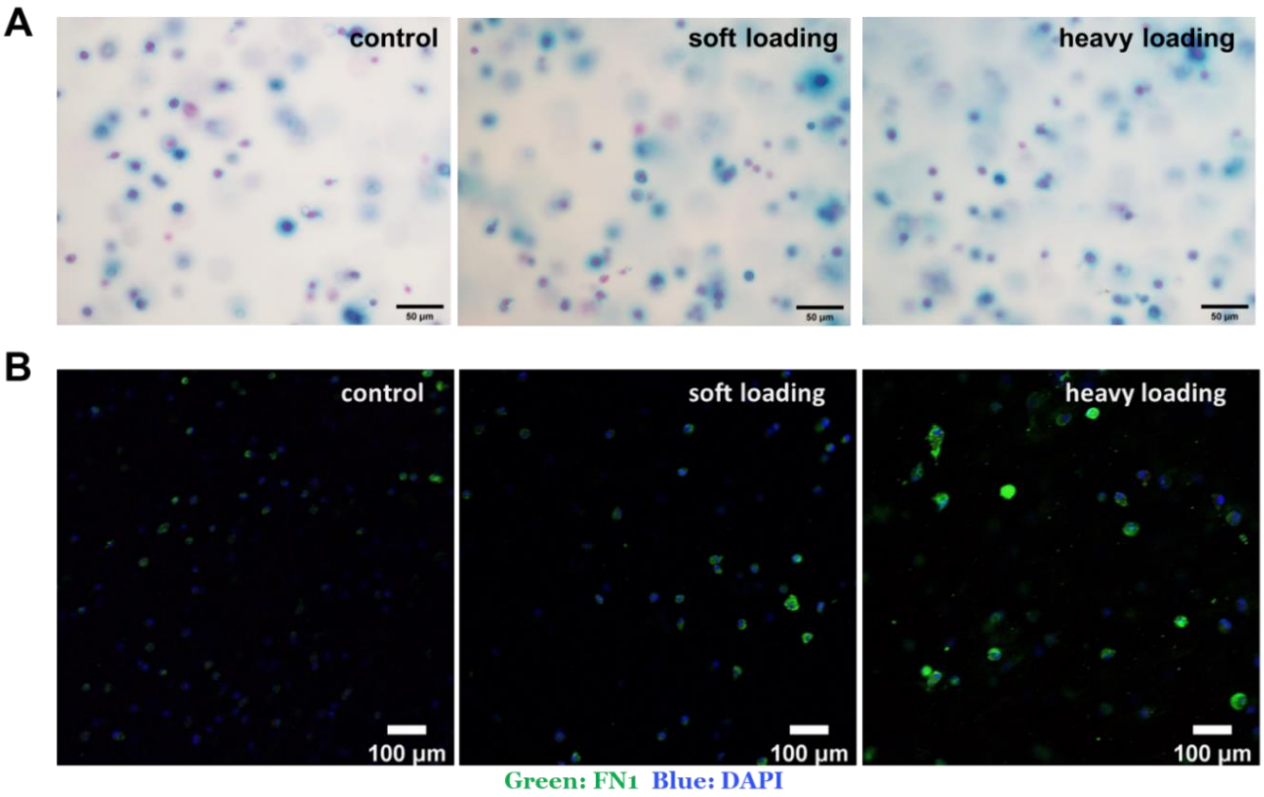

Figure S34. Representative Alcian Blue (A) and immunofluorescent staining (B) images of hPAC cell-laden **DN** hydrogels (3.6 wt% **PN** and 5 mM **SN** (SQ with 10 mol% SQ-DT and 5% molar SQ-RGD)) and with different types of mechanical loading (unloaded control, soft and heavy loading) after culture day 3 in chondrogenic media containing TGF-β1 with 3 min UV exposure (DAPI for blue, FN1 for green, and Type II collagen for red).

Reference

(1) Tong, C.; Wondergem, J. A. J.; Heinrich, D.; Kieltyka, R. E. Photopatternable, Branched Polymer Hydrogels Based on Linear Macromonomers for 3D Cell Culture Applications. *ACS Macro Lett.* **2020,** *9* (6), 882.

(2) Tong, C.; Wondergem, J. A. J.; van den Brink, M.; Kwakernaak, M. C.; Chen, Y.; Hendrix, M.; Voets, I. K.; Danen, E. H. J.; Le Devedec, S.; Heinrich, D.et al. Spatial and Temporal Modulation of Cell Instructive Cues in a Filamentous Supramolecular Biomaterial. *ACS Appl. Mater. Interfaces* **2022,** *14* (15), 17042.

(3) Kim, S. W.; Kim, D. Y.; Roh, H. H.; Kim, H. S.; Lee, J. W.; Lee, K. Y. Three-dimensional bioprinting of cell-laden constructs using polysaccharide-based self-healing hydrogels. *Biomacromolecules* **2019,** *20* (5), 1860.

(4) Yang, F.; Wang, J.; Cao, L.; Chen, R.; Tang, L.; Liu, C. Injectable and redox-responsive hydrogel with adaptive degradation rate for bone regeneration. *J Mater Chem B* **2014,** *2* (3), 295.

(5) Bomer, N.; den Hollander, W.; Ramos, Y. F.; Bos, S. D.; van der Breggen, R.; Lakenberg, N.; Pepers, B. A.; van Eeden, A. E.; Darvishan, A.; Tobi, E. W.et al. Underlying molecular mechanisms of DIO2 susceptibility in symptomatic osteoarthritis. *Ann Rheum Dis* **2015,** *74* (8), 1571.

(6) Farndale, R. W.; Buttle, D. J.; Barrett, A. J. Improved quantitation and discrimination of sulphated glycosaminoglycans by use of dimethylmethylene blue. *Biochimica et Biophysica Acta (BBA)-General Subjects* **1986,** *883* (2), 173.

(7) Liu, J.; Hilderink, J.; Groothuis, T. A.; Otto, C.; Van Blitterswijk, C. A.; de Boer, J. Monitoring nutrient transport in tissue-engineered grafts. *J. Tissue Eng. Regen. Med.* **2015,** *9* (8), 952.

(8) Blonk, J.; Don, A.; Van Aalst, H.; Birmingham, J. Fluorescence photobleaching recovery in the confocal scanning light microscope. *J. Microsc.* **1993,** *169* (3), 363.

Chapter 4

Visible Light Crosslinking of Hybrid Covalent and Supramolecular Double Networks for Dynamic Mechanical Loading of 3D Chondrocyte Cultures

Double network hydrogels are highly suitable for applications in 3D platforms for articular cartilage engineering because of their excellent mechanical properties and structural features that are comparable to the *in vivo* extracellular matrix. However, employing synthetic hydrogels to closely mimic the mechanical responses that occur in the tissue under cyclic compressive loading conditions remains challenging. Herein, we explore phenol photopolymerization with visible light to connect filamentous supramolecular and covalent networks to give rise to a double network hydrogel. Modulation of the crosslinking density led to changes in the complex mechanical characteristics of the double network hydrogels. Furthermore, biomimetic compression stress responses can be modulated by tuning component ratios. These hydrogels also exhibited fast stress relaxation in both shear and axial directions, with the relaxation rate mainly dependent on the supramolecular polymer concentration and crosslinking density. Crosslinking of the two networks permitted cyclic compressive loading of human primary articular chondrocyte cultures in 3D showing increased sulfated-glycosaminoglycan deposition relative to the free swelling condition after 2 days. Utilizing rapid visible light-induced bioorthogonal photopolymerization, this innovative approach enables the fabrication of double network hydrogels with customizable biomimetic mechanical characteristics by strategically adjusting chemical design parameters that is crucial for joint regeneration and can be used to develop advanced materials tailored for 3D *in vitro* modeling of cartilage and targeted therapeutic interventions for osteoarthritis.

This chapter was prepared as a research article: Ying Chen, Yolande Ramos[*]& and Roxanne E. Kieltyka[*]

4.1 Introduction

Articular cartilage is a remarkable natural material that can endure high contact pressures for human daily activities due to its excellent mechanical properties and low friction.[1,2] It is a biphasic material composed of collagen fibers and proteoglycans (PGs) with glycosaminoglycan (GAG) side chains and synovial fluid that differs in its presentation across cartilage leading to distinct mechanics across the tissue.[1,3-5] An essential part of this matrix is the pericellular matrix (PCM) that is immediately adjacent to the cell membrane and together with the cell forms the chondron. It is composed of fibrous network-like collagens (e.g., types II, VI, and IX), fibronectin, and proteoglycans (e.g., aggrecan, hyaluronan and decorin), transmitting both biophysical and biochemical cues from the tissues to the cells.[6] The PCM exhibits distinct mechanical properties from the surrounding chondrocyte extracellular matrix (ECM), and is altered during development and in disease like osteoarthritis (OA).[6-9] Nowadays, studies show that synthetic hydrogel materials, based on their mechanical properties, can be used to mimic and regenerate PCM with the proper external mechanical stimulus, highlighting the potential of mechanical loading on cartilage constructs *in vitro* to mimic the native environment and stimulate biosynthesis in chondrocytes.[10,11]

In the biphasic cartilage system, the cross-linked collagen fibers act as a first phase that sustains tension, whereas the synovial fluid acts as a second phase that swells yielding pores, which gives rise to the ability to dissipate energy upon loading through combining fluid-solid frictional dissipation with the inherent viscoelasticity of the solid matrix.[3] *In vivo*, cartilage experiences dehydration and rehydration on loading and can bear contact pressures greater than its compressive modulus due to fluid pressurization within its porous structure.[5] The time-dependent properties of cartilage result from the complex interplay between the solid matrix and fluid flow that can be characterized by poroelastic and viscoelastic mechanisms that impart a wide range of dissipative properties.[5] Hereby, poroviscoelastic (PVE) relaxation describes the combination of poroelastic and viscoelastic relaxation that happens simultaneously.[12,13] Poroelastic relaxation originates from stress-induced fluid flow (diffusion), which dissipates energy through fluid-solid frictional interaction, and its time constant depends on a characteristic diffusion length scale.[14,15] Viscoelastic relaxation is the property of a material that can resist deformation under stress due to the rearrangement and interactions of solid matrix macromolecules (i.e., collagen fibrils and PGs).[16-18] Rapid PVE relaxation can govern the rate-dependent mechanical response of intact cartilage and can protect the joints against external forces. To date, few examples consider the combination of these mechanical properties in their design to develop synthetic cartilage ECM mimics, most research focuses either on the poroelastic or viscoelastic property of the material.[19,20]

Double network (**DN**) hydrogels provide an opportunity to mimic the cartilage ECM because of their unique stiff and tough mechanical properties.[21] These hydrogels are composed of two independent networks that are crosslinked with one another, either through physical or chemical interactions,[11, 12] showing improved stiffness, mechanical strength and load-bearing properties that differ significantly from the independent networks.[8-10] However, most **DN** networks lack a fibrous network and dynamic biomimetic mechanics (e.g., viscoelasticity, plasticity, etc.)[22-34] that is found in

the native ECM. Supramolecular filaments are often introduced into **DN** hydrogels to improve stress relaxation because of their energy dissipation properties when subjected to external stimuli.[22,23,35-37] Moreover, most researchers currently concentrate on enhancing mechanical properties by utilizing a single type of chemical bond, the potential influence of chemical bond types and ratios in the synthetic network on stress relaxation in hydrogels has often been overlooked. Therefore, it is vital to develop complex network architectures that modulate these features to understand the range by which such materials can be altered for a given application.[1118,38,39] Light-based cross-linking methods are extensively employed in the preparation of **DN** materials due to their versatility and controlled deployment.[40,41] UV light (200-400 nm) is commonly used due to its high efficiency in initiating photopolymerization reactions.[41-43] Recently, visible light (400-700 nm) has also been widely explored, offering advantages such as reducing photodamage to living cells for biomedical application.[44,45]

We earlier demonstrated the formation of filamentous **DN** hydrogels that show biomimetic mechanical properties that are cartilage-like in their compression using bioorthogonal UV light-mediated polymerization strategy to crosslink supramolecular and covalent polymer networks through dynamic-covalent poly(disulfide) and poly(disulfide-norbornene)s (**Chapter 3**). We used this hybrid **DN** network for 3D cell culture of human primary articular chondrocytes under external cyclic mechanical loads to enhance the deposition of sulfated-glycosaminoglycans. Inspired by these results, we became interested in developing another **DN** hydrogel network based on the formation of covalent polymer crosslinks to further increase the mechanics of the network advancing our progression towards mimicking the properties of native tissues. In this study, we disclose a visible light-induced bioorthogonal strategy involving phenol photopolymerization crosslinking of supramolecular filament and covalent poly(ethylene glycol) networks to develop hybrid networks that are suitable for diurnal cyclic compressive loading of 3D chondrocyte cultures. Phenol crosslinking chemistry is a widely used method in biomaterial field due to its mild and fast crosslinking characteristic, the chemical ligation will permit the formation of networks connected through polyphenol networks with distinct dynamic characters in the **DN** hydrogels. In this **DN** network, we select a 4-arm polyethylene glycol with an additional orthogonal bond in the backbone to further increase the **DN** mechanical strength. Next, we conduct an in-depth examination of the interplay between supramolecular content and poly(ethylene glycol) network concentration, focusing on their impact on the mechanical stiffness, strength, and poroviscoelastic relaxation within the **DN** system. Importantly, we explore the capacity of **DN** hydrogel to endure cyclic compressive loading to assess its mechanical attributes in mimicking the load-bearing tissues that are crucial for investigating a spectrum of inquiries related to both developmental processes and disease-related phenomena.

4.2 Results and Discussion

Visible light crosslinking of hybrid supramolecular and covalent DN hydrogels

To prepare the **DN** hydrogels with light responsive phenols for crosslinking, we introduced phenol moiety (Phe) first on the periphery of the squaramide amphiphile derived from a typical tripodal squaramide-based gelator, C8-SQ[46] (Scheme 1A, Figure S1). We conjugated a tosyl (Ts)-protected

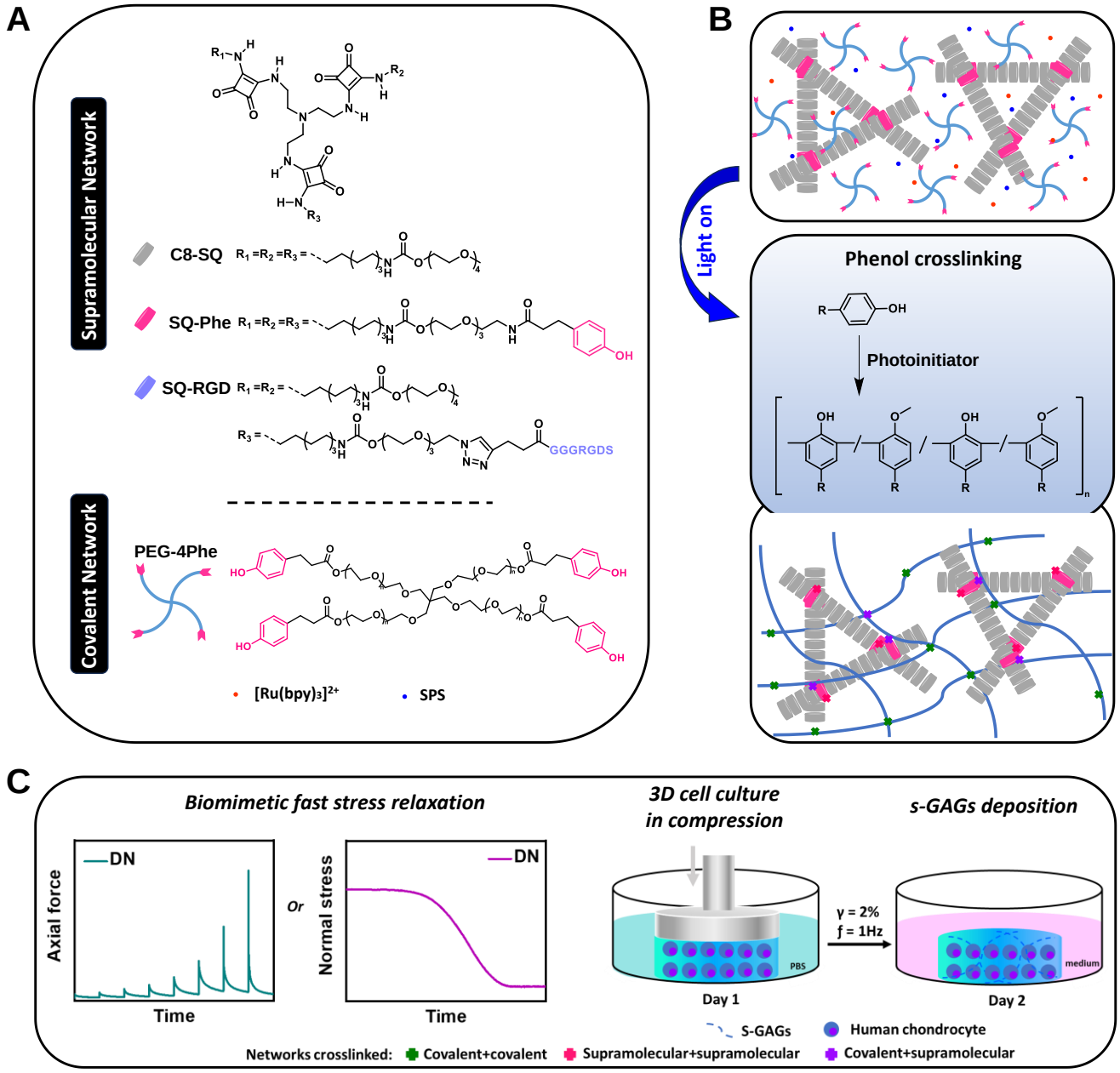

Scheme 1. (A) Supramolecular filament (SN: C8-SQ, SQ-Phe, and SQ-RGD) and covalent polymer (PN: PEG-4Phe) component to prepare **DN** hydrogels. (B) Mixing of components, phenol photopolymerization to form **DN** hydrogels. (C) Biomimetic cartilage mechanical properties can be achieved in compression and release (*left and middle left*). The bioorthogonal photopolymerization approach in the **DN** hydrogel permits 3D human chondrocyte culture with cyclic compression leading to increased s-GAGs deposition (*middle right and right, respectively*).

tetraethylene glycol with an azide and then reduced the azide into amine by catalytic hydrogenation, and further protected the amine with tert-butyloxycarbonyl (Boc). Afterward, we coupled the Boc-protected tetraethylene glycol with carboxybenzyl (Cbz)-protected 1,8-dibromodecane in the presence of sodium hydroxide through a carbamate moiety with a yield of ~33%. We then deprotected Cbz-protecting group by catalytic hydrogenation to reveal an amine moiety, which was further reacted with dibutyl squarate to yield the squaramide amphiphile in ~56%. Furthermore, we connected the squaramide amphiphile onto the tris(2-aminoethylamine) (TREN) core to obtain Boc-protected tripodal squaramide-based monomers in a yield of ~43%. In a final step, we used trifluoroacetic acid (TFA) to deprotect the Boc-protected amine group on the periphery of the tripodal amphiphile and coupled 3-(4-(tert-butoxy)phenyl)propanoic acid, and then deprotected the tert-butyl group by TFA to obtain the final phenol functionalized tripodal squaramide-based monomers (SQ-Phe) in a yield of ~43%. C8-SQ was synthesized as we reported before.[47] Subsequently, we introduced phenol on the 4-arm polyethylene glycol (Mn = 10 kDa) by using carbodiimide coupling chemistry, and deprotected by TFA to obtain a high degree of functionalization of PEG-4Phe as earlier reported.[48,49]

We prepared the **DN** hydrogels by co-assembling the tripodal squaramide-based supramolecular polymers with 5 mol% phenol (Phe) monomer (2-6 mM) (**SN**) and PEG-4Phe (PN, 1-2% wt%). More precisely, we incorporated the PEG-4Phe polymer into a solution containing supramolecular filaments in phosphate buffered saline (pH 7.4) after sonication on ice, and then brought them to room temperature (RT) overnight to form hydrogels. Subsequently, we added photoinitiator stock solutions of tris(bipyridine) ruthenium (II) chloride (Ru, 44 mM) and sodium persulfate (SPS, 440 mM) before applying visible light at 450 nm to crosslink the soft hydrogels to form **DN**s. The hydrogels remained transparent after photocrosslinking with a yellow colour (Figure S2). In this study, we prepared a series of hydrogels **DN1**-**6** by modulating the concentration of PEG-4Phe and supramolecular networks (Table S1). For **DN1**-**3**, PEG-4Phe concentration remained at 1%, while the concentration of the supramolecular network ranged from 2 mM to 6 mM. For **DN4**-**6**, PEG-4Phe concentration was fixed at 2%, with supramolecular concentration varying from 2 to 6 mM.

Augmentation of the supramolecular network stiffness with addition of the second network

We quantified the impact of combining the covalent network with filamentous supramolecular polymers and phenol photopolymerization on the mechanical characteristics of the **DN1** - **DN6** hydrogels in PBS (pH 7.4) by oscillatory rheology. In time sweep measurements after 3 min visible light irradiation, **DN** hydrogels storage moduli (G') showed greater than the individual components (Figure 1A-B, Table S1). For the single network hydrogels, the polymer network **PN** (1-2 wt%) with Ru (0.05 mM) and SPS (0.5 mM) showed a G' of ~1 kPa -2 kPa, and the supramolecular network **SN** (2-6 mM) reached ~450 Pa – 6.3 kPa (Table S1). For the double network **DN** hydrogels, incorporating the supramolecular **SN** with the covalent **PN** networks yielded G' ranging from ~10 kPa -35 kPa. This increase in storage modulus surpassed the combined values of the **SN** and **PN** individually and markedly exceeded that of the pre-UV exposed hydrogel (~1.5 Pa- 38.2 Pa), underscoring the synergistic effect of integrating these networks and their photocrosslinking. We could further tune the stiffness of these **DN** hydrogels by

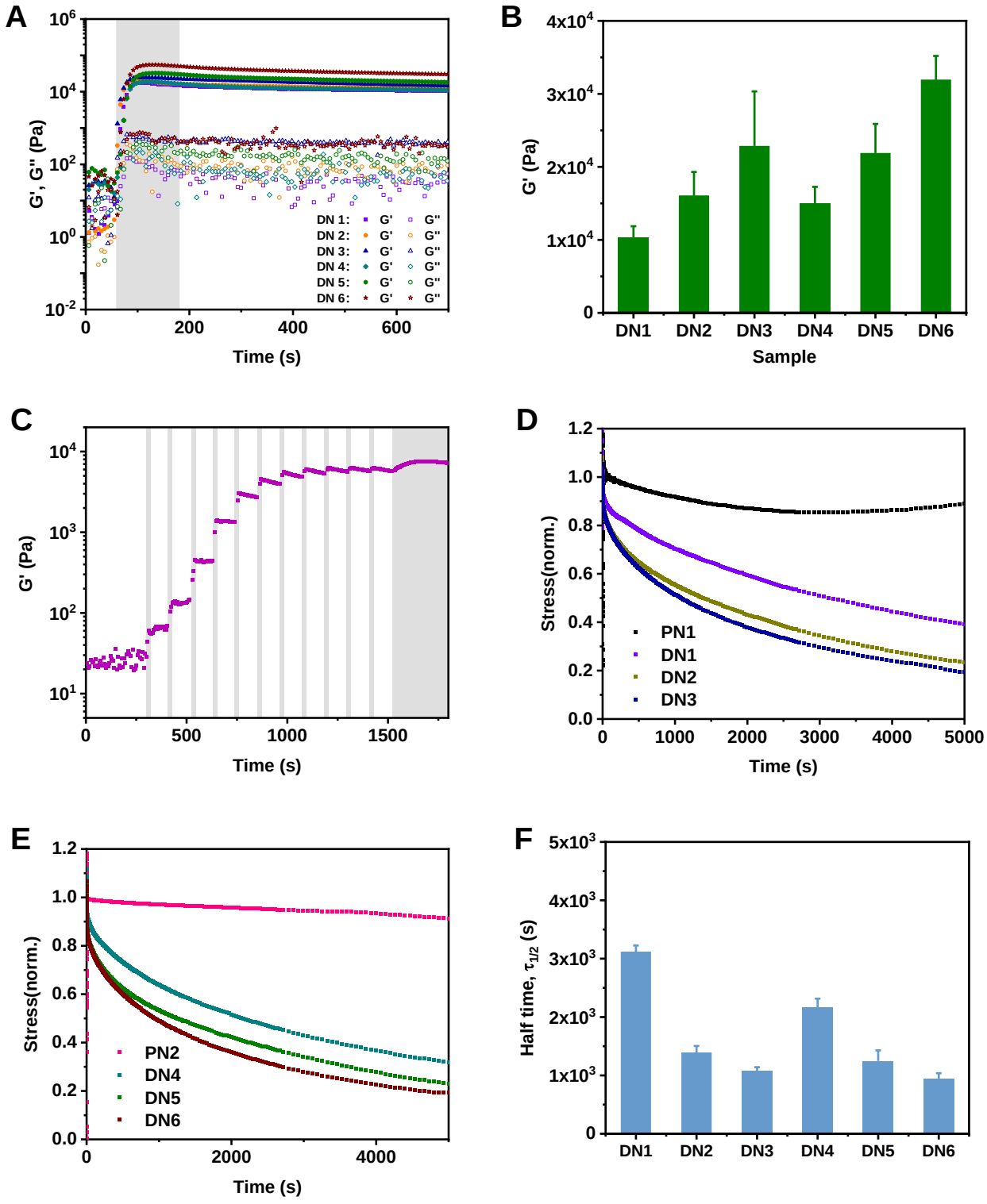

Figure 1. Oscillatory rheology measurements of **DN1-6** hydrogels in PBS at RT: (A) Time sweeps of **DN** hydrogels with 3 min visible light irradiation. (B) Storage modulus (G') at plateau hydrogels with and without 3 min visible light irradiation. (C) Averaged time sweep (N=3) with stepwise UV exposure of the **DN1** hydrogel. (D) Stress relaxation measurements (10% strain) of crosslinked **DN1**-**3** hydrogels. (E) Stress relaxation measurements (10% strain) of crosslinked **DN4**-**6** hydrogels. (F) Stress relaxation half-time of **DN1**-**6** hydrogels. Light source parameters: ~10 mW/cm^2, 400 - 500 nm filter with maximum absorbance at 450 nm. Grey regions indicate visible light exposure. Mean ± SD, N ≥ 3.

modulating the covalent (PEG-4Phe) or supramolecular polymer (SQ-5Phe) concentrations. For example, raising the SQ-5Phe monomer concentration from 2 - 6 mM in the 1 wt% PEG-4Phe networks (**DN1** - **DN3**), the storage modulus of crosslinked **DN** hydrogels grew from ~10 kPa (**DN1**) - ~23 kPa (**DN3**). In contrast, increasing the **PN** concentration to 2 wt%, boosted the storage modulus from 15 kPa (**DN4**) - 32 kPa (**DN6**). These outcomes are likely because due to the mechanism of cross-linking by the phenol group that undergoes photopolymerization with itself on both networks to achieve the stiffnesses of the **DN** material. Furthermore, application of visible light in a step-wise manner, also augmented the storage modulus of **DN1** from the ~20 Pa - ~10 kPa opening possibilities to modulate the network's mechanical properties in time in a user-defined manner (Figure 1C). Strain-dependent oscillatory rheology (ƒ=1Hz, γ=0.01% - 2000%) of photocrosslinked **DN1** - **DN6** hydrogels displayed a broad linear viscoelastic region (LVR) yielding at ~180% strain (Figure S3A). Frequency sweep data within the LVR (strain=0.05%, frequency=0.2 Hz – 1 Hz) of **DN1** - **DN6** hydrogels showed a linear profile with the G' being greater than the loss modulus (G'') across the whole range of frequencies studied (Figure S3B). These results shows that photocrosslinked double networks can be tuned to display stiffness within the range of the PCM of cartilage (40 kPa – 70 kPa)[8] and other soft tissues (10 kPa – 100 kPa).[50]

To understand the contribution of crosslinking both networks to the DN mechanical properties, we prepared a semi-interpenetrating network (**IPN**) with the same concentration as the **DN3** and **DN6** but without 5 mol% SQ-Phe crosslinking composition in the **SN** component that enables crosslinking of both polymers. The lack of crosslinks between both networks yielded storage moduli ranging from ~2.5 kPa – 8.5 kPa, which was higher than that of the **SN** and **PN** individually, yet lower than that of the **DN** hydrogels. These results indicate that physical characteristics of both networks and their chemical crosslinking serve an important role to achieve the **DN** properties.

Alteration of the hydrogel complex mechanical characteristics with visible light

The hydrogel complex mechanical features can impact cell behaviour in processes such as differentiation and morphogenesis, thus we investigated the viscoelastic and viscoplastic properties of **DN1-6** hydrogels in response to shear deformation. The viscoelasticity of the hydrogel can be determined by its stress relaxation response to a constant strain. We found that the stress relaxation process was predominantly contingent upon **SN** concentration rather than their stiffness (Figure 1D-F), contrary to typical trend where stiffer hydrogels show lower stress relaxation rate.[51,52] **DN1** relaxed ~61 % of the initial stress over the measurement time frame, while **DN2** and **DN3** showed a more pronounced relaxation of ~77 % and ~81 %, respectively. We found a similar trend for **DN4** (~68 %), **DN5** (~77 %), and **DN6** (~81 %). These results indicate that the addition of polymer network could not greatly affect the stress relaxation, but **SN** could help to release more stress. Furthermore, while the **DN** hydrogels exhibited heightened stress relaxation as the **PN** content increased from 1 to 2 wt% with a constant **SN** concentration of 2 mM, no significant alteration was observed with increasing **PN** content when **SN** concentrations were 4 mM or 6 mM. We further evaluated the stress relaxation rate of **DN1-6** by its half time ($\tau_{1/2}$), or the time point when stress release to half of the initial value. The curves showed a range from ~3100s to ~947s when tuning the supramolecular filament and polymer

concentration. In contrast, the **PN** hydrogels (**PN1** and **PN2**) exhibited minimal stress relaxation behavior, consistent with their elastic nature. These results emphasize the significance of supramolecular networks as they give rise to the viscoelastic behaviour recorded in these materials. These results further corroborate that the stress relaxation of these **DN**s is decoupled from stiffness and suggests that the fibrous supramolecular network could enhance the stress relaxation mechanism.

We further probed the viscoplastic response of the materials to the application of stress and its release by a creep and recovery test. We recorded subtle differences in plasticity in the recovery phase of the measurement for the different **DN** networks. **DN1** showed a slightly higher degree of plasticity (~14%), in contrast to **DN2** - **DN6** (~2% - 9%) after visible light crosslinking (Figure. S4). Moreover, the strong linear correlation with time for the creep curves (except **DN1**) points to an increased elastic character of the double networks due to the polyphenol crosslinks.

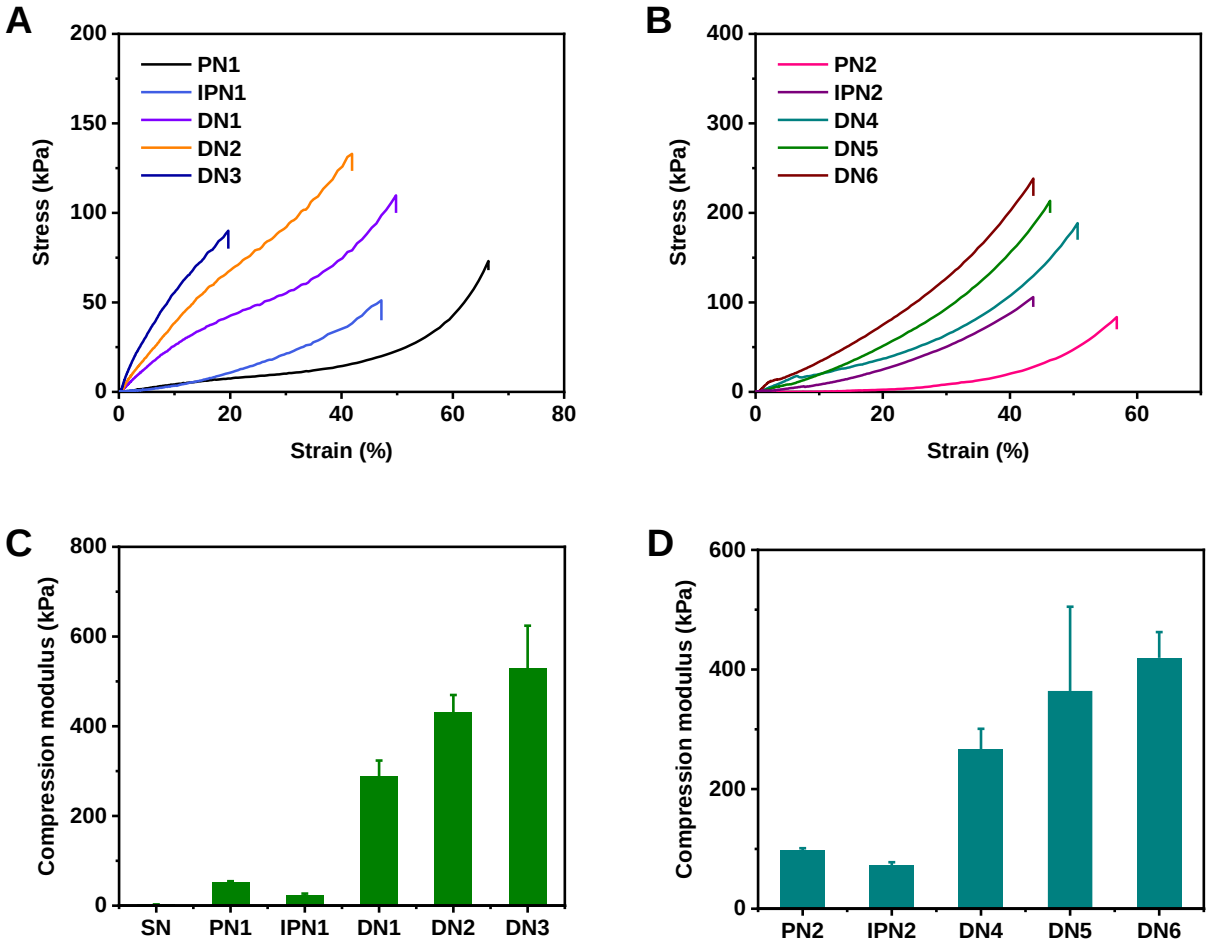

Figure 2. Compressive properties of the **SN**, **PN, IPN,** and **DN** hydrogels under a constant speed of 10 µm/s. Uniaxial stress-strain curves of (A) **PN1**, **IPN1**, and DN1-3 and (B) PN2, IPN2, and **DN4-6**. Compression modulus of (C) **SN**, **PN1**, **IPN1**, and DN1-3 and (D) PN2, IPN2, and **DN4-6**. Mean ± SD, N ≥ 3.

Table 1. Fracture strain, facture stress, fracture energy and compression modulus of **PN**, **IPN** and **DN** hydrogels under 10 µm/s speed, Mean ± SD, N ≥ 3.

Name	Fracture strain (%)	Fracture stress (kPa)	Fracture energy (kJ/m³)	Compression modulus (kPa)
SN	1.44±0.08	7.98±0.91	0.05±0.004	554.94±33.25
PN1	67.61±3.70	58.08±1.97	13.45±4.01	52.58±2.01
IPN1	46.29±1.24	48.05±4.35	9.08±1.12	23.67±2.54
DN1	54.38±3.37	108.44±35.85	43.16±2.12	288.44±35.05
DN2	35.55±3.59	110.88±18.93	18.31±2.65	430.59±39.14
DN3	19.11±6.96	90.03±23.37	9.25±3.24	529.43±94.75
PN2	67.68±1.88	72.93±1.32	23.72±2.22	97.98±3.21
IPN2	44.68±0.92	111.10±7.29	19.39±4.80	71.88±4.84
DN4	49.44±6.14	177.15±39.17	31.76±11.96	266.56±34.28
DN5	44.02±6.18	176.45±61.48	45.30±2.35	364.19±140.72
DN6	47.00±4.72	232.51±8.31	45.22±2.82	419.61±43.00

DN hydrogels withstand compressive loads

The ability to withstand high compressive forces is a defining feature of articular cartilage, therefore understanding the contribution of the supramolecular/polymer concentration, crosslinking type and density to the mechanical properties of the hydrogels is essential.[53] We performed axial force compression tests on the crosslinked **DN1**-**6**, **IPN1-2**, **PN1**-**2** and **SN** hydrogels in the rheometer. The **SN** hydrogel (6 mM) demonstrated brittle behaviour, fracturing at a stress of ~8 kPa (Figure S5). The **PN1**-**2** hydrogels showed high fracture strains (**PN1**: ~68 %, **PN2**: ~65 %), but relatively low fracture stresses (**PN1**: ~58 kPa, **PN2**: ~73 kPa) and fracture energies (**PN1**: ~13 kJ/m^3; **PN2**: ~24 kJ/m^3) (Figure 2A-B, Table 1). The compression curves displayed the typical appearance for polymer materials showing a gradual increase at low strains, followed by a dramatic increase above 45%.

When incorporating 1 wt% **PN** into **SN** to develop **DN1-3**, the resulting hydrogels exhibited greater brittleness with a higher **SN** concentration showing higher fracture stresses, but a lower fracture strain compared to the **PN1** hydrogel (Figure 2A-B, Table 1). Notably, **DN1** exhibited a fracture strain of ~54% with a corresponding fracture stress of ~108 kPa. While **DN3** demonstrated a fracture strain of ~19% along with a fracture stress of ~90 kPa. The fracture energy of **DN1** (~43 kJ/m^3) greatly improved compared with **PN1**, while **DN2** (~18 kJ/m^3) and **DN3** (~9 kJ/m^3) showed a noticeable downward trend. Further increasing the **PN** to 2 wt%, the fracture stress (~177 kPa - 233 kPa) and fracture energy (~32 kJ/m^3 – 45 kJ/m^3) greatly increased compared to **PN2**, and the fracture strain remained relatively constant (~44% - 49%). For comparison, we evaluated the **IPN** hydrogels under identical conditions revealing a fracture stress that is marginally higher than that of **PN** but lower than

that of **DN** (Figure S6), illustrating that the presence of crosslinks between **PN** and **SN** enhances their capacity to withstand stress.

Interestingly, all the **DN** hydrogels showed obvious two-stage compression curves compared with **PN** and **IPN** hydrogels. For **DN1**-**2** hydrogels initially exhibited a linear elastic behavior (< ~25% strain) with a downward concavity, followed by a nonlinear response characterized by an upward concavity until broken. When the supramolecular filament concentration increased in **DN3**, the first stage of the compression curves was prolonged, and **DN3** hydrogels were more brittle with a lower fracture strain and higher fracture stress. The **DN4**-**6** hydrogels exhibited a different trend displaying a slight break at low strain initially (< ~8%, ~23 kPa) in the compression tests, and similar increases with comparable fracture stress. Such behavior is consistent with the theory of linear poroelasticity.[54,55] We hypothesized that the first step primarily results from the supramolecular fibers resisting the stress and acting as a sacrificial network even during the early compression stages. In the second stage polymer network behaviour is observed, resisting most external forces. These findings emphasize the importance of adjusting the amounts of supramolecular fibers and polymer components to achieve a suitable **DN** network for specific applications.

The compression modulus of the **DN1-6** hydrogels grew with the increasing **SN** concentration while maintaining a consistent amount of **PN** (Figure 2C-D, Table 1). In contrast, the extent of this enhancement was slightly reduced as the **PN** concentration increased while maintaining the same **SN** concentration. Furthermore, upon removing the crosslinks between the **PN** and **SN** in the **IPN**, a slight increase in compressive modulus compared to the **PN** was observed, highlighting that the entangled supramolecular filaments could reinforce networks. These findings suggest that there is a synergy between the supramolecular and polymer components on the double network mechanical properties.

An important mechanical feature of cartilage is its poroelasticity that gives rise to its excellent functional performance in load bearing and lubrication. This characteristic encompasses fluid pressure and viscous flow within the ECM, playing an essential role in load-bearing, energy dissipation, solute and fluid transport and mechanotransduction.[56,57] To examine poroelasticity of the **DN**s and **PN**s, we evaluated the effect of loading speed on the **DN** and **PN** compressive properties. We reported a mildly higher compression moduli for **DN** hydrogels (Figure S7-13) deformed at a fast-loading speed of 100 µm/s as compared to 10 µm/s, whereas compression speeds below 10 µm/s resulted in much lower moduli but higher fracture strengths. For example, the fracture strain, stress and energy of **DN6** gel stayed relatively similar when the compression speed decreased from 100 µm/s to 10 µm/s. However, these parameters significantly increased with further reductions in speed. The augmented fracture strength of **DN6** at lower speeds indicates the influence of external stimuli on mechanical strength. At reduced speeds, polymer chains are given sufficient time to respond and endure external forces, thereby enhancing fracture strength. A similar trend was observed for **DN3** and **DN5**. However, the **DN1-2** and **DN4** showed the highest fracture strength at 1 µm/s, demonstrating that the mechanical compressive characters were shared impact of both network composition and external stimulus. These results suggest that the composite material can be optimized to emulate human daily activities that involve varying frequencies.

The supramolecular network enables compressive stress relaxation properties in DN hydrogels

A characteristic feature of cartilage is its ability to rapidly release the stress generated from compressive loads as a joint protection mechanism.[23,39,58] We measured the capacity of the **DN**s to relax successive compressive loads by rapidly applying an increase in strain over 600s in a stepwise manner. The **DN** hydrogels efficiently and instantaneously relaxed the imposed stress (> 85%) in a similar manner to cartilage (Figure 3A-B). The **PN** and **IPN** hydrogels also showed this response profile by relaxing the applied stress (> 80%) to a similar extent as the **DN** under identical conditions but with a reduced axial force response at the start of the load cycle (Figure S15-16). We further measured the capacity of these materials to dissipate energy with increasing cyclic strains to gain further insight into the contribution of the supramolecular network on this property. The hysteresis loops of the **DN** hydrogels expanded on elevating the strain or **SN** concentration (Figure 3C-D, S7-12, S14-15), and the **IPN** and **PN** hydrogels showed reduced dissipated energies in contrast to the **DN** hydrogels. These results highlight that the combination of both covalent and supramolecular networks and their crosslinking are needed to gain access to and maximize these mechanical responses.

Poroviscorelaxation behavior is a distinctive characteristic of articular cartilage's mechanical properties. The reorganization of the network due to external forces can impact liquid transport, potentially affecting biosignal transportation in native tissues.[12,59-62] We then examined the poroviscorelaxation behavior of hydrogels under a consistent normal strain (∼1s) while monitoring their ability to alleviate stress over time. **DN1-6** hydrogels exhibited a quick stress relaxation process, while **PN1-2** and **IPN1-2** hydrogels showed a slower process at the same time scale under a constant strain at 15% (Figure 3E-F, S14-15). Moreover, all the hydrogels exhibited two distinct fast relaxation processes at similar time scales (τ_1 and τ_2). Illustratively, the complete stress dissipation of **DN6** hydrogel required ∼1000s when subjected to a 15% strain. In contrast, both the **PN2** and **IPN2** hydrogels necessitated a more extended duration of 2000s to fully alleviate stress under identical conditions, illustrating that the supramolecular network and the polymerization crosslinkers serve as a sacrificial network primarily responsible for stress relaxation. The initial relaxation of **DN6** occurred during the second timeframe (∼7s) of the pause phase, with the hydrogel relaxing the mechanical load by ∼17% (Figure S16-17, Table S2). The second relaxation occurred around ∼249s with releasing a load of ∼88% The first relaxation time they stayed relatively constant for **DN1-3,** while the second relaxation stage reduced when the **SN** concentration increased. When polymer concentration increased to 2 wt%, the first relaxation time declined in **DN4-6** while the second relaxation was prolonged when the **SN** concentration increased. The shorter relaxation time could be attributed to the viscoelastic nature of the hydrogel resulting from the rapid fiber rupture. The longer relaxation time likely is connected to the network poroelasticity that originates from the loss of water in the gel. These results are likely related to the supramolecular polymer interactions and pore size of the network, demonstrating that the amount of polymer and supramolecular fiber network regulate its poroviscorelaxation behaviour. The augmentation of the **SN** concentration within the hydrogel corresponded to an increase in the relaxation amplitude, with relatively minimal alterations in the relaxation time.

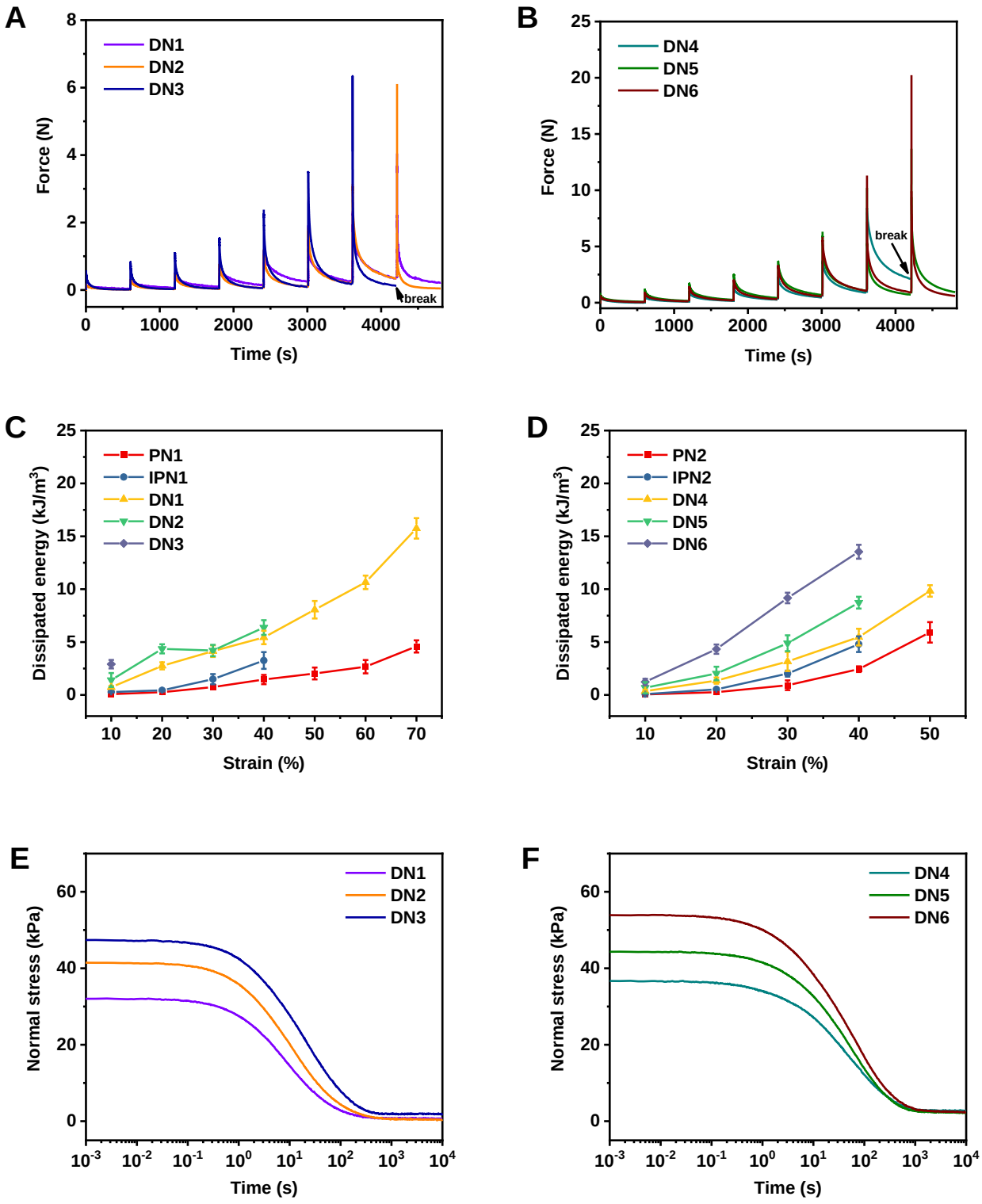

Figure 3. Step-stress relaxation curves of (A) **DN1-3**, and (B) **DN4-6** with increasing strain (5%) at the start of each loading cycle. Dissipated energy of at different maximum strains of (C) **PN1**, **IPN1** and **DN1-3**, (D) **PN2**, **IPN2** and **DN4-6** hydrogels, Mean ± SD, N ≥ 3. Poroviscorelaxation curves of (E) **DN1-3**, (F) **DN4-6** under 15% consistent normal strain.

Cross-sectional morphology and pore sizes of DN hybrid hydrogels

The pores of the hydrogel permit the exchange of oxygen and nutrients needed to sustain cell cultures.[63] Furthermore, their size and morphology will also affect the movement of water within the pores in response to an applied load impacting the mechanical behavior of the materials.[64] We imaged the pores by scanning electron microscopy (SEM) to check the pore structures and size from freeze-dried **DN** hydrogel cross-sections. The **DN** hydrogels exhibited pore structures with clear edges and a fibrous interconnected wall that supports the pores (Figure S18-19). The pore diameters fell within the range of ~13 µm - 21 µm and tended to decrease with a greater number of supramolecular filaments or polymer content, indicates that the incorporation of **SN** or **PN**, along with their crosslinking, in the **DN** hydrogels resulted in a reduction in pore size and a consequent increase gel mechanical properties as recorded in oscillatory rheology measurements. Transmission electron microscopy (TEM) images of diluted hydrogels **DN1** and **DN6** further confirmed their filament nanostructures (Figure S20).

The equilibrium water content (EWC) and stability under physiological conditions are critical features of hydrogel materials to determine for assessing their suitability for a given cell culture application.[65,66] We calculated the EWC for all crosslinked **DN1-6** and **PN1-2** hydrogels (Figure 4). All the hydrogels remained as gels after overnight equilibration before crosslinking, even with the addition of photoinitiators. After crosslinking by visible light (450 nm, LED) for 2 minutes, **PN1-2** hydrogels increased in weight by ~39 times - ~135 times leading to very high EWCs (~98% - ~100%). Owing to their higher network densities, **DN1** - **DN6** displayed slightly lower swelling ratios (29 - 45 times), and an EWC of ~96% - ~97%. Moreover, both **DN** and **PN** gels kept ~100% of their initial weight for 28 days showing little changes in mass or swelling ratio under physiological conditions. Gel inversion images on day 28 supports these measurements showing gels that are stable over the testing period. Overall, these **DN** hydrogels showed higher EWC than most other hydrogels, indicating their potential for long-term 3D cell culture.

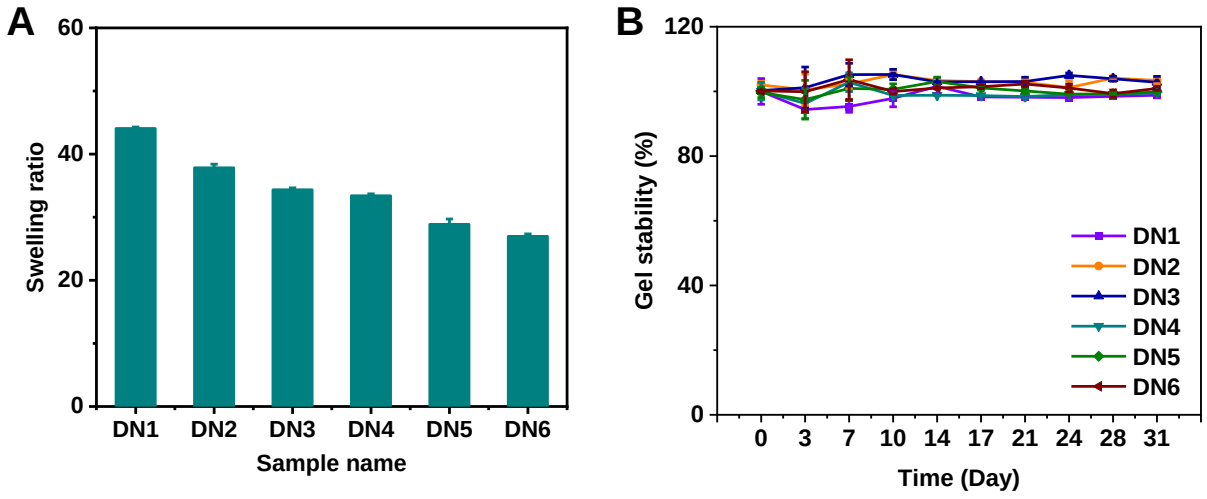

Figure 4. Characterization of **DN1-6** hydrogels. (A) Swelling ratios of photo-crosslinked **DN1-6** hydrogels in PBS after 24 hours. Mean ± SD, N ≥ 3. (B) Gel stability data of **DN1-6** hydrogels were kept in PBS at 37°C for 4 weeks. Mean ± SD, N ≥ 3.

Mechanical loading affects the matrix growth in 3D culture

To assess the suitability of visible-light-induced (450 nm) **DN** hybrid hydrogels as a synthetic platform for 3D cell culture applications, we first investigated cell viability of NIH 3T3 fibroblasts encapsulated within the hydrogels **DN1-6**. LIVE/DEAD staining revealed that all crosslinked **DN1-6** hydrogels exhibited high cell viability (>90% / 24h) (Figure S21-22). We then evaluated the viability of human primary articular chondrocytes (hPACs) within the materials. These primary cells also showed high cell viability (>90% / 24h, >80% / 48h) opening the door to examine the construction of 3D cartilage constructs within the materials *in vitro* (Figure S23-25).

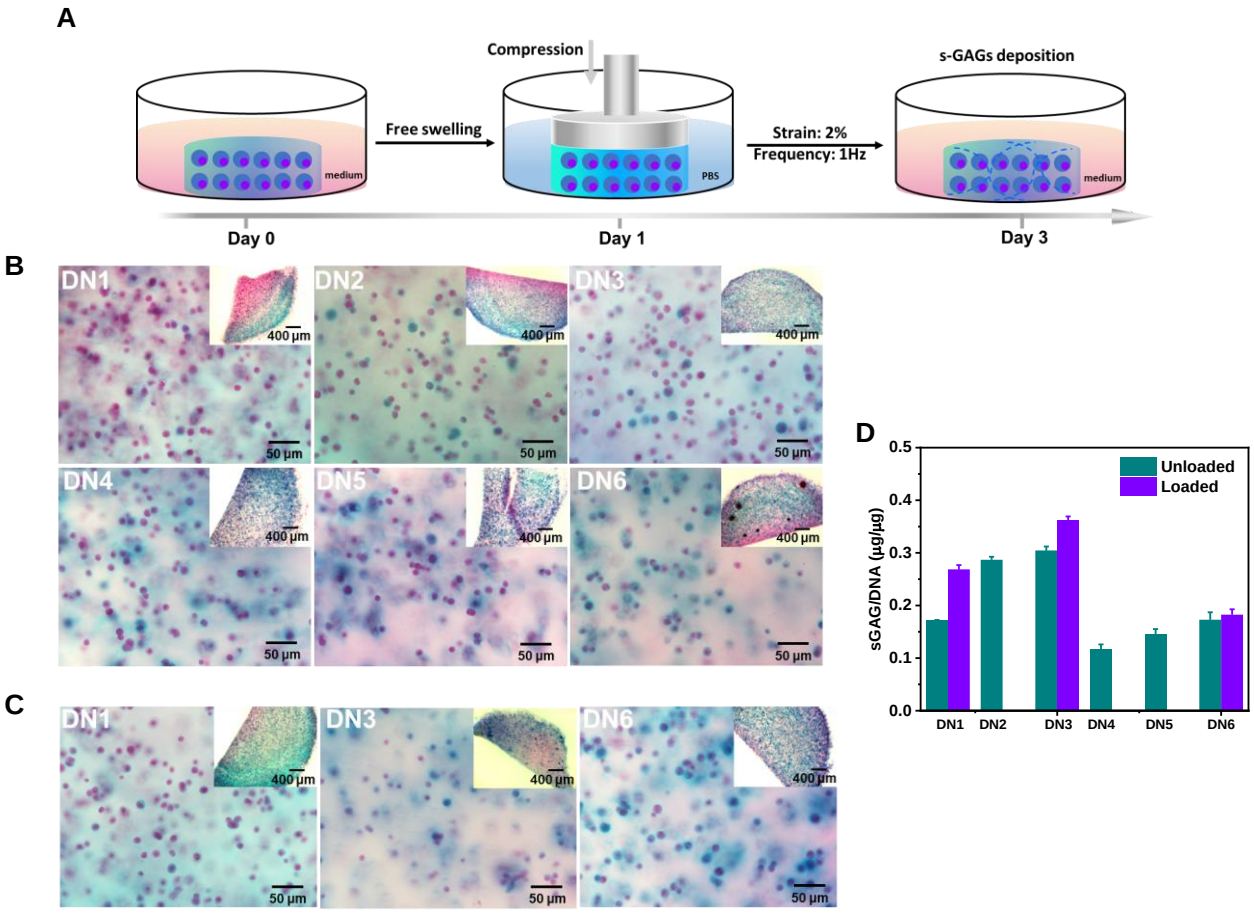

Figure 5. Influence of stiffness and soft loading on hPACs encapsulated in hydrogels **DN1-6**. (A) Scheme of hPACs-laden hydrogels and loading conditions during 3D chondrocyte culture. Alcian Blue staining for the s-GAGs with nuclear fast red counterstaining of hPACs in (B) crosslinked **DN1-6** hydrogels after 2 days culture in free swelling controls and (C) crosslinked **DN1, DN3** and **DN6** hydrogels after 2 days soft loading. Insert: an overview of hPACs-laden hydrogels. (D) s-GAGs deposition relative to DNA content using a DMMB assay. Visible light irradiation was applied through a benchtop of LED (~10 mW/cm^2, 450 nm).

Next, we investigated the effect of stiffness, a bioactive cue (SQ-RGD) and growth factor (TGF-β1) on hPACs by reading out matrix production within the gels.[1,67] Here we introduced a third monomer SQ-RGD based on C8-SQ with one arm modified with GGGRGDS peptide that binds cell surface integrins.[68] We stained the hPAC-laden hydrogels with Alcian Blue for sulfated-glycosaminoglycans (s-

GAGs) at the end of the culture period. **DN** hydrogels with the same polymer concentration, but with increased stiffness due to longer UV exposures showed increased degrees of matrix deposition. To further quantify matrix production, we performed the dimethyl-methylene blue (DMMB) assay. When comparing hydrogels **DN4**-**6**, **DN6** (~0.17 μg/μg) displayed the highest s-GAG quantity as compared to **DN5** (~0.14 μg/μg) and **DN4** (~0.12 μg/μg), which is on par with our previous results for hydrogel constructs of comparable stiffness (Figure 5). Hydrogels **DN1-3** exhibited a comparable pattern to **DN4-6**, but all of them demonstrated a higher level of s-GAGs deposition while maintaining an equivalent amount of the supramolecular network (**DN1**: ~0.17 μg/μg; **DN2**: ~0.28 μg/μg; **DN3**: ~0.30 μg/μg). In particular, **DN3** displayed the highest amount of s-GAG deposition among hydrogels **DN1-6**, surpassing **DN6** ~0.76 times and consistent with earlier reports suggesting that PEG hydrogels with excessive stiffness can hinder matrix deposition.[7,69,70] Removal of SQ-RGD in **DN6** did not impact matrix production in free swelling conditions, whereas the absence of TGF-β1 caused a noticeable decrease in s-GAGs deposition (Figure S26-27). Based on earlier reports that demonstrated the need for RGD peptides in mechanical loading experiments,[71] we used hydrogels **DN1-3** and **DN6** with 10% mole SQ-RGD for subsequent cyclic compressive loading experiments.

Cyclic compressive loading of the synthetic hydrogels *in vitro* can effectively enhance matrix production to mimic the native environment and stimulate biosynthesis in chondrocytes.[72-74] hPACs laden hydrogels (**DN1-3, DN6)** subjected to a soft compressive loading (2% strain, 1Hz) with a MACH-2 loading machine for two days (10 min/day) showed a pronounced effect on s-GAG deposition when compared to free swelling controls (**DN1**: ~0.27 μg/μg; **DN3**: ~0.36 μg/μg; **DN6**: ~0.18 μg/μg). Removal of SQ-RGD and TGF-β1 resulted in a slight increase in s-GAGs deposition consistent with the free swelling condition (Figure S26-27). Collectively, these results demonstrate that the **DN** hydrogels maintain the chondrogenic characteristics of hPACs and promote the generation of cartilaginous matrix with mechanical loading that can be useful for further exploration of these materials in chondrocyte culture.

4.3 Conclusion

We herein report the development of a supramolecular and covalent polymer-based **DN** hydrogel that can be applied for 3D chondrocyte culture with cyclic compressive loading. Rapid visible light photopolymerization between supramolecular and covalent networks using phenol chemistry yielded a double network hydrogel with covalent and non-covalent crosslinking strategies. Remarkably, the incorporation of filamentous supramolecular structures in the materials enhanced stress relaxation in both the shear and axial directions, even with increasing stiffness. The ratio of these chemical bonds could be tuned by the filamentous supramolecular and poly(ethylene glycol) network concentrations, therefore influencing the complex mechanics of the materials including their stress relaxation properties. The high compressive and fast, biomimetic stress relaxation behaviour of **DN** hydrogels permitted them to withstand cyclic compressive loads for 3D human primary articular chondrocytes culture. After two days of cyclic loading, the chondrocytes deposited crucial cartilage ECM polysaccharides and proteins as compared to the free swelling condition. Importantly, this visible-light induced phenol photopolymerization holds promise for fabricating mechanically enhanced double network hydrogels, particularly advantageous for supporting those sensitive 3D cell cultivation within dynamically loaded environments.

Reference

(1) Mostakhdemin, M.; Nand, A.; Ramezani, M. Articular and Artificial Cartilage, Characteristics, Properties and Testing Approaches-A Review. *Polymers (Basel)* **2021,** *13*, 2000.

(2) Makris, E. A.; Gomoll, A. H.; Malizos, K. N.; Hu, J. C.; Athanasiou, K. A. Repair and tissue engineering techniques for articular cartilage. *Nat Rev Rheumatol* **2015,** *11* (1), 21.

(3) Freedman, B. R.; Mooney, D. J. Biomaterials to Mimic and Heal Connective Tissues. *Adv. Mater.* **2019,** *31* (19), e1806695.

(4) Zhou, L.; Guo, P.; D'Este, M.; Tong, W.; Xu, J.; Yao, H.; Stoddart, M. J.; van Osch, G. J. V. M.; Ho, K. K.-W.; Li, Z.et al. Functionalized Hydrogels for Articular Cartilage Tissue Engineering. *Engineering* **2022,** *13*, 71.

(5) Yang, X.; Li, S.; Ren, Y.; Qiang, L.; Liu, Y.; Wang, J.; Dai, K. 3D printed hydrogel for articular cartilage regeneration. *Composites Part B: Engineering* **2022,** *237*, 109863.

(6) Wilusz, R. E.; Sanchez-Adams, J.; Guilak, F. The structure and function of the pericellular matrix of articular cartilage. *Matrix Biol.* **2014,** *39*, 25.

(7) Loebel, C.; Kwon, M. Y.; Wang, C.; Han, L.; Mauck, R. L.; Burdick, J. A. Metabolic labeling to probe the spatiotemporal accumulation of matrix at the chondrocyte–hydrogel interface. *Adv. Funct. Mater.* **2020,** *30* (44), 1909802.

(8) Guilak, F.; Nims, R. J.; Dicks, A.; Wu, C.-L.; Meulenbelt, I. Osteoarthritis as a disease of the cartilage pericellular matrix. *Matrix Biol.* **2018,** *71*, 40.

(9) Alexopoulos, L. G.; Williams, G. M.; Upton, M. L.; Setton, L. A.; Guilak, F. Osteoarthritic changes in the biphasic mechanical properties of the chondrocyte pericellular matrix in articular cartilage. *Journal of biomechanics* **2005,** *38* (3), 509.

(10) Yu, P.; Li, Y.; Sun, H.; Ke, X.; Xing, J.; Zhao, Y.; Xu, X.; Qin, M.; Xie, J.; Li, J. Cartilage-Inspired Hydrogel with Mechanical Adaptability, Controllable Lubrication, and Inflammation Regulation Abilities. *ACS Appl. Mater. Interfaces* **2022**, *14*, 27360.

(11) Timmermans, R. G. M.; Bloks, N. G. C.; Tuerlings, M.; van Hoolwerff, M.; Nelissen, R. G. H. H.; van der Wal, R. J. P.; van der Kraan, P. M.; Blom, A. B.; van den Bosch, M. H. J.; Ramos, Y. F. M.et al. A human *in vitro* 3D neo-cartilage model to explore the response of OA risk genes to hyper-physiological mechanical stress. *Osteoarthritis and Cartilage Open* **2022,** *4* (1), 100231.

(12) Caccavo, D.; Lamberti, G. PoroViscoElastic model to describe hydrogels' behavior. *Mater Sci Eng C Mater Biol Appl* **2017,** *76*, 102.

(13) Wang, Q.-M.; Mohan, A. C.; Oyen, M. L.; Zhao, X.-H. Separating viscoelasticity and poroelasticity of gels with different length and time scales. *Acta Mechanica Sinica* **2014,** *30* (1), 20.

(14) Nia, H. T.; Han, L.; Li, Y.; Ortiz, C.; Grodzinsky, A. Poroelasticity of cartilage at the nanoscale. *Biophys. J.* **2011,** *101* (9), 2304.

(15) Han, L.; Wang, M.; Li, P.; Gan, D.; Yan, L.; Xu, J.; Wang, K.; Fang, L.; Chan, C. W.; Zhang, H.et al. Mussel-Inspired Tissue-Adhesive Hydrogel Based on the Polydopamine-Chondroitin Sulfate Complex for Growth-Factor-Free Cartilage Regeneration. *ACS Appl. Mater. Interfaces* **2018,** *10* (33), 28015.

(16) Huang, D.; Huang, Y.; Xiao, Y.; Yang, X.; Lin, H.; Feng, G.; Zhu, X.; Zhang, X. Viscoelasticity in natural tissues and engineered scaffolds for tissue reconstruction. *Acta Biomater* **2019,** *97*, 74.

(17) Li, W.; Wu, D.; Hu, D.; Zhu, S.; Pan, C.; Jiao, Y.; Li, L.; Luo, B.; Zhou, C.; Lu, L. Stress-relaxing double-network hydrogel for chondrogenic differentiation of stem cells. *Mater Sci Eng C Mater Biol Appl* **2020,** *107*, 110333.

(18) Chaudhuri, O.; Cooper-White, J.; Janmey, P. A.; Mooney, D. J.; Shenoy, V. B. Effects of extracellular matrix viscoelasticity on cellular behaviour. *Nature* **2020,** *584* (7822), 535.

(19) Han, G.; Chowdhury, U.; Eriten, M.; Henak, C. R. Relaxation capacity of cartilage is a critical factor in rate- and integrity-dependent fracture. *Sci Rep* **2021,** *11* (1), 9527.
(20) Ma, C.; Du, T.; Niu, X.; Fan, Y. Biomechanics and mechanobiology of the bone matrix. *Bone Res.* **2022,** *10* (1), 59.
(21) Zhao, X.; Chen, X.; Yuk, H.; Lin, S.; Liu, X.; Parada, G. Soft Materials by Design: Unconventional Polymer Networks Give Extreme Properties. *Chem Rev* **2021,** *121* (8), 4309.
(22) Gu, Z.; Huang, K.; Luo, Y.; Zhang, L.; Kuang, T.; Chen, Z.; Liao, G. Double network hydrogel for tissue engineering. *Wiley Interdiscip Rev Nanomed Nanobiotechnol* **2018,** *10* (6), e1520.
(23) Sun, W.; Xue, B.; Li, Y.; Qin, M.; Wu, J.; Lu, K.; Wu, J.; Cao, Y.; Jiang, Q.; Wang, W. Polymer-Supramolecular Polymer Double-Network Hydrogel. *Adv. Funct. Mater.* **2016,** *26* (48), 9044.
(24) Rodell, C. B.; Dusaj, N. N.; Highley, C. B.; Burdick, J. A. Injectable and Cytocompatible Tough Double-Network Hydrogels through Tandem Supramolecular and Covalent Crosslinking. *Adv. Mater.* **2016,** *28* (38), 8419.
(25) Wang, H.; Zhu, D.; Paul, A.; Cai, L.; Enejder, A.; Yang, F.; Heilshorn, S. C. Covalently adaptable elastin-like protein - hyaluronic acid (ELP - HA) hybrid hydrogels with secondary thermoresponsive crosslinking for injectable stem cell delivery. *Adv. Funct. Mater.* **2017,** *27* , 1605609.
(26) Li, L.; Zhang, K.; Wang, T.; Wang, P.; Xue, B.; Cao, Y.; Zhu, L.; Jiang, Q. Biofabrication of a biomimetic supramolecular-polymer double network hydrogel for cartilage regeneration. *Materials & Design* **2020,** *189,* 108492.
(27) Hilderbrand, A. M.; Ford, E. M.; Guo, C.; Sloppy, J. D.; Kloxin, A. M. Hierarchically structured hydrogels utilizing multifunctional assembling peptides for 3D cell culture. *Biomater Sci* **2020,** *8* (5), 1256.
(28) Huang, L.; Abdalla, A. M. E.; Xiao, L.; Yang, G. Biopolymer-Based Microcarriers for Three-Dimensional Cell Culture and Engineered Tissue Formation. *Int J Mol Sci* **2020,** *21*, 1895.
(29) Feng, Z.; Zhao, J.; Li, Y.; Xu, S.; Zhou, J.; Zhang, J.; Deng, L.; Dong, A. Temperature-responsive in situ nanoparticle hydrogels based on hydrophilic pendant cyclic ether modified PEG-PCL-PEG. *Biomater Sci* **2016,** *4* (10), 1493.
(30) Tamesue, S.; Noguchi, S.; Kimura, Y.; Endo, T. Reversing Redox Responsiveness of Hydrogels due to Supramolecular Interactions by Utilizing Double-Network Structures. *ACS Appl Mater Interfaces* **2018,** *10* (32), 27381.
(31) Loebel, C.; Ayoub, A.; Galarraga, J. H.; Kossover, O.; Simaan-Yameen, H.; Seliktar, D.; Burdick, J. A. Tailoring supramolecular guest-host hydrogel viscoelasticity with covalent fibrinogen double networks. *J Mater Chem B* **2019,** *7* (10), 1753.
(32) Ouyang, L.; Highley, C. B.; Rodell, C. B.; Sun, W.; Burdick, J. A. 3D Printing of Shear-Thinning Hyaluronic Acid Hydrogels with Secondary Cross-Linking. *ACS Biomaterials Science & Engineering* **2016,** *2* (10), 1743.
(33) Richardson, B. M.; Walker, C. J.; Maples, M. M.; Randolph, M. A.; Bryant, S. J.; Anseth, K. S. Mechanobiological Interactions between Dynamic Compressive Loading and Viscoelasticity on Chondrocytes in Hydrazone Covalent Adaptable Networks for Cartilage Tissue Engineering. *Adv Healthc Mater* **2021,** *10* (9), e2002030.
(34) Richardson, B. M.; Walker, C. J.; Macdougall, L. J.; Hoye, J. W.; Randolph, M. A.; Bryant, S. J.; Anseth, K. S. Viscoelasticity of hydrazone crosslinked poly(ethylene glycol) hydrogels directs chondrocyte morphology during mechanical deformation. *Biomater Sci* **2020,** *8* (14), 3804.
(35) Chen, F. H.; Rousche, K. T.; Tuan, R. S. Technology Insight: adult stem cells in cartilage regeneration and tissue engineering. *Nat Clin Pract Rheumatol* **2006,** *2* (7), 373.
(36) Sophia Fox, A. J.; Bedi, A.; Rodeo, S. A. The basic science of articular cartilage: structure, composition, and function. *Sports Health* **2009,** *1* (6), 461.

(37) Soltanahmadi, S.; Raske, N.; de Boer, G. N.; Neville, A.; Hewson, R. W.; Bryant, M. G. Fabrication of Cartilage-Inspired Hydrogel/Entangled Polymer–Elastomer Structures Possessing Poro-Elastic Properties. *ACS Applied Polymer Materials* **2021,** *3* (5), 2694.
(38) Shirazi, R.; Shirazi-Adl, A.; Hurtig, M. Role of cartilage collagen fibrils networks in knee joint biomechanics under compression. *J Biomech* **2008,** *41* (16), 3340.
(39) Han, L.; Grodzinsky, A. J.; Ortiz, C. Nanomechanics of the Cartilage Extracellular Matrix. *Annu Rev Mater Res* **2011,** *41*, 133.
(40) Lim, K. S.; Galarraga, J. H.; Cui, X.; Lindberg, G. C.; Burdick, J. A.; Woodfield, T. B. Fundamentals and applications of photo-cross-linking in bioprinting. *Chem. Rev.* **2020,** *120* (19), 10662.
(41) Zhu, Y.; Chen, J.; Liu, H.; Zhang, W. Photo-cross-linked Hydrogels for Cartilage and Osteochondral Repair. *ACS Biomaterials Science & Engineering* **2023,** *9* (12), 6567.
(42) Summonte, S.; Racaniello, G. F.; Lopedota, A.; Denora, N.; Bernkop-Schnürch, A. Thiolated polymeric hydrogels for biomedical application: Cross-linking mechanisms. *J. Controlled Release* **2021,** *330*, 470.
(43) Muir, V. G.; Burdick, J. A. Chemically modified biopolymers for the formation of biomedical hydrogels. *Chem. Rev.* **2020,** *121* (18), 10908.
(44) Zheng, Z.; Eglin, D.; Alini, M.; Richards, G. R.; Qin, L.; Lai, Y. Visible light-induced 3D bioprinting technologies and corresponding bioink materials for tissue engineering: a review. *Engineering* **2021,** *7* (7), 966.
(45) Li, X.; Li, Y.; Zhang, X.; Xu, J.; Kang, J.; Li, B.; Zhao, B.; Wang, L. Cross-Linking Methods of the Silk Protein Hydrogel in Oral and Craniomaxillofacial Tissue Regeneration. *Tissue Engineering and Regenerative Medicine* **2024**, *1*, 529.
(46) Tong, C.; Liu, T.; Saez Talens, V.; Noteborn, W. E.; Sharp, T. H.; Hendrix, M. M.; Voets, I. K.; Mummery, C. L.; Orlova, V. V.; Kieltyka, R. E. Squaramide-based supramolecular materials for three-dimensional cell culture of human induced pluripotent stem cells and their derivatives. *Biomacromolecules* **2018,** *19* (4), 1091.
(47) Tong, C.; Liu, T.; Saez Talens, V.; Noteborn, W. E. M.; Sharp, T. H.; Hendrix, M.; Voets, I. K.; Mummery, C. L.; Orlova, V. V.; Kieltyka, R. E. Squaramide-Based Supramolecular Materials for Three-Dimensional Cell Culture of Human Induced Pluripotent Stem Cells and Their Derivatives. *Biomacromolecules* **2018,** *19* (4), 1091.
(48) Tong, C.; Wondergem, J. A. J.; Heinrich, D.; Kieltyka, R. E. Photopatternable, Branched Polymer Hydrogels Based on Linear Macromonomers for 3D Cell Culture Applications. *ACS Macro Lett.* **2020,** *9* (6), 882.
(49) Fairbanks, B. D.; Schwartz, M. P.; Halevi, A. E.; Nuttelman, C. R.; Bowman, C. N.; Anseth, K. S. A versatile synthetic extracellular matrix mimic via thiol-norbornene photopolymerization. *Advanced materials* **2009,** *21* (48), 5005.
(50) Means, A. K.; Grunlan, M. A. Modern Strategies To Achieve Tissue-Mimetic, Mechanically Robust Hydrogels. *ACS Macro Lett* **2019,** *8* (6), 705.
(51) Tang, S.; Richardson, B. M.; Anseth, K. S. Dynamic covalent hydrogels as biomaterials to mimic the viscoelasticity of soft tissues. *Prog. Mater Sci.* **2021,** *120*, 100738.
(52) Chaudhuri, O. Viscoelastic hydrogels for 3D cell culture. *Biomaterials science* **2017,** *5* (8), 1480.
(53) Sanchez-Adams, J.; Leddy, H. A.; McNulty, A. L.; O'Conor, C. J.; Guilak, F. The mechanobiology of articular cartilage: bearing the burden of osteoarthritis. *Curr. Rheumatol. Rep.* **2014,** *16* (10), 451.
(54) Doi, M. Gel dynamics. *J. Phys. Soc. Jpn.* **2009,** *78* (5), 052001.
(55) Yamaue, T. The stress diffusion coupling in the swelling dynamics of cylindrical gels. *The Journal of chemical physics* **2005,** *122* (8), 3466.
(56) Mow, V. C.; Wang, C. C.; Hung, C. T. The extracellular matrix, interstitial fluid and ions as a mechanical signal transducer in articular cartilage. *Osteoarthritis and Cartilage* **1999,** *7* (1), 41.

(57) Jahn, S.; Seror, J.; Klein, J. Lubrication of articular cartilage. *Annual review of biomedical engineering* **2016,** *18*, 235.
(58) June, R. K.; Mejia, K. L.; Barone, J. R.; Fyhrie, D. P. Cartilage stress-relaxation is affected by both the charge concentration and valence of solution cations. *Osteoarthritis Cartilage* **2009,** *17* (5), 669.
(59) Khayyeri, H.; Gustafsson, A.; Heuijerjans, A.; Matikainen, M. K.; Julkunen, P.; Eliasson, P.; Aspenberg, P.; Isaksson, H. A fibre-reinforced poroviscoelastic model accurately describes the biomechanical behaviour of the rat Achilles tendon. *PLoS One* **2015,** *10* (6), e0126869.
(60) Oftadeh, R.; Connizzo, B. K.; Nia, H. T.; Ortiz, C.; Grodzinsky, A. J. Biological connective tissues exhibit viscoelastic and poroelastic behavior at different frequency regimes: Application to tendon and skin biophysics. *Acta Biomater* **2018,** *70*, 249.
(61) Oyen, M. L. Mechanical characterisation of hydrogel materials. *Int. Mater. Rev.* **2013,** *59* (1), 44.
(62) Han, G.; Hess, C.; Eriten, M.; Henak, C. R. Uncoupled poroelastic and intrinsic viscoelastic dissipation in cartilage. *J Mech Behav Biomed Mater* **2018,** *84*, 28.
(63) Leal-Egaña, A.; Braumann, U.-D.; Díaz-Cuenca, A.; Nowicki, M.; Bader, A. Determination of pore size distribution at the cell-hydrogel interface. *Journal of nanobiotechnology* **2011,** *9* (1), 1.
(64) Loh, Q. L.; Choong, C. Three-dimensional scaffolds for tissue engineering applications: role of porosity and pore size. *Tissue Eng Part B Rev* **2013,** *19* (6), 485.
(65) Kerin, A.; Wisnom, M.; Adams, M. The compressive strength of articular cartilage. *Proc. Inst. Mech. Eng. H: J. Eng. Med.* **1998,** *212* (4), 273.
(66) Maganaris, C. N.; Paul, J. P.; J. Physiol., 1999.
(67) Huang, G.; Li, F.; Zhao, X.; Ma, Y.; Li, Y.; Lin, M.; Jin, G.; Lu, T. J.; Genin, G. M.; Xu, F. Functional and Biomimetic Materials for Engineering of the Three-Dimensional Cell Microenvironment. *Chem. Rev.* **2017,** *117* (20), 12764.
(68) Tong, C.; Wondergem, J. A. J.; van den Brink, M.; Kwakernaak, M. C.; Chen, Y.; Hendrix, M.; Voets, I. K.; Danen, E. H. J.; Le Devedec, S.; Heinrich, D.et al. Spatial and Temporal Modulation of Cell Instructive Cues in a Filamentous Supramolecular Biomaterial. *ACS Appl. Mater. Interfaces* **2022,** *14* (15), 17042.
(69) Lee, H.-p.; Gu, L.; Mooney, D. J.; Levenston, M. E.; Chaudhuri, O. Mechanical confinement regulates cartilage matrix formation by chondrocytes. *Nat. Mater.* **2017,** *16* (12), 1243.
(70) Tan, Y.; Huang, H.; Ayers, D. C.; Song, J. Modulating viscoelasticity, stiffness, and degradation of synthetic cellular niches via stoichiometric tuning of covalent versus dynamic noncovalent cross-linking. *ACS central science* **2018,** *4* (8), 971.
(71) Villanueva, I.; Weigel, C. A.; Bryant, S. J. Cell–matrix interactions and dynamic mechanical loading influence chondrocyte gene expression and bioactivity in PEG-RGD hydrogels. *Acta Biomater.* **2009,** *5* (8), 2832.
(72) Chen, C.; Tambe, D. T.; Deng, L.; Yang, L. Biomechanical properties and mechanobiology of the articular chondrocyte. *American Journal of Physiology-Cell Physiology* **2013,** *305* (12), C1202.
(73) Mauck, R. L.; Soltz, M. A.; Wang, C. C.; Wong, D. D.; Chao, P.-H. G.; Valhmu, W. B.; Hung, C. T.; Ateshian, G. A. Functional tissue engineering of articular cartilage through dynamic loading of chondrocyte-seeded agarose gels. *J. Biomech. Eng.* **2000,** *122* (3), 252.
(74) Bryant, S. J.; Chowdhury, T. T.; Lee, D. A.; Bader, D. L.; Anseth, K. S. Crosslinking density influences chondrocyte metabolism in dynamically loaded photocrosslinked poly (ethylene glycol) hydrogels. *Annals of biomedical engineering* **2004,** *32*, 407.

Supporting information

S4.1 Materials and methods

Materials

4 arm-poly(ethylene glycol) (4arm-PEG-OH, Mw: 10 kDa) was purchased from JenKem Technology. Deuterated solvents for NMR experiments were obtained from Euriso-top. Water was deionized before use. Formvar/Carbon 200 Mesh Copper grids were purchased from Electron Microscopy Sciences. Dulbecco's modified Eagle medium (DMEM) was received from Gibco, Life Technologies. Fetal bovine serum (FBS) was achieved from Biowest. The antibiotics penicillin and streptomycin were purchased from Gibco. µ-Slide 15 Well 3D chambered cover plates were purchased from Ibidi. N, N'-Dicyclohexylcarbodiimide, piperidine, Dulbecco's phosphate-buffered saline (DPBS, pH=7.4), calcein AM, propidium iodide (PI), Alcian Blue 8-GX, nuclear fast red-aluminum sulfate and all other commercially available chemicals were obtained from Sigma Aldrich at the highest purity available and directly used without further purification. 3-(4-(tert-butoxy)phenyl)propanoic acid,[1] monomers **C8-SQ**, **SQ-RGD**, **PEG-TOS (4)**, **PEG-N_3 (5)**, **C8-CBZ (6)** were synthesized as previously described[2]. Milli-Q water was employed for all the experiments. All compounds were stored at -20^{o}C before use.

Methods

^{1}H-NMR and ^{13}C-NMR spectra were collected at room temperature (RT) on a Bruker DMX-400. All supramolecular monomers were purified by high-performance liquid chromatography (HPLC) on a Shimadzu system equipped with two LC-20AR pumps, an SPD-20A UV-Vis detector and a Phenomenex Kinetex EVO C18 column. The mobile phases were CH_3CN and H_2O with 0.1% trifluoroacetic acid. Liquid chromatography-mass spectrometry (LC-MS) analysis was performed on a Finnigan Surveyor HPLC system (with UV-Vis detection from 200-600 nm) equipped with a Gemini C18 50 x 4.60 mm reverse phase column coupled to Finnigan LCQ Advantage Max mass spectrometer with ESI. A gradient of 10-90% of CH_3CN/H_2O with 0.1% trifluoroacetic acid over 13.5 minutes was used for the mobile phase. The supramolecular fibers were imaged on a JEOL JEM-1400 Plus transmission electron microscope (TEM). The surface morphology and pore sizes of the lyophilized hydrogels were imaged by scanning electron microscope (SEM). Oscillatory rheology experiments were performed on a Discovery Hybrid Rheometer (DHR-2) from TA Instruments with a Smart Swap visible light assembly with a quartz lower plate (20 mm) and an aluminum upper plate (8 mm) at RT at a fixed gap of 500 µm, visible light was applied through an OmniCure S2000 high-pressure mercury light source with a filter (λ = 400-500 nm, primary peak: 450 nm) equipped from Excelitas connected to the rheometer through a light guide (5 mm diameter). The visible light intensity was calibrated using an OmniCure radiometer sensor accessory. Compression experiments were performed under the same conditions on the rheometer but with a fixed gap of 1.2 mm and a maximum axial force of 50 N. Both NIH 3T3 fibroblast cells and human primary articular chondrocytes (hPACs)were cultured in Dubecco's modified Eagle medium (DMEM) with high glucose, with 10% fetal calf serum, 0.1% GlutaMAX, 0.2% penicillin and 0.2% streptomycin. hPACs were counted on NucleoCounter NC-200 from ChemoMetec. Images to assess cell viability in 3D cultures were captured on an LSM 710 confocal laser scanning microscope from Zeiss. Compressive mechanical loading of the 3D cell cultures in the hydrogels were performed continuously in cycles at RT on a MACH-

1 mechanical tester from Biomomentum. Confocal fluorescent images of immunostained 3D cell cultures were acquired on a Stellaris 8 confocal laser scanning microscope from Leica with a white light laser (440-790 nm) and Power HyD detectors. Alcian Blue staining images were taken in brightfield on a light microscope from Olympus. A microplate reader from BioTek Synergy HT was used to quantify sulfated glycosaminoglycan (s-GAGs) content through the dimethyl methylene blue (DMMB) assay using measured absorbance values at 525 and 595 nm. A benchtop LED light (~10 mW/cm², 450 nm) was employed to initiate crosslinking in all other samples except for the ones on the rheometer.

Synthetic routes

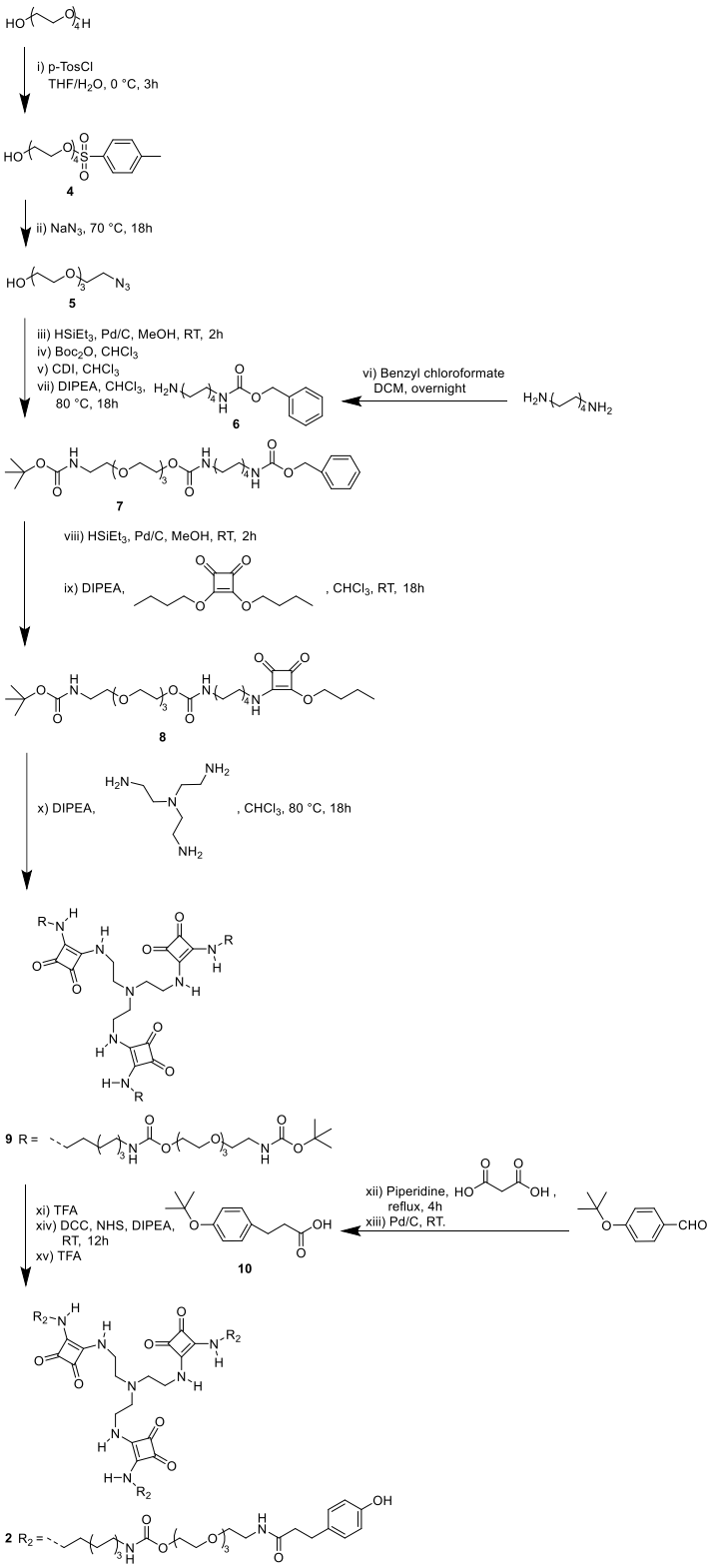

Figure S1. Synthetic route of monomer **SQ-Phe (2)**.

Synthetic procedures

Synthesis of 7

5 (2.68 g, 12.37 mmol) was dissolved in dry CH_3OH (5 mL), palladium on carbon (100.0 mg, 0.9 mmol) was added and degassed with N_2 for 10 min. Triethylsilane (3.95 mL, 24.74 mmol) was added dropwise and left stirring at RT for 2 hours, filtered through Celite, washed with CH_3OH, and concentrated to yield a clear oil which was used directly. $CHCl_3$ (20 mL) was added to the crude, followed by adding boc-anhydride (2.98 g, 13.64 mmol) and DIPEA (3.23 mL, 18.56 mmol) under RT for 3 hours before using rotary evaporation to concentrate which was used directly. The intermediate was confirmed by TLC. 1,1'-carbonyldiimidazole (3.02 g, 18.56 mmol) was added to the reaction of intermediate at RT stirring for 1h. The activated intermediate was verified by TLC. **6** (4.80 g, 17.2 mmol, 1.5 equiv) and $CHCl_3$ (20 mL) was added to the activated intermediate and the mixture was heated to reflux at 80°C overnight. Once the reaction was finished, $CHCl_3$ (30 mL) was added and washed 3x with water. The organic layers were combined, dried with sodium sulfate, and concentrated. The concentrate was purified using silica column chromatography (CH_2Cl_2/EtOAc, 99/1-95/5-90/10, v/v) and dried under vacuum to afford the product as a white solid.

Yield: 33.13%, 2.45 g. ^{1}H-NMR ($CDCl_3$, 400 MHz): 7.36-7.29 (m, 5H), 5.09 (s, 2H), 4.97 (br s, 1H), 4.91 (br s, 1H), 4.22-4.19 (m, 2H), 3.74-3.52 (m, 12H), 3.32-3.29 (m, 2H), 3.20-3.12 (m, 4H), 1.5-1.47 (m, 12H), 1.32-1.29 (m, 9H). ^{13}C-NMR ($CDCl_3$, 100 MHz): 156.59, 137.19, 130.21, 128.68, 128.25, 117.33, 85.91, 70.74, 70.67, 70.44, 69.88, 66.72, 63.95, 41.22, 40.54, 30.08, 29.29, 28.60, 28.06, 26.79. HRMS (ESI) m/z: $[M+H]^+$ calcd. for $C_{30}H_{52}N_3O_9$ 598.36981; found: 598.36931. LC-MS: t=7.73 min, m/z: 620.23 $[M+Na]^+$.

Synthesis of 8

Palladium on carbon (80.0 mg, 0.72 mmol) was added to a solution of **7** (0.933 g, 1.56 mmol) in dry CH_3OH (5 mL) and degassed with N_2 for 10 min. Triethylsilane (2.45 mL, 3.12 mmol) was added dropwise and left stirring at RT for 2 hours, filtered through Celite, washed with CH_3OH, concentrated and used directly. 3,4-dibutoxy-3-cyclobutene-1,2-dione (0.40 mL, 1.87 mmol) and DIPEA (992.87 µL, 5.7 mmol) were added into the intermediate dissolved in $CHCl_3$ (20 mL) and heated to reflux at 80°C overnight, $CHCl_3$ (30 mL) was added and extracted 3x with $CHCl_3$. The organic layers were combined, dried with sodium sulfate, and concentrated. The concentrate was purified using silica column chromatography (Pet ether/EtOAc, 10/90-90/10, v/v) and dried under vacuum to afford the product as a white solid.

Yield: 56.32%, 541.81 mg. ^{1}H-NMR ($CDCl_3$, 400 MHz): 7.82-7.78 (t, 1H), 5.50-5.47 (br s, 1H), 5.42-5.39 (br s, 1H), 4.76-4.72 (t, 2H), 4.24-4.18 (m, 2H), 3.73-3.55 (m, 12H), 3.45-3.40 (m, 2H), 3.32-3.28(m, 2H), 3.16-3.11 (m, 2H), 1.83-1.73 (m, 2H), 1.66-1.59 (m, 2H), 1.51-1.24 (m, 21H), 1.00-0.93 (m, 3H). ^{13}C-NMR ($CDCl_3$, 100 MHz): 189.18, 188.63, 182.76, 182.46, 176.77, 172.57, 172.33, 156.25, 155.80, 78.61, 72.84, 70.12, 70.08, 69.77, 69.22, 63.81, 63.36, 60.01, 44.43, 44.21, 40.57, 39.98, 31.65, 30.61, 30.21, 29.51, 28.75, 28.68, 28.06, 26.27, 25.96, 18.29, 18.17, 13.33. HRMS (ESI) m/z: $[M+H]^+$ calcd. for $C_{30}H_{54}N_3O_{10}$: 616.38037; found: 616.38008. LC-MS: t=7.33 min, m/z: found: 616.48 $[M+H]^+$.

Synthesis of 9

Tris(2-aminoethyl)amine (46.06 mg, 0.32 mmol) and DIPEA (167.22 µL, 0.96 mmol) were added into a solution of **8** (642.10 g, 1.04 mmol) dissolved in $CHCl_3$ (20 mL) under nitrogen. The reaction mixture was on reflux at 80°C overnight, concentrated and purified on silica column chromatography (EtOAc/CH_3OH-CH_2Cl_2/CH_3OH, 100/00-80/20, v/v). The product was concentrated by rotary evaporation and dried in a vacuum overnight to obtain a brownish oil.

Yield: 42.9%, 23.92 mg. ^{1}H-NMR (DMSO-d_6, 400 MHz): 7.73 (br s, 5H), 5.37-5.11 (m, 5H), 4.20-4.17 (m, 6H), 3.77-3.51 (m, 48H), 3.31-3.27 (m, 6H), 3.13-3.08(m, 6H), 2.71 (br s, 4H), 2.28 (br s, 2H), 1.61-1.26 (m, 63H). ^{13}C-NMR (DMSO-d_6, 100 MHz): 182.94, 169.22, 167.11, 156.66, 156.29, 79.34, 70.69, 70.61, 70.46, 70.35, 69.84, 63.90, 54.52, 44.83, 42.74, 41.17, 40.52, 31.26, 30.09, 29.40, 28.59, 26.90, 26.63, 18.98, 17.67, 12.62. HRMS (ESI) m/z: $[M+H]^+$ calcd. for $C_{84}H_{148}N_{13}O_{27}$: 1771.06021; found: 1771.06021. LC-MS: t= 6.77 min, m/z: 1770.20 $[M]^+$.

Synthesis of 10

10 was synthesized according to a published protocol[1]. In detail, 4-(tert-butoxy)benzaldehyde (1.22 mL, 7.05 mmol) was dissolved in pyridine (20 mL) under a nitrogen flow, and malonic acid (1.10 g, 10.53 mmol) was added. 10 min later, piperidine (207.51 µL, 2.10 mmol) was added dropwise and the solution was refluxed for 3 h. Afterward, hydrochloric acid (8 mL, 1 M) was used to acidify the solution extracted 3x with EtOAc (25 mL). The organics were combined, dried with sodium sulfate, and concentrated to obtain a yellowish solid. Next, the obtained yellowish solid was dissolved in dry THF (25 mL), palladium on carbon (500 mg, 4.69 mmol) was added and the mixture was stirred under a hydrogen balloon overnight, filtered through Celite, extracted with CH_2Cl_2 and CH_3OH, and concentrated. The concentrate was purified on silica column chromatography (EtOAc/n-hexanes, 90/10-50/50, v/v). The product was concentrated by rotary evaporation and dried in a vacuum overnight to obtain a white solid.

Yield: 42.9%, 2.5 g. ^{1}H-NMR (DMSO-d_6, 400 MHz): 7.15-7.09 (d, 2H), 6.90-6.84 (d, 2H), 2.83-2.73 (t, 2 H), 2.54-2.47 (t, 2 H), 1.27 (s, 9 H). ^{13}C-NMR (DMSO-d_6, 100 MHz): 153.73, 135.32, 128.76, 124.42, 78.58, 36.22, 30.27, 28.92. HRMS m/z: $[M+H]^+$ calcd. for $C_{13}H_{17}O_3$: 221.1178; found 221.1167. LC-MS: t= 2.02min, m/z: 221.01 $[M+H]^+$.

Synthesis of 2

N, N'-Dicyclohexylcarbodiimide (34.81 mg, 0.169 mmol, 1 equiv) was added to a solution of **10** (37.46 mg, 0.169 mmol) in dry CH_2Cl_2 (10mL) and reacted for 30 min at RT. N-Hydroxysuccinimide (19.45 mg, 0.169 mmol) was added to the reaction and further reacted overnight at RT. The mixture was filtered and concentrated to obtain a white NHS-activated product without further purification. In another flask, **9** (50 mg, 0.028 mmol) was dissolved in TFA/CH_2Cl_2 (2 mL, 1/1, v/v) and stirred at RT for 40 min before removing TFA by a gentle stream of nitrogen. Dry DMF (10 mL) and DIPEA (24.38 µL, 0.14 mmol) were added to the intermediate and stirred for 20 min. Subsequently, the NHS-activated product was added to the reaction and the mixture was stirred at RT overnight. Afterward, the mixture was flushed with nitrogen, followed by adding TFA/CH_2Cl_2 (5 mL, 1/1, v/v) and stirring for 2 hours. The crude was concentrated and purified on silica column chromatography (EtOAc/CH_3OH-CH_2Cl_2/CH_3OH,

100/00-80/20, v/v) to obtain a brownish oil. The compound was further purified by HPLC with UV detection and lyophilized to harvest the white solid compound.

Yield: 42.9%, 23.01 mg. ^{1}H-NMR (DMSO-d_6, 400 MHz): 9.47-8.68 (br s, 3H), 8.33-8.29 (s, 1H), 7.94-7.80 (t, 3H), 7.75-7.25 (br d, 6H), 7.22-7,12 (m, 3H), 7.00-6.91 (m, 6H), 6.67-6.56 (m, 6H), 4.08-3.96 (t, 6H), 3.62-3.30 (m, 54H), 3.21-3.12 (m, 6H), 2.35-2.22 (t, 6H), 2.98-2.88 (m, 6H), 2.71-2.61 (t, 6H), 1.56-1.32 (m, 12H), 1.32-1.09 (m, 24H); ^{13}C-NMR (DMSO-d_6, 100 MHz): 182.90, 172.10, 156.65, 155.91, 148.12, 131.87, 129.14, 115.19, 70.26, 70.23, 70.07, 69.66, 69.41, 63.49, 40.70, 38.98, 37.94, 31.19, 30.84, 29.90, 29.19, 29.13, 26.74, 26.36. HRMS (ESI) m/z: $[M+H]^+$ calcd. for $C_{96}H_{148}N_{13}O_{27}$: 1916.30345; found: 1916.06335. LC-MS: t= 6.05 min, m/z 1915.33 $[M]^+$.

PEG-4Phe

N, N'-Dicyclohexylcarbodiimide (DCC) (0.83 g, 4.0 mmol) was added dropwise into a stirring solution of 3-(4-(tert-butoxy)phenyl)propanoic acid (0.88 g, 4.0 mmol) in CH_2Cl_2 (10 mL) at RT. A white precipitate was immediately observed after the DCC addition. 4arm-PEG-OH (Mw: 10 kDa) (2.0 g, 0.2 mmol), pyridine (129.2 µL, 1.6 mmol) and DMAP (0.024 g, 0.2 mmol) were stirred at RT in CH_2Cl_2 (10 mL) in another flask separately. After 30 min stirring, the two solutions were combined, and the mixture was further reacted overnight at RT. Afterward, the mixture was filtered, and concentrated by rotary evaporation before being precipitated in cold diethyl ether, washed and re-dissolved in CH_2Cl_2. The precipitation step was repeated three times. The obtained concentrated liquid was then reacted with 50% TFA in CH_2Cl_2(v/v) overnight. The reacted solution was concentrated by a stream of nitrogen gas and removed TFA, re-dissolved in Milli-Q water, dialyzed for three days, and lyophilized overnight to obtain a white solid. Yield: 1.75 g, 87.5%. ^{1}H-NMR ($CDCl_3$, 400 MHz): 7.07-6.98 (d, 8H), 6.82-6.74 (d, 8H), 4.26-4.16 (d, 8H), 3.89-3.34 (m, 904H), 2.92-2.80 (t, 8H), 2.68-2.54 (t, 8H).

The degree of phenol group functionalization was confirmed by ^{1}H-NMR ($CDCl_3$, 400 MHz) using the integral ratio of the alkene protons on the PEG adjacent to ester bond (4.26-4.16 ppm, 7.42H), to that of actual value for complete conversion (4.26-4.16 ppm, 8H), which was found to be around 92.8%. The protons (3.89-3.34 ppm, 226H) were used for calibration.

Hybrid hydrogel preparation and gel inversion experiments

Stock solutions of C8-SQ (10 mM) and SQ-Phe (10 mM) were prepared separately by dissolving the monomers in DMSO with 3 min vortexing. Aliquots of C8-SQ (10 mM) and SQ-Phe (10 mM) were mixed at different ratios as needed. For example, to prepare C8-SQ/5SQ-Phe (with the total monomer concentration containing 5 mol% SQ-Phe) hydrogels at the required concentration and volume, C8-SQ (83.6 µL, 10 mM) and SQ-Phe (4.4 µL, 10 mM) stock solutions were pipetted into the glass vials (2.0 mL) with 1 min of gentle vortexing to obtain the C8-SQ/5SQ-Phe (8.8 mM, 100 µL) hydrogel. Subsequently, the solutions were dried overnight under a stream of nitrogen gas to obtain dried films. PBS (pH 7.4, 100 µL) was added to the films of supramolecular monomers and sonication was performed in an ice bath (~4 °C) yielding a clear solution. The sample was kept on ice until further usage. To prepare the **DN1-6** hydrogels, a stock solution of PEG-4Phe (10 wt %) was prepared in PBS (pH 7.4). The C8-SQ/5SQ-Phe (8.8 mM) hydrogel and PEG-4Phe (10%) were mixed after calculation to obtain the determined hydrogels. For example, to prepare **DN1** hydrogel (100 µL without photoinitiators), 22.7 µL of C8-

SQ/5SQ-Phe (8.8 mM) hydrogel, 10 µL of PEG-4Phe (10 wt %) and 57.3 µL PBS were mixed within the vail for further usage.

All the samples were left to equilibrate overnight before further use. Photoinitiator tris(bipyridine)ruthenium(II) chloride (Ru, 44 mM) and sodium persulfate (SPS, 440 mM) were prepared separately. Pre-determined volumes of Ru and SPS stock solutions were added into prepared gels and gently pipetted 10 times to evenly mix them before use. For example, for a 100 µL volume of the **DN** hydrogel, 1.25 µL of Ru (44 mM), 1.25 µL of SPS (440 mM) and 7.5 µL of PBS were added for **DN1-3**, 1.63 µL of Ru (44 mM), 1.63 µL of SPS (440 mM) and 6.74 µL of PBS for **DN4-6** were added. The mixture was pipetted gently to mix well prior to visible light-mediated crosslinking of the gels.

The critical gelation concentration (CGC) was defined as the minimum concentration of a given compound to form a hydrogel. The CGC of **PN** and **DN** hydrogels was determined by the gel inversion method. **PN1-2** and **DN1-6** hydrogels were prepared with PBS in 2 mL glass vials as described above. Digital photos of the inverted vials containing gels were taken before crosslinking, after crosslinking by irradiating with visible light for 2 min using a benchtop LED source (~10 mW/cm^2, 450 nm) and after incubating in 37^{o}C oven for 28 days (Figure S1-2).

Hydrogel Swelling Performance and Gel Stability Test

Hydrogel swelling ratios were measured after crosslinking and swollen for 24 h until a constant weight was reached. Gel stability data was acquired by weighing hydrogels at different time points. Hydrogels were prepared with PBS (100 µL) as described before in 2 mL glass vials, equilibrated overnight, prior to crosslinking with photoinitiators for 2 min by using a benchtop LED (λ=450 nm, ~ 10 mW/cm^2). The hydrogels were covered with PBS (300 µL) and kept at 37^{o}C in an oven for 4 weeks. Digital photos were obtained before crosslinking, after crosslinking and 28 days after maintenance in PBS at 37^{o}C. The weight was recorded at different time points as W*wet*. Hydrogels' W*equ* were recorded until the constant weight of hydrogels was reached. After 15 days, the hydrogels were lyophilized, and the dried products were weighed as W*dry*. Hydrogel swelling ratios were calculated using the formula: $Swelling\ Ratio = (Wequ - Wdry)/Wdry$. Gel stability was calculated using the formula: $Gel\ erosion\% = 100 \times (Wwet - Wdry)/Wequ$. Each condition was performed in triplicate.

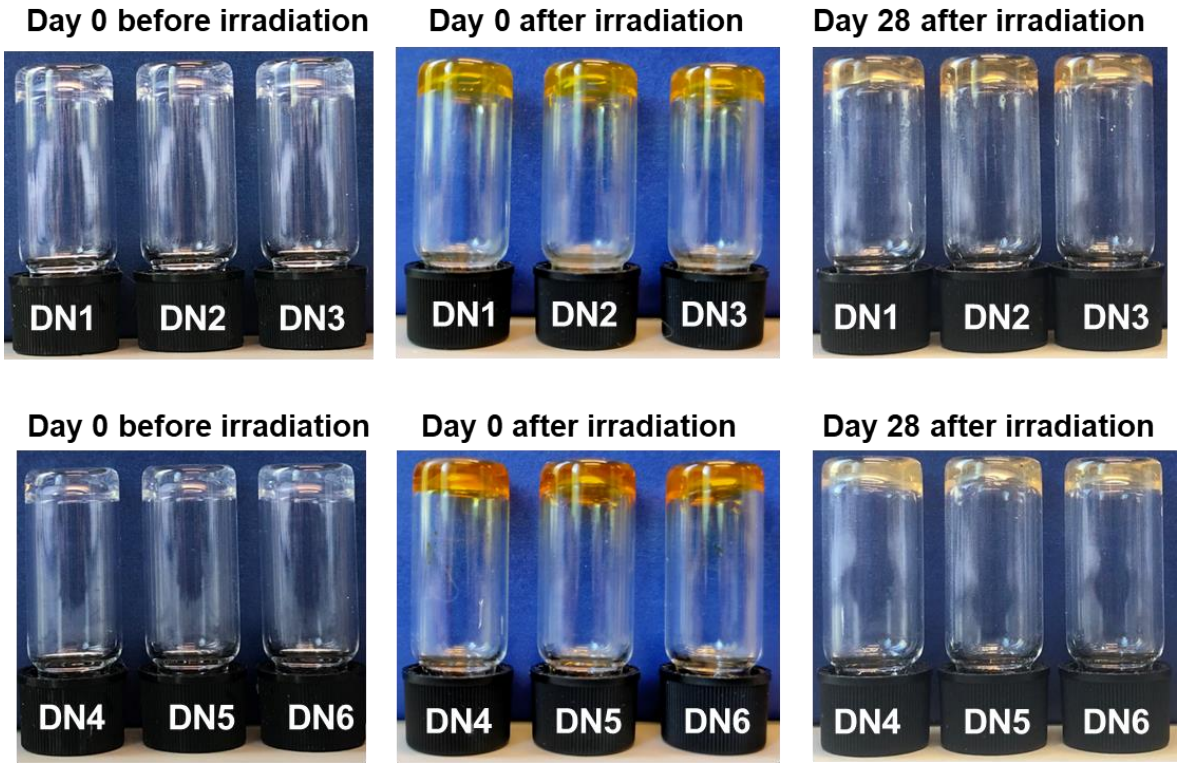

Figure S2. Gels inversion experiments of **DN1-6** hydrogels after 2 min visible light irradiation using a benchtop of LED.

Oscillatory rheology study

The prepared hydrogels (**SN**, **IPN1-2**, **DN1-6**) (45 µL) and **PN1-2** solutions (42 µL) prior to photocorsslinking were gently pipetted onto the quartz plate of the rheometer. The upper plate was then lowered to a gap distance of 500 µm. The loaded samples were equilibrated for 5 min before data collection and the samples were then exposed to visible light for 3 min. Time sweeps (frequency = 1.0 Hz, strain = 0.05%), frequency sweeps from 0.01 to 10 Hz (strain = 0.05%), and strain sweeps from 0.01 to 2000% (frequency = 1.0 Hz) were collected.

The stress relaxation behaviour of photocrosslinked hydrogels was measured at a constant strain of 10%. The creep and recovery behavior of photocrosslinked hydrogels were performed after a time sweep of 600 s with a fixed strain (0.01%) and frequency (1.0 Hz). The strain in response to a constant stress (300 Pa) was measured for 3600 s, after which the stress was removed, and the strain was measured for another 10,000 s. PBS was carefully added surrounding the hydrogels to prevent the drying process.

Table S1. Plateau storage moduli of the various hydrogels (**SN**, **PN1-2**, **IPN1-2** and **DN1-6**) with different compositions (e.g., supramolecular monomer concentration, SQ-Phe mol% in **SN**, total polymer concentration) and visible light exposure times. Averaged storage moduli are presented (N ≥ 3).

Sample name	Composition				Visible light exposure time (min)	Storage modulus before visible light exposure (Pa)	Storage modulus after visible light exposure (Pa)
	SN (mM)	**SQ** (mol%)	**SQ-Phe** (mol%)	**PEG** (wt%)			
SN	6	95	5	0	3	10 ± 4	3861 ± 698
PN1	0	0	0	1	10	S	1286 ± 198
PN2	0	0	0	2	10	S	2132 ± 259
IPN1	6	100	0	1	10	8 + 5	3858 ± 341
IPN2	6	100	0	2	3	8 + 4	9054 ± 293
DN1	2	95	5	1	3	5 ± 3	10306 ± 1563
DN2	4	95	5	1	3	6 ± 4	16083 ± 3216
DN3	6	95	5	1	3	10 ± 8	22873 ± 7465
DN4	2	95	5	2	3	5 ± 4	15031 ± 2234
DN5	4	95	5	2	3	6 ± 5	21902 ± 3978
DN6	6	95	5	2	3	11 ± 7	31956 ± 3233

[S]: Solution.

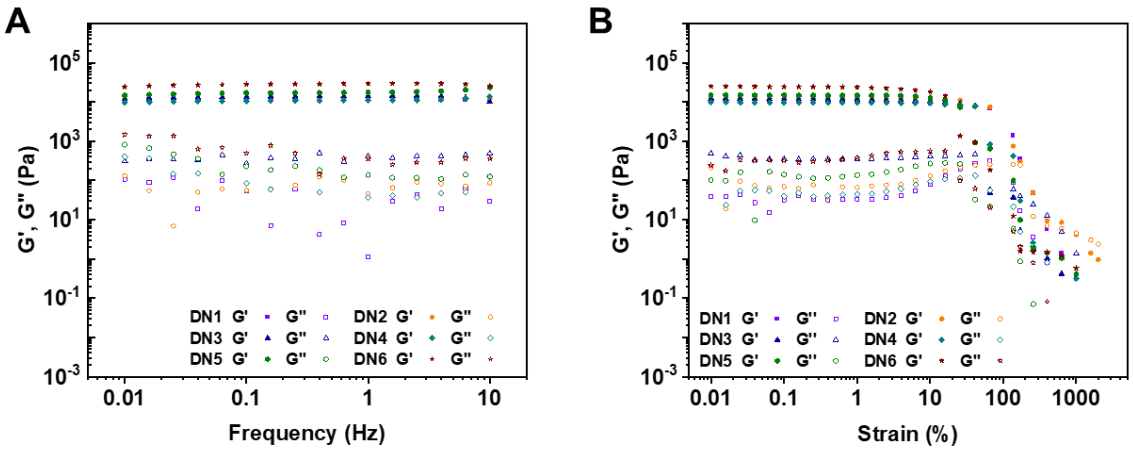

Figure S3. Averaged (N = 3) (A) frequency (0.1-10 Hz) and (B) strain (0.01-2000%) sweeps of **DN1** - **DN6** hydrogels after 3 min visible light irradiation at RT. The frequency sweep experiment was performed at a fixed strain (0.05%), and the strain experiment was collected at a constant frequency (1.0 Hz).

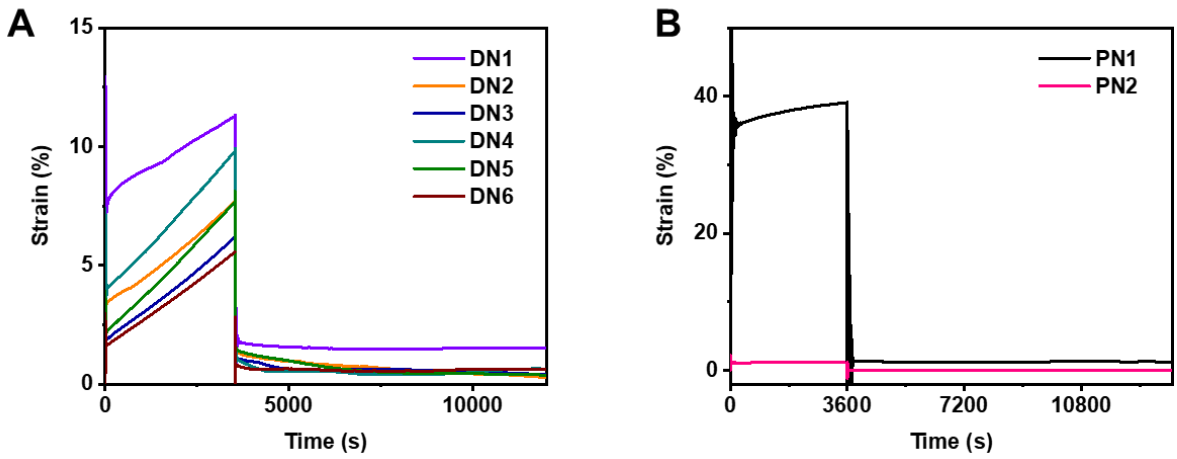

Figure S4. Creep and recovery test of (A) **DN1-6** and (B) **PN1-2** after photocrosslinking. A constant stress of 500 Pa was applied to the **DN1-6** samples and 50 Pa was applied to the **PN1-2** samples.

Compression test

The prepared samples before photocrosslinking (75 µL) were gently pipetted onto the quartz plate of the rheometer and the upper plate was lowered to 1.2 mm. The samples were equilibrated for 5 min before data collection. After a time sweep experiment of 60 s, the samples were photocrosslinked for 3 min to reach a plateau in storage modulus. PBS was carefully placed around the samples immediately after the samples were fully crosslinked to prevent evaporation during the measuring period. Afterward, an axial compression test was set up to compress the sample ~80 % of its initial height (0.2 mm gap) at different rates (100-0.1 µm/s). The compression modulus was calculated from the slope of the linear region of the compressive stress-strain curve (**SN**: strain = 0-1.35%, **PN**; **IPN** and **DN**: strain = 0-5%). Energy dissipation was probed on the photocrosslinked hydrogels by cyclic compression tests with an increasing strain percentage from 10% to 80% at a rate of 10 µm/s and then removing the load. The compression cycle was started immediately again after the release of the load. Compressive stress relaxation tests on the photocrosslinked hydrogels were performed starting with applying 10% strain to the sample at a rate of 100 µm/s. The hydrogels were compressed for 600 s at this strain percentage and stress relaxation was monitored. Steps of 10% strain were then applied to the material in sequence for the same amount of time until a maximum of 80% strain was achieved. The curves were plotted until the hydrogel was fractured. Poroviscoelastic relaxation tests on photocrosslinked hydrogels were measured by applying a 15% consistent strain at a rate of 150 µm/s, and the stress relaxation was monitored for another 10 000s. A two-term exponential decay model was used to fit the load-log(t) graphs at a compressive strain of 15% to obtain time constants[3,4]:

$$y = y_0 + Ae^{-\left(\frac{t}{\tau_1}\right)} + Be^{-C\left(\frac{t}{\tau_2}\right)^D}$$

Here, y_0 represents the load value (kPa) after complete stress-relaxation, t indicates the time during the pause phase (s), A and B are coefficients related to y_0 (kPa). Additionally, C and D are coefficients correlated to geometric compression and the strain limit, while τ_1 and τ_2 signify characteristic short-term and long-term stress-relaxation time scales, respectively. These six fitting

parameters (A, B, C, D, τ_1, and τ_2) were determined using a built-in nonlinear curve fitting tool in Origin (OriginLab Corporation) for stress-relaxation curve fitting. The time was set to 0s when the strain reached 15% and the maximum stress value obtained. The accuracy of the least-squares fitting algorithm was evaluated using residual plots, residual sum of squares, and adjusted R^2 values. The comparison to global minima was based on the sum of squared errors between the actual data points and the best-fit curve.

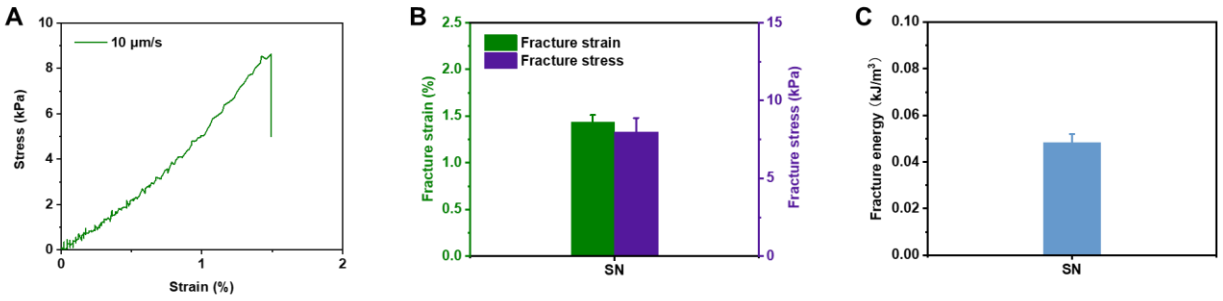

Figure S5. Mechanical properties of **SN** hydrogel: (A) Uniaxial stress-strain curves of **SN** at a 10 μm/s compression speed. (B) Compressive fracture strain, fracture stress **SN** hydrogel. (F) Fracture energy of **SN** hydrogel. Mean ± SD, N ≥ 3.

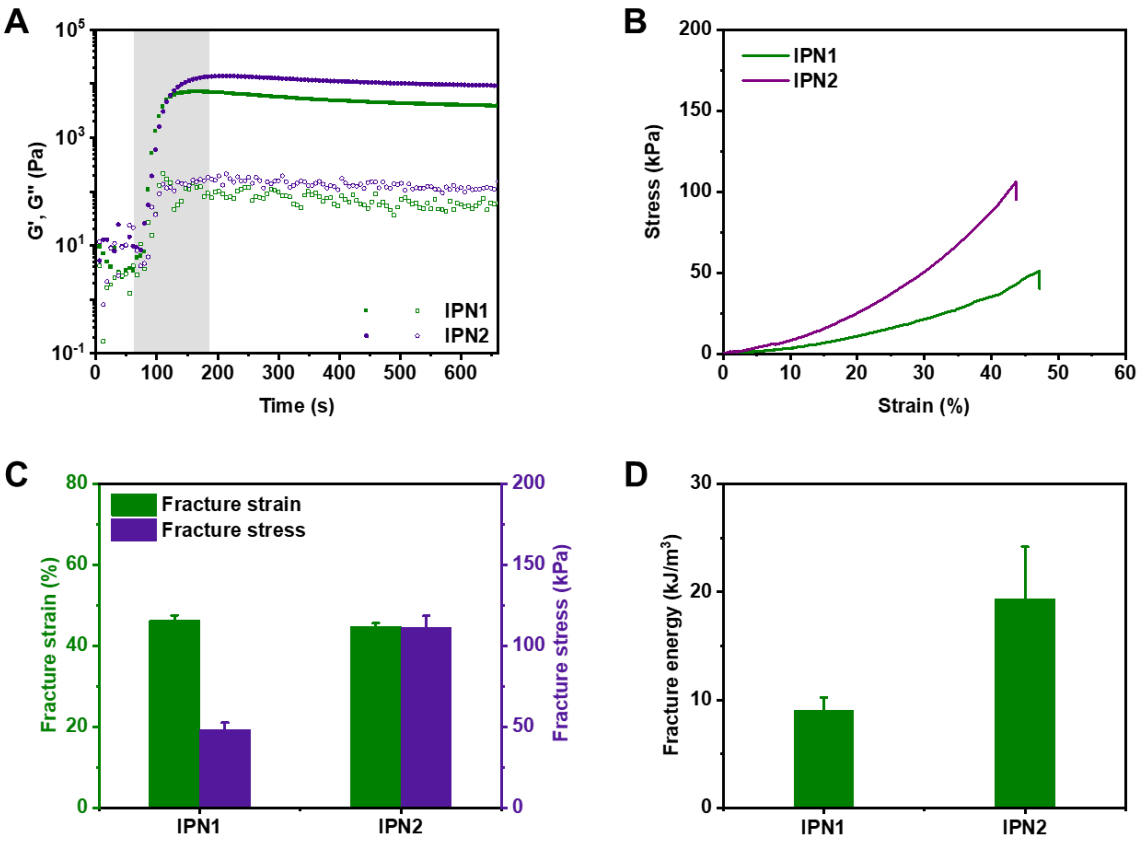

Figure S6. Mechanical properties of **IPN1-2** hydrogels: (A) Time sweep experiment after 3 min visible light exposure. Grey regions indicate visible light exposure. (B) Uniaxial stress-strain curves of **IPN1-2** hydrogels at 10 μm/s compression speed.

(C) Compressive fracture strain, fracture stress of **IPN1-2** hydrogels. (F) Fracture energy of **IPN1-2** hydrogels. Mean ± SD, N ≥ 3.

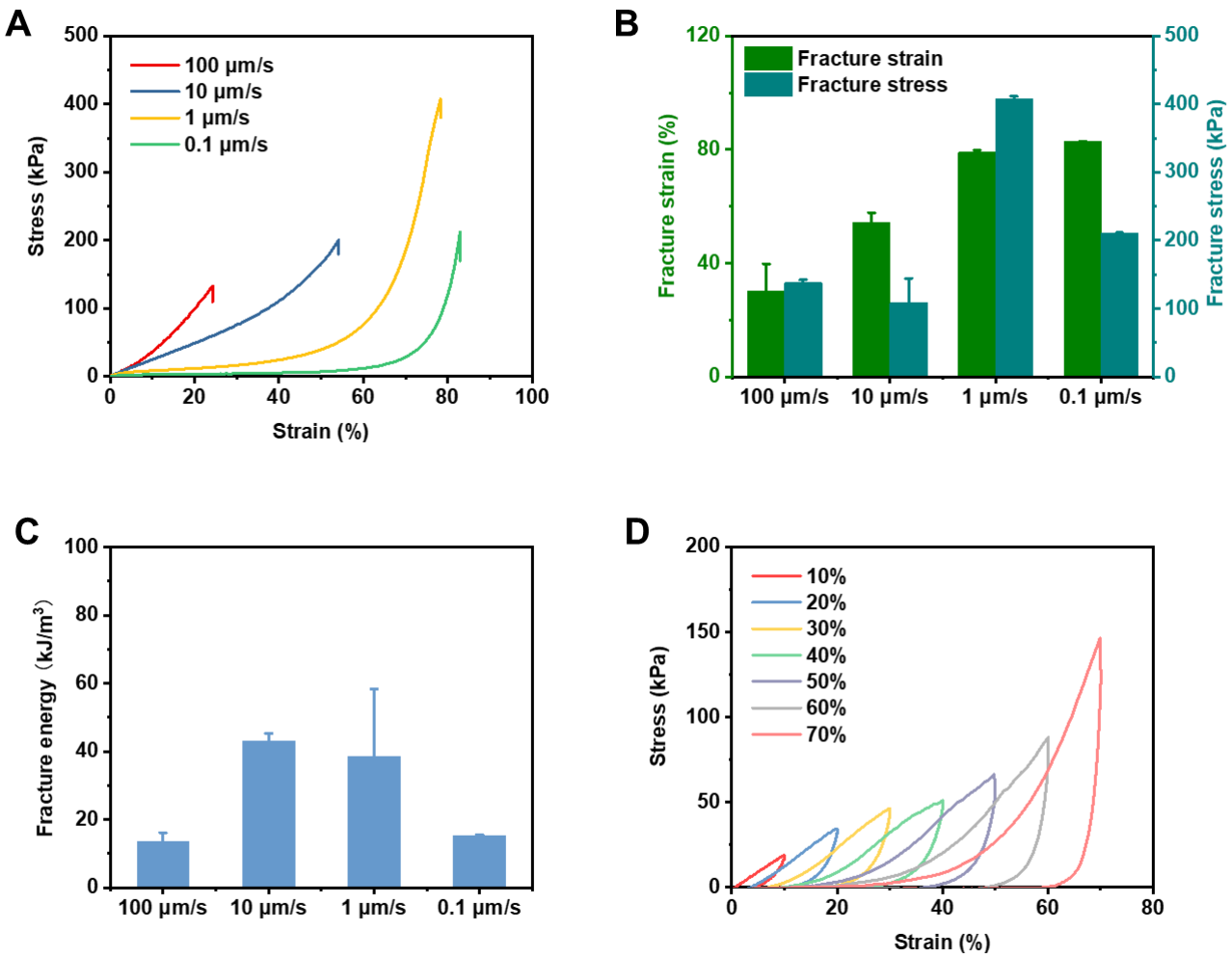

Figure S7. Mechanical properties of **DN1** hydrogel: (A) Uniaxial stress-strain curves at different compression speeds. (B) Compressive fracture strain, and fracture stress at different compression speeds. (C) Fracture energy at different compression speeds. (D) Step-stress relaxation curves with increasing strain (10%) at the start of each loading cycle. Mean ± SD, N ≥ 3.

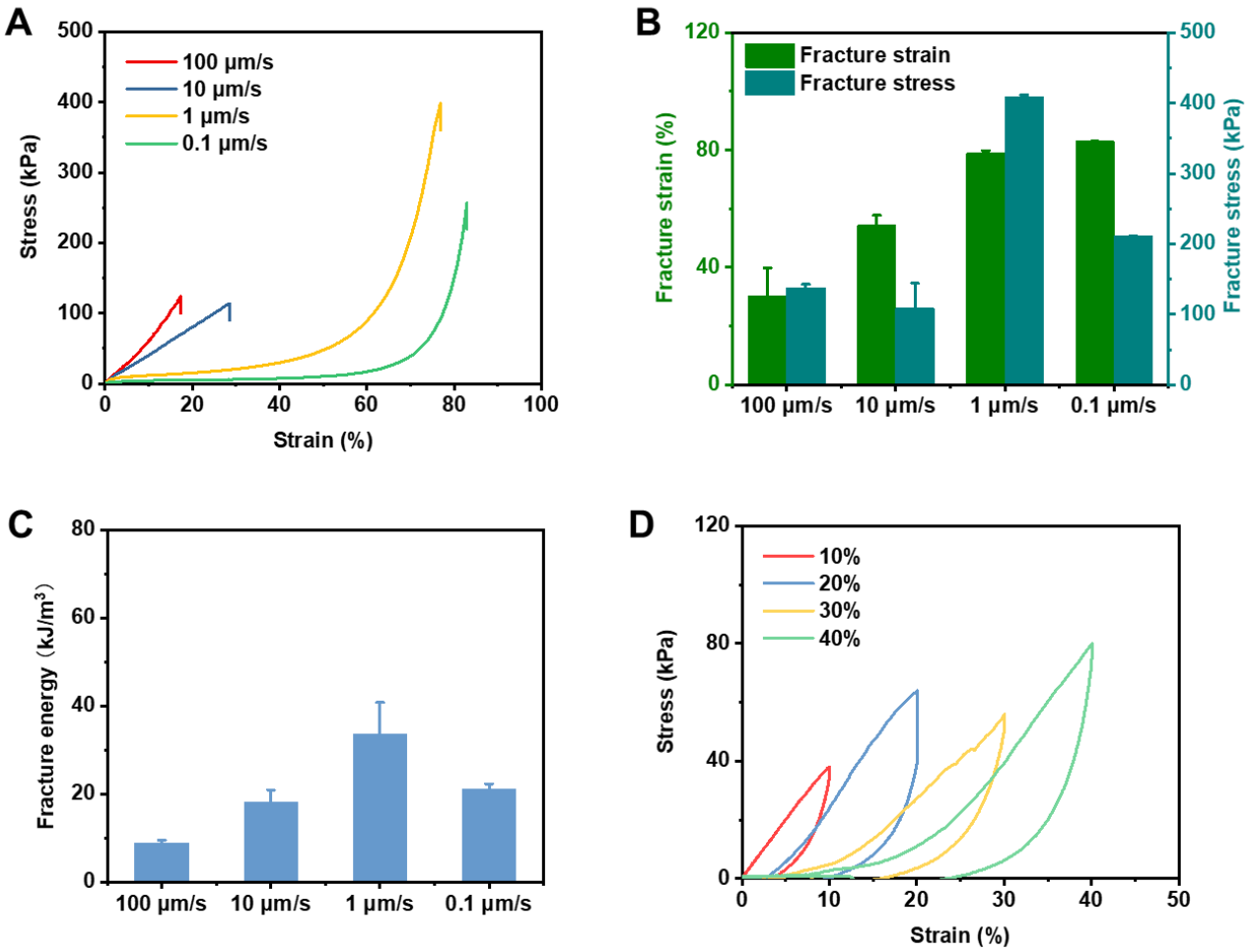

Figure S8. Mechanical properties of **DN2** hydrogel: (A) Uniaxial stress-strain curves at different compression speeds. (B) Compressive fracture strain, and fracture stress at different compression speeds. (C) Fracture energy at different compression speeds. (D) Step-stress relaxation curves with increasing strain (10%) at the start of each loading cycle. Mean ± SD, N ≥ 3.

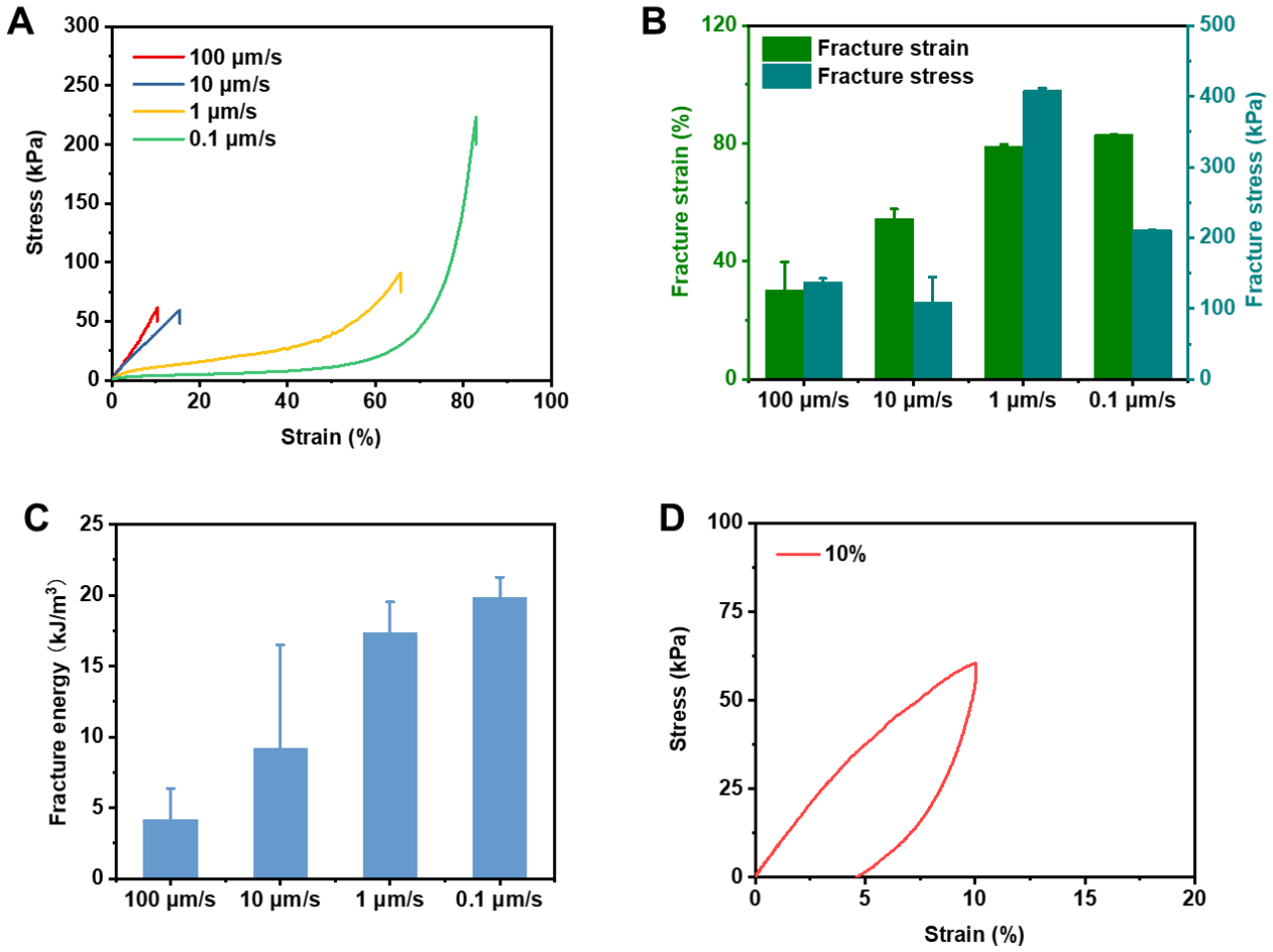

Figure S9. Mechanical properties of **DN3** hydrogel: (A) Uniaxial stress-strain curves at different compression speeds. (B) Compressive fracture strain, and fracture stress at different compression speeds. (C) Fracture energy at different compression speeds. (D) Step-stress relaxation curves with increasing strain (10%) at the start of each loading cycle. Mean ± SD, N ≥ 3.

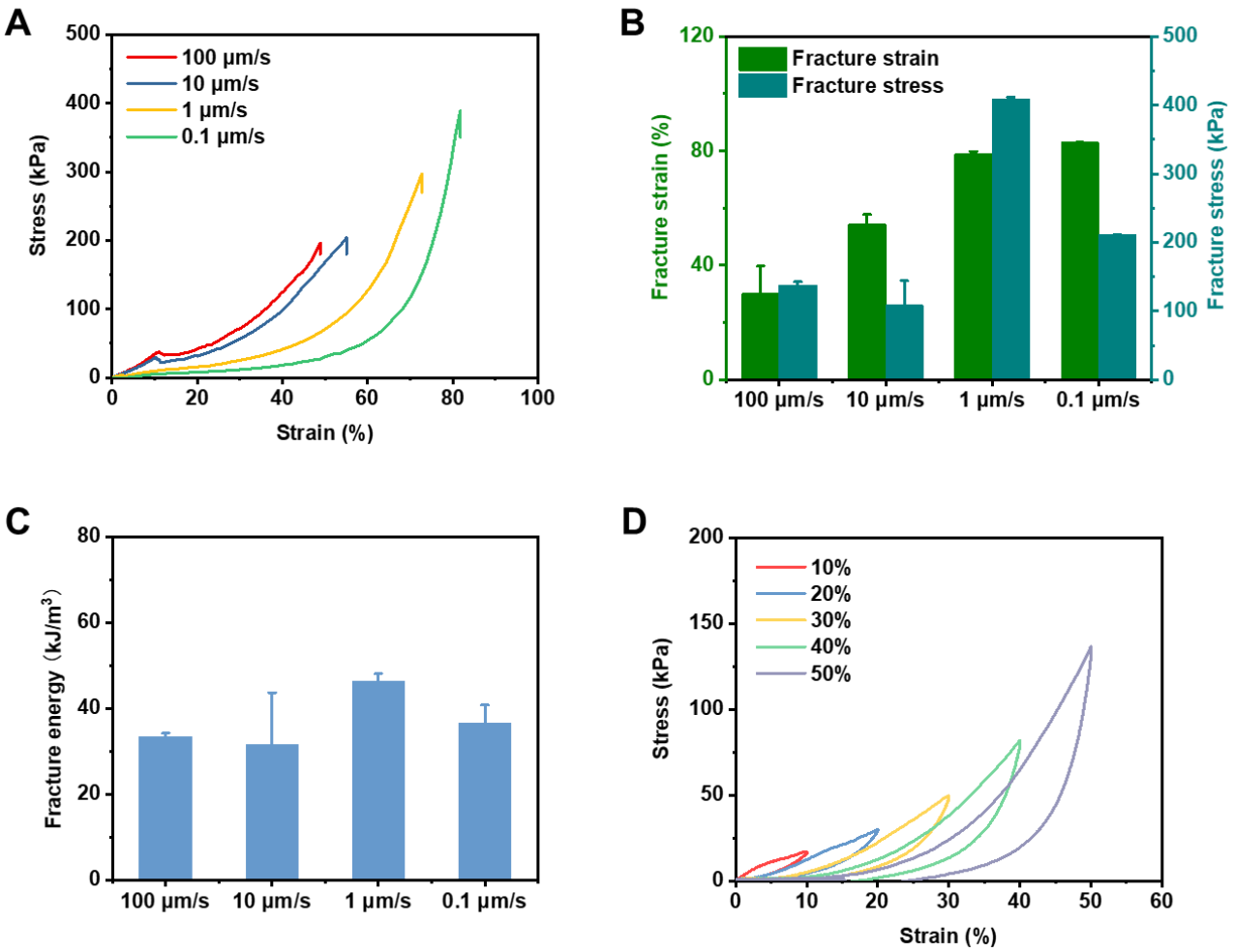

Figure S10. Mechanical properties of **DN4** hydrogel: (A) Uniaxial stress-strain curves at different compression speeds. (B) Compressive fracture strain, and fracture stress at different compression speeds. (C) Fracture energy at different compression speeds. (D) Step-stress relaxation curves with increasing strain (10%) at the start of each loading cycle. Mean ± SD, N ≥ 3.

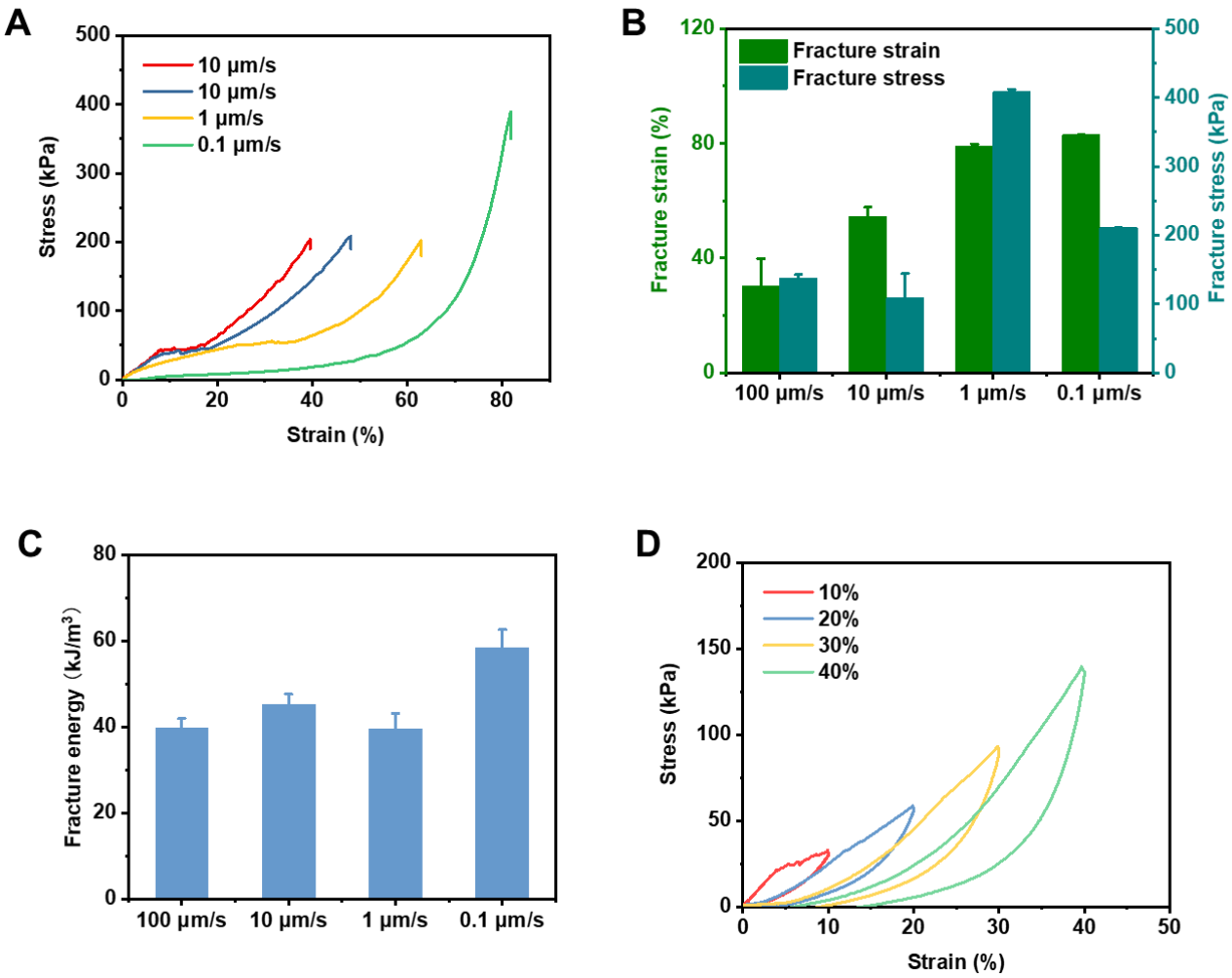

Figure S11. Mechanical properties of **DN5** hydrogel: (A) Uniaxial stress-strain curves at different compression speeds. (B) Compressive fracture strain, and fracture stress at different compression speeds. (C) Fracture energy at different compression speeds. (D) Step-stress relaxation curves with increasing strain (10%) at the start of each loading cycle. Mean ± SD, N ≥ 3.

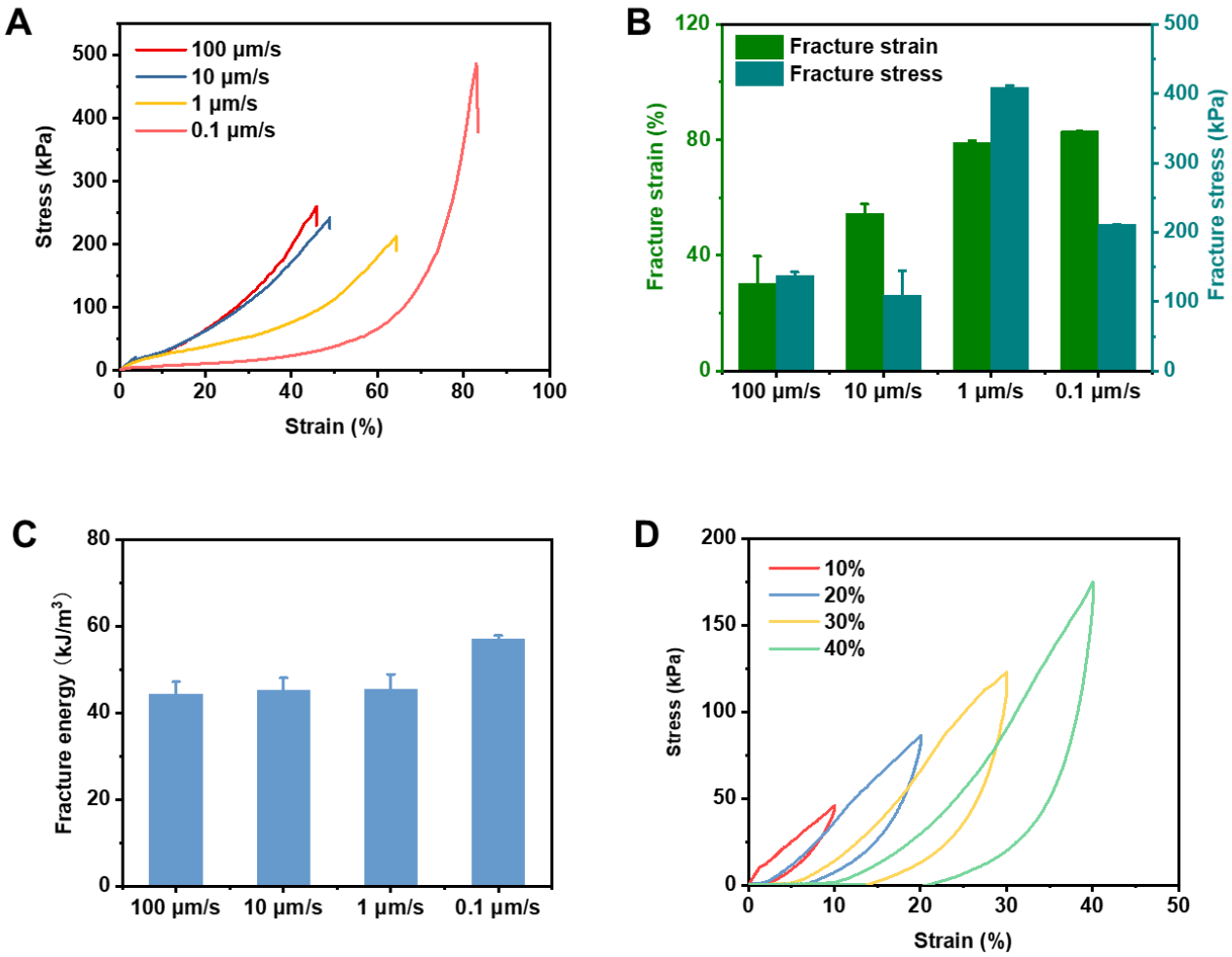

Figure S12. Mechanical properties of **DN6** hydrogel: (A) Uniaxial stress-strain curves at different compression speeds. (B) Compressive fracture strain, and fracture stress at different compression speeds. (C) Fracture energy at different compression speeds. (D) Step-stress relaxation curves with increasing strain (10%) at the start of each loading cycle. Mean ± SD, N ≥ 3.

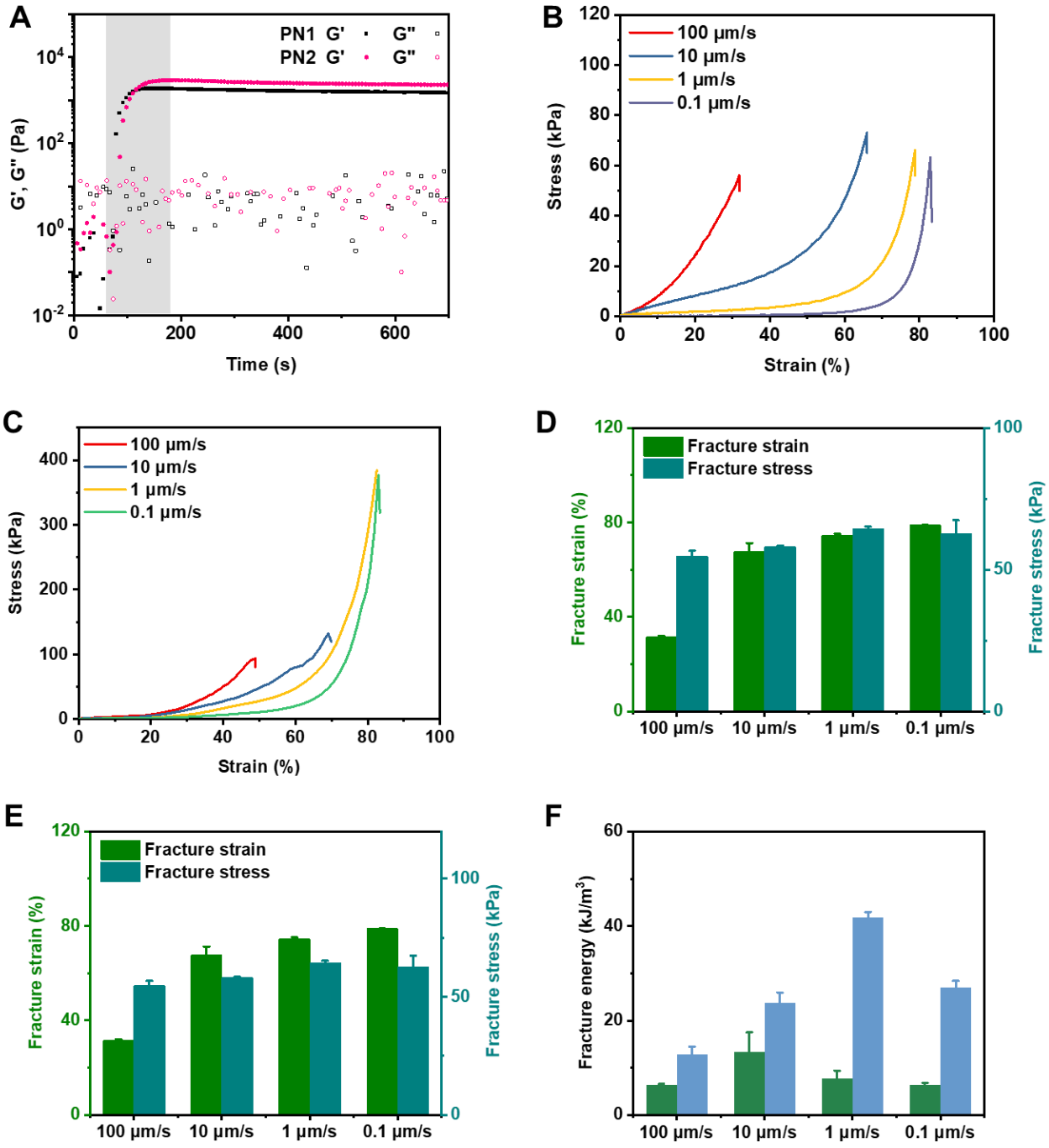

Figure S13. Mechanical properties of **PN1-2** hydrogels: (A) Time sweep experiment after 3 min visible light exposure. Uniaxial stress-strain curves of (B) **PN1** and (C) **PN2** at different compression speeds. Compressive fracture strain, fracture stress of (D) **PN1** and (E) **PN2** hydrogel. (F) Fracture energy of **PN1-2** hydrogels. Mean ± SD, N ≥ 3.

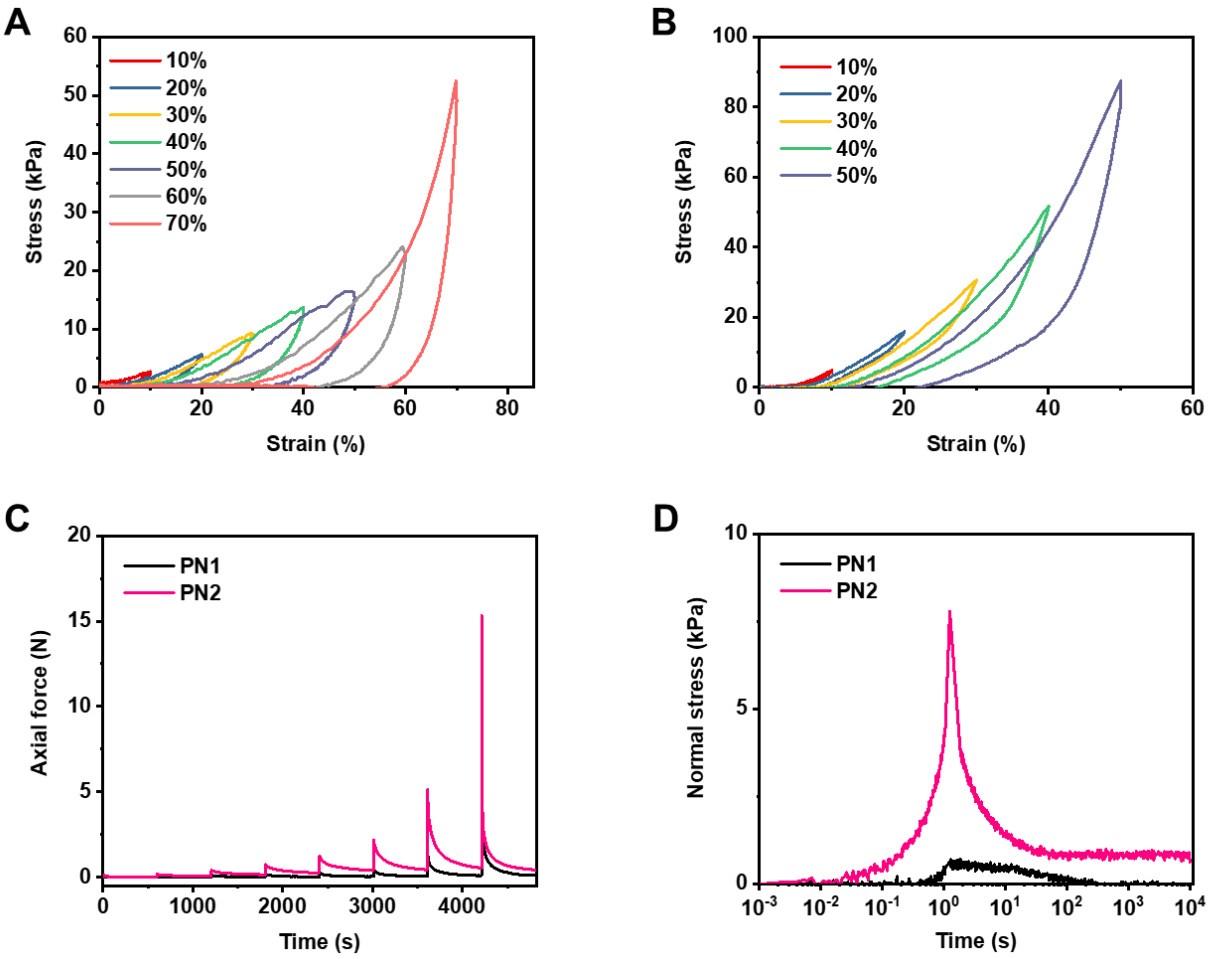

Figure S14. Uniaxial compression cycles of (A) **PN1** and (B) **PN2** hydrogels at different maximum strains. (C) Step-stress relaxation curves with increasing strain (10%) at the start of each loading cycle. (D) Poroviscoelastic relaxation curves of **PN1** and **PN2** hydrogel under a 15% instant strain.

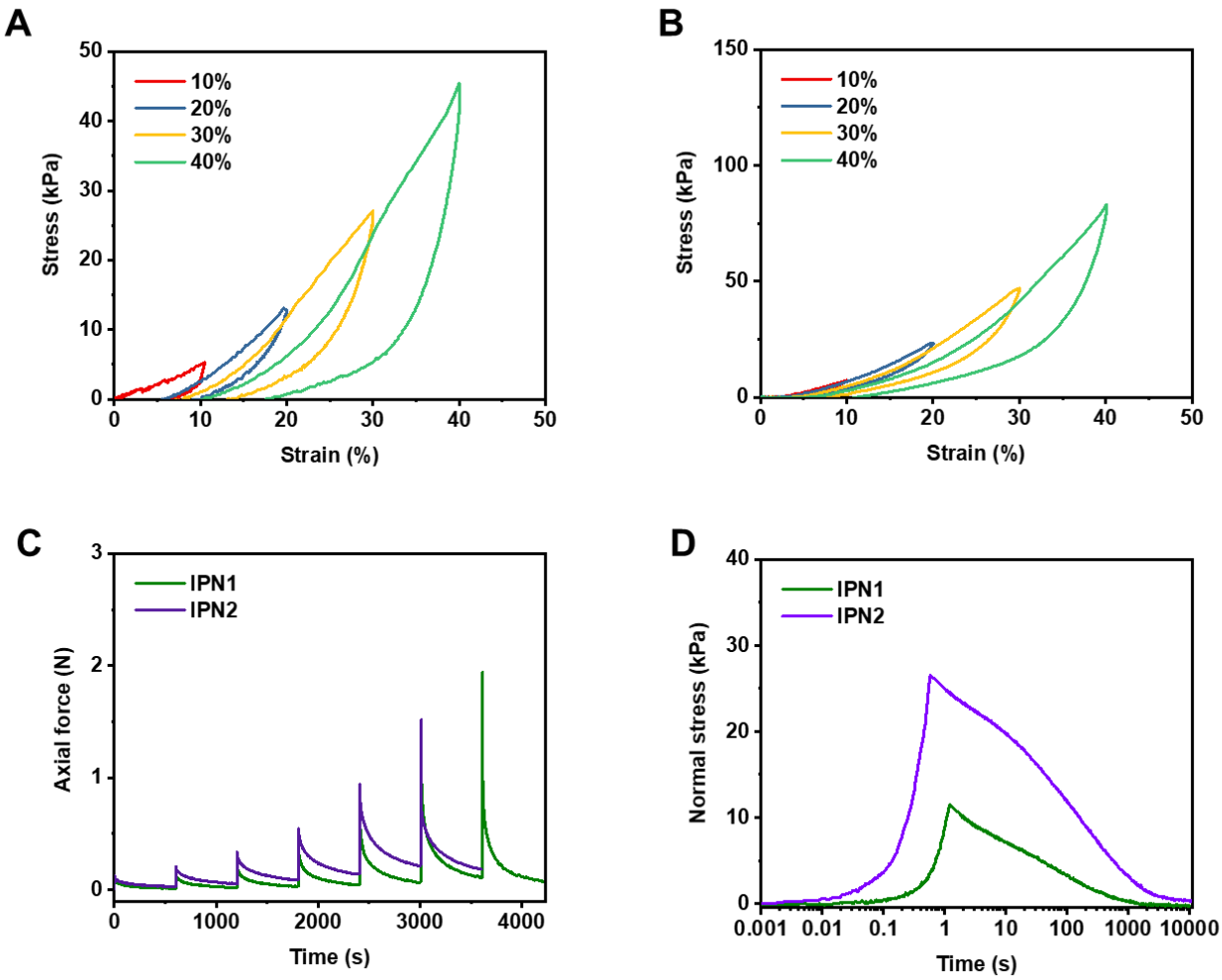

Figure S15. Uniaxial compression cycles of (A) **IPN1** and (B) **IPN2** hydrogels at different maximum strains. (C) Step-stress relaxation curves with increasing strain (10%) at the start of each loading cycle. (D) Poroviscoelastic relaxation curves of **IPN1** and **IPN2** hydrogel under a 15% instant strain.

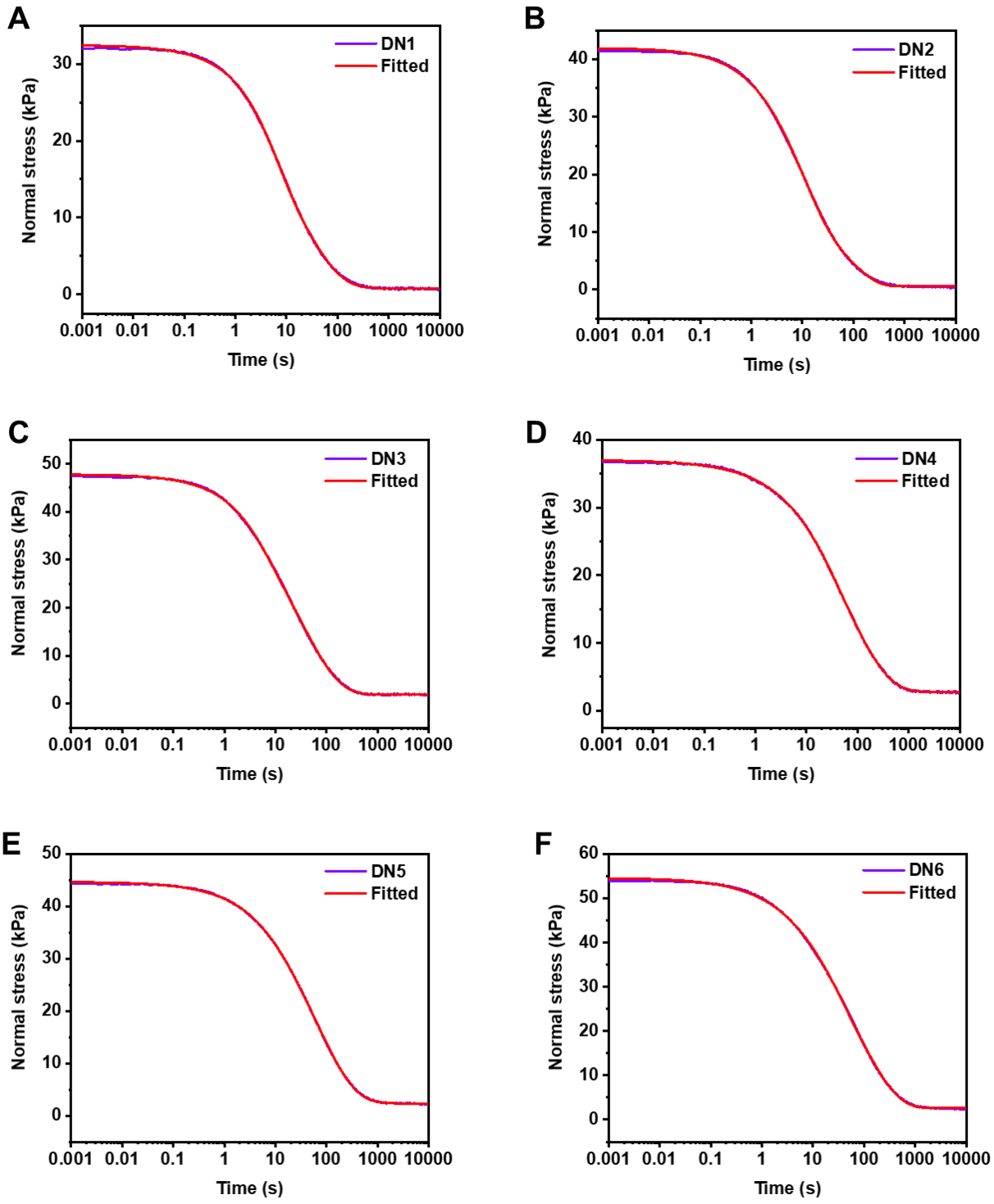

Figure S16. Fitting of the poroviscoelastic data to a two-term exponential decay model for the following hydrogels: (A) **DN1**, (B) **DN2**, (C) **DN3**, (D) **DN4**, (E) **DN5**, (F) **DN6**. R^2= 0.9958-0.9996.

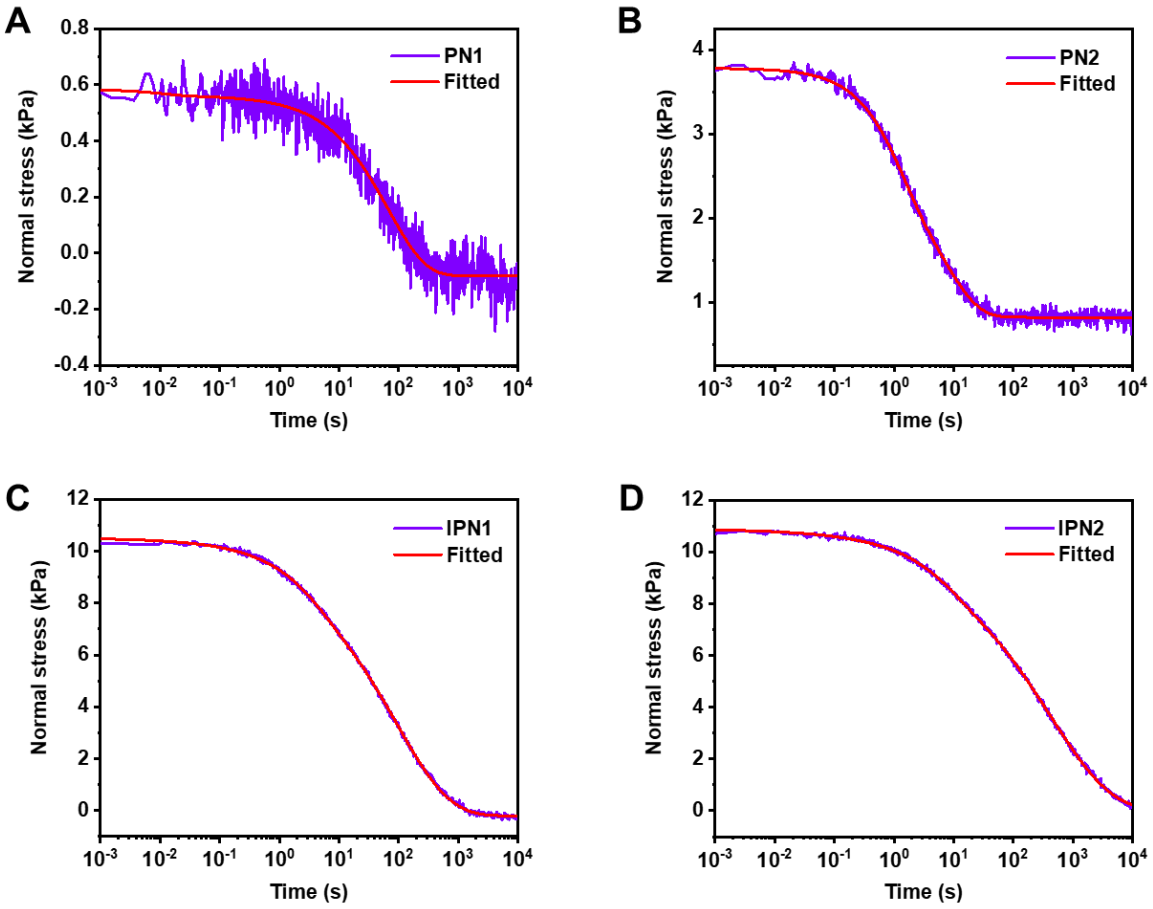

Figure S17. Fitting of the poroviscoelastic data to a two-term exponential decay model for the following hydrogels: (A) **PN1**, (B) **PN2**, (C) **IPN1**, (D) **IPN2**. R^2= 0.95363-0.9997.

Table S2. Fitting results of poroviscoelastic relaxation of different hydrogels.

	τ_1 (s)	τ_2 (s)	R^2
DN1	6.1083 ± 0.08444	1795.79775 ± 7233.36181	0.99952
DN2	5.74067 ± 3.16338	573.74555 ± 73.98957	0.99992
DN3	5.26353 ± 0.12849	175.56259 ± 422.43425	0.99992
DN4	24.50284 ± 0.9517	30.46237 ± 80.87255	0.99989
DN5	12.99155 ± 0.63101	174.13445 ± 277.648	0.99991
DN6	6.96119 ± 0.14635	249.85593 ± 360.5069	0.99997
IPN1	3.87477 ± 0.1738	1.40823 ± 6.6273	0.9997
IPN2	8.4959 ± 0.37531	70.65463 ± 768.36301	0.99965
PN1	0.01087 ± 0.02628	73.96757 ± 2035.46098	0.95363
PN2	1.11349 ± 0.09375	778.86237 ± 13296.12861	0.9968

Scanning electron microscopy (SEM)

Hydrogels (400 µL) were prepared as described above and irradiated with visible light for 5 min by an LED source. The hydrogels were subsequently freeze-dried overnight and fractured after briefly dipping the solids in liquid nitrogen using tweezers. The fractured pieces were directly applied onto two-sided conductive tape attached to an aluminum stub and coated for 2 min by a thin layer of gold (under vacuum) before imaging. The aperture size distribution of the hydrogel was measured at least 50 apertures per sample by using Fiji software.

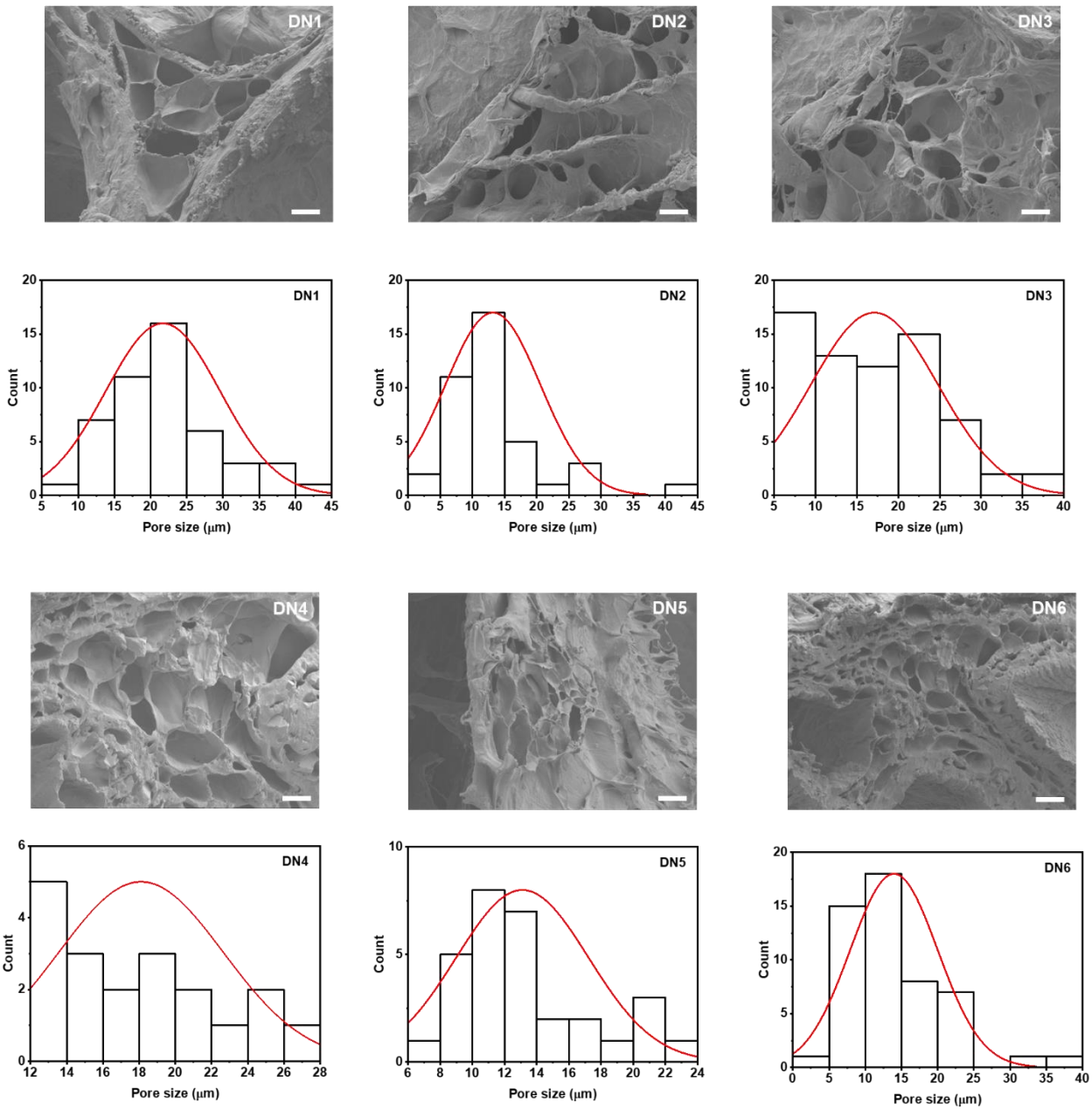

Figure S18. SEM images of various **DN1-6** hydrogels and their relative distribution of pore size. The pore size was measured from the SEM images using the Image J software. Scale bar: *20 μm*.

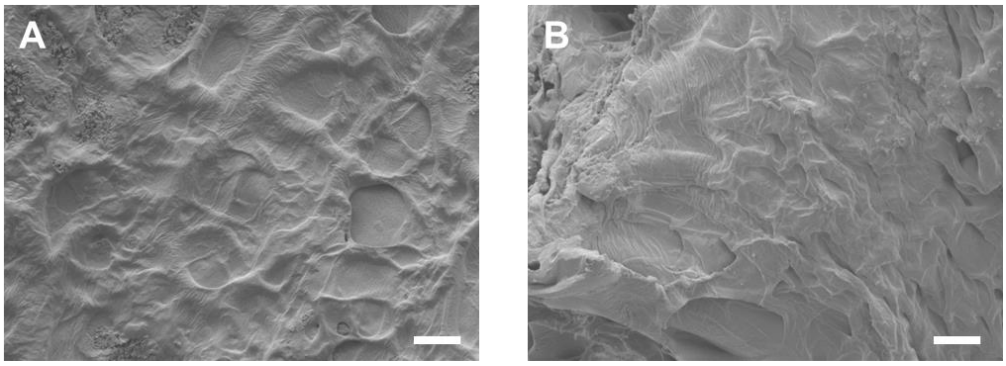

Figure S19. The cross-section SEM images of **DN** hydrogels: (A) **DN1** (B) **DN6**.

Transmission electron microscopy (TEM)

Hydrogels were prepared in PBS and equilibrated overnight as described above. The hydrogels were irradiated with visible light for 0 or 5 min. The samples with/without crosslinking were subsequently diluted with PBS to their measured concentrations (0.5 mM). Diluted solutions (15 µL) were carefully placed on a Formvar/Carbon 200 Mesh Copper grid and kept for 2 min. Afterward, uranyl acetate (1%, 10 µL) was blotted on the grid for 1 min and the grid was dried overnight at RT before imaging.

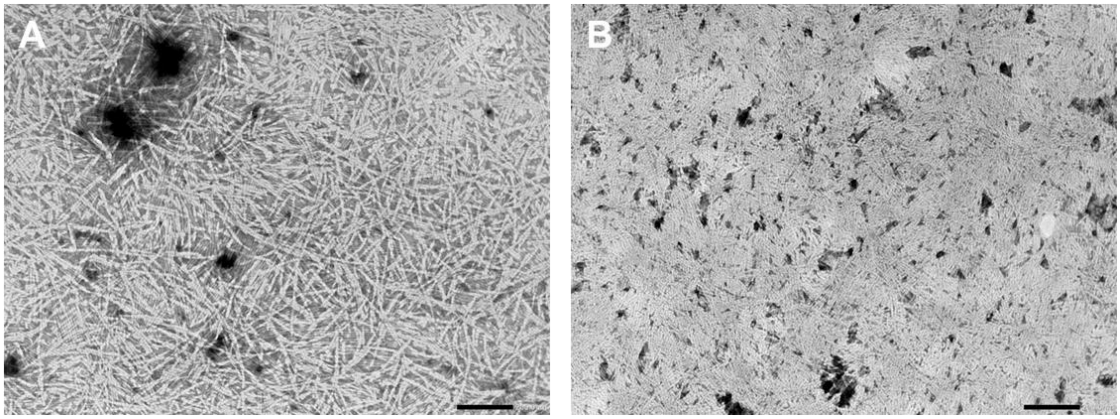

Figure 20. TEM images of diluted (A) **DN1** and (B) **DN6** after photocrosslinking. Scale bar: *200 nm*.

human primary articular chondrocytes (hPACs) culture

Collection and expansion of hPACs from the ongoing Research Arthritis and Articular Cartilage (RAAK) study were performed as earlier described.[5] In short, within 2 hours following joint replacement surgery of osteoarthritis patients, cartilage of the macroscopically unaffected (preserved) region of the joint was sampled in DMEM (high glucose) supplemented with 10% FBS, antibiotics penicillin (100 units/mL) and streptomycin (100 µg/mL) and collagenase Type I (2 mg/mL); and were incubated overnight under standard conditions. Subsequently, isolated chondrocytes were expanded for 2 passages in DMEM supplemented with 10% FBS, antibiotics (100 units/mL penicillin and 100 µg/mL streptomycin) and FGF-2 (0.5 ng/mL) prior to encapsulation into the hydrogel materials.

3D cell encapsulation and cell viability test

Cells were mixed with different **DN** hydrogels (prepared in PBS) and seeded in 15-well µ-Slide at a seeding cell density of 5 x 10^6 cells/mL. After crosslinking for 2 min by a benchtop LED, 3D constructs were covered with chondrogenic differentiation medium (50 µL) (DMEM high glucose supplemented with ascorbate (50 µg/mL), dexamethasone (0.1 µM), L-proline (40 µg/mL), sodium pyruvate (100 µg/mL), ITS-plus, antibiotics, and TGF-β1 (10 ng/mL) and cultured under standard conditions. Cell media was refreshed 3 times every 15 min after seeding and was changed daily during the experiment. The LIVE/DEAD (calcein AM/propidium iodide (PI)) assay was used to probe the cell viability after 3D encapsulation of the cells within the hydrogel. The mixed staining solutions of calcein AM (2.0 µM) and PI (1.5 µM) were prepared by diluting pre-prepared stock solutions of calcein AM (2.5 mM in DMSO) and PI (1.5 mM in PBS) with PBS (pH 7.4). After 24 h culture, the medium on top of the hydrogels was

removed before washing with PBS (2 x 50 µL). Subsequently, a mixture of staining solution (50 µL) was added to the hydrogels and the hydrogel-cell mixtures were incubated for 40 min at 37 °C without light. Subsequently, the staining solution was replaced with PBS and fixed for 30 min with a 4% paraformaldehyde (PFA) solution. Fluorescent Z-stack images were obtained using a 488 nm laser for excitation of calcein AM and a 532 nm laser for excitation of the PI dye. The Image J software package was used to process the collected raw images and count cell viability. LIVE/DEAD staining of hPACs was counted using the Fiji/ImageJ macro written for 3D analysis.

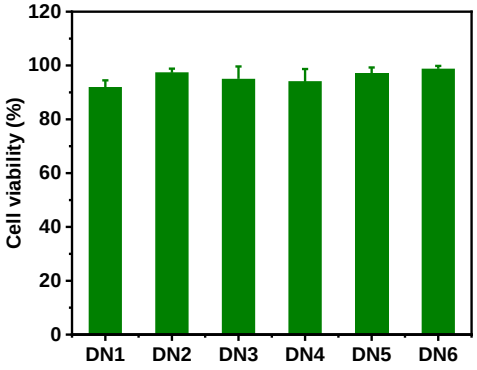

Figure S21. Cell viability of NIH 3T3 mouse fibroblasts encapsulated in crosslinked **DN1-6** hydrogels for 24 h. Mean ± SD, N ≥ 3.

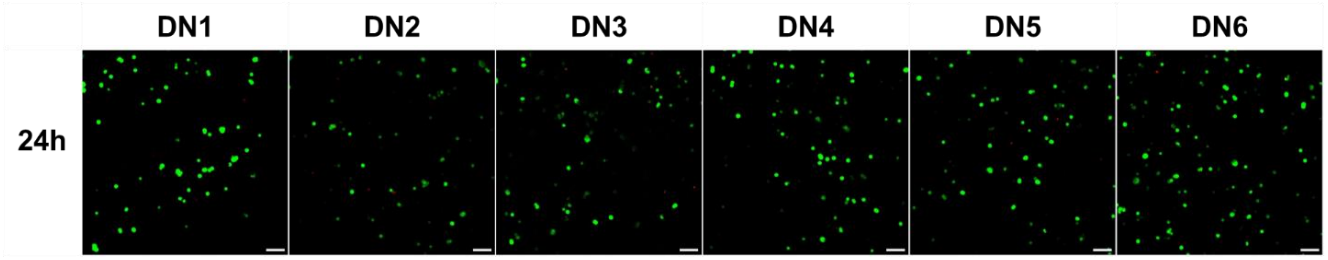

Figure S22. Confocal microscopy images of N3T3 cells encapsulated in crosslinked **DN1-6** hydrogels for 24 h. Calcein AM (green) and propidium iodide (red) mark the live and dead cells, respectively. Scale bar: *200 µm*.

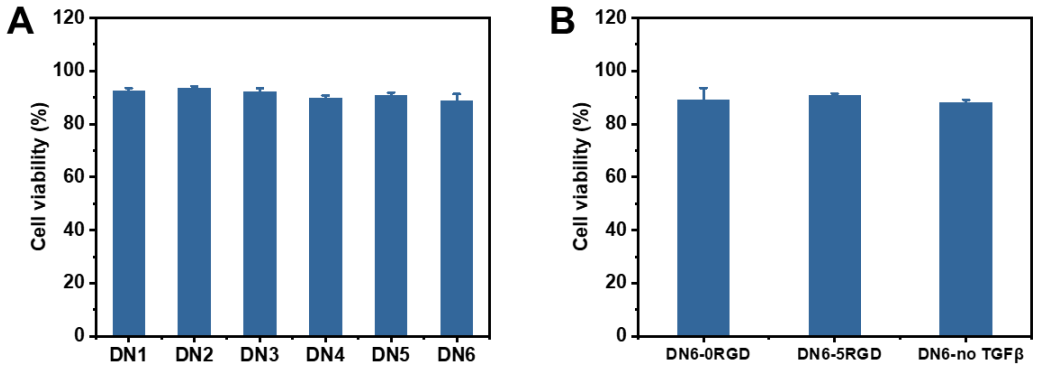

Figure S23. Cell viability of hPACs encapsulated in crosslinked (A) **DN1-6** hydrogels with 10 mol% SQ-RGD and (B) **DN6-5%RGD, DN6-0%RGD** and **DN6-no TGFβ** hydrogels for 24 h. Mean ± SD, N = 3. All cell-laden hydrogels were maintained in chondrogenic media containing TGF-β1 except for **DN6-no TGFβ** hydrogel.

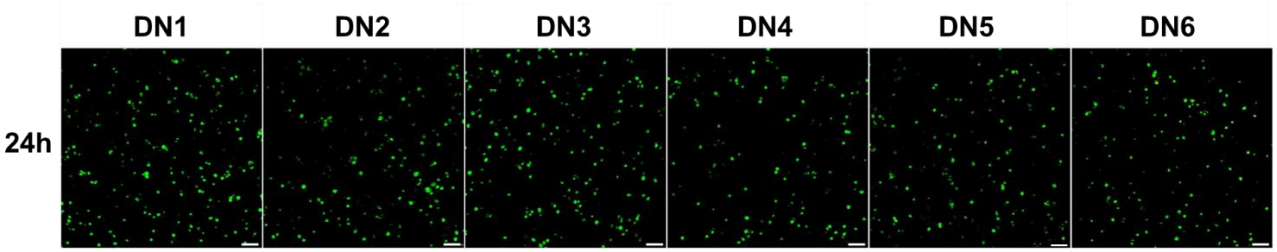

Figure S24. Confocal microscopy images of hPACs encapsulated in crosslinked **DN1-6** hydrogels with 10 mol% SQ-RGD for 24 h. Calcein AM (green) and propidium iodide (red) mark the live and dead cells, respectively. All cell-laden hydrogels were maintained in chondrogenic media containing TGF-β1.

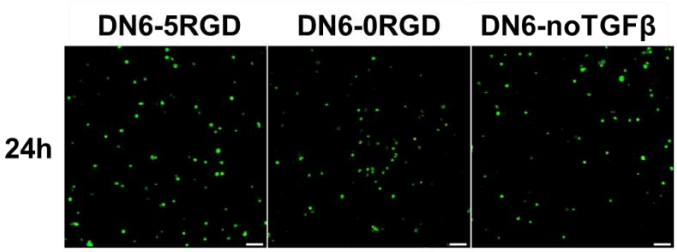

Figure S25. Confocal microscopy images of hPACs encapsulated in crosslinked **DN6-5%RGD, DN6-0%RGD** and **DN6-no TGFβ** hydrogels for 24 h. Calcein AM (green) and propidium iodide (red) mark the live and dead cells, respectively. All cell-laden hydrogels were maintained in chondrogenic media containing TGF-β1 except for **DN6-no TGFβ** hydrogel.

Mechanical loading experiment

Agarose culture wells with a diameter of 4 mm and a height of 1 mm were prepared by putting agarose (350 µL, 3%) in each well of a 24-well flat-bottom plate, using a 4 mm metal punch to create a small hole in the middle of the solidified agarose. The cell-laden hydrogel **DN** (20 µL) before photocrosslinking was gently pipetted into agarose wells. Then the hydrogels were exposed (2 min) to visible light using a benchtop LED. Chondrogenic differentiation media (500 µL) with TGF-β1 (10 ng/ml) was carefully pipetted on top of the construct. The plate was cultured under standard cell culture

conditions. Cell media was refreshed 3 times every 15 min after seeding and was changed daily during the experiment.

For short-term (2 days) loading, the cell culture medium was carefully removed from the culture plate and the hydrogels were washed once with PBS and then covered with PBS. Mechanical loading was performed continuously using cycles consisting of 10 min periods with 2% strain amplitude at the fixed frequency of 1.0 Hz at RT using the MACH-1 machine. After loading, the constructs were covered with chondrogenic differentiation media (500 µL) and further cultured under standard conditions. The control constructs were placed in the RT for 10 min with PBS and without subjecting the mechanical loading.

Alcian Blue staining

To perform Alcian Blue staining for sulfated glycosaminoglycans (s-GAGs), the hydrogel encapsulated hPACs were first fixed with 4% formaldehyde at RT for 20 min. The constructs were washed PBS (3 x 500 µL) and incubated with HCl (0.1N, 500 µL) for 10 min at RT. To detect s-GAGs, constructs were Alcian Blue 8-GX (1%) in HCl (0.1N) for 3 h and with HCl (0.1N, 3 x 500 µL), followed by adding HCl (0.1N, 500 µL) and incubated at RT overnight to remove the excess Alcian Blue. The constructs were washed with Milli-Q water (3 x 500 µL) before adding nuclear fast red (0.1% in 5% aluminum sulfate) to stain the cell nuclei and incubated for 10 min before washing with MilliQ water (3 x 500 µL) before imaging.

DMMB assay and DNA content analysis

The s-GAGs and DNA content at different time points were quantified using biochemical analysis. The wet cell-hydrogel constructs were first weighed and digested overnight at 60 °C with a papain digestion solution in PBS-EDTA (pH 7.1). The s-GAGs concentration was measured in a medium collected at pre-determined time points from the hydrogels. s-GAGs content of the digested samples was quantified using a dimethylmethylene blue (DMMB) assay, with shark chondroitin sulfate in PBS-EDTA (pH 7.1) as a reference. The collected medium from the chondrogenic compartment was diluted 30x before performing a DMMB staining measuring absorbance at 525 and 595 nm. The concentrations of DNA from the digested hydrogel samples were directly measured on a nanodrop.

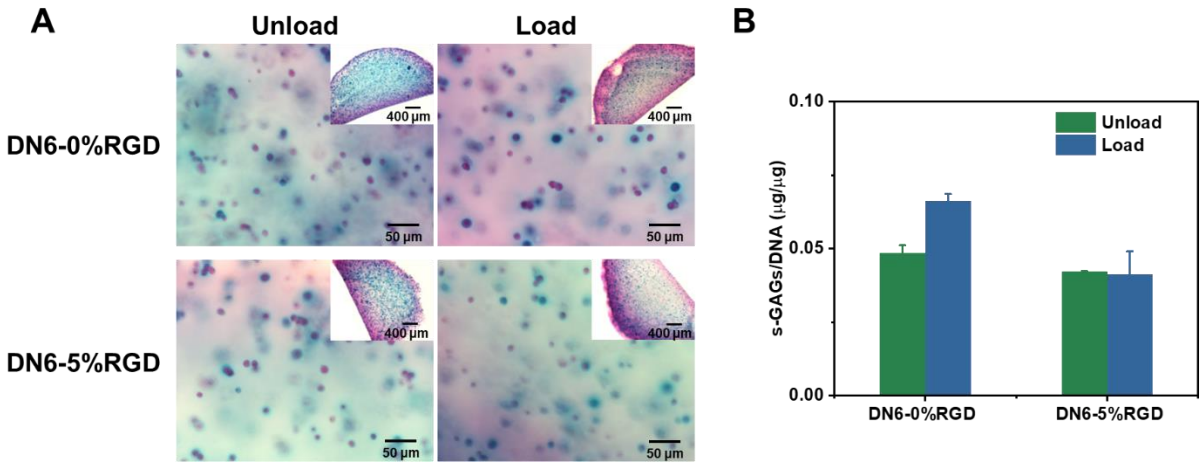

Figure S26. (A) Alcian Blue staining of s-GAGs with nuclear fast red counterstaining of hPACs in cell-laden **DN6-5%RGD, DN6-0%RGD** after 2 days culture or soft loading. (B) Results of biochemical analysis of s-GAGs deposition relative to DNA content in **DN6-5%RGD, DN6-0%RGD** after 2 days culture or soft loading. All the cell-laden hydrogels were maintained in chondrogenic media containing TGF-β1.

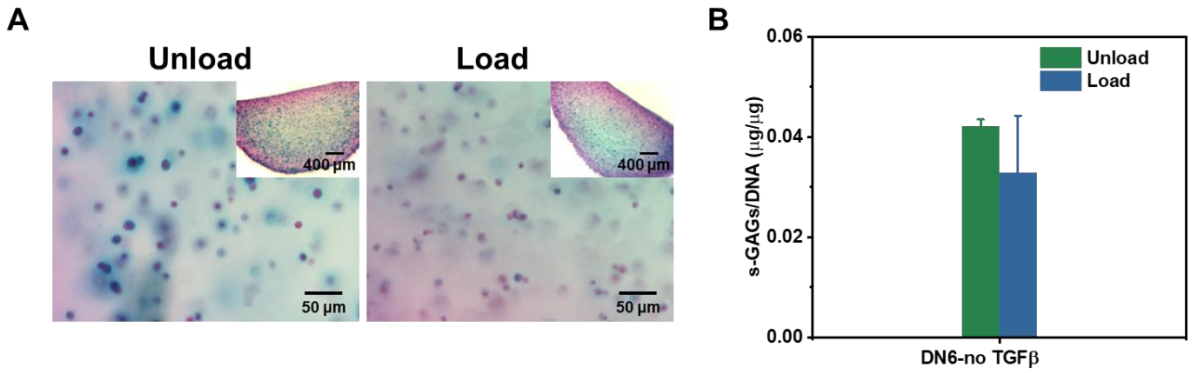

Figure S27. (A) Alcian Blue staining of s-GAGs with nuclear fast red counterstaining of hPACs in crosslinked **DN6-no TGFβ** hydrogels after 2 days culture or soft loading. (B) Results of biochemical analysis of s-GAG deposition relative to DNA content in crosslinked **DN6-no TGFβ** hydrogels after 2 days of culture or soft loading. All the cell-laden hydrogels were maintained in chondrogenic media without TGF-β1.

Reference

(1) Lengyel, G. A.; Horne, W. S. Design strategies for the sequence-based mimicry of side-chain display in protein β-sheets by α/β-peptides. Journal of the American Chemical Society 2012, 134 (38), 15906.

(2) Tong, C.; Wondergem, J. A. J.; van den Brink, M.; Kwakernaak, M. C.; Chen, Y.; Hendrix, M.; Voets, I. K.; Danen, E. H. J.; Le Devedec, S.; Heinrich, D.et al. Spatial and Temporal Modulation of Cell Instructive Cues in a Filamentous Supramolecular Biomaterial. ACS Appl. Mater. Interfaces 2022, 14 (15), 17042.

(3) Chan, E. P.; Deeyaa, B.; Johnson, P. M.; Stafford, C. M. Poroelastic relaxation of polymer-loaded hydrogels. Soft Matter 2012, 8 (31), 8234.

(4) Soltanahmadi, S.; Raske, N.; de Boer, G. N.; Neville, A.; Hewson, R. W.; Bryant, M. G. Fabrication of Cartilage-Inspired Hydrogel/Entangled Polymer–Elastomer Structures Possessing Poro-Elastic Properties. ACS Applied Polymer Materials 2021, 3 (5), 2694.

(5) Bomer, N.; den Hollander, W.; Ramos, Y. F.; Bos, S. D.; van der Breggen, R.; Lakenberg, N.; Pepers, B. A.; van Eeden, A. E.; Darvishan, A.; Tobi, E. W.et al. Underlying molecular mechanisms of DIO2 susceptibility in symptomatic osteoarthritis. Ann Rheum Dis 2015, 74 (8), 1571.

Chapter 5

Photothermal Filamentous Supramolecular and Covalent Double Network Hydrogels

Hybrid supramolecular and covalent double network hydrogels have drawn great attention due to their stiff and tough mechanical characters that can approximate the structure and function of load-bearing tissues. The use of nanoparticles in these networks provides opportunities to augment their mechanics and introduce responsive behaviors that can be remotely triggered with stimuli such as light for their eventual application as therapeutic materials. Herein, we introduce 15 nm gold nanoparticles with 1,2-dithiolane end-functionalized capping groups into the hydrogels that can be simultaneously crosslinked with the covalent and supramolecular networks containing the same reactive group and norbornene through photopolymerization. The addition of gold nanoparticles enhanced the double network hydrogel's mechanical characteristics, especially their energy dissipation property, and conferred tunable conductivity and photothermal properties consistent with the Au@PEG-DT concentration. The double network hydrogels showed injectability prior to photopolymerization and stayed stable in PBS after crosslinking. Stimulation of the plasmonic-photothermal effect of the gold nanoparticles with a laser light source at 532 nm enabled ablation of MDA-MB-231-B1 cells at precise positions in 3D cell culture.

This chapter was prepared as a research article: Ying Chen, Marijn van den Brink, Thomas J.F. Kock, Roxanne E. Kieltyka*

5.1 Introduction

Hydrogels are three-dimensional (3D) materials composed of crosslinked polymer chains to form a network that able to retain a high content of water and have found many applications in the fields such as tissue engineering, drug delivery, soft robotics, and others.[1-5] They have been extensively used as synthetic platforms to closely mimic native tissues due to their tunable physical properties, structural similarity and easy modification with biological cues.[6-8] However, hydrogels are usually applied as single networks that are brittle, limiting their ability to mimic the mechanically loaded stiff tissues.[9,10] To overcome this challenge, double network (**DN**) hydrogels can be formed, where a second polymer network is added to create a structure that exhibits higher mechanical strength and enhances energy dissipation when compared to traditional single hydrogel networks.[11-18] When filamentous supramolecular polymers are used as a sacrificial network they can impart these materials with features that mimic the structures and functions of biopolymers of the extracellular matrix (ECM).[19-23] These mechanical behaviour of these networks that arise due to the non-covalent character of the assemblies can further increase the recovery of the hydrogels, opening up new avenues to prepare hydrogels that mimic ECM properties for 3D cell culture in a wide range of applications.[19,23-25] The often-used chemical strategies only permit mechanical tuning of the materials, however their combination with stimuli-reponsive components can open the door to a wider range of biomedical applications including those that are therapeutic.[26-28]

The incorporation of nanoparticles (e.g., gold nanoparticles, graphene) is another strategy used to augment hydrogel mechanical properties.[29-34] Nanoparticles are embedded in the pores of the network through chemical and/or physical interactions with the network,[34-36] resulting in increased stiffness (0.01-1000 times) and toughness (0.01 - 1 MJ/m^{-3}), as well as improved energy dissipation capabilities.[29-32] This enhancement of mechanical properties is contingent upon the hybrid network's capacity to alleviate stress concentration through dynamic exchanges between polymer segments anchored to the particles and unabsorbed polymer strands.[37-40] Additionally, the nanoparticles can bring additional functions[41-47] consistent with their composition such as heat generation, electrical conductivity[48,49] and magnetic properties that can be attractive for diverse range of biological applications. In particular, gold nanoparticles due to their adaptable modification, and extraordinary optical and plasmonic properties[50,51] have been examined for their capacity to alter hydrogel mechanics while providing access to conductivity and the photo-thermal effect that is attractive for cancer therapy.[26,27] However, in many gold nanoparticle-integrated hydrogels, the particles are physically suspended instead of being crosslinked to the hydrogel network causing aggregation that leads to heterogeneity of material properties. Furthermore, most research efforts have been directed towards enhancing the mechanical properties of hydrogels based on natural polymers using gold particles, while there are few examples of synthetic hydrogels in this area.

We previously developed a **DN** hydrogel that shows biomimetic mechanical properties that are cartilage-like by crosslinking of a supramolecular and covalent polymer network through poly(disulfide) and poly(disulfide-norbornene)s. The **DN** consists of squaramide-based monomers[52]and covalent poly(ethylene glycol) polymers[53] that could sustain 14 days of cyclic compressive loading in 3D cell

culture. (**chapter 3**). Because gold nanoparticles can further impact the mechanical properties of the network while introducing a handle for stimuli-responsiveness due to the photothermal effect of the particles, we became interested in understanding their impact on the hybrid **DN** presented in Chapter **3**. To improve the dispersion and stability of AuNPs in **DN** hydrogels, the nanoparticles were functionalized with heterobifunctional oligo(ethylene glycol polymers) containing a thiol unit that can bind strongly to the gold surface and a 1,2-dithiolane for coupling to the **DN** simultaneously during its crosslinking with UV light at 365 nm. We then analyze the injectability, mechanics, conductivity, and photo-thermal effect of these networks, gaining insight into their potential to tune the behavior of this double network gel based on the nanoparticle concentration used. Finally, we demonstrate the acquired photo-thermal properties of the **DN** hydrogel with gold nanoparticle addition by the selective ablation of bone tumor cells with spatial control.

5.2 Results and Discussion

Nanocomposite double network hydrogel design and synthesis

A 4-arm poly(ethylene glycol) (PEG) macromonomer (in total 3 wt%) end-functionalized with DT or NB (PEG_4-DT or PEG_4-NB) composes the first network of the **DN** and **DN-Au** hydrogels (Scheme 1). These macromonomers were synthesized in one-step using carbodiimide coupling chemistry yielding a high degree of functionalization similar to the earlier reported linear macromonomers.[53] UV irradiation with lithium phenyl-2,4,6-trimethylbenzoylphosphinate (LAP, 1mM) lead to crosslinking of these two monomers to form a single network hydrogel material. The second network is a multicomponent supramolecular polymer consisting of tripodal squaramide-based monomers, including one outfitted with DT that is added in a 10 mol% (**SN**, 4 mM) ratio.[52] To prepare the **DN** hydrogels, we combine the DT and NB macromonomers into the supramolecular filaments in phosphate-buffered saline (pH 7.4) after sonication on ice. We then allowed the solution to reach room temperature (RT), to form the polymer hydrogel.

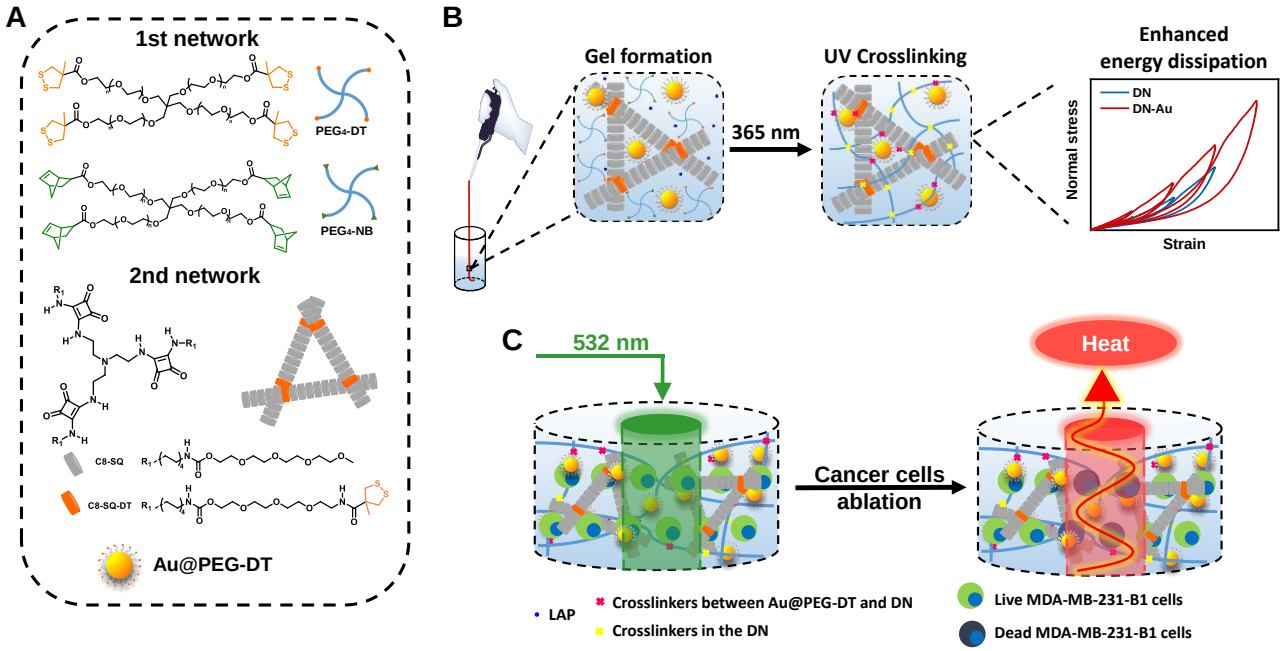

Scheme 1. (A) Double network hydrogels and components used in this study. (B) Extruded **DN-Au** hydrogel and subsequent **DN** photopolymerization strategy. (C) Photo-thermal effect of crosslinked gold nanoparticles (AuNPs) in the 3D **DN** hydrogel MDA-MB-231-B1 cells with light irradiation.

Next, we used the citric acid reduction process[54,55] to prepare citrate-coated gold nanoparticles (15 nm, Au@Citrate) and coupled them with SH-PEG_{5400}-DT (Mw: 5.4 kDa) to form a PEG shell around the particle with reactive groups (DT) for coupling to the **DN** (Figure S1).[53] Here, we synthesized SH-PEG_{5400}-DT by reacting linear thiol-PEG-hydroxy and DT with carbodiimide coupling chemistry resulting in a high degree of end-functionalization.[53] Relying on the stronger chemisorption of thiols on the gold surface relative to DT[56,57], we expected that the 1,2-ditholane units reside on the periphery of the PEG shell and available for crosslinking with the dithiolane network. We confirmed this by ^{1}H-NMR spectroscopy comparing the -CH_2 and -CH_3 protons on DT (3.05-2.9 ppm, 1.48-1.35 ppm) from the SH-

PEG_{5400}-DT coated gold nanoparticles (Au@PEG-DT) to that on SH-PEG_{5400}-DT polymer, where no discernable changes in chemical shift was found (Figure S2). The Au@PEG-DT nanoparticles retained their structure after the exchange of the capping group for the PEG with the DT unit, as demonstrated by red-shifting of the band at 518nm of Au@Citrate to 522nm with the addition of SH-PEG_{5400}-DT (Figure 1A). The transmission electron microscopy (TEM) and dynamic light scattering (DLS) further supported these results (Figure 1B-C, S3), pointing out that introduction of the DT at the periphery of the capping group does not have an impact on particle size or cause aggregation. Moreover, replacement of the PEG capping group lead to the effective exchange of citrate as evidenced by the significant change in zeta potential of the gold nanoparticles (AuNPs), from ~ -40.30 mV to ~ -21.26 mV for Au@Citrate and Au@PEG-DT, respectively (Figure 1D). As a control, we also synthesized Au@PEG nanoparticles lacking the DT group that showed similar optical and morphological properties to the Au@PEG-DT.

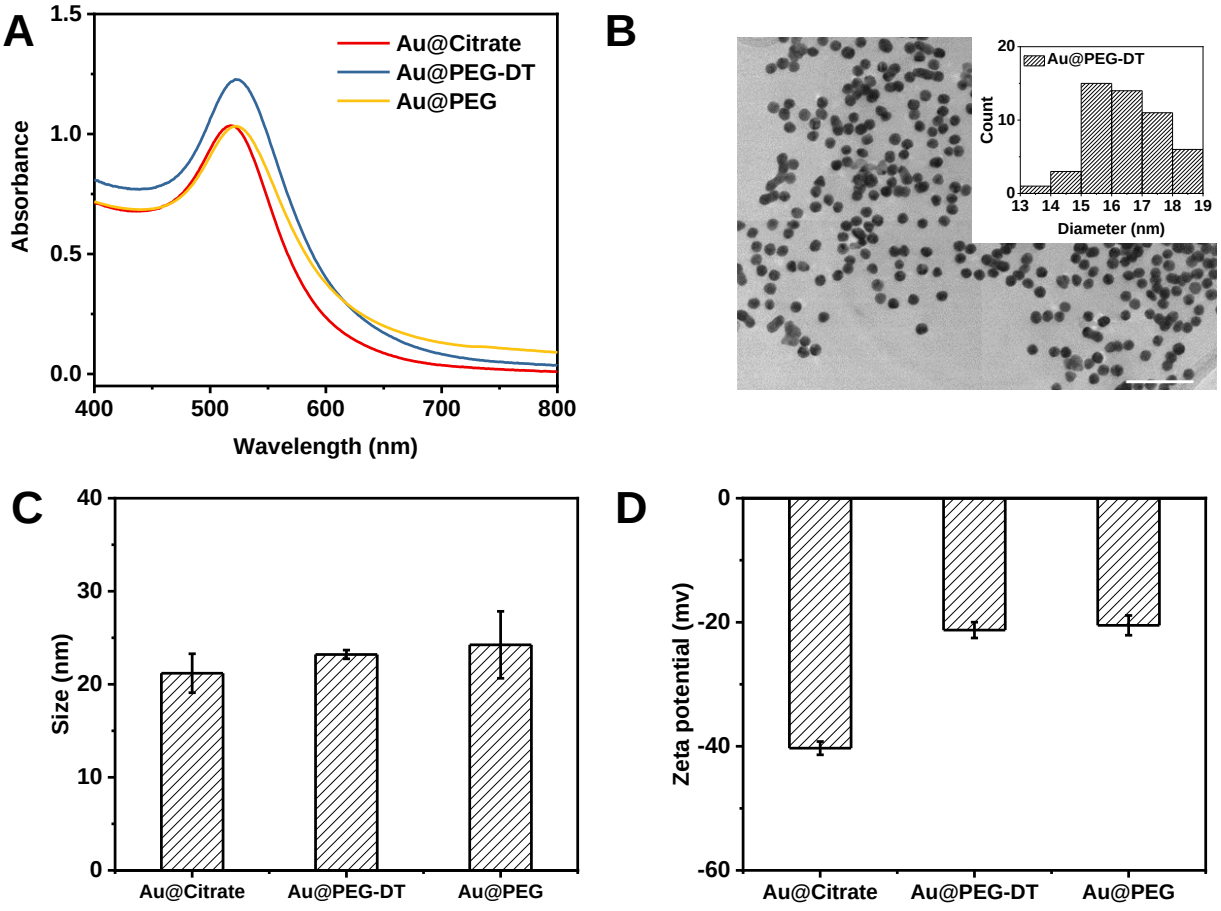

Figure 1. Characterization of AuNPs in water. (A) UV spectra of Au@Citrate and Au@PEG-DT. (B) TEM image of Au@PEG-DT (300 µg/ml). Scale bar: *100 nm*. (C) Hydrodynamic diameters of Au@Citrate and Au@PEG-DT measured by DLS. (D) Zeta potential of Au@Citrate and Au@PEG-DT. Mean ± SD, N ≥ 3.

We then prepared double network hydrogels **DN-Au$_x$** crosslinked with Au@PEG-DT particles under UV light at ~365 nm and a photoinitiator lithium phenyl-2,4,6-trimethylbenzoylphosphinate (LAP, 1mM). To permit efficient crosslinking of the hydrogels and subsequent imaging of 3D cell cultures, we kept the Au@PEG-DT at 1 mg/mL for the remainder of the study to high light transmittance. The crosslinking of these particles to the supramolecular and covalent polymer networks components yielded NB-DT and DT-DT bonds depending the ratio of the various components.[53] We then explored the impact of gold nanoparticles on the formation of the double network gels. The resulting **DN-Au** hydrogels appeared wine red in color varying in intensity from light to dark red depending on Au@PEG-DT concentration, even after photopolymerization as observed in gel inversion tests (Figure S4).

Quantification of mechanical properties of DN and DN-Au hydrogels

We probed the effect of adding Au@PEG-DT to the filamentous double network hydrogel on its mechanical properties using oscillatory rheology. In time sweep measurements, the storage modulus (G') of the **DN** network increased from ~80 Pa before UV exposure to ~10.12 kPa after crosslinking (Figure 2A and S5), and was comparable with the results for the **DN** in **Chapter 3**. When Au@PEG-DT increased from 0.1 mg/mL (**DN-Au$_{0.1}$**) to 0.25 mg/mL (**DN-Au$_{0.25}$**), the stiffness of crosslinked hydrogels increased from ~11.32 kPa to ~13.04 kPa, while further raising the nanoparticle concentration up to 1.0 mg/mL (**DN-Au$_{0.5}$** and **DN-Au$_{1.0}$**) led to slower rate of stiffness increase and steady decrease of the storage modulus (from ~10.22 kPa to ~7.34 kPa, respectively). This decrease in storage modulus is likely due to the reduced transmission of UV light through the uncrosslinked **DN-Au** gels due to the increased nanoparticle concentration that can interfere with the photopolymerization process. We exchanged Au@PEG-DT for 0.25 mg/mL Au@PEG that lacks the DT moiety to compare the effect of covalent crosslinking of the gold nanoparticles on the **DN** gel. The storage modulus of the **DN-Au@PEG$_{0.25}$** hydrogel with the same UV exposure as the **DN-Au$_{0.25}$** hydrogel showed slower rise in the storage modulus reaching a lower value than the **DN-Au$_{0.25}$** gel crosslinked with Au@PEG-DT of ~10.82 kPa (Figure S6A). The frequency sweep showed that this hydrogel is independent of the frequency from 0.1 Hz to 10 Hz (Figure S7). Strain sweeps claimed that the hydrogels were stable at low strain (<100%) and could break when the strain was higher than 200 %. Step-strain test sweep demonstrated that the uncrosslinked **DN-Au$_{0.25}$** hydrogel has excellent self-healing property (Figure S8). These results suggest that the gold nanoparticles are chemically crosslinked to the **DN** hydrogel and contribute to its mechanical properties as a function of their concentration.

Because of the capacity of nanocomposites to enhance the mechanical characteristics of **DN** hydrogels in compression,[58-60] we further evaluated the behaviour of the **DN-Au** networks under this type of mechanical load. Axial force compression tests in the rheometer demonstrated that inclusion of Au@PEG-DT at 0.25 mg/mL in the **DN** network increased the fracture strain from ~18.34 % to ~20.27 % and the compression modulus rose from ~492.62 kPa to ~574.86 kPa (Figure 2B-E, Table 1). Additionally, the **DN** hydrogels showed improved toughness with the addition of the gold nanoparticles, rising from ~11.84 to ~14.68 J/m^3, on par with other nanocomposite enhanced hydrogels.[61,62] Consistent with the decrease in stiffness when increasing the Au@PEG-DT concentration from 0.25 mg/mL to 1 mg/mL,

these hydrogels also showed a reduced ability to sustain compressive loads in contrast to the **DN** hydrogel without the added gold particles. At an Au@PEG-DT concentration of 1 mg/mL (**DN-Au$_1$**), the

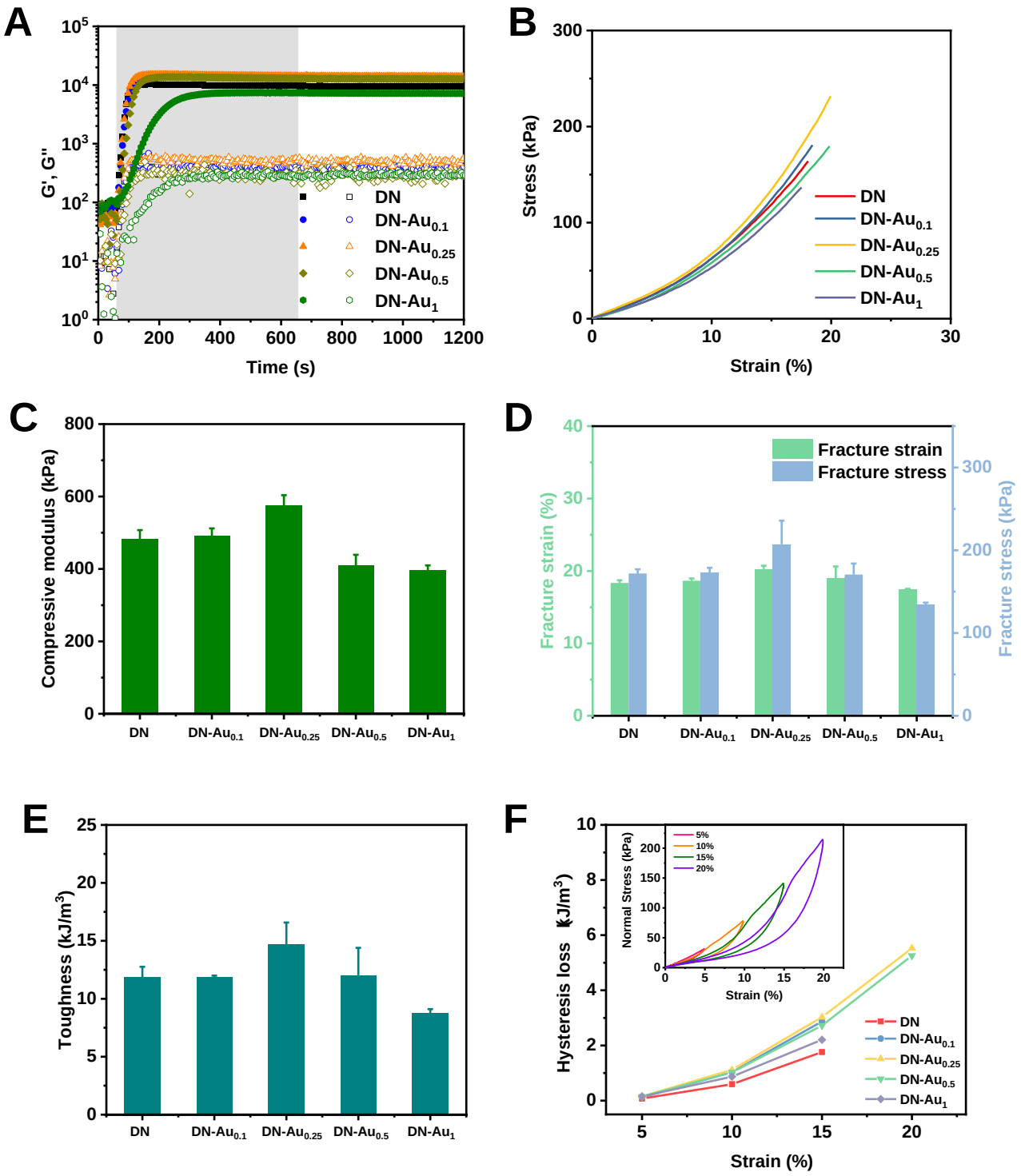

Figure 2. Mechanical properties of **DN** and **DN-Au** hydrogels measured at a constant compression speed (10 μm/s): (A) Oscillatory rheology time sweep measurements of hydrogels with varied Au@PEG-DT concentrations before and after 10 min UV irradiation using a fixed strain (γ = 0.05%) and frequency (ƒ = 1.0 Hz) at room temperature. Grey regions indicate UV exposure. (B) Uniaxial stress-strain curves. (C) Compressive modulus. (D) Compressive fracture strain and stress. (E) Compressive toughness. Mean ± SD, N ≥ 3. (F) Hysteresis loss of photocrosslinked **DN** and **DN-Au** hydrogels. Insert: Cyclic

hysteresis curves of photocrosslinked **DN-Au$_{0.25}$** hydrogel at different maximum strains (γ_{max}) using a loading-unloading test. Conditions for UV irradiation: ~10 mW/cm^2, 320-500 nm filter with maximum absorbance at 365 nm.

hydrogel showed a reduced fracture strain of ~17.50%, compressive modulus at ~396.81 kPa and toughness of ~8.77J/m^3. Addition of the Au@PEG nanoparticles **DN-Au@PEG$_{0.25}$** resulted in a higher fracture strain (~20.03%) but a reduced fracture stress (~154 kPa) and fracture energy (~8.75 kJ/m^3) in contrast to the **DN** hydrogel lacking nanoparticles (Figure S6B-6D). Hence, the nanoparticle crosslinkers can enhance the compressive mechanical properties of the supramolecular and covalent **DN** as the lack of chemical bonding reduces their response to compression.

We further examined the effect of the cross-linked AuNPs on the energy dissipation properties of **DN** and **DN-Au** hydrogels by compressive loading-unloading cycles at different maximum compression strains (λ_{max}) increasing from 5 to 25 %. All **DN-Au** exhibited obvious hysteresis loops that increased in parallel with the compression strain (λ_{max}) like the DN hydrogel (Figure 2F and S9). For example, the dissipated energy of **DN-Au$_{0.25}$** increased from ~0.16 kJ/m^3 (λ_{max} = 5%) to ~5.53 kJ/m^3 (λ_{max} = 25%). In contrast, the **DN** network in the lacking Au@PEG-DT showed a reduction in the dissipated energy from 0.12 (λ_{max} = 5%) to ~1.76 kJ/m^3 (λ_{max} = 15%) and the one with Au@PEG (0.25 mg/mL) that lacking DT for crosslinking falls in the range of ~0.11 to ~2.61 kJ/m^3 (λ_{max} = 15%) (Figure S10). These results indicate that physical introduction of the gold nanoparticles improve the energy dissipation properties of **DN-Au** hydrogels and their dynamic-covalent crosslinking through DT can further enhance this property.

Table 1. Fracture strain, facture stress, fracture energy and compression modulus of **DN** and **DN-Au** hydrogels under 10 µm/s speed, Mean ± SD, N ≥ 3.

Name	Fracture strain (%)	Fracture stress (kPa)	Fracture energy (kJ/m^3)	Compression modulus (kPa)
DN	18.34 ± 0.37	171.81 ± 5.06	11.84 ± 0.92	492.62 ± 27
DN-Au$_{0.1}$	18.6525 ± 0.61	172.81 ± 6.13	11.873 ± 0.12	491.41 ± 20.57
DN-Au$_{0.25}$	20.27 ± 0.46	207.45 ± 28.38	14.68 ± 1.90	574.86 ± 18
DN-Au$_{0.5}$	18.97 ± 1.65	170.66 + 13.30	12.03 ± 2.37	408 ± 30.49
DN-Au$_{1}$	17.50 ± 0.019	134.52 ± 2.81	8.77 ± 0.33	396.81 ± 19
DN-Au@PEG$_{0.25}$	20.07 ± 3.60	158.63 ± 20.6	10.94 ± 0.37	426.81 ± 25.43

Structural characteristics of the DN hydrogel

We performed electron microscopy and equilibrium swelling experiments to gain insight into the structural characteristics of the **DN-Au** hydrogels that underlie the recorded rheological changes with Au@PEG-DT addition. In (cryogenic) transmission electron microscopy (Cryo-TEM) the **DN** and **DN-Au** solutions showed long and flexible (~5 nm nm) filamentous structures even after crosslinking with well-dispersed Au@PEG-DT throughout the **DN-Au** hydrogels that lacked aggregation (Figure S11-S12).

Moreover, some AuNPs appeared associated with the supramolecular filaments, most likely due to photocrosslinking of the squaramide-based DT monomers with the Au@PEG-DT nanoparticles. We further probed the **DN** and **DN-Au** hydrogel structures at the microscale after UV exposure by scanning electron microscopy (SEM). The pore size of the **DN** hydrogel (~13 µm) decreased slightly with the incorporation of Au@PEG-DT at 0.5 mg/mL (~12 µm). Increasing the concentration up to 1 mg/mL resulted in an even smaller pore size (~8 µm) filled with nanoparticles and blurred pore edges (Figure S13). The micrometer scale of the pores likely arises due the freeze-drying method used to prepare the gels for imaging. These observations point to a difference in network structure with increasing gold nanoparticle concentration and align with the earlier measured reduced mechanics by oscillatory rheology. These studies demonstrate that the **DN** and **DN-Au** hydrogels exhibit a filamentous nature with sufficiently large pore sizes that can be tuned by nanoparticle concentration, rendering them suitable for 3D cell culture application.[63,64]

To gain insight into the extent of crosslinking and retention of Au@PEG-DT in the **DN** for their subsequent applications in 3D cell culture, we conducted an equilibrium water content and gel stability assays. We prepared the **DN** and **DN-Au** hydrogels above the CGC (critical gelling concentration)[65] and photocrosslinked them with 10 min UV irradiation (375 nm), (Figure 3) the photocrosslinked hydrogels on day 2 were 20-30 times heavier than the starting materials.[66] The decline in swelling ratio among the samples can be attributed to the increase in polymer and nanoparticle concentrations. Gel stability tests display that the **DN** and **DN-Au** hydrogels retained approximately 100% of their initial weight for 15 days without degradation in water. We then investigated the diffusion of AuNPs@PEG-DT using UV measurements and observed a minimal release of AuNPs from the network (Figure S4), further pointing out their effective covalent crosslinking to the materials. These results showed that the maintenance of the gels and gold nanoparticles within them after several media changes, showed that the materials can sustain conditions typically associated with 3D cell culture.

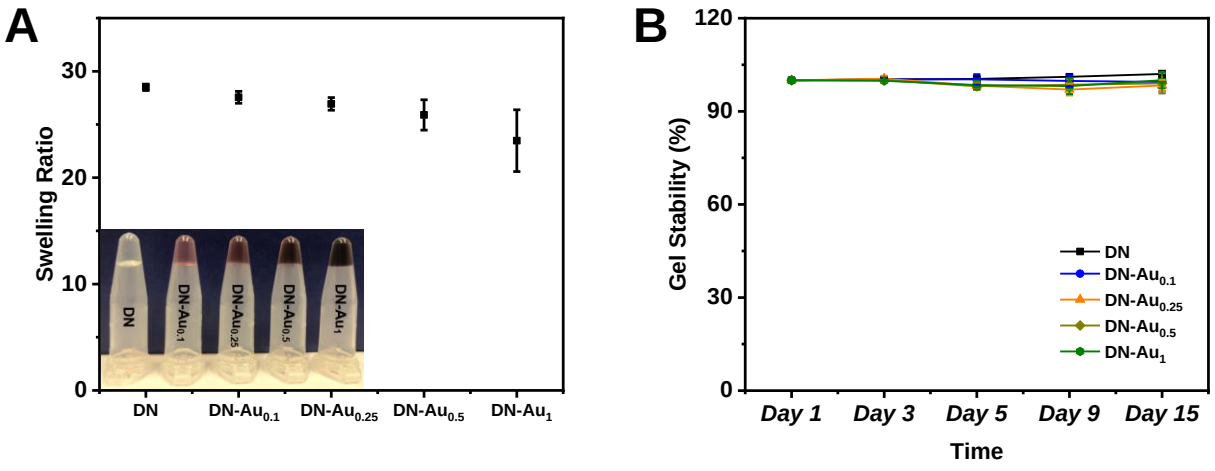

Figure 3. DN and **DN-Au** hydrogels (A) Swelling ratio. Insert: digital photo inverted hydrogels tested. (B) Gel stability tests over 15 days.

Evaluation of DN-Au hydrogel conductive and photothermal properties

AuNPs can confer additional features to hydrogel materials such as conductivity and photohermal behaviour due to their inherent physicochemical properties.[67-69] We performed a set of electrochemical performance tests to understand the relationship between the Au@PEG-DT concentration and the **DN-Au** hydrogel conductive properties. When Au@PEG-DT concentration increased from 0 mg/mL to 1 mg/mL, the conductivity rose modestly from ~8.22 x 10^{-4} S/m to ~9.88 x 10^{-4} S/m (Figure 4A). These findings are in line with other metal nanoparticle-hydrogel networks that report similar subtle increase in conductivity.[70]

Besides their conductivity, the optical absorption characteristics of AuNPs allow for conversion of incident light into thermal energy.[71] We tested the photo-thermal effect of the **DN** and **DN-Au** hydrogels using a 1 W 532 nm visible light source and a sensitive thermometer. Hydrogels with a higher Au@PEG-DT concentration resulted in a greater temperature increases when irradiated under the same condition (Figure 4B). Incorporation of Au@PEG-DT raised the gel temperature to ~71.05°C in **DN-Au$_{0.1}$**, and further increasing their concentration in **DN-Au$_{0.5}$** drove a temperature increase of relative to **DN**. On removing the light source, the **DN** and **DN-Au** hydrogels cooled down to room temperature after 10 minutes. This photo-thermal effect could be cycled at least 3 times without attenuation. We then assessed extrudability of the uncrosslinked **DN-Au** hydrogels for their eventual application as inks for printing applications or as injectable materials. The **DN-Au$_{0.25}$** hydrogel can be extruded into a noodle shape using a micropipette (Figure 4C-D). We then applied the crosslinking process to the extruded gel with a benchtop LED at 375 nm for 10 min. The photopolymerized material retains its shape in water, showing potential for 3D printing applications.

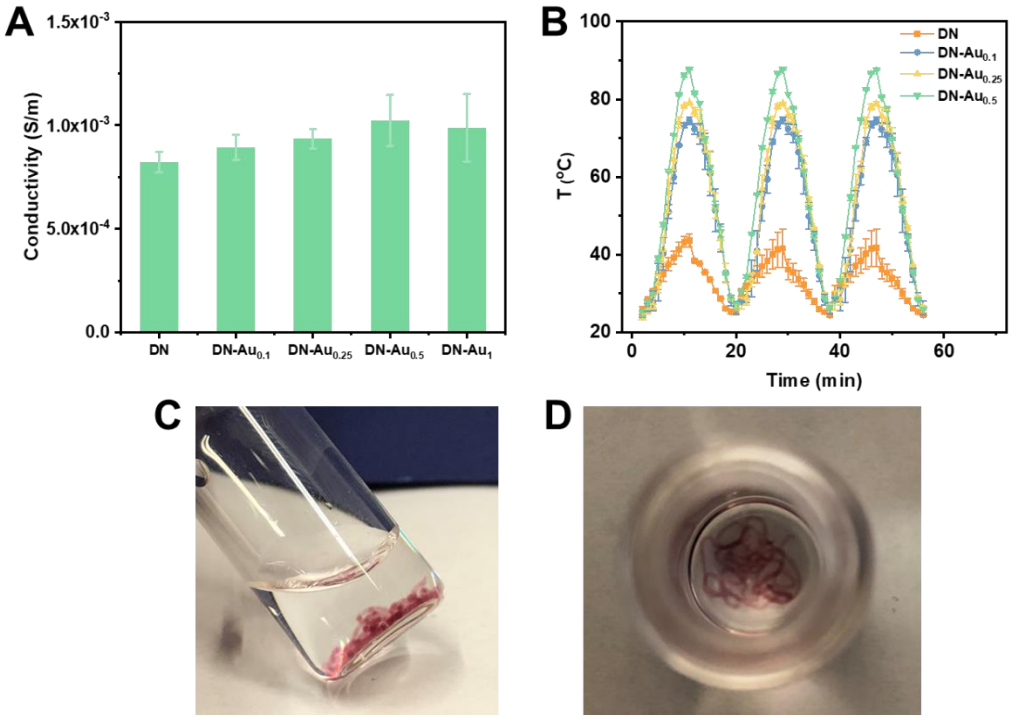

Figure 4. (A) Conductivity of different crosslinked **DN** and **DN-Au** hydrogels. (B) Cyclic photo-thermal effect of crosslinked **DN** and **DN-Au$_{0.1}$** - **DN-Au$_{0.5}$** hydrogels irradiated with light at 532 nm. Digital photos of extruded **DN-Au$_{0.25}$** after photopolymerization and kept in water for 1 day: (C) side view. (D) top view.

Photothermal ablation of cancer cells in DN-Au hydrogels

The photothermal property of AuNPs is attractive for cancer therapy applications *in vivo* where the focus is on tumor cell ablation in a highly selective and minimally invasive manner.[72-78] To examine the suitability of composite **DN-Au** hydrogels for cell ablation, we first assessed cell viability of encapsulated NIH 3T3 fibroblasts in the various hydrogel compositions and concentrations. We observed high cell viabilities reaching over 90% after 24h culture and 80% after 48h in 3D culture with 5 min 375 nm UV exposure (Figure S14-S15) by a Live/Dead Assay with calcein AM/propidium iodide staining.

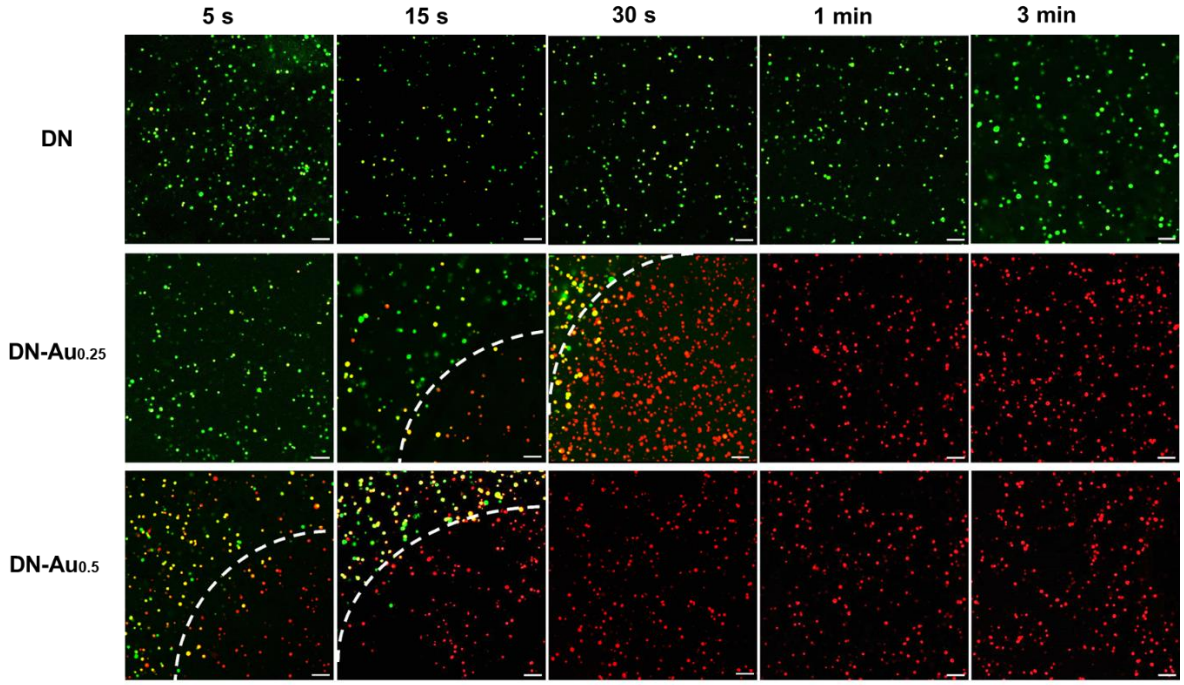

Figure 5. Confocal microscopy images of stained live (calcein AM) and dead (propidium iodide) MDA-MB-231-B1 cells encapsulated and incubated in **DN** and **DN-Au** in 3D for 24 h and subsequently irradiated under a 532 nm (1 W) visible light laser for varying time intervals. Scale bar: *100 µm*.

Next, we explored the capacity to selectively ablate a cancer cell line from bone metastases, MDA-MB-231-B1, within **DN-Au** hydrogels using green light. Cell viability of MDA-MB-231-B1 cells in crosslinked **DN** and **DN-Au** hydrogels after 24 h culture in the absence of green light was over 90% (Figure S16-S17). We then assessed the photothermal effects of the **DN** and **DN-Au** hydrogels on cell viability by a Live/Dead stain after irradiating the cancer cell-laden hydrogels in 3D with a 532 nm visible light laser (1 W) at different time points (0 s - 3 min). Application of the light source on the **DN** hydrogel without gold nanoparticles could not cause cell death even with a 3 min exposure (Figure 5 and S18). In contrast, the **DN-Au$_{0.5}$** could efficiently convert the light into heat and induce cell death within 5 s,

while the **DN-Au$_{0.25}$** hydrogel needed a longer exposure time of 15 s to observe the same effect. These results align with earlier photothermal data where greater Au@PEG-DT concentrations resulted in a larger temperature increase in the hydrogels. Furthermore, upon brief irradiation of the **DN-Au** hydrogels, we found that the dead cell area expanded proportionally with both the concentration of Au@PEG-DT and the duration of irradiation, resulting in non-viable cells across the **DN-Au$_{0.25}$** and **DN-Au$_{0.5}$** hydrogels after a 3-minute light exposure. These results indicated that the photoablation position can be precisely controlled by the 532 nm laser or the gold nanoparticle concentration. These findings demonstrate a positive correlation between the concentration of AuNPs and light dosage on cell photoablation, and the irradiated position can be precisely controlled by the laser position, opening the door to mapping spatial effects of temperature on cell behaviour in a 3D environment.

5.3 Conclusions

We herein report a gold-nanoparticle crosslinked filamentous supramolecular and covalent double network hydrogel through the simultaneous photopolymerization of 1,2-dithiolane and norbornene on the various components. By varying the concentration of gold nanoparticles, tunable mechanical properties, conductive and photothermal properties within these hybrid hydrogels can be achieved. Cross-linking of the gold nanoparticles to the double network yields increased energy dissipation similar to stiff and tough tissues such as cartilage. Prior to photopolymerization the materials can be extruded thorugh a syringe and remained stable in buffered solution showing printability. Furthermore, these hydrogels showed excellent cycling of the photo-thermal effect due to the gold nanoparticles. Further harnessing the photothermal effect in the presence of MDA-MB-231-B1 cells, cell ablation can be executed in a spatial manner by tuning the laser dose and nanoparticle concentration. These nanocomposite materials provide new opportunities to use toughen supramolecular polymer materials while studying their cell behaviour under extreme thermal conditions in a local manner, and open the door for potential 3D applications in photothermal treatment of cancer.

References

(1) Kunwar, P.; Ransbottom, M. J.; Soman, P. Three-Dimensional Printing of Double-Network Hydrogels: Recent Progress, Challenges, and Future Outlook. *3D Printing and Additive Manufacturing* **2021**, *9* (5), 435.

(2) Muir, V. G.; Burdick, J. A. Chemically Modified Biopolymers for the Formation of Biomedical Hydrogels. *Chem Rev* **2021,** *121* (18), 10908.

(3) Yu, C.; Schimelman, J.; Wang, P.; Miller, K. L.; Ma, X.; You, S.; Guan, J.; Sun, B.; Zhu, W.; Chen, S. Photopolymerizable Biomaterials and Light-Based 3D Printing Strategies for Biomedical Applications. *Chem Rev* **2020,** *120* (19), 10695.

(4) Yu, H.; Gao, R.; Liu, Y.; Fu, L.; Zhou, J.; Li, L. Stimulus‐Responsive Hydrogels as Drug Delivery Systems for Inflammation Targeted Therapy. *Advanced Science* **2023**, 2306152.

(5) Sithole, M. N.; Mndlovu, H.; du Toit, L. C.; Choonara, Y. E. Advances in Stimuli-responsive Hydrogels for Tissue Engineering and Regenerative Medicine Applications: A Review Towards Improving Structural Design for 3D Printing. *Current Pharmaceutical Design* **2023** *13*, 10186.

(6) Green, J. J.; Elisseeff, J. H. Mimicking biological functionality with polymers for biomedical applications. *Nature* **2016,** *540* (7633), 386.

(7) Kyburz, K. A.; Anseth, K. S. Synthetic mimics of the extracellular matrix: how simple is complex enough? *Annals of biomedical engineering* **2015,** *43*, 489.

(8) Zhao, Z.; Chen, X.; Dowbaj, A. M.; Sljukic, A.; Bratlie, K.; Lin, L.; Fong, E. L. S.; Balachander, G. M.; Chen, Z.; Soragni, A. Organoids. *Nature Reviews Methods Primers* **2022,** *2* (1), 94.

(9) Chivers, P. R. A.; Smith, D. K. Shaping and structuring supramolecular gels. *Nat. Rev. Mater.* **2019,** *4* (7), 463.

(10) Tong, C.; Liu, T.; Saez Talens, V.; Noteborn, W. E.; Sharp, T. H.; Hendrix, M. M.; Voets, I. K.; Mummery, C. L.; Orlova, V. V.; Kieltyka, R. E. Squaramide-based supramolecular materials for three-dimensional cell culture of human induced pluripotent stem cells and their derivatives. *Biomacromolecules* **2018,** *19* (4), 1091.

(11) Hutmacher, D. W. Scaffolds in tissue engineering bone and cartilage. *Biomaterials* **2000,** *21* (24), 2529.

(12) Huang, X.; Li, J.; Luo, J.; Gao, Q.; Mao, A.; Li, J. Research progress on double-network hydrogels. *Adv. Healthc. Mater.* **2021,** *29*, 102757.

(13) Sun, W.; Xue, B.; Li, Y.; Qin, M.; Wu, J.; Lu, K.; Wu, J.; Cao, Y.; Jiang, Q.; Wang, W. Polymer-Supramolecular Polymer Double-Network Hydrogel. *Adv. Funct. Mater.* **2016,** *26* (48), 9044.

(14) Nakayama, A.; Kakugo, A.; Gong, J. P.; Osada, Y.; Takai, M.; Erata, T.; Kawano, S. High Mechanical Strength Double-Network Hydrogel with Bacterial Cellulose. *Adv. Funct. Mater.* **2004,** *14* (11), 1124.

(15) Chen, Q.; Chen, H.; Zhu, L.; Zheng, J. Fundamentals of double network hydrogels. *J Mater Chem B* **2015,** *3* (18), 3654.

(16) Nonoyama, T.; Gong, J. P. Double-network hydrogel and its potential biomedical application: A review. *Proc Inst Mech Eng H* **2015,** *229* (12), 853.

(17) Ni, X.; Xing, X.; Deng, Y.; Li, Z. Applications of Stimuli-Responsive Hydrogels in Bone and Cartilage Regeneration. *Pharmaceutics* **2023,** *15* (3), 982.

(18) Monemian, S.; Korley, L. T. Exploring the role of supramolecular associations in mechanical toughening of interpenetrating polymer networks. *Macromolecules* **2015,** *48* (19), 7146.

(19) Goor, O.; Hendrikse, S. I. S.; Dankers, P. Y. W.; Meijer, E. W. From supramolecular polymers to multi-component biomaterials. *Chem. Soc. Rev.* **2017,** *46* (21), 6621.

(20) Radvar, E.; Azevedo, H. S. Supramolecular Peptide/Polymer Hybrid Hydrogels for Biomedical Applications. *Macromol Biosci* **2019,** *19* (1), e1800221.

(21) Webber, M. J.; Appel, E. A.; Meijer, E. W.; Langer, R. Supramolecular biomaterials. *Nat. Mater.* **2016,** *15* (1), 13.
(22) Yang, L.; Tan, X.; Wang, Z.; Zhang, X. Supramolecular Polymers: Historical Development, Preparation, Characterization, and Functions. *Chem Rev* **2015,** *115* (15), 7196.
(23) Du, X.; Zhou, J.; Shi, J.; Xu, B. Supramolecular Hydrogelators and Hydrogels: From Soft Matter to Molecular Biomaterials. *Chem Rev* **2015,** *115* (24), 13165.
(24) Hafeez, S.; Decarli, M. C.; Aldana, A.; Ebrahimi, M.; Ruiter, F. A.; Duimel, H.; van Blitterswijk, C.; Pitet, L. M.; Moroni, L.; Baker, M. B. In Situ Covalent Reinforcement of a Benzene-1, 3, 5-Tricarboxamide Supramolecular Polymer Enables Biomimetic, Tough, and Fibrous Hydrogels and Bioinks. *Adv. Mater.* **2023,** *35* (35), 2301242.
(25) Li, H.; Wang, H.; Zhang, D.; Xu, Z.; Liu, W. A highly tough and stiff supramolecular polymer double network hydrogel. *Polymer* **2018,** *153*, 193.
(26) Elkhoury, K.; Russell, C. S.; Sanchez-Gonzalez, L.; Mostafavi, A.; Williams, T. J.; Kahn, C.; Peppas, N. A.; Arab-Tehrany, E.; Tamayol, A. Soft-nanoparticle functionalization of natural hydrogels for tissue engineering applications. *Adv. Healthc. Mater.* **2019,** *8* (18), 1900506.
(27) Tan, H.-L.; Teow, S.-Y.; Pushpamalar, J. Application of metal nanoparticle–hydrogel composites in tissue regeneration. *Bioengineering* **2019,** *6* (1), 17.
(28) Hasan, A.; Khattab, A.; Islam, M. A.; Hweij, K. A.; Zeitouny, J.; Waters, R.; Sayegh, M.; Hossain, M. M.; Paul, A. Injectable hydrogels for cardiac tissue repair after myocardial infarction. *Advanced Science* **2015,** *2* (11), 1500122.
(29) Viola, M.; Piluso, S.; Groll, J.; Vermonden, T.; Malda, J.; Castilho, M. The Importance of Interfaces in Multi-Material Biofabricated Tissue Structures. *Adv Healthc Mater* **2021,** *10* (21), e2101021.
(30) Sano, K.; Ishida, Y.; Aida, T. Synthesis of Anisotropic Hydrogels and Their Applications. *Angew Chem Int Ed Engl* **2018,** *57* (10), 2532.
(31) Han, L.; Yan, L.; Wang, M.; Wang, K.; Fang, L.; Zhou, J.; Fang, J.; Ren, F.; Lu, X. Transparent, Adhesive, and Conductive Hydrogel for Soft Bioelectronics Based on Light-Transmitting Polydopamine-Doped Polypyrrole Nanofibrils. *Chem. Mater.* **2018,** *30* (16), 5561.
(32) Xing, W.; Tang, Y. On mechanical properties of nanocomposite hydrogels: Searching for superior properties. *Nano Materials Science* **2021**, *4*, 83.
(33) Arno, M. C.; Inam, M.; Weems, A. C.; Li, Z.; Binch, A. L.; Platt, C. I.; Richardson, S. M.; Hoyland, J. A.; Dove, A. P.; O'Reilly, R. K. Exploiting the role of nanoparticle shape in enhancing hydrogel adhesive and mechanical properties. *Nature communications* **2020,** *11* (1), 1420.
(34) Chen, W.; Kouwer, P. H. Combining mechanical tuneability with function: biomimetic fibrous hydrogels with nanoparticle crosslinkers. *Adv. Funct. Mater.* **2021,** *31* (47), 2105713.
(35) Cui, Z.-K.; Kim, S.; Baljon, J. J.; Wu, B. M.; Aghaloo, T.; Lee, M. Microporous methacrylated glycol chitosan-montmorillonite nanocomposite hydrogel for bone tissue engineering. *Nature communications* **2019,** *10* (1), 3523.
(36) Kim, Y.-H.; Yang, X.; Shi, L.; Lanham, S. A.; Hilborn, J.; Oreffo, R. O.; Ossipov, D.; Dawson, J. I. Bisphosphonate nanoclay edge-site interactions facilitate hydrogel self-assembly and sustained growth factor localization. *Nature communications* **2020,** *11* (1), 1365.
(37) Rose, S.; Dizeux, A.; Narita, T.; Hourdet, D.; Marcellan, A. Time dependence of dissipative and recovery processes in nanohybrid hydrogels. *Macromolecules* **2013,** *46* (10), 4095.
(38) Meng, X.; Qiao, Y.; Do, C.; Bras, W.; He, C.; Ke, Y.; Russell, T. P.; Qiu, D. Hysteresis-Free Nanoparticle-Reinforced Hydrogels. *Adv. Mater.* **2022,** *34* (7), 2108243.

(39) Pafiti, K.; Cui, Z.; Adlam, D.; Hoyland, J.; Freemont, A. J.; Saunders, B. R. Hydrogel composites containing sacrificial collapsed hollow particles as dual action pH-responsive biomaterials. *Biomacromolecules* **2016,** *17* (7), 2448.
(40) Gao, G.; Du, G.; Sun, Y.; Fu, J. Self-healable, tough, and ultrastretchable nanocomposite hydrogels based on reversible polyacrylamide/montmorillonite adsorption. *ACS Appl. Mater. Interfaces* **2015,** *7* (8), 5029.
(41) Liu, X.; Miller, A. L., 2nd; Park, S.; Waletzki, B. E.; Zhou, Z.; Terzic, A.; Lu, L. Functionalized Carbon Nanotube and Graphene Oxide Embedded Electrically Conductive Hydrogel Synergistically Stimulates Nerve Cell Differentiation. *ACS Appl. Mater. Interfaces* **2017,** *9* (17), 14677.
(42) Min, J. H.; Patel, M.; Koh, W. G. Incorporation of Conductive Materials into Hydrogels for Tissue Engineering Applications. *Polymers (Basel)* **2018,** *10*, 1078.
(43) Thoniyot, P.; Tan, M. J.; Karim, A. A.; Young, D. J.; Loh, X. J. Nanoparticle-Hydrogel Composites: Concept, Design, and Applications of These Promising, Multi-Functional Materials. *Adv Sci (Weinh)* **2015,** *2* (1-2), 1400010.
(44) Dannert, C.; Stokke, B. T.; Dias, R. S. Nanoparticle-Hydrogel Composites: From Molecular Interactions to Macroscopic Behavior. *Polymers (Basel)* **2019,** *11*, 275.
(45) Chen, T.; Hou, K.; Ren, Q.; Chen, G.; Wei, P.; Zhu, M. Nanoparticle-Polymer Synergies in Nanocomposite Hydrogels: From Design to Application. *Macromol. Rapid Commun.* **2018,** *39* (21), e1800337.
(46) Elkhoury, K.; Russell, C. S.; Sanchez-Gonzalez, L.; Mostafavi, A.; Williams, T. J.; Kahn, C.; Peppas, N. A.; Arab-Tehrany, E.; Tamayol, A. Soft-Nanoparticle Functionalization of Natural Hydrogels for Tissue Engineering Applications. *Adv Healthc Mater* **2019,** *8* (18), e1900506.
(47) Tan, H. L.; Teow, S. Y.; Pushpamalar, J. Application of Metal Nanoparticle(-)Hydrogel Composites in Tissue Regeneration. *Bioengineering (Basel)* **2019,** *6,* 17.
(48) Dvir, T.; Timko, B. P.; Brigham, M. D.; Naik, S. R.; Karajanagi, S. S.; Levy, O.; Jin, H.; Parker, K. K.; Langer, R.; Kohane, D. S. Nanowired three-dimensional cardiac patches. *Nat Nanotechnol* **2011,** *6* (11), 720.
(49) Navaei, A.; Rahmani Eliato, K.; Ros, R.; Migrino, R. Q.; Willis, B. C.; Nikkhah, M. The influence of electrically conductive and non-conductive nanocomposite scaffolds on the maturation and excitability of engineered cardiac tissues. *Biomater Sci* **2019,** *7* (2), 585.
(50) Huang, X.; El-Sayed, M. A. Gold nanoparticles: Optical properties and implementations in cancer diagnosis and photothermal therapy. *Journal of Advanced Research* **2010,** *1* (1), 13.
(51) Wahid, F.; Zhao, X.-J.; Jia, S.-R.; Bai, H.; Zhong, C. Nanocomposite hydrogels as multifunctional systems for biomedical applications: Current state and perspectives. *Composites Part B: Engineering* **2020,** *200*.
(52) Tong, C.; Wondergem, J. A. J.; van den Brink, M.; Kwakernaak, M. C.; Chen, Y.; Hendrix, M.; Voets, I. K.; Danen, E. H. J.; Le Devedec, S.; Heinrich, D.et al. Spatial and Temporal Modulation of Cell Instructive Cues in a Filamentous Supramolecular Biomaterial. *ACS Appl. Mater. Interfaces* **2022,** *14* (15), 17042.
(53) Tong, C.; Wondergem, J. A. J.; Heinrich, D.; Kieltyka, R. E. Photopatternable, Branched Polymer Hydrogels Based on Linear Macromonomers for 3D Cell Culture Applications. *ACS Macro Lett.* **2020,** *9* (6), 882.
(54) John Turkevich, P. C. S., James Hillie. A study of the nucleation and growth processes in the synthesis of colloidal gold. *Synthesis Of Colloidal Gold* **1951**, 55.
(55) Frens., G. Controlled Nucleation for the Regulation of the Particle Size in Monodisperse Gold Suspensions. *Nature Physical Science* **1973,** *241(105)*, 20.
(56) Pacchioni, G. A not-so-strong bond. *Nature Reviews Materials* **2019,** *4* (4), 226.
(57) Bard, A.; Rondon, R.; Marquez, D. T.; Lanterna, A. E.; Scaiano, J. C. How Fast Can Thiols Bind to the Gold Nanoparticle Surface? *Photochem. Photobiol.* **2018,** *94* (6), 1109.
(58) Dannert, C.; Stokke, B. T.; Dias, R. S. Nanoparticle-hydrogel composites: from molecular interactions to macroscopic behavior. *Polymers* **2019,** *11* (2), 275.

(59) Bapat, R. A.; Chaubal, T. V.; Dharmadhikari, S.; Abdulla, A. M.; Bapat, P.; Alexander, A.; Dubey, S. K.; Kesharwani, P. Recent advances of gold nanoparticles as biomaterial in dentistry. *Int. J. Pharm.* **2020,** *586*, 119596.
(60) Yadid, M.; Feiner, R.; Dvir, T. Gold nanoparticle-integrated scaffolds for tissue engineering and regenerative medicine. *Nano Lett.* **2019,** *19* (4), 2198.
(61) Jaiswal, M. K.; Xavier, J. R.; Carrow, J. K.; Desai, P.; Alge, D.; Gaharwar, A. K. Mechanically stiff nanocomposite hydrogels at ultralow nanoparticle content. *ACS nano* **2016,** *10* (1), 246.
(62) Gaharwar, A. K.; Dammu, S. A.; Canter, J. M.; Wu, C.-J.; Schmidt, G. Highly extensible, tough, and elastomeric nanocomposite hydrogels from poly (ethylene glycol) and hydroxyapatite nanoparticles. *Biomacromolecules* **2011,** *12* (5), 1641.
(63) Murphy, C. M.; O'Brien, F. J. Understanding the effect of mean pore size on cell activity in collagen-glycosaminoglycan scaffolds. *Cell adhesion & migration* **2010,** *4* (3), 377.
(64) Loh, Q. L.; Choong, C. Three-dimensional scaffolds for tissue engineering applications: role of porosity and pore size. **2013**, 19, 485.
(65) Tong, C.; Liu, T.; Saez Talens, V.; Noteborn, W. E. M.; Sharp, T. H.; Hendrix, M.; Voets, I. K.; Mummery, C. L.; Orlova, V. V.; Kieltyka, R. E. Squaramide-Based Supramolecular Materials for Three-Dimensional Cell Culture of Human Induced Pluripotent Stem Cells and Their Derivatives. *Biomacromolecules* **2018,** *19* (4), 1091.
(66) Park, H.; Guo, X.; Temenoff, J. S.; Tabata, Y.; Caplan, A. I.; Kasper, K.; Mikos, A. G. Effect of Swelling Ratio of Injectable Hydrogel Composites on Chondrogenic Differentiation of Encapsulated Rabbit Marrow Mesenchymal Stem Cells *In Vitro*. *Biomacromolecules* **2009,** *10*, 541.
(67) Miao, Z.; Gao, Z.; Chen, R.; Yu, X.; Su, Z.; Wei, G. Surface-bioengineered gold nanoparticles for biomedical applications. *Current Medicinal Chemistry* **2018,** *25* (16), 1920.
(68) Jiang, J.; Xu, S.; Ma, H.; Li, C.; Huang, Z. Photoresponsive hydrogel-based soft robot: A review. *Materials Today Bio* **2023**, 100657.
(69) Cabuzu, D.; Cirja, A.; Puiu, R.; Mihai Grumezescu, A. Biomedical applications of gold nanoparticles. *Curr. Top. Med. Chem.* **2015,** *15* (16), 1605.
(70) Xu, Y.; Rothe, R.; Voigt, D.; Hauser, S.; Cui, M.; Miyagawa, T.; Patino Gaillez, M.; Kurth, T.; Bornhäuser, M.; Pietzsch, J. Convergent synthesis of diversified reversible network leads to liquid metal-containing conductive hydrogel adhesives. *Nature communications* **2021,** *12* (1), 2407.
(71) Rengan, A. K.; Jagtap, M.; De, A.; Banerjee, R.; Srivastava, R. Multifunctional gold coated thermo-sensitive liposomes for multimodal imaging and photo-thermal therapy of breast cancer cells. *Nanoscale* **2014,** *6* (2), 916.
(72) Zhi, D.; Yang, T.; O'hagan, J.; Zhang, S.; Donnelly, R. F. Photothermal therapy. *J. Controlled Release* **2020,** *325*, 52.
(73) Hussein, E. A.; Zagho, M. M.; Nasrallah, G. K.; Elzatahry, A. A. Recent advances in functional nanostructures as cancer photothermal therapy. *International journal of nanomedicine* **2018**, 2897.
(74) Liu, S.; Pan, X.; Liu, H. Two‐dimensional nanomaterials for photothermal therapy. *Angew. Chem.* **2020,** *132* (15), 5943.
(75) Wu, Y.; Wang, H.; Gao, F.; Xu, Z.; Dai, F.; Liu, W. An Injectable Supramolecular Polymer Nanocomposite Hydrogel for Prevention of Breast Cancer Recurrence with Theranostic and Mammoplastic Functions. *Adv. Funct. Mater.* **2018,** *28*, 1801000.
(76) Hwang, S.; Nam, J.; Jung, S.; Song, J.; Doh, H.; Kim, S. Gold nanoparticle-mediated photothermal therapy: current status and future perspective. *Nanomedicine* **2014,** *9* (13), 2003.

(77) Yang, W.; Liang, H.; Ma, S.; Wang, D.; Huang, J. Gold nanoparticle based photothermal therapy: Development and application for effective cancer treatment. *Sustainable Materials and Technologies* **2019,** *22*, e00109.
(78) Riley, R. S.; Day, E. S. Gold nanoparticle‐mediated photothermal therapy: applications and opportunities for multimodal cancer treatment. *Wiley Interdisciplinary Reviews: Nanomedicine and Nanobiotechnology* **2017,** *9* (4), e1449.

Supporting information

S5.1 Materials and methods

Materials

SH-PEG_{5400}-NH_2 (Mw: 5 kDa) and SH-PEG_{5000} (Mw: 5 kDa) was obtained from Iris Biotech. 4 arm-PEG-OH (Mw: 10 kDa) from Jenkem Technology. Deuterated solvents for NMR experiments were obtained from Euriso-top. Formvar/Carbon 200 mesh copper grid and lacey carbon 200 mesh grids were purchased from Electron Microscopy Sciences. Dulbecco's phosphate buffered saline (DPBS, pH=7.4) was purchased from Sigma Aldrich. Dulbecco's modified Eagle medium (DMEM), antibiotics penicillin and streptomycin were received from Gibco, Life Technologies. Fetal bovine serum (FBS) was produced from Biowest. The antibiotics penicillin and streptomycin were purchased from Gibco. Collagenase Type I was obtained from Worthington Biochemical Corporation. µ-Slide 8 Well and 15 Well 3D chambered coverplates were purchased from Ibidi. **C8-SQ** (**4**) and **C8-SQ-DT** (**5**) were synthesized as previous reported.[1,2] N-hydroxysuccinimide, N,N'-dicyclohexylcarbodiimide and all other commercially available chemicals were purchased from Sigma Aldrich at the highest purity available and used without further purification. Milli-Q water was employed for all the experiments. All reaction vessels for gold nanoparticles synthesis were washed carefully with aqua regia before use. Gold nanoparticles was stored at -4°C and the rest compounds were stored at -20°C for further usage.

Methods

^{1}H-NMR and ^{13}C-NMR spectra were recorded on a Bruker DMX-400. All supramolecular monomers were purified by high performance liquid chromatography (HPLC) on a Shimadzu system equipped with two LC-20AR pumps, an SPD-20A UV-Vis detector and Phenomenex Kinetex EVO C18 column. The mobile phases were CH_3CN and H_2O with 0.1% trifluoroacetic acid. Liquid chromatography-mass spectrometry (LC-MS) analysis was performed on a Finnigan Surveyor HPLC system equipped (UV detection from 200-600 nm) with a Gemini C18 50 x 4.60 mm reverse phase column coupled to Finnigan LCQ Advantage Max mass spectrometer with ESI. For the mobile phase, a gradient of 10-90% of CH_3CN/H_2O with 0.1% trifluoroacetic acid over 13.5 minutes was used. UV absorption spectra were acquired at room temperature (RT) on a Cary 300 UV-Vis spectrophotometer from 400 to 800 nm using a quartz cuvette with a path length of 1 cm. The hydrodynamic diameter and zeta potential tests were performed on Malvern Zetasizer Nano S. Oscillatory rheology experiments were performed on a Discovery Hybrid Rheometer (DHR-2) from TA Instruments with a Smart Swap UV assembly with a quartz lower plate (20 mm) and a aluminum upper plate (8 mm) at RT using a fixed gap of 300 µm, UV light (λ = 320-500 nm, primary peak: 365 nm) was applied through an Omnicure S2000 high-pressure mercury light source from Excelitas connected to the rheometer through a light guide (5 mm diameter). The UV intensity was calibrated using a Silverline radiometer sensor (20 mm) accessory designed for the quartz parallel plate. The compressive properties were assessed under the same conditions on DHR-2 at a fixed gap of 1 mm and a maximum axial force of 50 N. The diameters and of the gold nanoparticles were imaged on a JEOL JEM-1400 Plus transmission electron microscope (TEM). The distributions of gold nanoparticles in the **DN** and **DN-Au** hydrogels were imaged on TEM and cryogenic electron

microscope (cryo-EM) on a Talos L120C operating at 120 kV, samples were plunge frozen on a Vitrobot Mark IV, both from Thermo Fisher Scientific. The surface morphology and pore sizes of the lyophilized hydrogels were imaged by scanning electron microscope (SEM) using a JSM-7600F microscope from JEOL under high vacuum with an acceleration voltage of 2.0 kV. The conductivity measurement was assessed using a Metrohm Autolab Potentiostat by scanning from 1 MHz to 1 Hz in 10 frequency measurement points per at 0 V to prevent localized oxidation. Photo-thermal effect was accessed by using Lighthouse Photonics Sprout laser at 532 nm and K-Type Digital Thermometer. Cells were cultured in Dubecco's modified Eagle medium (DMEM) with high glucose, with 10% fetal calf serum, 0.1% glutamax, 0.2% penicillin and 0.2% streptomycin. Images for cell viability assessment in 3D cultures were captured on a Stellaris 8 confocal laser scanning microscope from Leica with a supercontinuum white light laser (440-790 nm) and Power HyD detectors, the excitation wavelengths of 486 nm (Calcein AM) and 532 nm (propidium iodide), and emission filters of 500-545 nm (Calcein AM) and 594-686 nm (propidium iodide) were used, respectively. Live and dead cells were counted using a Fiji/ImageJ macro written for 3D analysis of LIVE/DEAD cells. The confocal pictures were processed using Fiji/ImageJ software. A benchtop LED light (~10 mW/cm², 375 nm) was employed to initiate crosslinking in all other samples except for the ones on the rheometer.

Experimental Details

Synthesis of hydrogel components

DT (1)

4-methyl-1,2-dithiolane-4-carboxylic acid (**DT**) was synthesized as reported before.[1,3] Briefly, 3,3-Dichloropivalic acid (2.00 g, 11.69 mmol) and water (15 mL) were mixed in a 3-neck round bottom flask. Sodium carbonate (1.14 g, 10.76 mmol) was added slowly. When 3,3 dichloropivalic acid was fully dissolved under stirring, an aqueous solution (5 mL) containing potassium thioacetate (2.71 g, 23.64 mmol) was added dropwise over a period of a few minutes. The solution was then heated to 100 °C and refluxed for 8 h. Then, sodium carbonate (3.84 g, 35.85 mmol) was added slowly, and the yellow solution turned green, then yellow again after a few minutes. After disappearance of the starting material, dimethyl sulfoxide (DMSO, 1.8 mL) was added, and the solution was refluxed for another 8 h at 100 °C. The reaction mixture was cooled to RT and acidified with 1 M hydrochloric acid. A yellow precipitate was collected, washed with ice-cold water and dried in an oven overnight at 60 °C. Yield: 660 mg, 34%. ^{1}H-NMR (400 MHz, DMSO-D_6): 3.59 (s, 1H), 3.56 (s, 1H), 3.01 (s, 1H), 2.98 (s, 1H), 1.40 (s, 3H). ^{13}C-NMR (DMSO-D_6, 100 MHz): 170.43, 55.53, 45.62, 22.13.

HS-PEG$_{5400}$-DT (2)

1,2-Dithiolane-3-carboxylic acid (500.00 mg, 3.00 mmol), N,N'-dicyclohexylcarbodiimide (DCC) (618.99 mg, 3.00 mmol) and N-hydroxysuccinimide (NHS) (350.00 mg, 3.00 mmol) were dissolved in dry CH_2Cl_2 (10 mL). The reaction was stirred overnight at RT under nitrogen gas. The reaction mixture was collected and filtered twice, and the filtrate was dried on a rotary evaporator at 40 °C under vacuum (700 mbar) to get a light-yellow compound (DT-NHS). Afterwards, to a stirring solution of HS-PEG$_{5400}$-NH_2 (200.00 mg, 0.04 mmol) solution in dry CH_2Cl_2 (5 mL), DT-NHS (79.30 mg, 0.19 mmol) and DIPEA (63.34 µL, 0.37 mmol) were added and reacted

overnight under nitrogen gas. The mixed solution was filtered and concentrated by a stream of nitrogen gas before being precipitated in cold diethyl ether, washed and re-dissolved in CH_2Cl_2 (10 mL). The precipitation step was repeated 3 times, then H_2O (2 mL) was added to dissolve the obtained solid and the product was lyophilized overnight to obtain a white solid. Yield: 186 mg, 90%. ^{1}H-NMR (400 MHz, $CDCl_3$): 3.47-3.84 (m, 486H), 3.31-3.33 (t, 4H), 2.99-3.02 (d, 2H), 2.49-2.51 (t, 2H), 2.95 (s, 3H).

PEG4-NB

To a stirring solution of 5-norbornene-2-carboxylic acid (**NB**, 183.63 µL, 1.50 mmol) in dry CH_2Cl_2 (5 mL), DCC (309.51 mg, 1.50 mmol) was added and the mixture was kept at RT for 30 min. Subsequently, the reaction mixture was added to a solution (5 mL) containing 4-arm polyethylene glycol (Mw: 10 kDa) (500 mg, 0.05 mmol), pyridine (40.23 µL, 0.50 mmol) and 4-dimethylaminopyridine (DMAP, 12.22 mg, 0.10 mmol), and stirred overnight at RT. The mixed solution was filtered and concentrated by a stream of nitrogen gas before being precipitated in cold diethyl ether, washed and re-dissolved in CH_2Cl_2 (10 mL). The precipitation step was repeated 3 times, then H_2O (2 mL) was added to dissolve the obtained solid and dialyzed for 3 days. The product was lyophilized overnight to obtain a white solid. Yield: 494 mg, 94%. ^{1}H-NMR (400 MHz, $CDCl_3$): 5.94-6.21 (m, 8H), 4.16-4.28 (m, 8H), 3.47-3.85 (m, 909H).

PEG4-DT

To a stirring solution of **DT** (131.00 mg, 0.80 mmol) in dry CH_2Cl_2 (5 mL), DCC (165.06 mg, 0.80 mmol) was added and the mixture was reacted at RT for 30 min. Subsequently, the reaction mixture was added to a solution (5 mL) containing 4-arm polyethylene glycol (Mw: 10 kDa) (500 mg, 0.05 mmol), pyridine (40.23 µL, 0.50 mmol) and 4-dimethylaminopyridine (DMAP, 12.22 mg, 0.10 mmol), and stirred overnight at RT. The reaction mixture was filtered and concentrated by a stream of nitrogen gas before being precipitated in cold diethyl ether, washed and re-dissolved in CH_2Cl_2 (10 mL). The precipitation step was repeated 3 times, then H_2O (2 mL) was added to dissolve the obtained solid and dialyzed for 3 days. The product was lyophilized overnight to obtain a white solid. Yield: 487.6 mg, 87%. ^{1}H-NMR (400 MHz, $CDCl_3$): 4.32-4.33 (m, 8H), 3.83-3.85 (m, 8H), 3.74-3.69 (d, 8H), 3.48-3.67 (m, 961H), 3.43 (s, 8H), 2.95-2.98 (d, 8H), 1.51 (s, 12H).

Au@Citrate

Gold nanoparticles (15 nm) were synthesized following the methods of Turkevich and French.[4,5] Milli-Q water (24 mL) was refluxed and stirred in a 3-neck round bottom flask. A chloroauric acid ($HAuCl_4$) solution (25.4 mM, 985 µL) was added and kept boiling for 3 min, followed by a 1% wt. trisodium citrate dehydrate solution (5 mL). The mixture was refluxed for 30 min, during which the color of the solution turned from yellow to transparent to greyish/violet and then to deep red. The reaction mixture was cooled to RT, washed 2 times with Milli-Q water (12000 rpm, 40 min) and concentrated before usage.

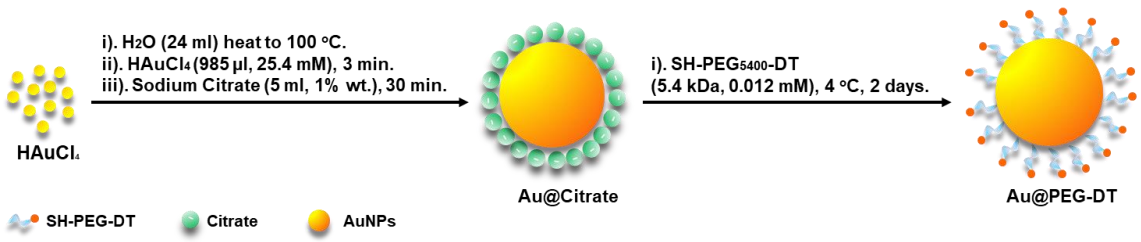

Figure S1. Synthesis route of **Au@Citrate** and **Au@PEG-DT**.

Au@PEG-DT

Au@PEG-DT nanoparticles were prepared by a ligand exchange reaction on gold.[6] Briefly, to an aqueous solution of **Au@Citrate** nanoparticles (10 mL, approximately 0.005 mM), **2** (60 mg, 0.012 mM) was added. The reaction was incubated for 3 days in the dark at 4 °C on a peptideshaker. The nanoparticles solution was washed 3 times by Milli-Q water to remove the excess ligand (12000 rpm, 40 min) and concentrated before usage. The concentration of **Au@PEG-DT** was obtained by ICP-MS.

Au@PEG

Au@PEG nanoparticles were prepared the same process as **Au@PEG-DT**, here we used SH-PEG_{5000} instead of **HS-PEG_{5400}-DT.**

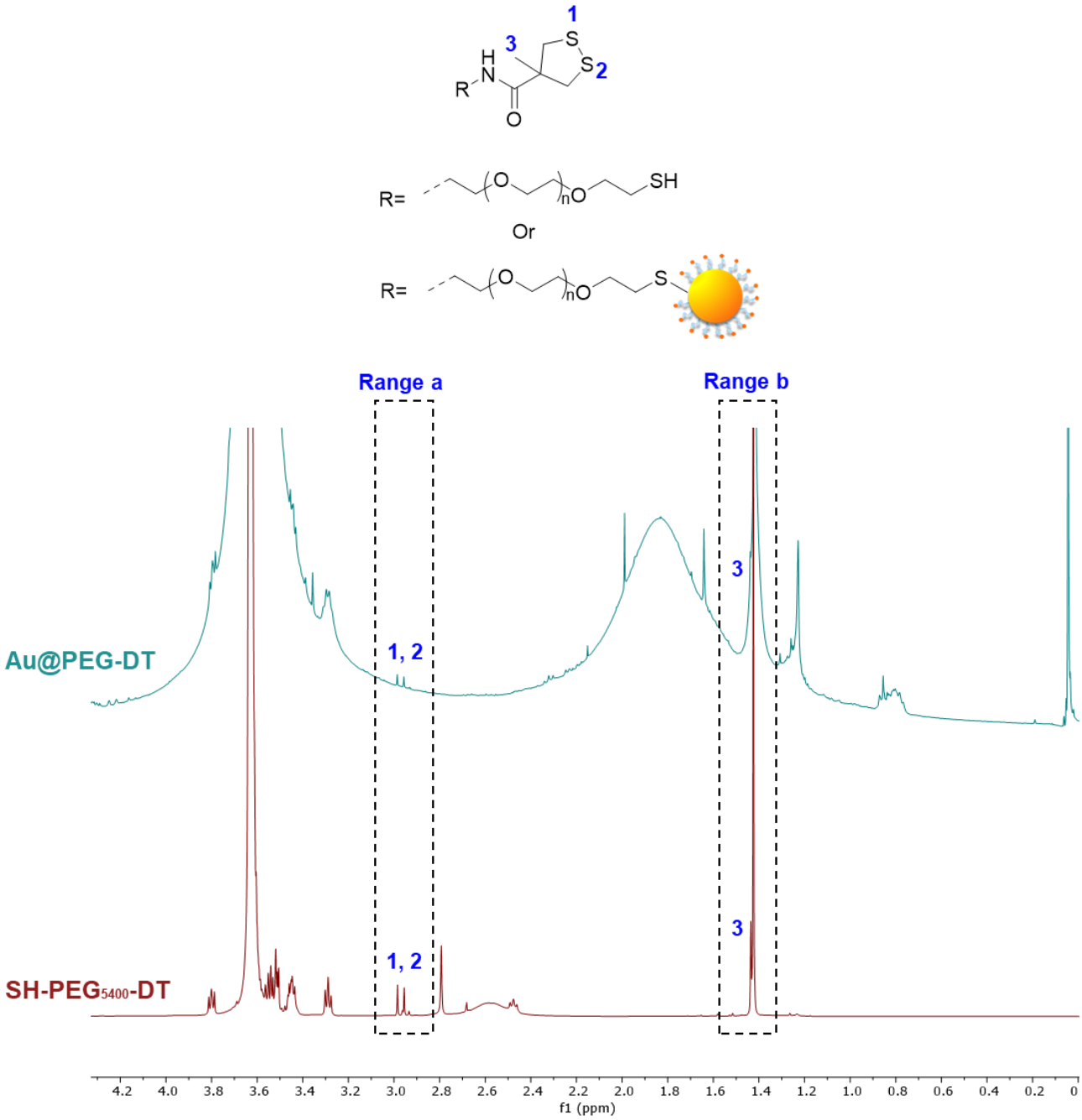

Figure S2. ^{1}H-NMR (400 Hz, 298K, $CDCl_3$) comparation spectrum of **Au@PEG-DT**(blue) and **HS-PEG$_{5400}$-DT**(red).

DLS and Zeta potential measurements

Au@Citrate (~1 mM) and **Au@PEG-DT** (~0.8 mM) solutions in Milli-Q water were prepared and measured at 25 °C. The hydrodynamic diameter and zeta potential was based on average of 5 measurements.

UV-Vis spectroscopy

Au@Citrate (~1 mM), **Au@PEG-DT** (0.8 mM) and **Au@PEG** (~0.8 mM) solutions in Milli-Q water were prepared after synthesis to obtain the UV spectra. The individual samples were left to equilibrate for 2 min at RT prior to measurements.

Transmission electron microscopy (TEM)

Aqueous gold nanoparticle solutions (5 µL, 300 ug/ml) in Milli-Q water were drop-casted on a Formvar/Carbon 200 mesh copper grid and dried at RT overnight before imaging.

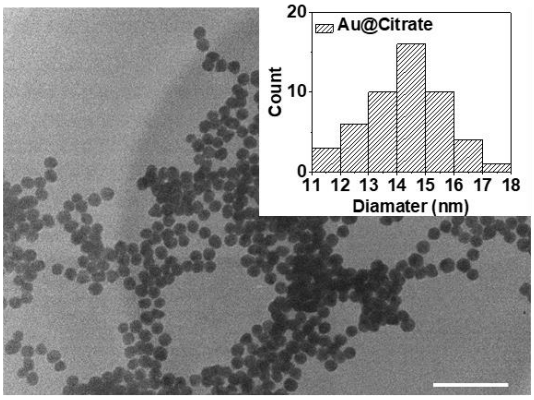

Figure S3. TEM picture of **Au@Citrate** (300 µg/ml). Insert: size distribution of AuNPs. Scale bar: *100 nm*.

Multicomponent hydrogels preparation

First, stock solutions of **C8-SQ** (10 mM) and **C8-SQ-DT** (10 mM) were prepared separately by dissolving the compounds in DMSO with 3 min of vortexing. To acquire **C8-SQ/10C8-SQ-DT** (10 molar percentages of **C8-SQ-DT** of the total monomer concentration) hydrogels (100 µL, 8 mM), **C8-SQ** (72 µL) and **C8-SQ-DT** (8 µL) stock solutions were pipetted into the glass vials (2.0 mL) with 1 min of gentle vortexing. Subsequently, the solutions were dried overnight under a stream of nitrogen gas. Water (100 µL) was added to the film of supramolecular monomers to prepare a hydrogel at final monomer concentration of 8 mM. Sonication was performed in an ice bath yielding a clear solution. To prepare the double network with gold nanoparticles, **PEG$_4$-NB** (10 wt%), **PEG$_4$-DT** (10 wt%) and **Au@PEG-DT** (7.68 mg/mL) or **Au@PEG** (6.8 mg/mL) solutions were added to the solution of supramolecular and left overnight equilibration. Lithium Phenyl(2,4,6-trimethylbenzoyl)phosphinate (LAP, 20 mM) was mixed with the **DN** hydrogel before crosslinking. The hydrogels without and with **Au@PEG-DT** were called **DN** and **DN-Au**, respectively. The hydrogels with 0.25 mg/mL **Au@PEG** were called **DN-Au@PEG$_{0.25}$**. For all the **DN**, **DN-Au** and **DN-Au@PEG$_{0.25}$** hydrogels in this paper, the final concentration of supramolecular hydrogel was 4 mM, LAP was 1 mM, functionalized group of **PEG$_4$-NB** and **PEG$_4$-DT** were 1.5 mM, respectively. **Au@PEG-DT** concentration was varied from 0.1 mg/mL to 1 mg/mL to obtain different **DN-Au** hydrogels, namely, **DN-Au$_x$** (**x** mg/mL **Au@PEG-DT** in the hydrogel). For example, to prepare **DN-Au$_{0.25}$** (100 µL), 14.49 µL Milli Q water, 15.96 µL **PEG$_4$-NB** (10 wt%), 16.30 µL **PEG$_4$-DT** (10 wt%) and 3.25 µL **Au@PEG-DT (**7.68 **mg/mL)** were added into 50 µL **C8-SQ/10C8-SQ-DT** (8 mM), evenly mixed by pipetted 10 times and left overnight equilibration to allow gelation to occur. 5 µL LAP (20 mM) was added and pipetted 10 times prior to other measurements. The uncross-linked gelation protocol was

utilized for all hydrogels discussed in this paper, with the exception of those that were specially illustrated.

Gel inversion test

For gel inversion tests, **DN** and **DN-Au** hydrogels (100 µL) were prepared in glass vials (2 mL) and crosslinked with a LED for 10 min. Milli-Q water (150 µL) was layered on top of each hydrogel and replaced every 2 days. Digital photos were taken on Day 0 before and after crosslinking and on Day 15 at the end of the experinment.

Figure S4. Gel inversion test before and after UV irradiation at Day 0 and at Day 15 at the end of the experiment.

Oscillatory rheology

DN and **DN-Au** hydrogels were prepared according to previously established uncross-linked gelation protocol, and gently pipetted on to the quartz plate under a fixed gap at 0.7 mm. Before data collection, the loaded samples were equilibrated for 5 min to allow the hydrogels to self-recover. After a time sweep experiment for 60 s, the hydrogels were stiffened by applying a UV light for 10 min. All the oscillatory time sweeps were performed at a strain amplitude (γ) of 0.05% and a frequency (ƒ) of 1 Hz. Frequency sweeps were assessed in a frequency range of 0.01 Hz to 10 Hz at a constant strain amplitude (γ = 0.05%). Strain sweeps were performed in a range of strain amplitudes of 0.01 % to 1000 % at a fixed frequency (ƒ = 1.0 Hz).

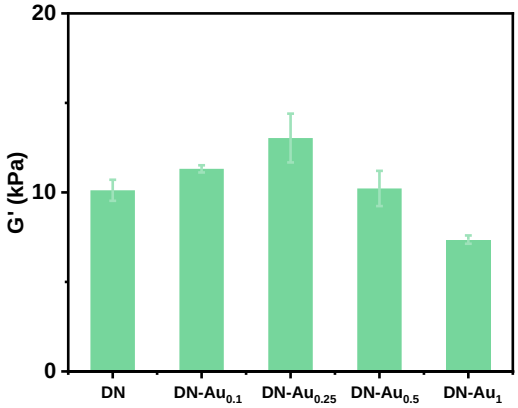

Figure S5. Plateau storage moduli (G') of photo-crosslinked **DN** and **DN-Au** hydrogels in Milli Q water at RT. Mean ± SD, N≥3.

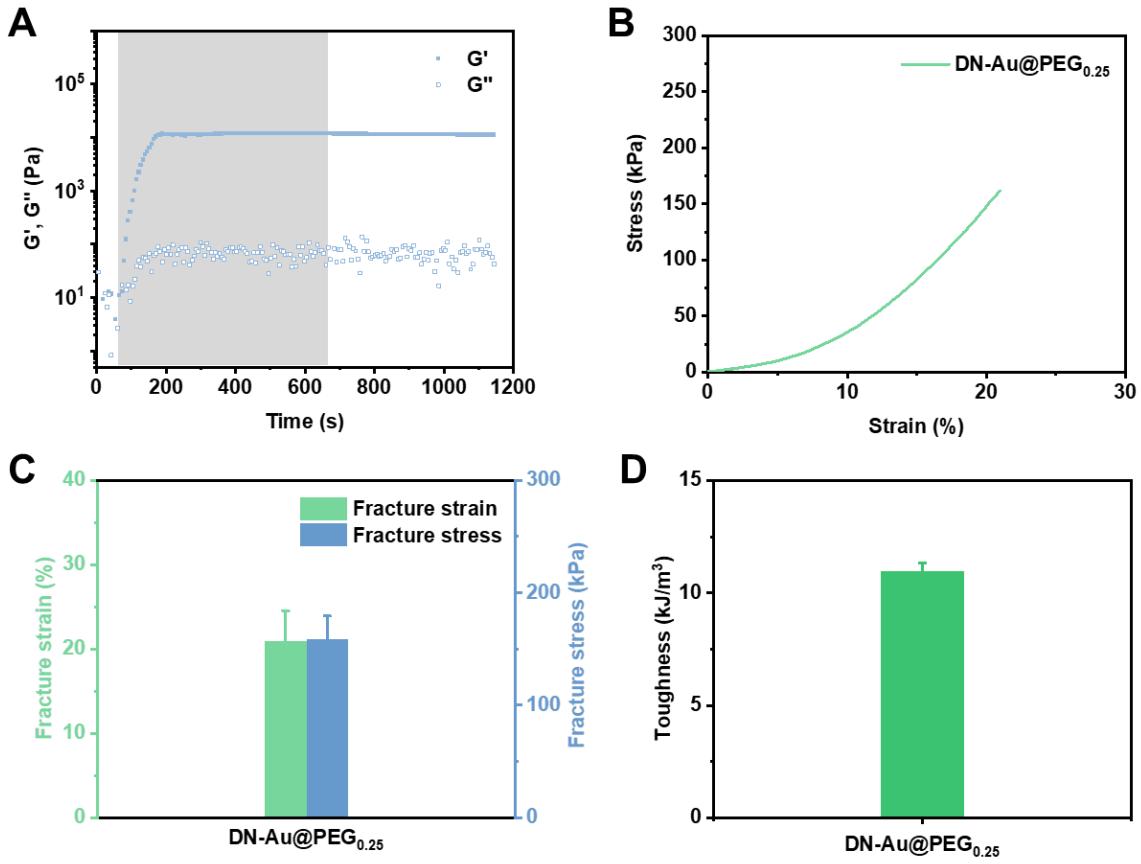

Figure S6. Mechanical properties **DN-Au@PEG$_{0.25}$** hydrogel: (A) Time sweep measurements of hydrogel before/after 10 min UV irradiation using a fixed strain (γ = 0.05%) and frequency (ƒ = 1.0 Hz) at room temperature. Grey regions indicate UV exposure. (B) Compression stress-strain response of UV crosslinked **DN-Au@PEG$_{0.25}$** hydrogel under a constant compression speed (10 µm/s) for 80 s at room temperature. (C) Compressive fracture strain and compressive fracture stress of UV crosslinked **DN-Au@PEG$_{0.25}$** hydrogel under a constant compression speed (10 µm/s). Mean ± SD, N≥3. (D). Compressive toughness of UV crosslinked **DN-Au@PEG$_{0.25}$** hydrogel under a constant compression speed (10 µm/s). Mean ± SD, N ≥ 3.

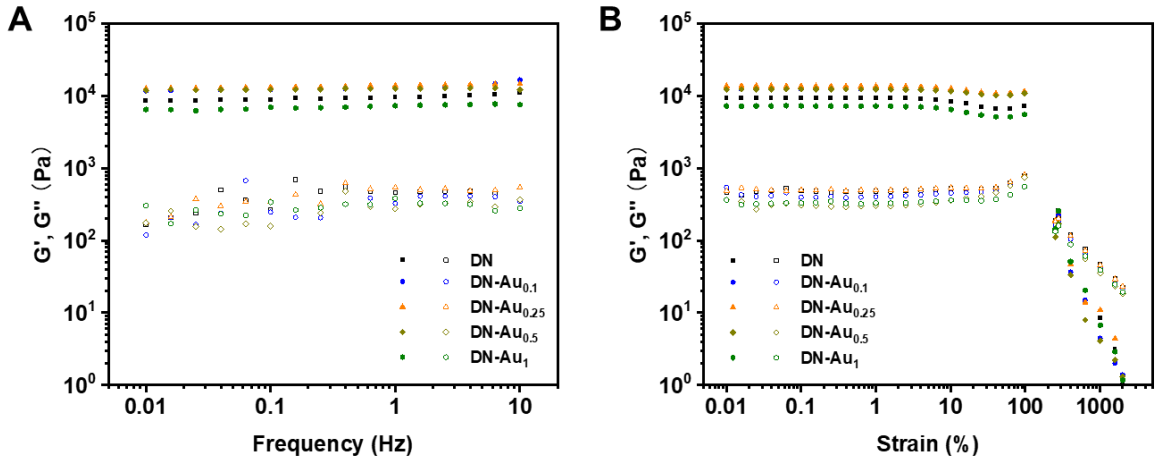

Figure S7. Oscillatory rheology measurements of UV crosslinked **DN** and **DN-Au** hydrogels in Milli Q water at RT: (A) Frequency sweep (γ = 0.05%). (B) Amplitude sweep (ƒ = 1.0 Hz).

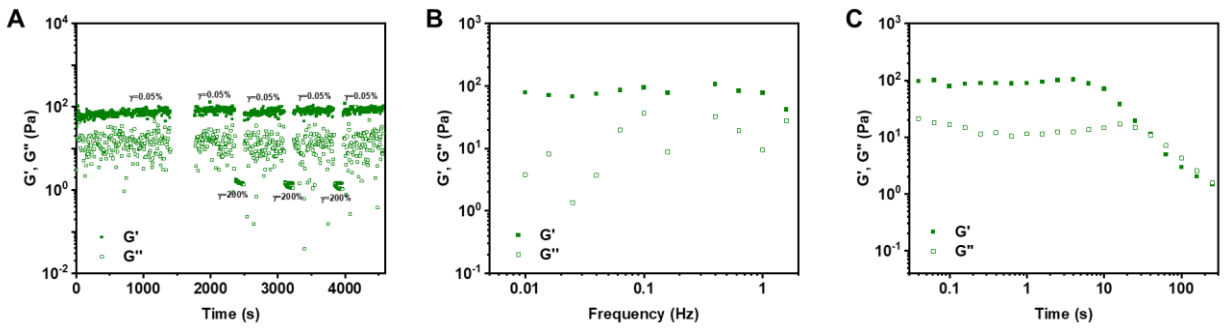

Figure S8. Oscillatory rheology measurements of **DN-Au$_{0.25}$** hydrogel in MilliQ water at RT: (A) Time sweep measurements (ƒ = 1 Hz, γ = 0.05%) and self-recovery process. The absence of data prior to applying a high strain (200%) can be attributed to conducting a frequency sweep prior to the measurement (ƒ = 0.01 to 2 Hz, γ = 0.05%). (B) Frequency sweep (γ = 0.05%). (C) Amplitude sweep (ƒ = 1 Hz).

Compression study

DN and **DN-Au** hydrogels were prepared according to previously established uncross-linked gelation protocol, and gently pipetted on to the quartz plate of the rheometer and the upper plate was lowered to 1 mm, equilibrated for 5 min before data collection. After a time sweep experiment for 60 s, the samples were irradiated with UV light for 10 min to reach a plateau in storage modulus. Subsequently, an axial experiment was set up compressing the sample to 50% of its initial height (500 µm gap) with a constant speed of 10 µm/s. Energy dissipation within the photocrosslinked gels were probed under the same conditions as the cyclic axial compression test using increasing strain percentages from 5% to 25% at a speed of 10 µm/s. The normal stress was plotted versus Cauchy strain (or engineering strain, the change in gap percentage as measured with respect to its initial setting) to get the compression curves of the hydrogels. The compressive fracture strain or stress was defined as the strain or stress at the breaking point. Toughness was calculated by the area under the stress-strain curve up to the point of fracture. The cyclic hysteresis curves were plotted as the compression curves before fracture. The dissipated energy was estimated by the area between loading - unloading curves.

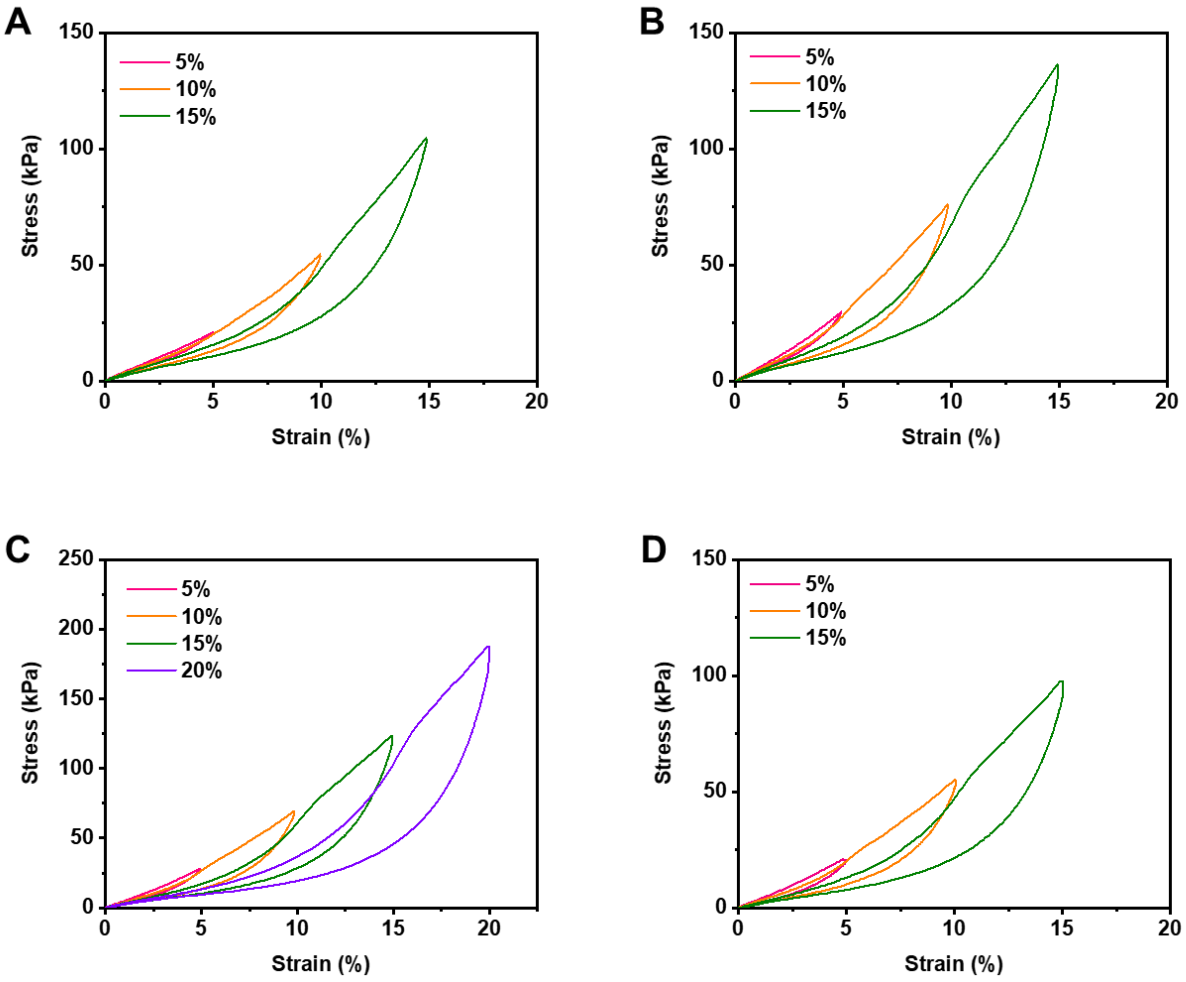

Figure S9. Cyclic hysteresis curves of UV crosslinked **DN** and **DN-Au** hydrogels at different maximum strains (λ_{max}) using a loading - unloading test under a constant compression speed (10 µm/s) at RT before break: (A) **DN**, (B) **DN-Au$_{0.1}$**, (C) **DN-Au$_{0.5}$**, (D) **DN-Au$_{1}$**.

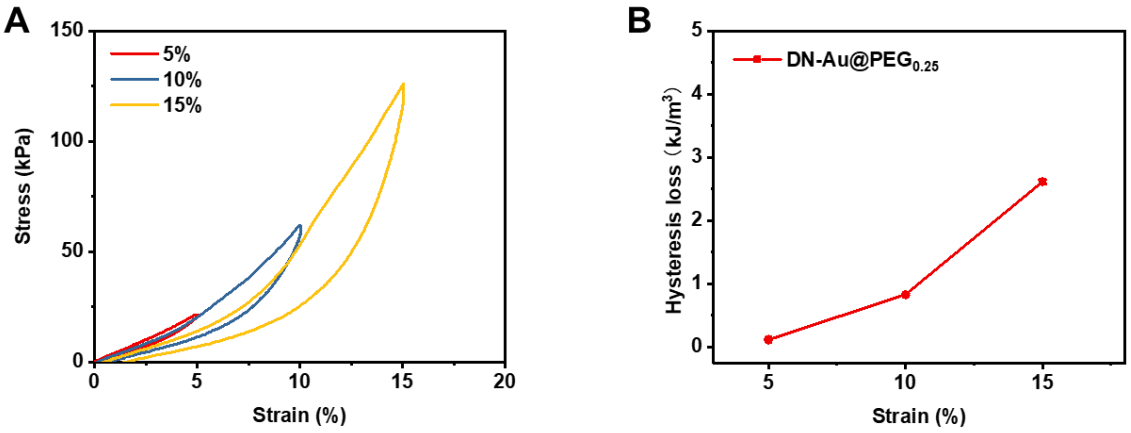

Figure S10. Mechanical properties **DN-Au@PEG$_{0.25}$** hydrogel: (A) Cyclic hysteresis curves of UV photocrosslinked hydrogel at different maximum strains (λ_{max}) using a loading - unloading test under a constant compression speed (10 µm/s) at RT before break. (B) Hysteresis loss of photocrosslinked hydrogel. Mean ± SD, N ≥ 3.

(Cryogenic) Transmission Electron microscopy ((Cryo)-TEM)

DN and **DN-Au** hydrogels (100 µL) were prepared according to previously established uncross-linked gelation protocol. The hydrogels were then diluted (10 times) to obtain their respective measured concentrations (0.4 mM of **C8-SQ/10C8-SQ-DT**, 0.15 mM NB of **PEG$_4$-NB**, 0.15 mM DT of **PEG$_4$-NB**, 0 mg/mL - 0.05 mg/mL of **Au@PEG-DT** and 0.1 mM LAP), and exposed to a LED for 10 min. Solution (10 µL) was carefully placed on Formvar/Carbon 200 mesh copper grid for 2 min and was removed by a paper, then uranyl acetate (10 µL, 1 %) was blotted on grid for 1 min and was removed by a paper. The grid was dried overnight at RT before imaging. The diameters of the gold nanostructures were measured manually in Fiji/ImageJ.

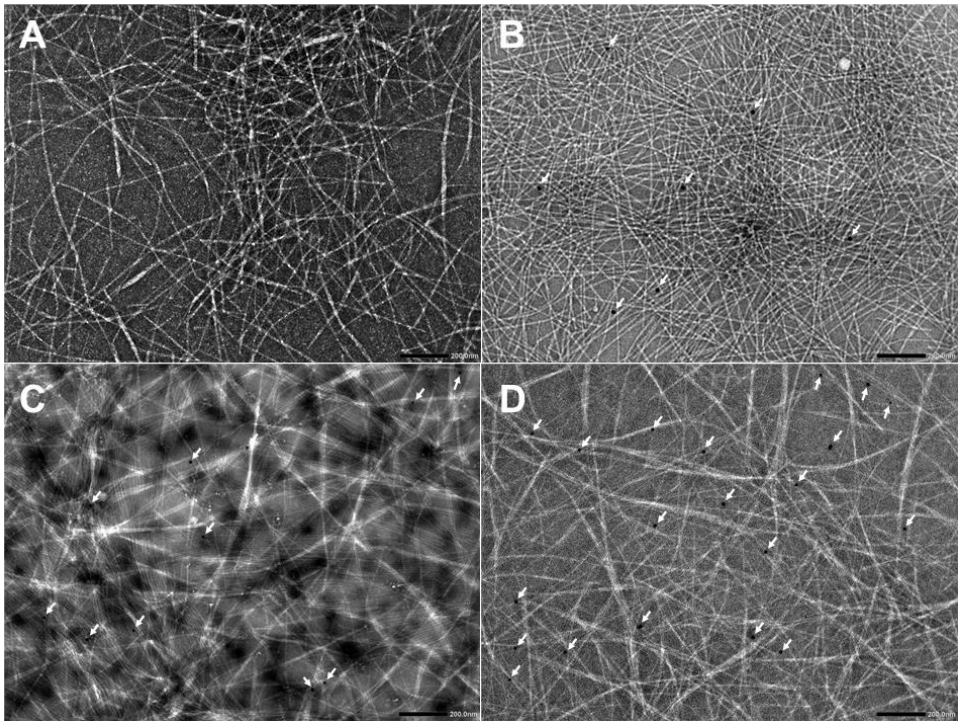

Figure S11. TEM images of diluted **DN** and **DN-Au** hydrogels after UV crosslinking: (A) **DN** (0.4 mM of **C8-SQ/10C8-SQ-DT**, 0.15 mM NB of **PEG$_4$-NB**, 0.15 mM DT of **PEG$_4$-DT**). (B) **DN-Au$_{0.1}$** (0.4 mM of **C8-SQ/10C8-SQ-DT**, 0.15 mM NB of **PEG$_4$-NB**, 0.15 Mm DT of **PEG$_4$-DT**, 0.01 mg/mL of **Au@PEG-DT**). (C) **DN-Au$_{0.25}$** (0.4 mM of **C8-SQ/10C8-SQ-DT**, 0.15 mM NB of **PEG$_4$-NB**, 0.15 mM DT of **PEG$_4$-DT**, 0.025 mg/mL of **Au@PEG-DT**). (D) **DN-Au$_{0.5}$** (0.4 mM of **C8-SQ/10C8-SQ-DT**, 0.15 mM NB of **PEG$_4$-NB**, 0.15 mM DT of **PEG$_4$-DT**, 0.05 mg/mL of **Au@PEG-DT**). Scale bar: *200 nm*.

DN-Au$_{0.25}$ and **DN-Au$_{0.5}$** hydrogels (100 µL) were prepared according to previously established uncross-linked gelation protocol. The hydrogels were then diluted (10 times) to obtain diluted **DN-Au$_{0.25}$** (0.4 mM of **C8-SQ/10C8-SQ-DT**, 0.15 mM NB of **PEG$_4$-NB**, 0.15 Mm DT of **PEG$_4$-DT**, 0.025 mg/mL of **Au@PEG-DT** and 0.1 mM LAP) and **DN-Au$_{0.5}$** hydrogels (0.4 mM of **C8-SQ/10C8-SQ-DT**, 0.15 mM NB of **PEG$_4$-NB**, 0.15 Mm DT of **PEG$_4$-DT**, 0.05 mg/mL of **Au@PEG-DT** and 0.1 mM LAP), and exposed to a LED for 10 min. Afterwards, the solution (3 µL, 0.5 mM) was applied to a freshly glow-discharged lacey carbon 200 mesh Cu grid and the excess liquid was blotted off for 3 seconds at 100% humidity and

plunge-frozen in liquid ethane using a Vitrobot plunge-freezer (FEI VitrobotTM Mark III, Thermo Fisher Scientific, Waltham, MA, USA). Images were recorded on a BM-Ceta (4k x 4k) at a nominal magnification of 73000x (1.34 Ångstrom per pixel) and defocus of -2.0 to -3.0 µm.

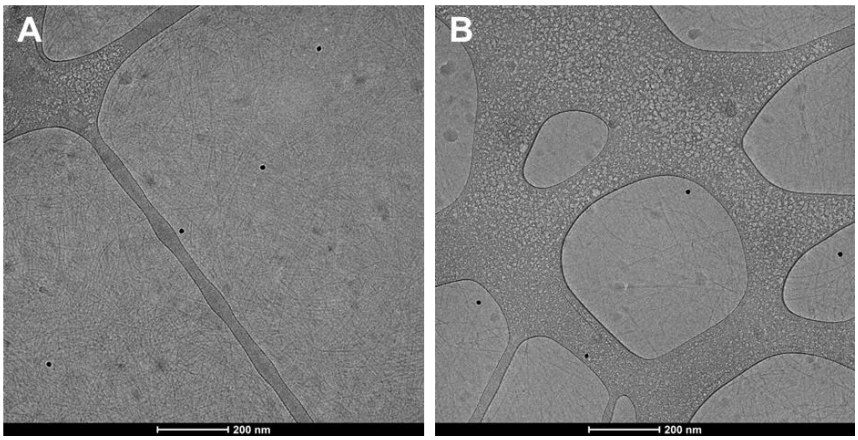

Figure S12. Cryo-TEM images of diluted **DN-Au** hydrogels after UV crosslinking: A) **DN-Au$_{0.25}$** (0.4 mM of **C8-SQ/10C8-SQ-DT**, 0.15 mM NB of **PEG$_4$-NB**, 0.15 Mm DT of **PEG$_4$-DT**, 0.025 mg/mL of **Au@PEG-DT** and 0.1 mM LAP). B) **DN-Au$_{0.5}$** (0.4 mM of **C8-SQ/10C8-SQ-DT**, 0.15 mM NB of **PEG$_4$-NB**, 0.15 Mm DT of **PEG$_4$-DT**, 0.05 mg/mL of **Au@PEG-DT** and 0.1 mM LAP). Scale bar: *200 nm*.

Scanning electron microscope (SEM)

DN and **DN-Au** hydrogels (200 µL) were prepared according to previously established uncross-linked gelation protocol, then exposed to a LED for 10 min. All the samples were lyophilized and fractured in liquid N_2 prior to SEM image. The pore diameters of the hydrogel nanostructures were measured manually in Fiji/ImageJ.

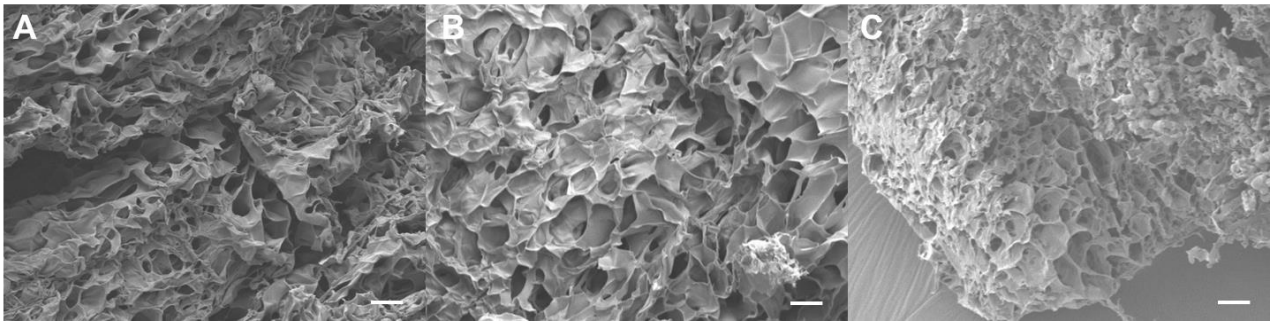

Figure S13. SEM images of **DN** and **DN-Au** hydrogels after crosslinking: (A) **DN**, (B) **DN-Au$_{0.5}$**, (C) **DN-Au$_1$**. Scale bar: *10 µm*.

Equilibrium Swelling ratio and Gel stability test

Hydrogel swelling ratios and gel stability data were acquired by weighing hydrogels at different time points. Hydrogels (100 µL) were prepared according to the gelation protocol in glass vials (2 mL) and crosslinked with a LED for 10 minutes. After crosslinking, the hydrogels were covered with Milli Q water (300 µL) and kept at RT. The weights of hydrogels were recorded at different time points as W*wet*. Hydrogels' W*equ* were recorded when hydrogels were fully swelled to reach swelling equilibrium. After

15 days, the hydrogels were lyophilized and the dried product was weighed as Wdry. Hydrogels swelling ratios was calculated using the formula: $Swelling\ Ratio = (Wequ - Wdry)/Wdry$. Gel stability was calculated using the formula: $Gel\ erosion\% = 100 \times (Wwet - Wdry)/Wequ$. Each test had three parallels.

Conductivity Test

DN and **DN-Au** hydrogels (150 µL) were prepared according to previously established uncross-linked gelation protocol in a non-conductive 9 well Teflon mold with dimensions of 4 mm × 10 mm and at a height of 4 mm, then exposed to a LED for 10 min. Two 2.5 mm x 20 mm Pd electrodes were incorporated into hydrogels at a fixed distance of 8 mm before measurements to provide electrode contact. Here the contacted dimensions of Pd electrodes and hydrogel is 4 x 4 mm. When -Z'' (Ω) reached to 0 Ω, Z'(Ω) was taken to calculate the conductivity by using the formula: $\sigma(S/m) = \frac{0.008}{Z'(\Omega)*2.5*4*0.0001}$.

Photo thermal Test

DN and **DN-Au** hydrogels (150 µL) were prepared according to previously established uncross-linked gelation protocol, then exposed to a LED for 10 min. Milli-Q water (150µL) was placed on top the hydrogels before irradiation with 532 nm laser (1 W) to prevent drying. Temperatures were recorded at different time points to make the curves.

Manual implementation of 3D hydrogel printing

The **DN-Au$_{0.25}$** hydrogel (300 µL) was prepared in a glass vial (2 mL) as described in the gelation protocol without UV irradiation. The uncrosslinked hydrogel was extruded from a micropipetor into water (500 µL) in a glass vial (2 mL). Subsequently, the extruded hydrogel was crosslinked using a LED for 10min. A video was made during the extrusion process and pictures were taken 1 day after crosslinking.

3D cell culture studies

Cell viability tests of NIH 3T3 mouse fibroblasts and bone metastases breast cancer cell-lines (MDA-MB-231-B1). **DN** and **DN-Au** hydrogels were prepared in PBS (pH ~7.4) as described in the gelation protocol without UV irradiation. Cell suspensions were pipetted with hydrogels and seeded in 15-well µ-Slide Angiogenesis plates (Ibidi) at a cell density of 10^6 cells/mL. The hydrogels were crosslinked with UV light by a LED for 5 min, cell medium (50 µL) was then pipetted on top of the hydrogels and was replaced every hour for the first three hours to remove excess LAP. Hereafter, medium was replaced once a day. Before application of the LIVE/DEAD staining, the medium on top of the hydrogels was then removed before washed with 50 µL of PBS for twice. Subsequently, staining solution (40 µL of 2 µM calcein AM and 1.5 µM propidium iodide) was added and incubated for 40 min at 37 °C. The supernatant was replaced with PBS before imaging. Cells were counted using the Fiji/ImageJ macro written for 3D analysis of live and dead cells.

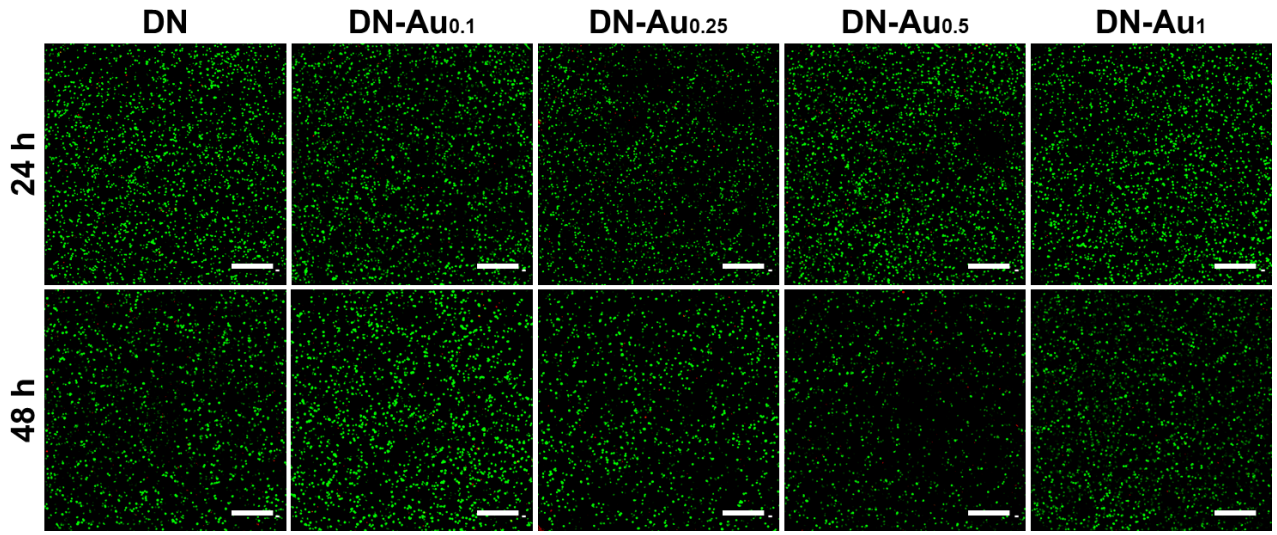

Figure S14. Confocal imaging of NIH 3T3 mouse fibroblasts viability in **DN** and **DN-Au** hydrogels for 24 h and 48 h. Calcein AM (green) and propidium iodide (red) mark the live and dead cells, respectively. Scale bar: *500 μm*.

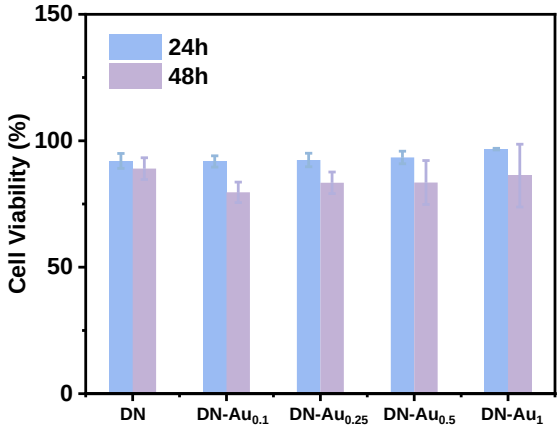

Figure S15. Cell viability of NIH 3T3 mouse fibroblasts encapsulated in **DN** and **DN-Au** hydrogels at 24 h and 48 h. Mean ± SD, N = 3.

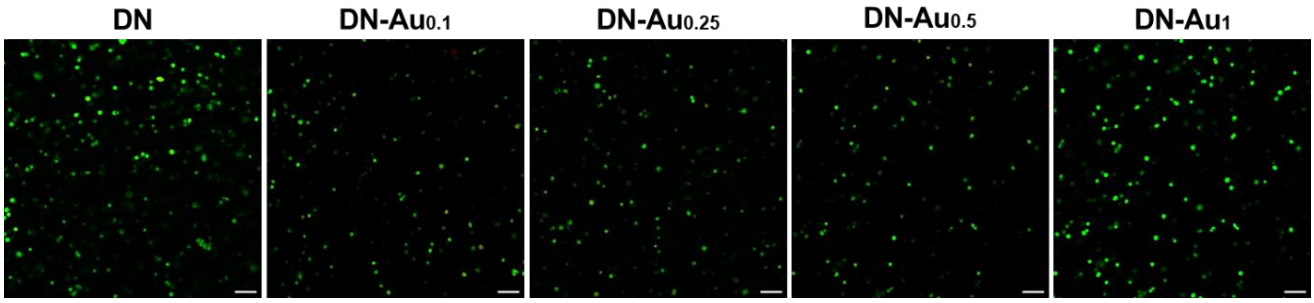

Figure S16. Confocal microscopy images of MDA-MB-231 cells encapsulated in **DN** and **DN-Au** hydrogels for 24 h without different 532 nm laser irradiation. Calcein AM (green) and propidium iodide (red) mark the live and dead cells, respectively. Scale bar: *100 μm*.

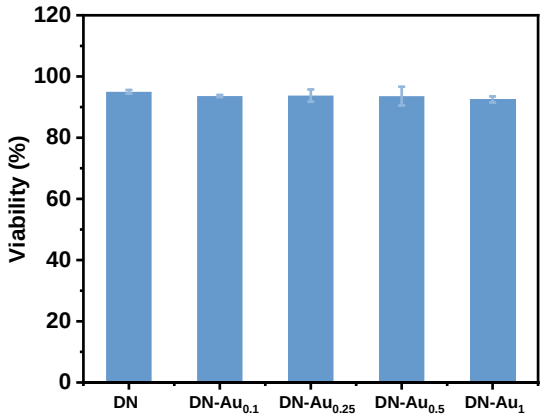

Figure S17. Cell viability of MDA-MB-231-B1 cells encapsulated in **DN** and **DN-Au** hydrogels for 24 h. Mean ± SD, N ≥ 3.

3D phototherapy *in vitro*

Agarose hydrogels (3%, 350 µL) were first prepared in 24-well plates. A hole was made in the center of the agarose hydrogel, with dimensions of 8mm diameter and 1mm height, which was used to seed the cell-laden hydrogels. **DN** and **DN-Au** hydrogels were prepared in PBS (pH ~7.4) as described in the gelation protocol without UV irradiation. Cell suspensions were pipetted with hydrogels and seeded at a cell density of 10^7 cells/mL. The hydrogels were crosslinked with UV light from a benchtop LED (375 nm, ~ 10 mW/cm^2) for 5 min, cell medium (500 µL) was then pipetted on top of the hydrogels and was replaced every hour for the first three hours to remove excess LAP. 24 h later, cell-laden hydrogels were carefully washed with PBS (twice, 500 µL), placed in µ-Slide 8 well plates with PBS (50 µL) inside, and irradiated using a visible light laser at 532 nm with a beam spot of ~6 mm in diameter at a power of 1 W for different time. After the PBS was removed, the staining solution (200 µL of 2 µM calcein AM and 1.5 µM propidium iodide) was immediately added and incubated for 40 min at 37 °C. The supernatant was replaced with PBS before imaging.

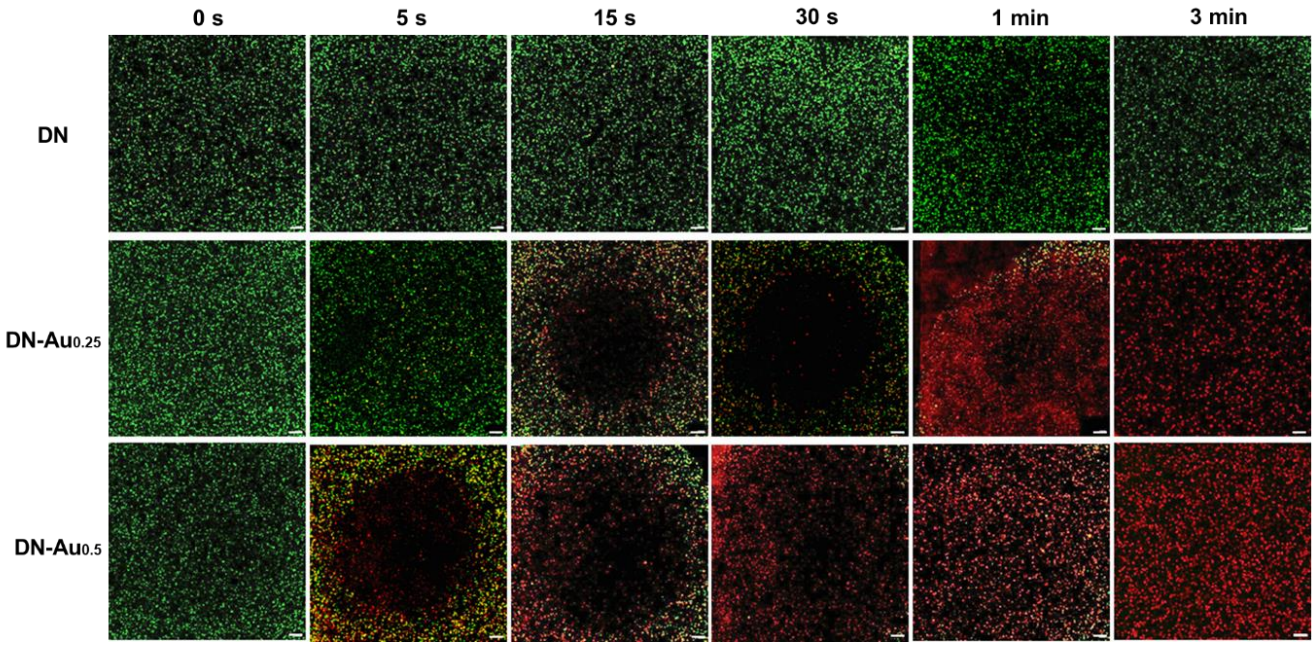

Figure S18. Confocal microscopy images of MDA-MB-231-B1 cells encapsulated in **DN**, **DN-Au$_{0.25}$** and **DN-Au$_{0.5}$** hydrogels after 24 h with different 532 nm laser irradiation. Calcein AM (green) and propidium iodide (red) mark the live and dead cells, respectively. Scale bar: *200 µm*.

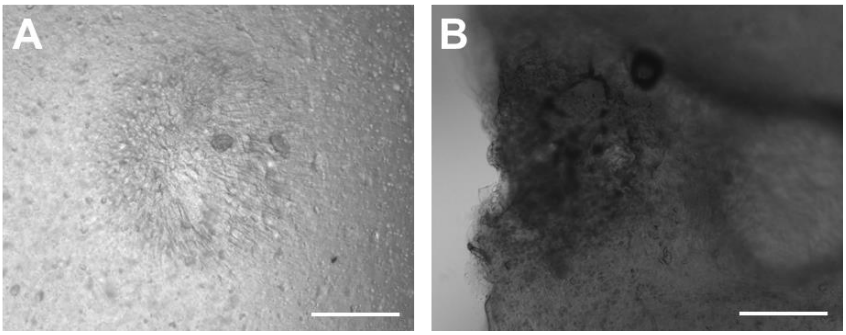

Figure S19. Confocal microscopy images of burned **DN-Au$_{0.25}$** hydrogel encapsulated with MDA-MB-231-B1 after different 532 nm laser irradiation time. (A) 30 s (B) 1 min. Scale bar: *500 µm*.

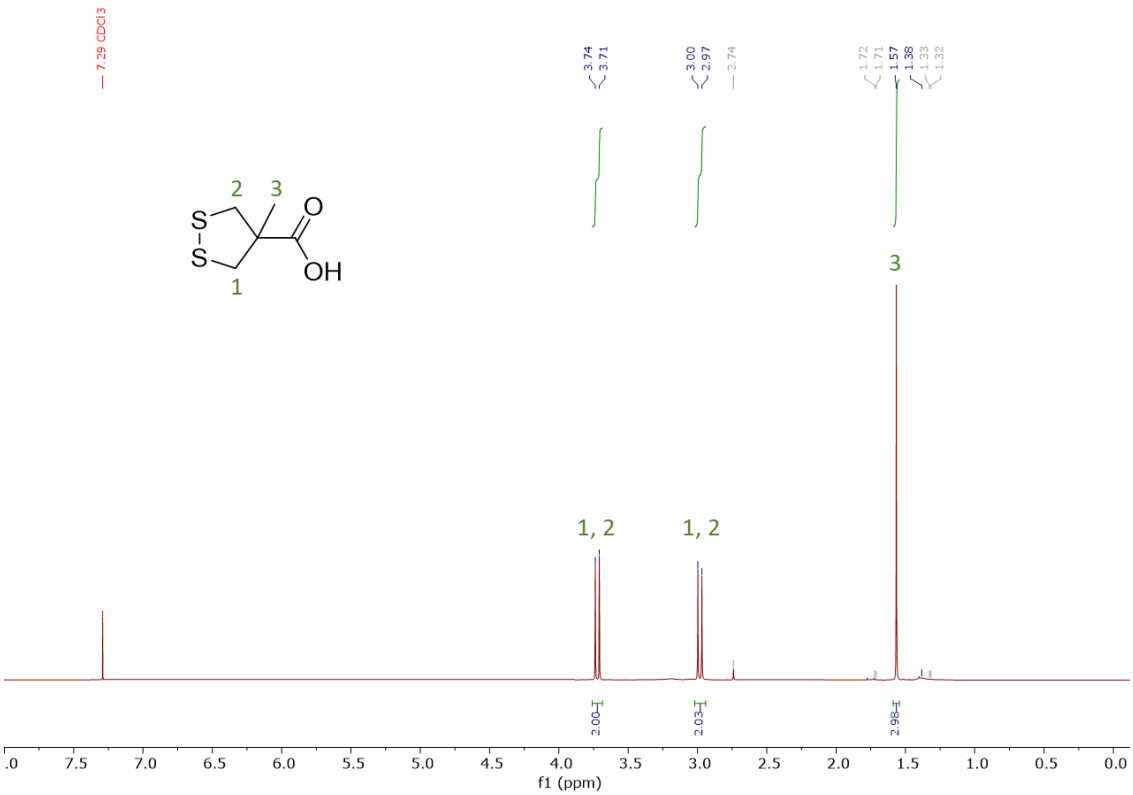

Figure S20. ^{1}H-NMR (400 Hz, 298K, $CDCl_3$) spectrum of **DT**.

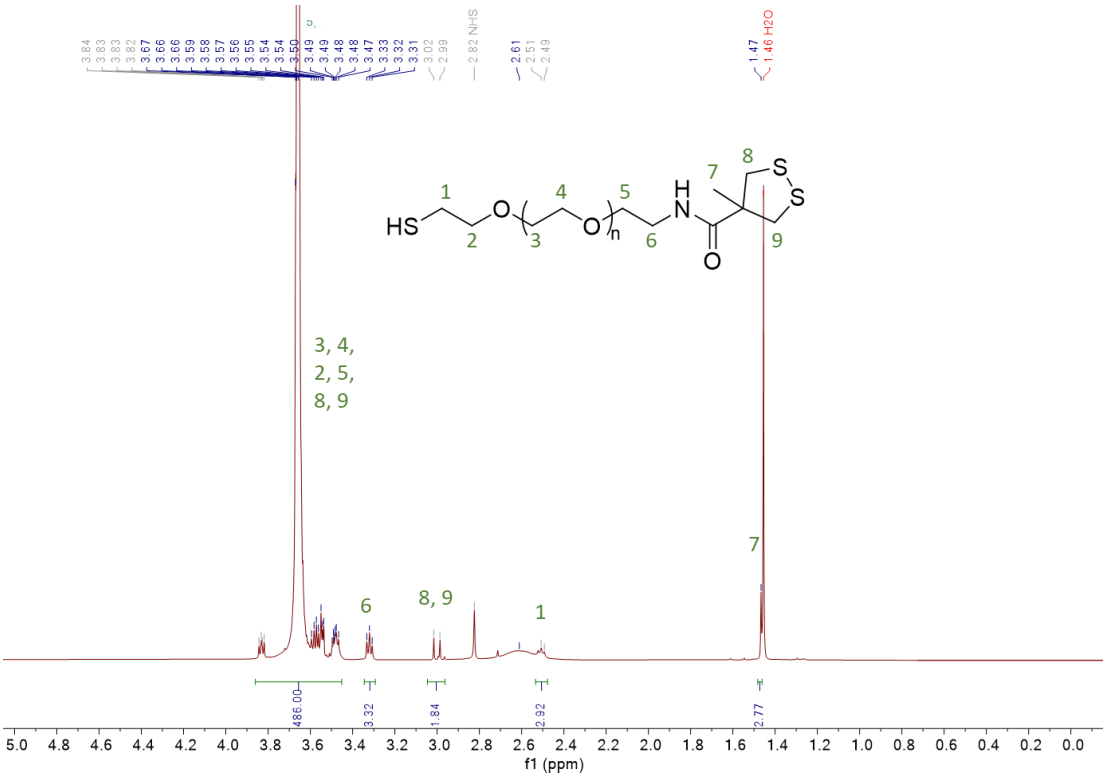

Figure S21. ^{1}H-NMR (400 Hz, 298K, $CDCl_3$) spectrum of **HS-PEG$_{5400}$-DT**. The degree of functionalization was 92%.

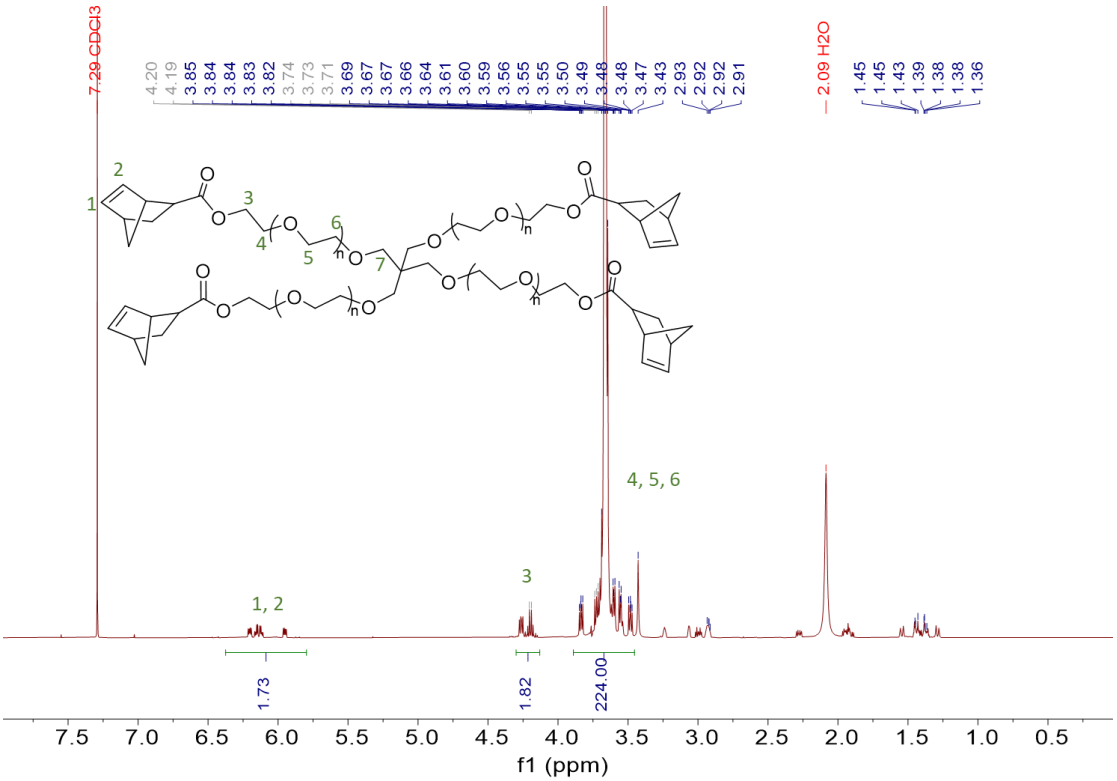

Figure S22. ^{1}H-NMR (400 Hz, 298K, $CDCl_3$) spectrum of **PEG$_4$-NB**. The degree of functionalization was 91%.

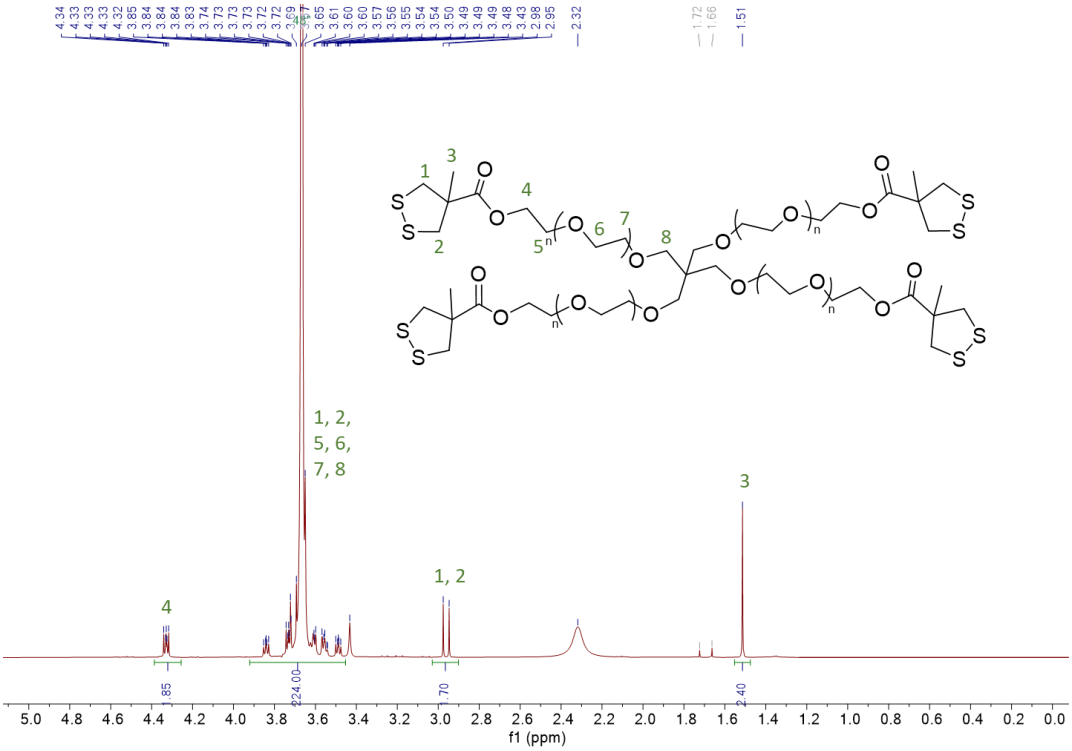

Figure S23. ^{1}H-NMR (400 Hz, 298K, $CDCl_3$) spectrum of **PEG$_4$-DT**. The degree of functionalization was 92%.

Reference

(1) Tong, C.; Wondergem, J. A. J.; van den Brink, M.; Kwakernaak, M. C.; Chen, Y.; Hendrix, M.; Voets, I. K.; Danen, E. H. J.; Le Devedec, S.; Heinrich, D.et al. Spatial and Temporal Modulation of Cell Instructive Cues in a Filamentous Supramolecular Biomaterial. *ACS Appl Mater Interfaces* **2022,** *14* (15), 17042.

(2) Tong, C.; Liu, T.; Saez Talens, V.; Noteborn, W. E. M.; Sharp, T. H.; Hendrix, M.; Voets, I. K.; Mummery, C. L.; Orlova, V. V.; Kieltyka, R. E. Squaramide-Based Supramolecular Materials for Three-Dimensional Cell Culture of Human Induced Pluripotent Stem Cells and Their Derivatives. *Biomacromolecules* **2018,** *19* (4), 1091.

(3) Marat, X. L.-L., K.; Marrot, L. Administration of Dithiolane Compounds for Photoprotecting the Skin. *US8530511B2* **2013**.

(4) JOHN TURKEVICH, P. C. S., JAMES HILLIE. A study of the nucleation and growth processes in the synthesis of colloidal gold. *SYNTHESIS OF COLLOIDAL GOLD* **1951**.

(5) FRENS., G. Controlled Nucleation for the Regulation of the Particle Size in Monodisperse Gold Suspensions. *Nature Physical Science* **1973,** *241(105)*, 20.

(6) Thambiliyagodage, C. Ligand exchange reactions and PEG stabilization of gold nanoparticles. *Current Research in Green and Sustainable Chemistry* **2022,** *5*.

Chapter 6

Summary and outlook

6.1 The importance of supramolecular-based hydrogels

Supramolecular hydrogels have emerged as advanced artificial platforms for *in vitro* engineering of the cellular microenvironment within living systems. Despite the advantages offered by non-covalent dynamic interactions, which confer dynamic and reversible properties to the material, their application in stiff and load-bearing tissue engineering has been limited. In this work, I systematically modulated the design of supramolecular monomers based on squaramides, covalent polymers, and their mixtures to tune the mechanical characteristics of the resulting hydrogels to direct cell behavior for mimicking the extracellular matrix (ECM). Hence, the information presented in this thesis contributes to the expansion of current fundamental knowledge regarding the assembly of squaramide-based supramolecular hydrogels and their *in vitro* studies, which serve as a basis for exploring functional supramolecular biomaterials. This chapter summarizes the main discoveries within this thesis, their implications for the field, and provides an outlook for advancing research on the respective topics.

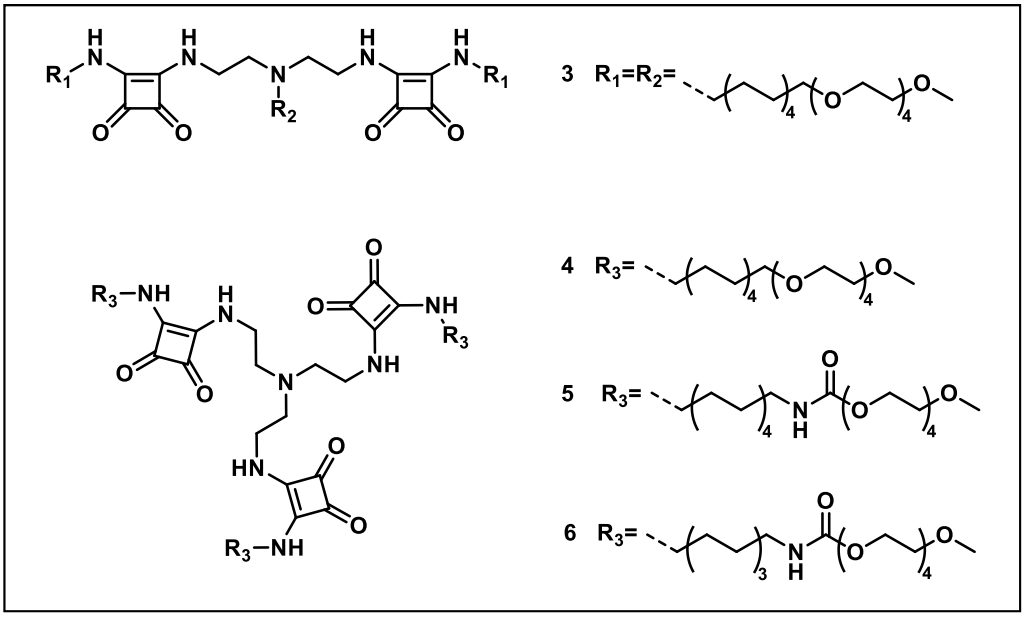

Figure 1. Chemical structures of squaramide-based gelators developed/used in this thesis. **3**, **4** and **5** were used in **Chapter 2**. **6** (**C8-SQ**) was used in **Chapter 3**. **5** and **6** are parental squaramide-based gelators that are commonly used for modifications and applications.

In **Chapter 2**, a small library of tripodal squaramide monomers was examined in an aqueous environment with respect to their self-assembly behavior and thermoresponsive properties. The tripodal squaramide-based hydrogelator as earlier reported by our group yields fibrous hydrogel at the critical gelation concentration, showing the importance of hydrophobic and hydrogen bonding interactions for supramolecular hydrogel formation. To gain a deeper view of the balance of hydrophilicity and hydrophobicity, and hydrogen bonds on gel formation, a family of tripodal squaramide-based monomers were designed and synthesized in moderate yields (Figure 1), and their self-assembly properties were investigated and compared with the corresponding parent tripodal squaramide-based hydrogelator. The exchange of the carbamates with the ether linkages resulted in a reduction in hydrogel stiffness, whereas the reduction of the number of squaramide units and

hydrophilic and hydrophobic properties resulted in the ability to form gel phase materials. The observed effects on gelation likely result from the reduced degrees of polymerization of the squaramide monomers, with a reduction in the number of the squaramide synthons affecting their entanglement. Furthermore, hydrogels **3**-**5** exhibited lower critical solution temperature (LCST) behavior, opening the door for developing thermoresponsive hydrogels. Specifically, hydrogels **4** and **5** maintained their original shapes but experienced shrinkage, ultimately transforming into highly oriented materials upon heating to 130°C and subsequent cooling to room temperature. Collectively, these findings not only underscore the essential structural features guiding the gelation and thermoresponsiveness of tripodal squaramide-based monomers in water but also suggest their potential adaptability to structural modifications for future endeavors aimed at their transformation into functional supramolecular biomaterials.

Based on these results, it is obvious that the design of supramolecular hydrogelators necessitates careful consideration of several factors.[1] Foremost among these is the hydrophilic-hydrophobic balance, serving as the main force driving the self-assembly process . Additionally, the characteristics of hydrogen bonds, encompassing their quantity, positioning, and types, exert considerable influence on intramolecular and intermolecular forces. Other factors, such as π-π stacking, also affect the dynamics of the system.

Our group previously functionalized tripodal squaramide-based monomers with 1,2-dithiolanes (DT) to trigger photocrosslinking within the networks.[2] This modification facilitated the precise control of material mechanics in supramolecular hydrogels by establishing dynamic covalent bonds among the fibers to increase the stiffness of the ECMs. Inspired by these results, I demonstrated the potential to modulate the mechanical properties of supramolecular hydrogels by coupling phenol groups (Phe) onto the squaramide-based monomer (**SQ-Phe**) derived from **Chapter 2** for *in situ* covalent photopolymerization by visible light stiffening the hydrogel while modulating its complex mechanical characteristics (e.g., strain-stiffen, stress relaxation, viscoplasticity) (figure 2A-C). Strikingly, co-assembly of a small amount (up to 5 mol%) of the reactive **SQ-Phe** monomer with the native squaramide-based monomer (**C8-SQ**) resulted in a dramatic increase in the stiffness of the hydrogels. By tuning the concentration of the hydrogel or the quantity of **SQ-Phe**, this filamentous supramolecular hydrogel displayed strain-stiffening, strain-enhanced stress relaxation, and viscoplasticity properties like biopolymers (e.g., actin, fibrin) of the ECM that are used for developing organ and tissue models. Moreover, the supramolecular hydrogel affected the growth of individual 3T3 cells, fostered the formation of anisotropic spheroids under a 3D environment without additional bioactive cues (e.g., RGD), in which their morphology could be modulated by the strategic adjustment of crosslinker concentration and fiber density (figure 2D). Additionally, the neuronal stem cells could be 3D differentiated into nerve cells within these supramolecular hydrogels in a soft environment. Overall, this study demonstrates the broad applicability of supramolecular hydrogel for diverse 3D cell cultures where anisotropy of the substrate is desired, with the potential to guide stem cells to differentiate for tissue engineering and disease modeling applications.

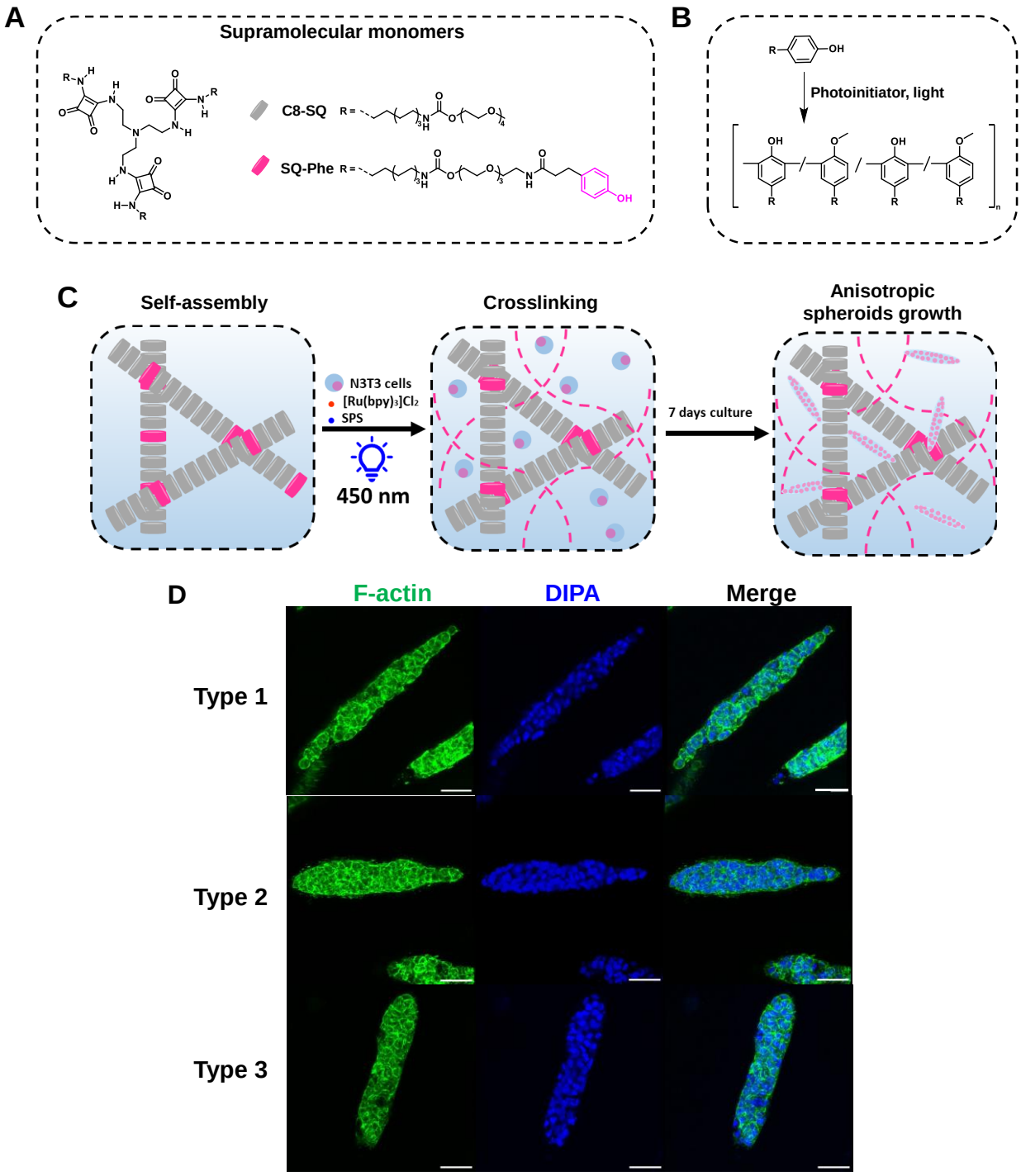

Figure 2. (A) Supramolecular monomer (**C8-SQ**, **SQ-Phe**) components are used to prepare hydrogels. (B) Phenol photopolymerization for crosslinking supramolecular nanofilaments. (C) The visible light-induced photopolymerized supramolecular networks for 3D cell culture promote anisotropic spheroid growth. (D) Representative confocal images of three major morphological growth patterns of NIH 3T3 fibroblast spheroids stained with F-actin and DAPI in tripodal squaramide-based hydrogels with different amounts of **SQ-Phe** after 10 days culture. Scale bar: *100 μm*.

While the reinforcement of supramolecular hydrogel's mechanical properties can be achieved through nanoscale fiber crosslinking that can mimic certain features of the ECM, significant challenges

still exist in the application of filamentous supramolecular polymers as stiff tissues especially where loading is necessary. **Chapter 3** disclosed a rapid ring-opening photopolymerization of DT and norbornene (NB) to prepare a covalent network through chain-growth polymerization simultaneously, that crosslinks nanoscale supramolecular filaments, yielding a tough double network hydrogel that can sustain dynamic compression in 3D cell culture. These hydrogels show cartilage-like mechanical characteristics, namely their biomimetic complex mechanical properties, stress response and relaxation under compression that can be tuned according to component ratios and concentrations using light. The distinctive mechanical properties are connected to their inhomogeneous network architectures, generated through the polymerization of monomers, resulting in the concurrent formation and reinforcement of poly(disulfide)s and poly(disulfide-norbornene)s networks that are achieved through UV exposure at the same wavelength. Notably, the potential of this double network for 3D culture was exploited through the encapsulation of human primary articular chondrocytes (hPACs) where the cells show high cell viability. Moreover, the cyclic compressive loading was applied on hPACs-laden hydrogels in 3D, resulting in increased deposition of sulfated- glycosaminoglycans after daily loading for 14 days. Notably, exploiting the photoreactive macromonomers, I mechanically pattern the materials at cell-relevant length scales to engineer spatially distinct mechanical domains, stiff and soft, to mimic developmental and disease conditions encountered in cartilage with superimposed compressive loading. The enclosed covalent network fortification strategy combined with bioorthogonal photopolymerization provides a base to tune the mechanics of filamentous supramolecular biomaterials, opening avenues to expand their 3D cell culture application where cyclic mechanical loading is involved. Compared with **Chapter 3**, this work introduced dynamic covalent bonds into **DN** hydrogels that provide the potential for degradability in the designing of stiff hydrogels.

Chapter 4 demonstrated a visible light-induced photopolymerization of phenol groups (**Phe**) to simultaneously prepare double networks (**DN**s) by using the filamentous supramolecular polymer (with 5% mol **SQ-Phe**) and poly(ethylene glycol) network (functionalized with **Phe** group) for 3D culture with cyclic compressive loading. These networks maintained the filamentous supramolecular structure but overcame the mechanical fragility of the supramolecular materials. Importantly, these hydrogels show biomimetic complex mechanical properties, such as a cartilage-like stress response, and relaxation under compression that can be tuned according to component ratios and concentrations. The incorporation of filamentous supramolecular structures was observed to expedite stress relaxation in both shear and axial direction, even in cases where the stiffness was elevated. These **DN** hydrogels can be used for human primary articular chondrocytes culture in 3D and cyclic compressive loading of these gels for 2 days showed enhanced deposition of sulfated-glycosaminoglycans (s-GAGs) compared to the free swelling condition. These **DN** hydrogels demonstrate potential for multiple applications in 3D cell cultures across diverse tissue types requiring compressive loading, opening avenues to map the essential chemical parameters in the next-generation hydrogels for advanced 3D *in vitro* modeling and targeted regenerative therapies, especially osteoarthritis (OA).

Stimuli-responsive hydrogels provide possibilities to control hydrogel properties in response to external stimuli, which has been applied in many aspects such as controlled drug delivery, sensing materials, and tissue engineering.[3] **Chapter 5** disclosed a stimulus-responsive **DN** hydrogels with

mechanical properties that mimic the compressive properties of cartilage and the potential to provide localized heating that can be used for various *in vitro* and *in vivo* aims, including therapy. In this work, I used the chemistry and **DN** material from **Chapter 4** and incorporated the 15 nm gold nanoparticles to create a dual-network hydrogel with enhanced mechanical properties and additional functions. The uncrosslinked hydrogels were injectable and the injected shape could stay stable in PBS after crosslinking. Additionally, the addition of gold nanoparticles enhanced the energy dissipation ability of the hydrogels as well as introduced tunable conductivity and photothermal properties when irradiated with 532 nm. The hydrogel showed good cytocompatibility and the photo-thermal effect successfully applied in the MDA-MB-231-B1 3D cancer model. The phototherapy effect is positively correlated with AuNPs concentration and light dosage, and the position could be precisely controlled by the laser, providing the potential applications of squaramide-based hydrogels for photothermal therapy involving cancerous tissues and valuable insights for studying complex diseases.

6.2 Future Perspective

The modification of tripodal squaramide-based gelators may appearstraightforward, yet it involves several considerations to achieve the desired self-assembly. Several factors come into play, such as the hydrophilic-hydrophobic balance of the monomer that can play a dominating role. As we can see, both DT and Phe functionalized squaramide-based monomers exhibit limited solubility under physiological conditions. While co-self-assembly can mitigate this limitation permitting the dissolution of the functionalized monomers for co-assembly to attain the maximum stiffness of the supramolecular material. Another critical factor is the crosslinking conditions, including light type and intensity, crosslinking speed, and photoinitiator quantities, all of which may affect cell behaviour. Consequently, implementing a mild crosslinking method becomes essential for subsequent biological studies.

While notable progress has been made in enhancing supramolecular hydrogels' compressive properties, the current achievements fall short of meeting the properties of native cartilage tissues (Figure 3). They require further refinement to reach levels comparable to native cartilage, which can withstand stress on the order of megapascals and exhibit recoverability. While the supramolecular materials are toughened by the disclosed approaches in this thesis, they still exhibit softening in response to loading over time. This limits their use for long-term applications and will need to be addressed in future designs. Furthermore, our present materials are primarily characterized under compressive forces, and investigations into stretching properties remain relatively scarce in the supramolecular hydrogel field. Therefore, a meticulous molecular structure design, careful selection of appropriate chemical bonds for network formation, and consideration of polymer types and ratios become paramount in developing stretchable hydrogels, which is pivotal for creating smart materials with versatile applications.

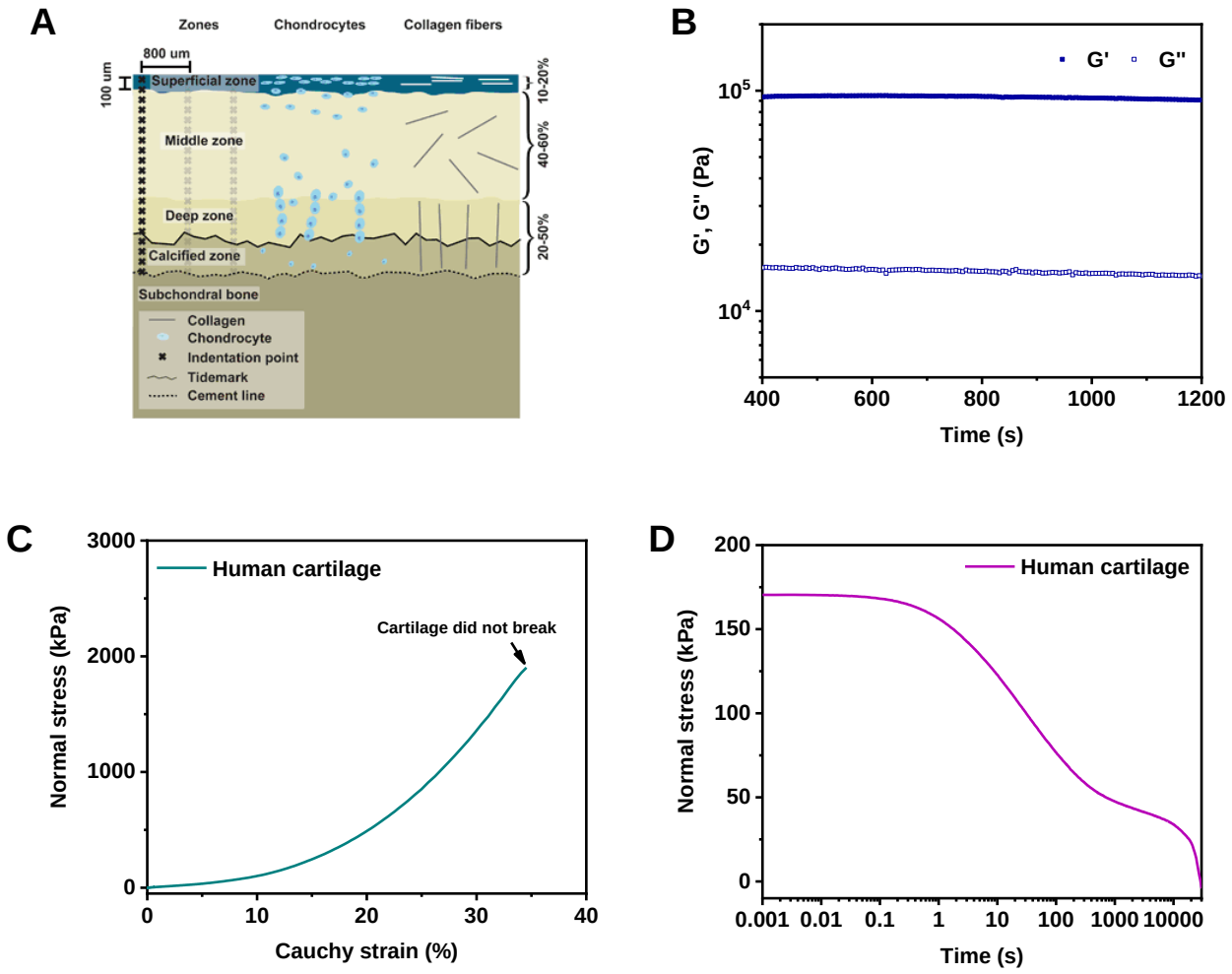

Figure 3. (A) Cross section of human knee joint including four zones: superficial zone (10–20%), middle zone (40–60%), deep zone (20–50%) and calcified zone.[4] (B) Time sweeps measurements of human cartilage at RT. (C) Uniaxial stress-strain curves of human cartilage under a consistent speed of 10 µm/s, the cartilage did not break at the end of the measurement. (D) Poroviscorelaxation curves of human cartilage under 15% consistent normal strain.

In vivo, environments exhibit dynamic complexity, characterized by varied human ECM compositions in different regions, each contributing to specific physiological functions. Nowadays, complex mechanical properties (e.g., strain-stiffening, viscoelasticity, viscoplasticity, poroelasticity) have been introduced into the hydrogel field (native and synthetic) to better understand specific cell behaviors. Therefore, in the future, it will also be crucial to delve into the intricate interplay between the complex mechanical properties of hydrogels and cellular behavior. Besides, integrating peptides onto the supramolecular monomer is imperative for enhancing biocompatibility and fostering a conducive cellular environment to promote beneficial cell functions (figure 4). This exploration aims to unveil increasingly sophisticated mechanical and biological characteristics that closely emulate diverse tissues. Identifying specific complex mechanical and biological properties influencing cellular behavior is imperative, and precision in orchestrating these properties is essential to sculpting a framework for controlling cell phenotypes and fostering the growth of organs or specific tissues.

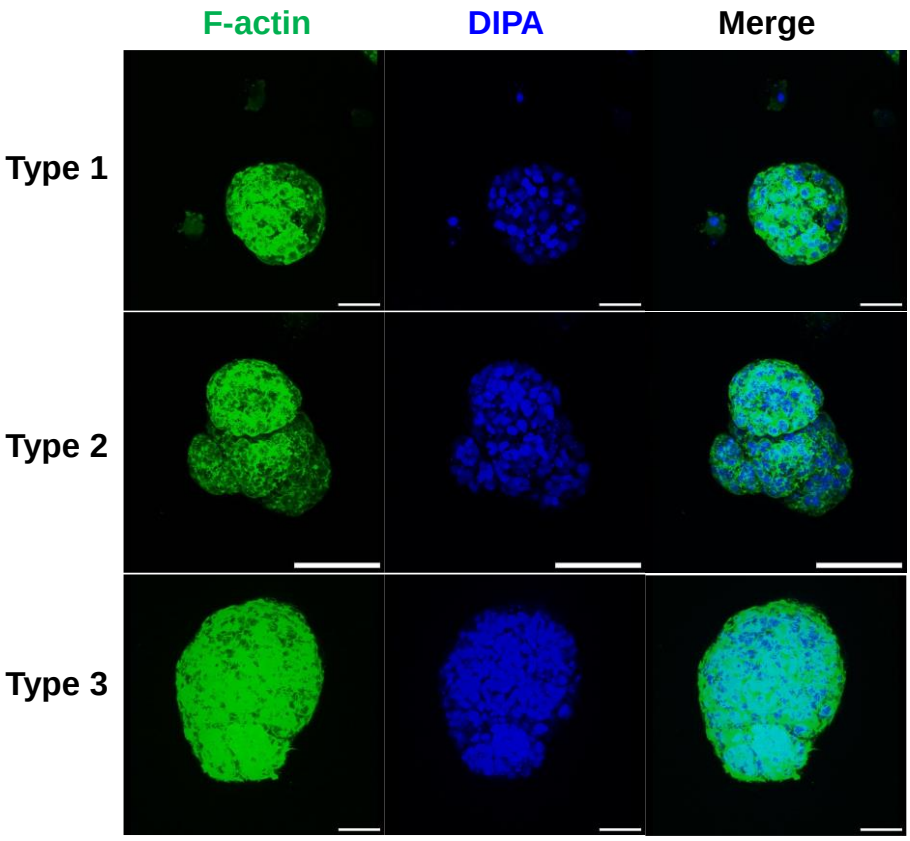

Figure 4. Representative confocal images of three major morphological growth patterns of NIH 3T3 fibroblast spheroids in tripodal squaramide-based hydrogels with bioactive cues (RGD) after 10 days of culture and stained with F-actin and DAPI. Scale bar: *100 μm*.

Reference

(1) Dong, R.; Pang, Y.; Su, Y.; Zhu, X. Supramolecular hydrogels: synthesis, properties and their biomedical applications. *Biomater Sci* **2015,** *3* (7), 937.

(2) Tong, C.; Wondergem, J. A. J.; Heinrich, D.; Kieltyka, R. E. Photopatternable, Branched Polymer Hydrogels Based on Linear Macromonomers for 3D Cell Culture Applications. *ACS Macro Lett.* **2020,** *9* (6), 882.

(3) V á zquez - Gonz á lez, M.; Willner, I. Stimuli - responsive biomolecule - based hydrogels and their applications. *Angew. Chem. Int. Ed.* **2020,** *59* (36), 15342.

(4) Antons, J.; Marascio, M. G. M.; Nohava, J.; Martin, R.; Applegate, L.; Bourban, P.; Pioletti, D. Zone-dependent mechanical properties of human articular cartilage obtained by indentation measurements. *Journal of Materials Science: Materials in Medicine* **2018,** *29*, 1.

Nederlandse samenvatting

Supramoleculaire hydrogelen zijn geavanceerde kunstmatige materialen voor *in vitro* engineering van de micro-omgeving in levende cellen. Ondanks de voordelen van niet-covalente dynamische interacties, die dynamische en omkeerbare eigenschappen aan het materiaal verlenen, is hun toepassing in stijve en dragende weefselengineering tot nu toe beperkt gebleven. In dit proefschrift heb ik supramoleculaire monomeren op basis van squaramides en covalente polymeren ontworpen en deze gemengd om de invloed van de mechanische eigenschappen van de resulterende hydrogelen op cellen te bestuderen en om de extracellulaire matrix (ECM) na te bootsen. De studies beschreven in dit proefschrift dragen bij aan de fundamentele kennis over de samenstelling van squaramide-gebaseerde supramoleculaire hydrogelen, het verkennen van functionele supramoleculaire biomaterialen en mogelijke toepassingen in biomedische toepassingen.

In **Hoofdstuk 2** werd een kleine bibliotheek van tripodale squaramide-monomeren onderzocht in een waterige omgeving met betrekking tot hun zelf-assemblagegedrag en thermoresponsieve eigenschappen. De eerder gerapporteerde tripodale squaramide-gebaseerde hydrogelator vormt vezelachtige hydrogel boven de kritische gelatieconcentratie, wat het belang van hydrofobe en waterstofbindende interacties voor de vorming van een supramoleculaire hydrogel aantoont. Om een beter inzicht te krijgen in de hydrofiliciteit/hydrofobiciteit balans en het effect van waterstofbindingen op gelvorming werd een familie van tripodale squaramide-gebaseerde monomeren ontworpen en gesynthetiseerd. De zelf-assemblage-eigenschappen werden onderzocht en vergeleken met de oorspronkelijke tripodale squaramide-gebaseerde hydrogelator. De vervanging van de carbamaten door etherbindingen verlaagde de stijfheid van de hydrogel, terwijl de vermindering van het aantal squaramide-eenheden en hydrofiele en hydrofobe eigenschappen leidde tot de vorming van gel-fasematerialen. De waargenomen effecten op gelering zijn waarschijnlijk het gevolg van de verminderde polymerisatiegraad van de squaramide-monomeren, waarbij een vermindering van het aantal squaramide-synthons hun verstrengeling beïnvloedt. Bovendien vertoonden hydrogels **3**-**5** een lager kritische oplossings-temperatuur gedrag, wat de ontwikkeling van thermoresponsieve hydrogels mogelijk maakt. Hydrogels **4** en **5** behielden hun oorspronkelijke vorm, maar ondergingen krimp, wat uiteindelijk leidde tot de vorming van sterk georiënteerde materialen bij verwarming tot 130°C en daaropvolgende afkoeling tot kamertemperatuur. Samengevat laten deze studies zien dat niet alleen de essentiële structurele kenmerken die de gelering en thermoresponsiviteit van tripodale squaramide-gebaseerde monomeren in water sturen, maar suggereren ook de mogelijke aanpasbaarheid aan structurele modificaties voor toekomstige functionele supramoleculaire biomaterialen.

Op basis van deze resultaten is het duidelijk dat het ontwerp van supramoleculaire hydrogelators zorgvuldige overweging van verschillende factoren vereist. De belangrijkste hiervan is de balans tussen hydrofiele en hydrofobe eigenschappen, die als de belangrijkste kracht dient voor het zelf-

assemblageproces. Bovendien oefenen de kenmerken van waterstofbindingen, inclusief hun aantal, positionering en typen, aanzienlijke invloed uit op intra- en intermoleculaire krachten. Andere factoren, zoals π-π interacties beïnvloeden ook de dynamiek van het systeem.

In een vorige studie werden tripodale squaramide-gebaseerde monomeren gemodificeerd met 1,2-dithiolaanen om fotocrosslinking mogelijk te maken. Deze monomeermodificatie faciliteerde de precieze controle van materiaaleigenschappen in supramoleculaire hydrogelen door de vorming van dynamische covalente bindingen tussen de vezels resulterende in de controle van de stijfheid van de ECM's. Geïnspireerd door deze resultaten werd de mogelijkheid om de mechanische eigenschappen van supramoleculaire hydrogels te moduleren met behulp van fenolgroepen (Phe) in het squaramide-gebaseerde monomeer (**SQ-Phe**) bestudeerd. *In situ* covalente polymerisatie van SQ-Phe door zichtbaar licht van de hydrogel beïnvloedde de complexe mechanische eigenschappen (bijvoorbeeld rek-stijving, spanningsontspanning, viscoplastisiteit). Opvallend was dat de co-assemblage van een kleine hoeveelheid (tot 5 mol%) van het reactieve **SQ-Phe** monomeer met het oorspronkelijke squaramide-gebaseerde monomeer (**C8-SQ**) resulteerde in een sterke toename van de hydrogelstijfheid. Door de concentratie van de hydrogel of de hoeveelheid **SQ-Phe** af te stemmen, vertoonde deze filamenteuze supramoleculaire hydrogel rek-stijving, rek-versterkte spanningsontspanning en viscoplastische eigenschappen zoals biopolymeren (bijvoorbeeld actine, fibrine) van de ECM die worden gebruikt voor de ontwikkeling van organen en weefselmodellen. Bovendien beïnvloedde de supramoleculaire hydrogel de groei van individuele 3T3-cellen, bevorderde het de vorming van anisotrope sferoïden onder een 3D-omgeving zonder extra bioactieve liganden zoals RGD, waarbij hun morfologie kon worden gemoduleerd door de optimalisatie van crosslinkerconcentratie en vezeldichtheid. Daarnaast konden de neuronale stamcellen 3D worden gedifferentieerd in zenuwcellen binnen deze supramoleculaire hydrogels in een zachte omgeving. Deze studie toont de brede toepasbaarheid van supramoleculaire hydrogels voor diverse 3D-celculturen aan waar anisotropie van het substraat gewenst is, met het potentieel om stamcellen te sturen voor weefselengineering en ziektemodelleringstoepassingen.

Hoewel de versterking van de mechanische eigenschappen van supramoleculaire hydrogelen kan worden bereikt door nanovezelcrosslinking die bepaalde kenmerken van de ECM nabootsen, bestaan er nog aanzienlijke uitdagingen bij de toepassing van filamentaire supramoleculaire polymeren als stijve weefsels, vooral waar belasting nodig is. **Hoofdstuk 3** beschrijft een studie waarbij ringopeningsfotopolymerisatie van 1,2-dithiolanes (DT) en norborneen (NB) en kettinggroeipolymerisatie gebruikt werd om een covalent netwerk te maken resulterend in gecrosslinkte supramoleculaire filamenten in een taaie dubbelnetwerkhydrogel die dynamische compressie in 3D-celcultuur kan weerstaan. Deze hydrogelen vertonen kraakbeenachtige mechanische eigenschappen, namelijk hun biomimetische complexe mechanische eigenschappen, spanningsreactie en ontspanning onder compressie die kunnen worden afgestemd op basis van componentverhoudingen en concentraties met behulp van licht. De mechanische eigenschappen zijn verbonden met hun

inhomogene netwerkarchitecturen, gegenereerd door de polymerisatie van monomeren, resulterend in de gelijktijdige vorming en versterking van poly(disulfide)s en poly(disulfide-norborneen)s netwerken door middel van UV-bestraling bij dezelfde golflengte. De mogelijke toepassing van dit dubbele netwerk voor 3D-cultuur werd onderzocht door menselijke primaire articulair chondrocyten (hPACs) te kweken met een goede levensvatbaarheid. Bovendien resulteerde de cyclische compressieve belasting op hPACs-belaadde 3D-hydrogel in verhoogde afzetting van gesulfateerde glycosaminoglycanen na dagelijkse belasting gedurende 14 dagen. Door gebruik te maken van de fotoreactieve macromonomeren werden de materialen voorzien van een ruimtelijk onderscheidende mechanische domeinen, stijf en zacht, om ontwikkelings- en ziekteomstandigheden na te bootsen die aanwezig is in kraakbeen met bovenliggende compressieve belasting. Deze strategie voor netwerkversterking door covalente bindingen gecombineerd met bioorthogonale fotopolymerisatie biedt een basis om de mechanica van filamentaire supramoleculaire biomaterialen af te stemmen. Dit geeft nieuwe mogelijkheden om 3D-celculturen waar cyclische mechanische belasting bij betrokken is, te bestuderen. Deze studie van dynamische covalente bindingen in DN-hydrogelen introduceert daarom de mogelijkheid om hydrogeldegradatie te controleren in stijve hydrogels.

In **Hoofdstuk 4** werd zichtbaar licht geïnduceerde fotopolymerisatie van fenolgroepen (**Phe**) gebruikt om gelijktijdig dubbele netwerken (**DN**s) te bereiden door gebruik te maken van het filamentaire supramoleculaire polymeer (met 5% mol **SQ-Phe**) en poly(ethyleenglycol) netwerk (gefunctionaliseerd met **Phe**-groep) voor 3D-cultuur met cyclische compressieve belasting. Deze netwerken behielden de filamentaire supramoleculaire structuur met een hogere mehanische sterkte. Deze hydrogelen bezitten biomimetische complexe mechanische eigenschappen, zoals een kraakbeenachtige spanningsreactie en ontspanning onder compressie die kunnen worden afgestemd op basis van componentverhoudingen en concentraties. De opname van filamentaire supramoleculaire structuren bleek de spanningsontspanning in zowel de schuif- als axiale richting te versnellen, zelfs in gevallen waar de stijfheid was verhoogd. Deze **DN**-hydrogelen kunnen worden gebruikt voor menselijke primaire articulair chondrocyten-cultuur in 3D en cyclische compressieve belasting van deze gels gedurende 2 dagen vertoonde een verbeterde afzetting van gesulfateerde glycosaminoglycanen (s-GAGs) vergeleken met de vrije zweltoestand. Deze **DN**-hydrogelen kunnen toegepast worden voor 3D-celculturen van diverse weefseltypes die compressieve belasting vereisen. Tevens maakt het nieuwe toepassingen mogelijk door de essentiële chemische parameters in de volgende generatie hydrogelen voor geavanceerde 3D-in vitro modellering en gerichte regeneratieve therapieën, vooral osteoartritis (OA), in kaart te brengen.

Stimuli-responsieve hydrogelen bieden mogelijkheden om de fysische eigenschappen te controleren in reactie op externe prikkels, wat is toegepast in vele aspecten zoals gecontroleerde medicijnafgifte, sensorische materialen en weefselkweek. **Hoofdstuk 5** beschrijft een stimulus-responsieve **DN**-hydrogel met mechanische eigenschappen die de compressieve eigenschappen van kraakbeen nabootsen en het potentieel om lokale verwarming te bieden die kan worden gebruikt voor

verschillende in vitro en in vivo doeleinden, waaronder therapie. In deze studie heb ik de chemie en DN-materialen uit **Hoofdstuk 4** gebruikt en 15 nm goudnanodeeltjes toegevoegd om een dual-network hydrogel te creëren met verbeterde mechanische eigenschappen en functies. De niet-gecrosslinkte hydrogels waren injecteerbaar en bleef stabiel in PBS na crosslinking. Bovendien verbeterde de toevoeging van goudnanodeeltjes het energieabsorptievermogen van de hydrogelen en introduceerde het instelbare geleidbaarheid en fotothermische eigenschappen wanneer bestraald met 532 nm. De hydrogel vertoonde goede cytocompatibiliteit en het fotothermische effect werd succesvol toegepast in het MDA-MB-231-B1 3D-kankermodel. Het fotothermische effect is afhankelijk van de AuNPs-concentratie, lichtdosering en lokale belichting was mogelijk door gebruik te maken van een laser lichtbron, wat potentiële toepassingen van squaramide-gebaseerde hydrogels voor fotothermische therapie bij kankerweefsel dichterbij brengt en waardevolle inzichten voor het bestuderen van complexe ziekten biedt.

Curriculum vitae

Ying Chen was born on July 22, 1992, in Wuyi, China. She graduated from Wuyi First Senior High School in 2010 and pursued a BSc degree in Polymer Science at Hunan University, where she developed an initial interest in science. Afterwards, she began her MSc studies in Polymer Science at Zhejiang University under the supervision of Professor Dr. Zhengwei Mao, where she developed a keen interest in biomaterials. Ying obtained her MSc degree in 2017 and subsequently joined BASF in Shanghai as an assistant chemist. During her nearly two years at BASF, she gained significant experience in emulsion polymerization and contributed to the development of commercial products.

In 2019, Ying joined the Supramolecular & Biomaterials Chemistry (SBC) group at the Leiden Institute of Chemistry, under the supervision of Professor Dr. A. Kros and Dr. Roxanne E. Kieltyka, to pursue her Ph.D. Her doctoral research focused on squaramide-based tripodal supramolecular hydrogels and the advancement of functional materials aimed at understanding cellular responses within synthetic 3D environments. She employed a range of chemical, analytical, and biological methodologies to gain profound insights into the applications of synthetic hydrogels in various biological contexts.

Ying's Ph.D. studies involved collaborations with Professor Dr. M. Drukker (LACDR), Professor Dr. E.S. Jagalska (IBL), and Dr. Y.F.M. Ramos (LUMC). She presented her research through posters at the CHAINS conferences in 2019 and 2020. She delivered oral presentations at IUPAC and CHAINS conferences in the Netherlands in 2023. Ying also had scientific conduct course, summer school science communication, and gave practical courses to the bachelors during her PhD. All the experience helped Ying to develop lots of advanced academic skills such as critical thinking and analysis, technical proficiency, grant writing and application, and teaching. She also gained many soft-skills like problem-solving, time management, ethical and professional conduct. These competencies equip her for diverse career paths in and beyond academia. Currently, Ying is working as a process engineer in medical device field, and she is excited to continue her career in innovative biomaterials and apply her expertise to advance the field further in the future.

List of Publications

Publications relating to this thesis

1. ***Ying Chen***,[+] Ciqing Tong,[+] Roxanne E. Kieltyka*, Ditholane-Norbornene Photopolymerization of a Hybrid Covalent and Filamentous Supramolecular Biomaterial Permits Cyclic Compressive Loading in 3D Cell Culture, *submitted*.
2. ***Ying Chen***, Roxanne E. Kieltyka*, A Photoresponsive Filamentous Supramolecular-Nanocomposite Double Network Gel for 3D Cancer Therapy, *submitted*.
3. ***Ying Chen***, Roxanne E. Kieltyka*, Fast stress relaxation of Multi-topologies Double Network Hydrogel for Cyclic Loading in 3D Chondrocyte Culture, *to be submitted*.
4. ***Ying Chen***, Roxanne E. Kieltyka*, A bio-orthogonal Crosslinked Filamentous Supramolecular Biomaterial for Anisotropic 3D neuron stem cell culture and differentiation, *to be submitted*.
5. ***Ying Chen***,[+] Francesca Lauria,[+] Roxanne E. Kieltyka*, Understanding the Self-Assembly of Tripodal Squaramide-Based Monomers through Structural Substitution, *to be submitted*.
6. ***Ying Chen***, Roxanne E. Kieltyka*, Biomimetic Poroviscorelaxation in a Hybrid Covalent and Filamentous Supramolecular Biomaterial in 3D Cell Culture, *in preparation*.
7. ***Ying Chen***, Roxanne E. Kieltyka*, Biomimetic Strain-stiffening in bio- orthogonal dynamic-covalent hydrogel networks, *in preparation*.
8. Ciqing Tong, Joeri A. J. Wondergem, Marijn van den Brink, Markus C. Kwakernaak, ***Ying Chen***, Marco M. R. M. Hendrix, Ilja K. Voets, Erik H. J. Danen, Sylvia Le Dévédec, Doris Heinrich, and Roxanne E. Kieltyka*, Spatial and Temporal Modulation of Cell Instructive Cues in a Filamentous Supramolecular Biomaterial. ACS Appl. Mater. Interfaces, 2022, 14, 17042-17054.

Publications from other work

9. Cuixia Bi, Jin Chen, ***Ying Chen***, Yahui Song, Anran Li, Shuzhou Li, Zhengwei Mao,* Changyou Gao, Dayang Wang, Helmuth Möhwald, and Haibing Xia*,Realizing a Record Photothermal Conversion Efficiency of Spiky Gold Nanoparticles in the Second Near-Infrared Window by Structure-Based Rational Design. Chem. Mater., 2018, 30, 2709-2718.
10. Hong Zhu*, ***Ying Chen***, Fang-Jie Yan, Jin Chen, Xin-Feng Tao, Jun Ling, Bo Yang, Qiao-Jun He, Zheng-Wei Mao*. Polysarcosine brushes stabilized gold nanorods for *in vivo* near-infrared photothermal tumor therapy. Acta Biomaterial, 2017, 50, 534-545.
11. ***Ying Chen***, Zhengqing Xu, Xinfeng Tao, Hong Zhu, Zhengwei Mao*, Jun Ling*. Gold nanoparticles coated with polysarcosine brushes to enhance their colloidal stability and circulation time in vivo. Journal of Colloid and Interface Science, 2016, 483, 201-210.

12. Guoping Sheng, ***Ying Chen***, Lijie Han, Zhengwei Mao*. Encapsulation of indocyanine green into cell membrane capsules for photothermal cancer therapy. Acta Biomaterialia, 2016, 43, 251-261.

13. Lijie Han, ***Ying Chen***, Jie Niu, Lihua Peng, Zhengwei Mao*, Changyou Gao*. Encapsulation of a photosensitizer into cell membrane capsules for photodynamic therapy. RSC Adv.,2016, 6, 37212-37220.

14. Wei Yu, ***Ying Chen***, Zhengwei Mao*. Hollow Polyelectrolyte Microcapsules as Advanced Drug Delivery Carriers. Journal of Nanoscience and Nanotechnology, 2016, 5435-5446.

15. Wei Yu, Wenbo Zhang, ***Ying Chen***, Xiaoxue Song, Weijun Tong*, Zhengwei Mao*, Changyou Gao*. Cellular uptake of poly(allylamine hydrochloride) microcapsules with different deformability and its influence on cell functions. Journal of Colloid and Interface Science, 2016, 465, 149-157.

16. Wenjing Zhang, Pengfei Jiang, ***Ying Chen***, Peihua Luo, Guanqun Li, Botuo Zheng, Wei Chen, Zhengwei Mao*, Changyou Gao*. Suppressing the cytotoxicity of CuO nanoparticles by uptake of curcumin/BSA particles. Nanoscale, 2016, 8, 9572-9582.

17. Li-Hua Peng, Yan-Fen Huang, Chen-Zhen Zhang, Jie Niu, ***Ying Chen***, Yang Chu, Zhi-Hong Jiang, Jian-Qing Gao*, Zheng-Wei Mao*, Integration of antimicrobial peptides with gold nanoparticles as unique non-viral vectors for gene delivery to mesenchymal stem cells with antibacterial activity. Biomaterials, 2016, 103, 137-149.

Acknowledgement

“The World is Not Made of Atoms, But of Stories”

I am very grateful for the opportunity to write a pivotal page of my life in Leiden. My journey began with the support of Roxanne and Alexander, who allowed me to work in Leiden university. This period has been enriched with lots of valuable experiences and stories. As this page concludes, it brings a rewarding culmination, not only in scientific research but also in personal growth. Therefore, I am delighted to say that:

“In the End, It’s Not the Years in My Life That Count, It’s the Life in My Years”

I own my deepest gratitude to the SBC group, to the supervisors, my collaborators, my students and my colleagues. I am also profoundly thankful to my family and friends for their unwavering support, and to my bouldering team for helping me build physical strength. You all contributed in your own way to the creation of this thesis.

Thank you!